This electronic thesis or dissertation has been downloaded from Explore Bristol Research, http://research-information.bristol.ac.uk

Author:
Sutcliffe, Joseph E

Title:
A Study of the Crystallography and Ageing Behaviour of the U-Nb Binary Alloy System

General rights
Access to the thesis is subject to the Creative Commons Attribution - NonCommercial-No Derivatives 4.0 International Public License. A copy of this may be found at https://creativecommons.org/licenses/by-nc-nd/4.0/legalcode This license sets out your rights and the restrictions that apply to your access to the thesis so it is important you read this before proceeding.

Take down policy
Some pages of this thesis may have been removed for copyright restrictions prior to having it been deposited in Explore Bristol Research. However, if you have discovered material within the thesis that you consider to be unlawful e.g. breaches of copyright (either yours or that of a third party) or any other law, including but not limited to those relating to patent, trademark, confidentiality, data protection, obscenity, defamation, libel, then please contact collections-metadata@bristol.ac.uk and include the following information in your message:

- Your contact details
- Bibliographic details for the item, including a URL
- An outline nature of the complaint

Your claim will be investigated and, where appropriate, the item in question will be removed from public view as soon as possible.

A Study of the Crystallography and Ageing Behaviour of the U-Nb Binary Alloy System

By

JOSEPH SUTCLIFFE

School of Physics
UNIVERSITY OF BRISTOL

A dissertation submitted to the University of Bristol in accordance with the requirements of the degree of DOCTOR OF PHILOSOPHY in the Faculty of Science.

AUGUST 2019

Word count: approximately 60,000

ABSTRACT

The crystallography of metastable phases in the uranium-niobium binary alloy system has been investigated by x-ray diffraction with an emphasis placed on the derivation of structural parameters such as atomic sites and atomic displacements. Application of an anisotropic microstrain broadening model to Rietveld refinements has permitted the investigation of microstructural sources of strain. In the α'' phase alloys, the C112$_1$/m space group has been shown to provide a good solution when supplied with anisotropic broadening capabilities, whereas in the γ° alloys, it is suggested that there may be some additional nuances that are not fully encapsulated by the P4/nmm structure.

Subsequently, the behaviour of these alloys under low temperature ageing (< 200°C), known to significantly affect mechanical properties of these alloys, has been investigated. XRD showed structures of crystallographic phases to be largely unchanged under ageing but indicated subtle changes in strain, which may be pointing to a nano-scale rearrangement of the structure of mechanical twins, as has been suggested by other authors recently. Evidence for significant chemical segregation at low temperatures could not be found.

Clear phase changes have been observed at higher temperatures by in-situ synchrotron x-ray diffraction with a $\gamma^\circ \rightarrow \alpha''$ reaction shown at medium temperatures (400°C) and complete phase separation by diffusion present at high temperatures (500°C). An intermediate cubic phase was also observed in some cases en-route to full phase separation.

Preparation of these alloys was also investigated. The routines used were assessed to produce surfaces from which mechanically induced stresses had been removed. Ultimately, this enabled collection of high quality EBSD patterns that enabled visualisation of the microstructure and reliable XRD pattern data.

ACKNOWLEDGEMENTS

I would like to express my thanks for all the help that I have received over the course of this PhD project. I first thank AWE and the Engineering and Physical Sciences Research Council for the funding providing over the course of this project. I would like to acknowledge the help of Tim Cartwright of AWE who was responsible for the industry-side support.

My thanks go to my two supervisors, Ross Springell and Tom Scott, for their direction throughout this project. I would like to thank Ed Darnbrough and Sophie Rennie, who as post-doctoral researchers of the Interface Analysis Centre, were particularly helpful people to have around, mainly as sounding boards.

I am grateful for the time that Chris Jones managed to find in his busy schedule to provide his insights into the preparation of uranium and correct operation of the electron microscopes. I would also like to thank Ian Griffiths for running some samples on the TEM at Oxford and assistance in crafting TEM and APT specimens. I must also acknowledge the work that Tomas Martin did in running the samples on the APT instrument and processing the data in his role as lab manager of the Oxford Atom Probe Group at the time. I would also like to thank Mattia Cattelan for his assistance in running various mostly extraneous projects on the NanoESCA facility, Rob Burrows for invaluable discussions on electropolishing and Gerry Lander for some helpful comments on crystallographic structures.

I am indebted to the help that I received from the members of the IAC who were kind enough to sacrifice a week to support the I12 experiment: Sophie Rennie, Chris Jones, Lottie Harding, Eleanor Lawrence Bright, Ed Darnbrough and Ross Springell. From Diamond Light Source, I would like to thank Oxana Magdysyuk, Stefan Michalik and Nghia Vo for their support in setting up the beamline, guiding us through the use of the equipment and processing the data.

I am appreciative of all the work that Keith Hallam has put in to facilitate this project in his role as Radiation Protection Supervisor.

I would finally like to thank the members of the Interface Analysis Centre at the University of Bristol for helping to make this an enjoyable experience.

AUTHOR'S DECLARATION

I declare that the work in this dissertation was carried out in accordance with the requirements of the University's Regulations and Code of Practice for Research Degree Programmes and that it has not been submitted for any other academic award. Except where indicated by specific reference in the text, the work is the candidate's own work. Work done in collaboration with, or with the assistance of, others, is indicated as such. Any views expressed in the dissertation are those of the author.

SIGNED: .... DATE: ....

TABLE OF CONTENTS

Page

List of Tables **xi**

List of Figures **xiii**

1 Introduction and Review of the Crystallographic Phases of Uranium and Uranium Alloys **1**

1.1 Uranium . . . 1

1.1.1 Alpha, α-U . . . 3

1.1.2 Beta, β-U . . . 5

1.1.3 Gamma, γ-U . . . 6

1.2 Niobium . . . 7

1.3 Uranium Alloys . . . 8

1.3.1 Stable Phases . . . 9

1.3.2 Metastable Phases . . . 11

1.3.3 Shape Memory Effect in Uranium Alloys . . . 16

1.3.4 Phase Transformations in Metastable Uranium Alloys . . . 19

2 Analytical Techniques **29**

2.1 Electron Microscopy . . . 29

2.1.1 Introduction . . . 29

2.1.2 Electron Gun . . . 30

2.1.3 Lenses & Optics . . . 32

2.1.4 Interaction of Electrons . . . 34

2.1.5 Instruments . . . 39

2.2 Focused Ion Beam Microscopy . . . 40

2.2.1 Sources . . . 41

2.2.2 Sample preparation . . . 41

2.2.3 Instruments . . . 42

2.3 Atom Probe Tomography . . . 44

2.3.1 Preparation of APT Samples . . . 44

2.4 X-Ray Crystallography 47
2.4.1 Introduction 47
2.4.2 Geometries 48
2.4.3 X-ray sources 49
2.4.4 Analysis of Diffraction Patterns by Rietveld Refinement 53

3 Preparation of Uranium and Uranium Alloys and Analysis of Surfaces 57
3.1 Introduction 57
3.2 Experimental Details 58
3.2.1 Materials 58
3.2.2 Mechanical Polishing 59
3.2.3 Electrochemical Configuration 59
3.2.4 Characterisation 60
3.3 Results 62
3.3.1 Uranium 62
3.3.2 Uranium Alloys 74
3.4 Discussion 89
3.4.1 Uranium 89
3.4.2 Uranium Alloys 91
3.5 Conclusions 92

4 Assessment of the Crystal Structures of the Metastable Uranium Alloys, α'' and γ^o 93
4.1 α'' Phase 93
4.1.1 Introduction 93
4.1.2 Experimental 94
4.1.3 Results 95
4.1.4 Discussion 100
4.1.5 Conclusion 103
4.2 γ° Phase 103
4.2.1 Introduction 103
4.2.2 Experimental 104
4.2.3 Results 105
4.2.4 Discussion 107
4.2.5 Conclusion 111

5 Long Term Investigations into the Low Temperature Ageing of the UNb5, UNb6 and UNb7 Alloys 113
5.1 Introduction 113

5.2 Experimental 116
5.3 Results 118
5.3.1 Mechanical Testing 118
5.3.2 XRD 122
5.3.3 EBSD 127
5.3.4 TEM 128
5.3.5 APT 132
5.4 Discussion 136
5.5 Conclusion 142

6 Investigations into the High Temperature Ageing of the UNb5 and UNb7 Alloys 143
6.1 Introduction 143
6.2 Experimental Configuration 145
6.2.1 Diffractometer Calibration 147
6.2.2 Heater Calibration 148
6.2.3 Temperature Profiles 148
6.3 Results 149
6.3.1 UNb5 Unaged State 149
6.3.2 UNb5 Transient 151
6.3.3 UNb7 Unaged State 165
6.3.4 UNb7 Transient 166
6.4 Discussion 180
6.4.1 UNb5 180
6.4.2 UNb7 180
6.4.3 General/Experimental 182
6.5 Conclusions 183

7 Summary and Future Work 185
7.1 Preparation of Uranium Alloys 185
7.2 Structures of the Metastable Phases 186
7.3 Low Temperature Transformations 187
7.4 High Temperature Transformations 188

A Calibration of the Nickel Heater 189

B Calculating Thermal Expansion Coefficients 193

C Analysis of Stress-Strain Curves 195

Bibliography 201

LIST OF TABLES

TABLE **Page**

4.1 Results of the fitting of Figure 4.1 using a Rietveld refinement fitting procedure. Values for α-U are taken from Lander *et al.* [148]. Fitting statistics have not been reported for UNb5 (3) as the structural parameters shown here have been derived from UNb5 (1) via symmetry operations. 98

5.1 Results of the stress-strain tests of UNb5 and UNb7 alloys aged at 150 °C. Standard deviation is based on 3 measurements of 3 different samples. In the case that a sample failed prematurely, the standard deviation becomes half the range between the mean of the two successful tests. The unaged data has been sourced from Volz *et al.* [279], using Engauge digitizer [179]. 119

A.1 Linear thermal expansion coefficients of nickel. Data originates from Touloukian *et al.* [267]. 189

LIST OF FIGURES

FIGURE **Page**

1.1 Unit cell of the α-U phase based on the lattice parameters and structure identified by Jacob and Warren [127]. This and all subsequent representations of the structures of cells have been produced using the VESTA program [181]. 4

1.2 α-U viewed along the [1 0 0] direction. The projected hexagonal structure is shown in the (1 0 0) plane with the out of phase atoms separated by the blue plane. The corrugated layers along (0 1 0) planes is also visible in this orientation. 5

1.3 Structure of β-U at 722 °C based on the description given by Lawson *et al.* [153]. Top image shows a 3D view of the unit cell, whereas, the bottom image views the β-U phase down the [0 0 1] direction. The two sets of near-hexagonal rings are visible when viewed in this orientation. 6

1.4 Structure of the γ phase based on the observations of Chiotti *et al.*. The lattice parameters shown here relate to a temperature of 773 °C. [48]. 7

1.5 Binary phase diagram of the U-Nb system. The red portion of the diagram denotes the region around the eutectoid. The eutectoid compositions present the most advantageous materials when prepared by quenching due to corrosion, irradiation and mechanical property benefits. Image has been redrawn using the data of [143, 158]. . 10

1.6 Structure of the U_2Mo phase with red spheres denoting uranium atoms and green spheres denoting molybdenum atoms. The U_2Mo phase possesses the I4/mmm space group with the *2a* sites occupied by Mo atoms and *4e* sites occupied by U atoms situated at $z/c = 0.328$. 11

1.7 Metastable structures of the uranium-rich end of the uranium-niobium binary phase diagram at regular steps of composition in weight percentage. Structures are based on the works of Anagnostidis *et al.*, Tangri and Chaudhuri, and Jackson [7, 122, 252]. Lattice parameters have been interpolated from the three sources where an exact match to to constant-stepped compositions shown here were not present. Lattices are shown in a 3-dimensional configuration as well as parallel to each principal axis. . . . 12

1.8 Martensitic twins structure observed in the U-13 at.% Nb and deduced by Field *et al.* using selected area TEM diffraction [85]. This image has been reproduced based on the original presented by Field *et al.* [85]. 14

1.9 Metastable phase diagram for the uranium-niobium system in the region of the eutectoid. Image has been reproduced based on an original constructed by Vandermeer [276]. 16

1.10 Schematic stress-strain curves of, *a* regular metals, *b* shape memory alloys and *c* superelastic alloys. *A* denotes the austenitic phase, *TM* refers to a twinned martensite, *DM* refers to a detwinned martensite and *PM* refers to partially detwinned martensite. 24

1.11 Stress-temperature phase diagram of an example shape memory alloy. The paths of the three stress-strain curves shown in Figure 1.10 are annotated on this diagram. . 25

1.12 A reproduced schematic of the stress-strain curve found in the α'' phase UNb alloys based on an original by Field *et al.* [85]. Field *et al.* suggests the curve can be explained as comprising four distinct regions labelled on the diagram as *A*-*D* [85]. *A* corresponds to elastic straining of the heavily twinned α'' phase martensite. *B* was put to motion of $\{\bar{1}72\}$ twins. In *C*, the cooperative migration of fine $\{\bar{1}30\}$ twins and $\{\bar{1}72\}$ twins was suggested to be responsible for eliminating fine twins producing single-orientation regions. *D* is plastic deformation which is mediated by slip. 26

1.13 Isothermal transformation diagram for an iron-carbon alloy at the eutectoid composition. In addition to the austenite and (twinned) martensite phases already encountered, and denoted by the symbols A and TM respectively, ageing steel also produced the pearlite and bainite microstructures, P and B. Bainite and pearlite are both equilibrium microstructures comprising ferrite, α-Fe, and cementite, Fe_3C. In this example, the transitions to pearlite and bainite are not clearly separated producing a single C-curve. The phases shown here are for illustrative purposes and not necessarily accurate depictions of the true phases. 27

1.14 Schematic isothermal transformation diagram for the UNb6 alloy based on the original figure produced by Hackenberg *et al.* [106]. Transformation temperatures, evaluated by Vandermeer [274], have been annotated on the diagram to show the martensitic start and finish points, M_s and M_f, as well as the temperature signifying the transition to the γ° phase, T_c. *C*-curves have been labelled using the same convention as that used by Hackenberg *et al.* [106]. The following mechanisms have been labelled as 1 - 5 respectively; low-temperature hardening, medium-temperature hardening, high-temperature hardening, discontinuous precipitation, discontinuous coarsening. 28

2.1 Schematic diagrams of thermionic, left, and field emission, right, electron sources. . . 31

2.2 Schematic of a SEM. Figure is based on the Zeiss Sigma model which was used to collect the majority of EBSD data [297]. 33

2.3 Interaction of energetic electrons with matter. Often referred to as the bulb of interaction, the diagram quantitatively shows the origin of the resulting particles and waves. Left hand side shows the case for SEM where the sample is considerably thicker than the penetration depth of electrons. Right hand side shows the scenario for TEM where the penetration depth of electrons exceeds the sample thickness permitting passage of electrons through the sample. 34

2.4 Kikuchi/electron backscatter pattern that was collected from an unaged UNb5 sample. Left side shows a pattern that has had a background subtraction applied. Right side shows the result of indexing the pattern with a material file representing the UNb5 α'' phase. Labelled positions refer to zone indexes. 37

2.5 HAADF and MAADF of 5000 hr aged UNb7, assumed to be alternating γ° phase twin variants bound by a grain boundary. Significant contrast in the MAADF image indicating structural inconsistencies, yet almost no contrast in the HAADF image confirms that the structural effects observed here are not related to compositional differences. 39

2.6 Diagrammatic representation of the liquid metal ion source used in focused ion beam (FIB) instruments. 41

2.7 Free-standing TEM lamella that has been cut out of the sample using staircase cross sections. The lamella will be subsequently bonded to the macromanipulator needle before being cut free of the sample at the base and transferred to the Cu grid. 42

2.8 TEM foil affixed to the Cu grid as viewed edge-on, left, and side-on, right. The platinum adhesive may be seen on the left of the images. The foil will subsequently require a low kV polish at glancing angles to remove the final tens of nanometres. 43

2.9 Slice and view cross sections produced from a UNb7 sample aged to 350°C for 2 hours. The two frames are separated by 500 nm. Small levels of curtaining can be seen to have developed due to differences in densities bewteen the homogeneous alloy and portions that have experienced fine-scale phase separation around carbide inclusions. 43

2.10 Local Electrode Atom Probe Tomography Layout. In this example, three ionisation events have occurred in the same cycle. The evaporated, doubly charged niobium ion escapes the sample and travels towards the detector with the highest velocity, v, striking it at time T. A singly charged niobium ion, accelerated to a lesser extent by the local electrode, travels at $1/\sqrt{2}\,v$, reaching the detector at $\sqrt{2}$T. A singly charged uranium ion travels at $0.44\,v$, reaching the detector at $2.29\,T$. 45

2.11 The first stage of APT sample preparation involves excavating a prism by digging wide trenches either side of the region of interest. The prism is 5μm wide, 10μm tall and 20μm long, and has been placed to intersect a triple point. 45

2.12 A portion of the lifted-out wedge, roughly 2μm deep has been affixed to the silicon tip by deposited platinum. 46

2.13 Needle is subsequently sharpened through annular milling to a fine point with tip radius around 100 nm. All platinum has been removed from the needle. 46

2.14 Schematic representation of the Bragg-Brentano geometry used by the laboratory diffractometer. The dashed line represents the focusing circle on which the source and detector travel. 49

2.15 Schematic representation of the Debye-Scherrer geometry that was used during the high temperature experiment conducted at Diamond on the I12 beamline. 50

2.16 Schematic of a modern x-ray tube source. This image has been modelled on the Philips Empyrean source, the x-ray tube used in the Panalytical X'Pert Pro MPD [201]. . . . 51

3.1 A schematic of the experimental configuration used during electropolishing. The three electrode cell comprises a reference electrode, a counter electrode and the working electrode. The potentiostat was used to control all experiments by applying a potential between the reference and working electrodes and measuring the current via the counter electrode. 60

3.2 An example linear sweep curve obtained from a uranium sample in the 3-part polishing solution. This data set was collected with a scan rate of 50 mV/s. Key features have been annotated on the graph and are discussed in the text. The potentials of the annotated points have subsequently been used in chronoamperometry scans to evaluate the effects of potential on polishing quality. 63

3.3 Data from a chronoamperometry scan conducted at a potential of 7.0 V plotted on three x axis scales. Current density as a function of time is plotted on a linear scale (black curve), logarithmic scale (blue curve) and on a square root scale (red curve). The Cottrell plot, i vs $t^{-1/2}$ (red curve) permits the easy identification of diffusion controlled processes as linear sections on this axis. 64

3.4 EBSD maps of specimens that were all been polished for equal durations, 210 s, but at varying potentials. The potentials used for polishing were based on the positions of features in the linear sweep curve of Figure 3.2. Panels a through e show confidence ranging from blue to red on the colour scale. Panel f shows a conventional EBSD map of the same area as panel d, with crystallographic orientation on the colour scale and image quality on the greyscale. In each instance, maps are 100 x 50 μm in size and the scale bar serves each panel. 66

3.5 Chronoamperometry scans showing the relationships between current density and time for the five polishing potentials used to investigate the effect of polishing potential. At potentials greater than the activation potential, current is limited to around 23 mA/cm^2 after the initial, instantaneous response to the change in potential. The lower potentials of 1.0 and 2.0 V did not produce effective polishing, which is assumed to be linked to the fact that current limiting polishing was not achieved. Data points are connected by spline curves to add clarity. 67

3.6 EBSD maps of the specimens polished at 5.5 V for exponentially increasing durations. Panels *a* through *e* show confidence ranging from blue to red on the colour scale. Panel *f* shows a conventional EBSD map of the same area as panel *e*, with crystallographic orientation on the colour scale and image quality on the greyscale. In each instance, maps are 100 x 50 μm in size and the scale bar serves each panel. 68

3.7 EBSD maps of the surface of the optimally prepared uranium sample in a preparation routine that included diamond paste polishing. Panel *a* shows a conventional map where crystallographic orientation is shown on the colour scale and confidence index is incorporated in as the greyscale. Panel *b* shows a map of the phases on the colour scale and confidence index on the greyscale. A carbide cluster is shown clearly in this figure, however, much of the carbide material has been etched away through polishing leaving pits and resulting in much of the cluster going un-indexed. 69

3.8 Panel *a* shows a large EBSD map of the optimally prepared uranium sample with an inverse pole figure legend, texture plot and example Kikuchi pattern shown in panels *b* to *d* respectively. The Kikuchi pattern in panel *d* has been collected with 1 x 1 binning to evaluate the potential of performing cross correlation EBSD on this material using a similar preparation method. 70

3.9 XRD pattern fitted by Rietveld refinement. A preferred orientation model based on spherical harmonics was included in the fit which resulted in the inset texture plot. . 71

3.10 Fitted Williamson-Hall plot produced from single peak data extracted from Figure 3.9. The gradient of the the linear best fit line was evaluated as $(8.8 \pm 1.9) \times 10^{-4}$. Error bars do not completely account for the scatter in the data away from the line of best fit, which may suggest that the complex deformation pathways of uranium may be independently affecting reflections. 72

3.11 $\mathrm{Sin}^2\psi$ plot for the (115), (135) and (223) reflections. Data was collected in positive tilt (of the ω-axis) mode to ensure that the beam footprint did not exceed the size of the specimen. These reflections were chosen as intense peaks at high angles in 2θ are required to access and be able to detect peaks at high values of $\sin^2\psi$. 73

3.12 Linear sweep voltammogram of the UNb6 alloy in the 85% phosphoric acid solution conducted with a scan rate of 50 mV/s. The cathodic section of the curve is shown of the left at negative potentials and the anodic section on the right at positive potentials. The plateau at high anodic potentials was affected by oxygen evolution to a greter extent than the uranium equivalent, Figure 3.2. 75

3.13 Linear sweep voltammograms of the UNb6 alloy in the 85% phosphoric acid solution for a range of scan rates. A constant surface area was used for each run to minimise errors. Additionally, the same solution was used for each scan rate, albeit with a suitably long incubation time between each run to allow the solution to return to a steady state. 76

3.14 Chronoamperometry curve of the UNb7 alloy in the 85% phosphoric acid solution under a constant potential of 1.9 V. A steady-state current density of 17-18 mA/cm^2, slightly less than that observed in the case of uranium polishing, Figure 3.3, was observed at longer polishing times. 77

3.15 Linear sweep voltammogram (inset) and chronoamperometry scan of the UNb6 alloy polished at 5 V for 45 mins. The red portion of the curve was caused by increasing the stirrer rate from 90 to 180 rpm. Excessive agitation of the solution resulted in a decreased effectiveness of electropolishing until the previous stirring rate was restored. 78

3.16 Feature produced by the polishing of the UNb6 alloy for 1 hour at 5 V. A miniscus formed on the sampe leaving an outcrop that was not immersed in the solution and therefore not polished. From this feature and a similar one on the other side of the sample, it is possible to estimate that approximately 20 μm has been polished away at roughly 1/3 μm per minute. 79

3.17 Left, surface of the UNb7 alloy following 20 mins of electropolishing at 1.9 V imaged by SEM. Right, sample is imaged at 70 ° for EBSD mapping, right. Scale is correct only for horizontal distances. The surface features a mixture of etched and proud carbides. Based on their morphology, the brighter carbides are thought to be the Nb_2C inclusions whereas the dull and etched away carbides are predicted to be UC. The bottom left of the image shows a fiducial marker. 80

3.18 Reconstructed inclusion particle cluster from the UNb6 alloy examined using the slice and view technique on the dualbeam. Pink regions denote the Nb_2C phase, green regions denote the UN phase and red denoted the UO_x phase. 81

3.19 Left, surface of the UNb6 alloy following 60 mins of electropolishing at 5 V. Top right, Nb_2C carbide cluster in the UNb6 alloy viewed at 70°. Bottom right, carbide of the UNb7 alloy following 20 mins of electropolishing at 1.9 V viewed at 70°. 82

3.20 X-ray diffraction patterns of the UNb7 alloy throughout the polishing process. The data has been presented twice on different axes with the linear scale shown in the lower panel and a logarithmic scale on the upper panel. The phase resembles a bcc structure immediately after cutting using an Accutom-5 fitted with an alumina cutting wheel. With progressive polishing the characteristic γ° phase expected in this material is observable. Weak, higher order γ° peaks, indistinguishable from the background, have not been labelled. 83

3.21 EBSD inverse pole figure orientation map of the UNb5 alloy polished at 3.5 V for 20 min. Black spots are un-indexed carbides or pits created by their removal during the electropolishing process. Patterns have been indexed using the 'unconventional' phase description as detailed in Chapter 4. 85

3.22 EBSD inverse pole figure orientation map of the UNb6 alloy polished at 3.4 V for 60 min. Patterns have been indexed using the 'unconventional' phase description as detailed in Chapter 4. 86

3.23 EBSD inverse pole figure orientation map of the UNb7 alloy polished at 3.1 V for 20 min. Patterns have been indexed using the γ phase due to negative pseudo-symmetry effects. The result is a map that shows microstructural features more clearly at the expense of intra-granular crystallographic relationships. 87

3.24 EBSD inverse pole figure orientation map of the UNb7 alloy covering a large area. Although the grain sizes are large and only around a couple of hundred grains have been indexed, the inverse pole figure shows a lack of dominating texture. 88

3.25 Two additional EBSD inverse pole figure orientation maps of the UNb6 alloy showing the apparent heterogeneity in microstructure as a result of crystal structure. The maps have been indexed using the 'unconventional' phase description as detailed in Chapter 4. 88

3.26 EBSD map of a pure uranium sample that has experienced localised annealing resulting in the considerable growth of some grains. This map was collected on the FEG-SEM following electropolishing and argon ion sputtering. 90

4.1 Rietveld fitted x-ray diffraction pattern of the UNb5 alloy with the structure shown inset. Lattice parameters were derived to be a = 2.891(4) Å, b = 5.755(8) Å and c = 4.984(7) Å with $\angle\gamma = 91.054(1)^\circ$. The pattern has been fitted with anisotropic microstrain and without the requirement of preferred orientation corrections. 96

4.2 Microstrain profile of the UNb5 alloy as derived from the fitting of Figure 4.1. The surface is defined by the unit cell vectors so for instance the x and y axes shown here are bisected by the [110] vector and the microstrain for that point is plotted. 97

4.3 Crystallographic structure of the α and α'' phases viewed down the [001] directions. As uranium and niobium atoms are in solution without any ordering, both atomic species are coloured the same colour (purple) for clarity. 98

4.4 Comparison of the crystallographic structure of the α'' phases in each of the two space group definitions. 99

4.5 Rietveld fitted x-ray diffraction pattern of the UNb6 alloy with the structure shown inset. Lattice parameters were derived to be a = 2.900(1) Å, b = 5.755(2) Å and c = 4.975(2) Å with $\angle\gamma = 92.6034(1)^\circ$. The pattern has been fitted with anisotropic microstrain and without the requirement of preferred orientation corrections. 100

4.6 Microstrain profile of the α'' phase of the UNb6 alloy as derived from the fitting of Figure 4.1. 101

4.7 Interatomic distances of α'' phase nearest neighbour atoms with equivalent data for α [148], γ^s [293] and γ [122] phases as detailed in the literature, displayed for comparison.102

4.8 Structure of Yakel's U-16.60 at% Nb-5.64 at%Zr alloy [293]. There is no chemical ordering in this structure, atoms are randomly distributed. Atoms are coloured to reflect the constant probability of finding uranium (red), niobium (blue) and zirconium (grey) at any position. *2c* atoms on the (1 0 0) plane have been displaced by $z/c = 0.05$ along the c direction whereas the atoms (0 1 1) plane are anti-correlated and are displaced by the same magnitude in the opposite direction. Coordinates of the *2a* and *2c* Wyckoff positions are (0, 0, 0) and (0.5, 0, 0.5-z/c). 104

4.9 Fitted pattern of the UNb7 alloy using the P4/nmm space group. The cell is represented in the inset using the P$\bar{4}$m2 centering convention, thereby differing from Yakel's original model. 105

4.10 Fitted pattern of the UNb7 alloy using the P112$_1$/n space group. 106

4.11 Fitted pattern of the UNb7 alloy using both the α'' and γ° phases. Plot inset shows the microstrain distribution for the dominant γ° phase. 107

4.12 Composite plot of the variation of lattice parameters in the uranium-niobium alloy system as drawn from the sources of Anagnostidis *et al.*, Tangri and Chaudhuri, Jackson and Vandermeer [7, 122, 252, 275], and the values obtained in this chapter for the UNb5, UNb6 and UNb7 alloys. 108

4.13 Interatomic nearest neighbour distances for the γ° and α'' phases with equivalent data for α [148], γ^s [293] (shown in transparent blue) and γ [122] phases as detailed in the literature, displayed for comparison. 110

4.14 Relationship between the γ° and α'' phases. Purple atoms show the atomic positions of the α'' phase, whereas, the atomic sites of the γ° phase are shown by the red atoms. The figure is essentially the same as that proposed by Carpenter and Vandermeer [38], apart from a translation in the plane that has been applied to the cells to account for the 'non-conventional' setting for the γ° phase. 111

5.1 XRD patterns of the UNb7 alloy throughout ageing at 150 °C. Performing an accurate Rietveld refinement where microstrain dominates on a limited 2θ range is challenging, however, the patterns appear to show the γ° phase replaced by the α'' phase. This data presented here was previously reported in Scott *et al.* but has been replotted and annotated [221]. 115

5.2 TEM micrographs of the unaged UNb7 alloy which was described as 'showing the presence of nano-scale banding ascribed to subtle chemical segregation'. This figure presented here was originally reported in Scott *et al.* [221]. 115

5.3 TEM micrographs of the 5000hr aged UNb7 alloy which was described as '[having] evolved further than spinodal decomposition, developing angular nanoscale platelets assumed to be the α'' phase'. This figure presented here was originally reported in Scott *et al.* [221]. 116

5.4 An example of a stress-strain curve that has been analysed using the code presented in Appendix C. Points of interest identified by analysis of the gradient of the data have been annotated onto the curves. 117

5.5 Engineering stress-strain charts of the UNb5 evolving through isothermal ageing at 150 °C. The unaged data has been sourced from Volz *et al.* using Engauge digitizer [179]. Otherwise, the data were provided by AWE plc. 120

5.6 Engineering stress-strain charts of the UNb7 evolving through isothermal ageing at 150 °C. The data were provided by AWE Plc. 121

5.7 Relationship between the hardness and upper tensile strength of unaged and aged specimens. High adjusted R-squared value of 0.982 suggests a strong link between the two parameters as would be expected. Plotting with axes inverted and converting to the Brinell scale [12, 25] for easier comparison with literature sources gives a gradient of 1.27 ± 0.14 MPa. 122

5.8 Microstrain of the α'' phase of the UNb5 alloy throughout ageing at temperatures up to 200 °C. 123

5.9 Microstrain of the α'' phase of the UNb6 alloy throughout ageing at temperatures up to 200 °C. 124

5.10 Microstrain of the α'' phase within the UNb7 alloy throughout ageing at temperatures up to 200 °C. 125

5.11 Microstrain of the γ° phase within the UNb7 alloy throughout ageing at temperatures up to 200 °C. 126

5.12 Phase fraction of the α'' phase within the UNb7 alloy throughout ageing at temperatures up to 200 °C. 127

5.13 XRD patterns of the UNb7 alloys received from AWE Plc in an aged state. Left side shows the original XRD measurements originally reported by Scott *et al.* [221], right side shows the remeasured data. Full scans were recorded when remeasuring the alloys, a limited range is displayed here for comparison. 128

5.14 Comparison between the XRD pattern of the 5000 hr aged UNb7 alloy in Figure 5.13 and the pattern from a poorly prepared sample in which it was discovered that there was a poor electrical connection to the sample during electropolishing. Data quality is worse for the poorly prepared sample which only received a cursory investigative scan. 129

5.15 Comparison between the XRD patterns of the unaged UNb7 alloy and a UNb7 alloy coupon heated at 200 °C for 80 days. As two different wavelengths were used in collecting these datasets (synchrotron and copper source), the data has been plotted with the scattering vector, Q, on the x axis with the equivalent 2θ scale for a copper source ($\lambda = 1.54$Å) shown above. 130

5.16 EBSD map of the UNb5 alloy aged for 160 days at 150 °C. An example of the unaged UNb5 alloy can be found in Figure 3.21. It has not been possible to acquire an EBSD map of like orientations given the difficulties in collecting EBSD data from this alloy and the low symmetry of the crystal structure. 131

5.17 EBSD map of the UNb6 alloy aged for 160 days at 150 °C. An example of the unaged UNb5 alloy can be found in Figure 3.22. It has not been possible to acquire an EBSD map of like orientations given the difficulties in collecting EBSD data from this alloy and the low symmetry of the crystal structure. 131

5.18 Left, EBSD map of the UNb7 alloy aged for 160 days at 150 °C. Right, EBSD map of the unaged UNb7 alloy showing similar grain orientations as to that seen in the 160 day, 150 °C aged UNb7 alloy. 132

5.19 Complementary HAADF and MAADF images of the UNb7 alloy aged at 150 °C for 1500 hrs. 133

5.20 MAADF overview and HAADF atomic resolution TEM image of the UNb7 alloy aged at 150 °C for 1500 hrs. 133

5.21 HAADF and MAADF, left and right respectively, TEM images showing twinning in the 5000 hr aged UNb7 sample. 134

5.22 HAADF and MAADF, left and right respectively, TEM images showing stacking faults in the 5000 hr aged UNb7 sample. 134

5.23 BF, HAADF and MAADF TEM images and a SAED pattern (top-left, top-right, bottom-left and bottom-right respectively) of the UNb7 alloy aged at 150°C for 5000 hrs. Information pertaining to the scale for the diffraction pattern in the bottom right panel has been lost preventing accurate indexing of this structure. 135

5.24 5000 hr aged UNb7. MAADF of foil on left and HAADF of atomic resolution image. . 136

5.25 An atom probe tomography needle of the UNb7 alloy aged at 150°C for 5000 hrs, as viewed by three reconstructions of the same specimen. The distribution of uranium and niobium can be seen as still highly uniform with no signs of phase separation having taken place. 137

5.26 Nearest neighbour distribution of niobium atoms in the UNb7 alloy aged at 150°C for 5000 hrs. Mean position was calculated to be 0.3193 ± 0.0009 nm, which is very close to the randomised distribution shown by the red line. 138

5.27 Zhang *et al.*'s proposed defect migration within the twin variant structure mechanism. The left side shows unaged (as-quenched) twins, whereas the right side represents material that has been thermally aged promoting defect migration to twin boundaries. Image reproduced from Zhang *et al.* [298]. 139

6.1 Isothermal transformation diagram of the U-Nb-Zr alloy. Image from Dean [61]. More isothermal transformation diagrams for uranium alloys may be found in the 'Atlas of time-temperature diagrams for nonferrous alloys' [282]. 145

6.2 Isothermal transformation diagrams diagram of the U-Nb alloy. Image from Hackenberg *et al.* [105]. 145

6.3 Elements of the experimental configuration used for the in-situ experiment at the I12 beamline. The left hand side shows the Macor sample holder and heater. The right hand side shows its position within the evacuated UHV experimental cell. 146

6.4 Diffraction pattern of the CeO_2 calibration as collected by the 2D detector. The Debye-Scherrer geometry has produced rings that upon azimuthal integration return a 1-dimension diffraction pattern. 147

6.5 Fitted diffraction data of the CeO_2 calibration. The weighted pattern residual, R_{wp}, was minimised at 2.90%. The bump at 1° represents an amorphous glass peak and so was not included in the fit. 147

6.6 Diffraction pattern of the nickel foil. Rings show evidence of texture. The background of the glass is present in this pattern producing the diffuse ring in the centre of the image. 148

6.7 Schematics of the temperature profiles of the UNb5 alloys during this study. Ageing treatments similar to those applied to the UNb7 alloy were used for the UNb5 alloy for easy comparison. Sample 2 was found to have fully transformed by the 200 minute mark enabling the heating to be stopped and time devoted to heater calibration. . . . 149

6.8 Schematics of the temperature profiles of the UNb7 alloys during this study. Sample 1 was used to gauge the behaviour of the alloy and determine rough rates for transitions. Samples 2 and 3 experienced the final ageing profiles with nominal ‘set temperatures’ of 100, 150 and 200 °C that had been intended to last roughly 7 hours in total with a 5 hour isothermal treatment and approximately hour long heating and cooling ramps. . 149

6.9 The diffraction pattern of a single frame representing an area of $0.2 \times 0.2\,\mathrm{mm}^2$ in the UNb5 alloy. 150

6.10 The summed diffraction pattern of all frames in the 121-frame map representing an area of $2 \times 2\,\mathrm{mm}^2$ in the UNb5 alloy. 150

6.11 An equal area IPF of the texture in the UNb5 alloy in the initial, unaged state. The contour plot is measured in multiples of random distribution. 151

6.12 Fitted diffraction pattern of the unaged UNb5 alloy. Data is shown by open black circles, the fit by the red line and the residual by the blue line. 152

6.13 Evolution of lattice parameters of the α'' phase for the UNb5 sample heated to 400 °C. The entire cycle is represented here with the heating period extending up to 450 s, the isothermal section lasting until 24720 s and the cooling period lasting until a total time of 29120 s. The negative thermal expansion coefficient in the *b*-axis may be inferred from the behaviour of the red dots on heating and cooling. 153

6.14 Lattice parameters of the α'' phase in cooling in the UNb5 alloy aged at 400°C. 154

6.15 Thermal expansion coefficients of the axes of the α'' phase in the cooling of the UNb5 alloy from 400°C. 155

6.16 Equal area IPFs showing the evolving texture of the UNb5 alloy heated to 400°C. The data in a represents the material before heating, b was taken at 400°C 6.5 hours after heating began and c was obtained after the sample had been allowed to cool. 156

6.17 Evolution of the fractions of the α'', α and γ phases in the 450°C aged UNb5 sample as a function of time. Data points have been thinned by a factor of two for clarity. . . 157

6.18 Time dependence of microstrain in the α'', α and γ phases throughout ageing of the UNb5 alloy at 450 °C. 158

6.19 Contour plot of the diffraction patterns during the initial ramping of the UNb5 sample to (500 °C). 159

6.20 Phase fractions of the α'', α and γ phases as a function of time in the UNb5 alloy heated to 500°C. 160

6.21 Variation in the lattice parameters of the α phase of the 500 °C aged UNb5 alloy with time. Data starts at 400 s once the α'' phase has been consumed. Heating is turned off at 11160 s. 162

6.22 Lattice parameters of the as-transformed UNb5 alloy as a function of temperature in cooling. 163

6.23 Thermal expansion coefficients of the axes of the α and γ phases. Quadratic fits of Figure 6.22 are shown prominently, cubic fits of Figure 6.22 are shown in the background.164

6.24 STEM bright-field (BF) image of the 500 °C aged UNb5 alloy. 164

6.25 STEM high angle annular dark-field (HAADF) image of the 500 °C aged UNb5 alloy. 164

6.26 The diffraction pattern of a single frame representing an area of $0.2 \times 0.2\,\text{mm}^2$ in the UNb7 alloy. 165

6.27 The summed diffraction pattern of all frames in the 121-frame map representing an area of $2 \times 2\,\text{mm}^2$ in the UNb7 alloy. 165

6.28 Fitted pattern of the map data. The crystal structure of the γ° phase is shown as an inset which was modelled best using the P4/nmm space group. Lattice parameters were determined to be $a = 5.0114(6)\,\text{Å}$ and $c = 3.366(1)\,\text{Å}$. Fractional position of the *2g* atom along the c axis z/c = 0.435(3). R_{wp}= 6.65 %, $RF^2_{\gamma^o}$ = 11.37 %. 166

6.29 Reduced equal area inverse pole figure taking into account the 4/mmm Laue class symmetry of the crystal. Effects of texture can be seen to have been mitigated by the map sampling. Relative intensities across crystal orientations may be seen to vary by as much as 20 %. 166

6.30 Lattice parameters of the γ° phase as a function of temperature during the initial heating ramp of the UNb7 alloy to 400 °C. Data points have been joined up using an Akima spline to illustrate the trend, particularly from room temperature to 200 °C. . 168

6.31 Lattice parameters of the γ° phase during ageing of the UNb7 alloy to 400 °C in the scenarios of modelling the patterns with only the γ° phase and modelling with the γ° and α'' phases. 168
6.32 Phase fraction by weight of the γ° and the α'' phases in the UNb7 alloy heated to 400 °C.168
6.33 Lattice parameters of the γ° and α'' phases as a function of time during the isothermal heating stage of the UNb7 alloy at 400 °C. 168
6.34 Microstrain of the α'' and γ° phases in the UNb7 alloy as a function of time at 400 °C. 169
6.35 Lattice parameters of the γ° phase of the UNb7 alloy as a function of time at 450°C. . 170
6.36 Microstrain of the γ° and α'' phases of the UNb7 alloy as a function of time at 450°C. 171
6.37 Fitted pattern of the UNb7 alloy at room temperature following heating to 450 °C for 6.5 hours. $R_{wp} = 5.59\,\%$, $RF^2_{\gamma^{\circ}} = 6.74\,\%$, $RF_{\gamma^{\circ}} = 3.68\,\%$, $RF^2_{\alpha''} = 8.33\,\%$, $RF_{\alpha''} = 3.89\,\%$. $a_{\gamma^{\circ}} = 5.0137(5)$ Å, $c_{\gamma^{\circ}} = 3.363(2)$ Å, $a_{\alpha''} = 2.927(1)$ Å, $b_{\alpha''} = 5.912(3)$ Å, $c_{\alpha''} = 4.993(2)$ Å and $\angle\gamma_{\alpha''} = 91.51(6)\,°$. 172
6.38 FIB-cut cross section of the 450 °C aged sample. The carbide in view has through ageing, been the nucleation site of cellular decomposition. The top of the image shows the oxide layer that has developed during the ageing. For scale, the image is 10.3 μm across. 173
6.39 Variation in lattice parameter with temperature in the initial heating of the sample. At 372 °C the sample can be said to have gone through a tetragonal to cubic transition, locking into a lattice parameter of 3.52 Å, the same starting lattice parameter for pure bcc γ-uranium. The grey hexagons on the right hand side of the plot shows the size of the a axis were the definition of the γ° cell still being used. 174
6.40 Contour plot of the diffraction patterns arising from the initial heating of the UNb7 sample to 500 °C. 175
6.41 Evolution of the γ° / γ phase volumes and phase composition of the UNb7 alloy through ageing at 500 °C. Cooling data following the end of the isothermal heating shows the volume of the niobium rich γ phase decrease. The phase fraction shows anomalous behaviour in cooling that may be ascribed to incorrect temperature factors. Volume of the γ° phase at room temperature before isothermal heating started was 42.267 Å^3. Volume shown here is normalised for the γ phase definition, γ° phase data has been reduced by a factor of two to show the trend. 176
6.42 Content of the γ phase during isothermal heating of the UNb7 alloy at 500 °C as a function of time. 177
6.43 Changes to the microstrain during isothermal heating at 500 °C and cooling in the UNb7 alloy. Microstrain in the γ phase was shown to increase significantly during the transition to the α phase eventually levelling off at about 35000. 178
6.44 Lattice parameters of the α phase in the transformed UNb7 alloy under cooling from 500 °C. 178

6.45 Thermal expansion coefficients of each of the three unit cell axes of the α phase in the transformed UNb7 alloy in cooling from 500 °C. 178
6.46 FIB-cut cross section of the 500 °C aged UNb7 sample. Within the two original grains in view numerous domains of banded material have formed. 179
6.47 An APT needle of a UNb7 alloy that had been heated to 500°C for 2 hours. The ageing of this alloy was done separately to the treatments of the in-situ diffraction experiment. Separation has progressed very far with an almost pure uranium phase shown in green and a blue region that is high in niobium but also contains some uranium. The uranium rich-regions can be seen to have oxidised (during transfer) much quicker than the niobium-rich regions, as expected. 181

A.1 Thermal expansion coefficient of nickel (heater calibrant) with temperature. The dotted blue line shows the fit using all data points. The solid red line shows the fit having excluded the last data point which is beyond the bounds of the experiment conducted at I12. Errors have been taken to be the precision of measurements. 190

LIST OF ACRONYMS

ADF	Annular Dark Field
APT	Atom Probe Tomography
BCC	Body Centered Cubic
BF	Bright Field
CCD	Charge-Coupled Device
CTEM	Conventional Transmission Electron Microscope
DAWN	Data Analysis WorkbeNch
DB	Dualbeam
DIC	Differential Interference Contrast
DLS	Diamond Light Source
DM	Detwinned Martensite
EBSD	Electron Backscatter Diffraction
EBSP	Electron Backscatter Pattern
EDS	Energy Dispersive x-ray Spectroscopy
EDX	Energy Dispersive x-ray Spectroscopy
EELS	Electron Energy Loss Spectroscopy
EIS	Electrochemical Impedance Spectroscopy
EPMA	Electron Probe Microanalysis
EXAFS	Extended X-ray Absorption Fine Structure
FCC	Face Centered Cubic
FEG	Field Emission Gun
FIB	Focused Ion Beam
GSAS	General Structure Analysis System
HAADF	High Angle Annular Dark Field
HCP	Hexagonal Close Packed
HRTEM	High Resolution Transmission Electron Microscope
IPF	Inverse Pole Figure
LMIS	Liquid Metal Ion Source
MAADF	Medium Angle Annular Dark Field
MPD	Multi-Purpose Diffractometer
PALS	Positron Annihilation Lifetime Spectroscopy
PM	Partially Detwinned Martensite
RDE	Rotating Disk Electrode
SAED	Selected Area Electron Diffraction
SANS	Small Angle Neutron Scattering
SAXS	Small Angle X-ray Scattering
SEM	Secondary Electron Microscopy/Microscope
SIMS	Secondary Ion Mass Spectrometry
SMA	Shape Memory Alloy
SME	Shape Memory Effect
STEM	Scanning Transmission Electron Microscopy/Microscope
TEM	Transmission Electron Microscopy/Microscope
TKD	Transmission Kikuchi Diffraction
TM	Twinned Martensite
UHV	Ultra High Vacuum
XPS	X-ray Photoelectron Spectroscopy
XRD	X-ray Diffraction

Portions of the work on the polishing of and characterisation of uranium surfaces in Chapter 3 titled *'Preparation and analysis of strain-free uranium surfaces for electron and x-ray diffraction analysis'* has been published in Materials Characterization [251].

A working paper titled *'Low Temperature Ageing Behaviour of U-Nb γ° Phase Alloys'* based on results presented in Chapter 5 may be found on the ArXiv [249].

CHAPTER

1

INTRODUCTION AND REVIEW OF THE CRYSTALLOGRAPHIC PHASES OF URANIUM AND URANIUM ALLOYS

This chapter reviews the stable and metastable phases of uranium and its alloys, and the work that has been performed to date to understand their structure and the mechanism of their formation. Few thermodynamically stable phases may be produced in uranium alloys at room temperature. However, metastable phases produced by quenching possess complex structures that have required numerous successive studies to understand the crystallography. These phases have been established to occur by structural ordering and martensitic reactions, which facilitate the shape memory effect in these alloys. A review of the shape memory effect in uranium alloys is therefore also discussed along with the deformation mechanics, particularly mechanical twinning, which are integral to the shape memory effect. This chapter finally concludes with a discussion of the work that has been conducted to date to understand the phase transformations that are known to occur in these alloys in response to elevated temperatures.

1.1 Uranium

Uranium was formally discovered by Klaproth in 1789 and subsequently named after the recently disovered planet Uranus [56]. However, Péligot was the first to separate out pure uranium in 1841. Klaproth had managed to produce an oxide of uranium which he had mistaken for the metal [98]. Klaproth dissolved pitchblende, now known as uraninite, in nitric acid separating out UO_2 from U_3O_8, and heated it with charcoal to produce a black powder [80]. Péligot showed that the UO_2 precipitate was an oxide and not the element, which he extracted by reducing uranium tetrachloride with potassium. Uranium had historically been used to colour glasses yellow or green before its official discovery [36, 109].

The heaviest naturally occurring element, uranium possesses an atomic number of 92 and assumes a mass number between 232 and 238. Naturally occurring uranium exhibits three isotopes, none of which are stable [87]. However, of the three major isotopes found in nature (^{234}U, ^{235}U and ^{238}U), ^{238}U is the most abundant isotope (99.274%) and possesses a half-life of 4.47 billion years [59, 128]. As uranium is a weak alpha emitter, chemical toxicity presents a greater danger to human health than the radioactive component [29, 204].

Using uranium, Henri Becquerel discovered the phenomenon of radioactivity in 1896 [98]. Henri Becquerel had a supply of uranium salts from two previous generations of Becquerels who had used them to investigate the phosphorescence exhibited in many of these materials [5, 22, 257]. Upon hearing of Röntgen's discovery of x-rays only weeks previously [213], Becquerel left uranium salts near covered photographic plates in an attempt to investigate whether there existed a connection between phosphorescence and x-rays [5, 257]. He later found the photographic plate to have become fogged. Becquerel established uranium to be responsible for the emission of penetrating rays as regardless of whether the salt displayed phosphorescence, the plates would have experienced the same effect. For his discovery, Henri Becquerel would be awarded half of the 1903 Nobel Prize [257]. The co-winners of that year's prize were Pierre and Marie Curie for their research into what they would describe as the 'radioactivity' discovered by Becquerel [259].

Uranium subsequently received the attention of numerous other future Nobel Prize winners and notable scientists such as Enrico Fermi, Lise Meitner and Otto Hahn [255, 258]. In 1934, Curie and Joliot discovered artificial radioactivity by irradiating various light elements with alpha particles [131]. Fermi subsequently published his results on the artificial radioactivity caused by neutron bombardment [82]. Fermi subjected nearly every element known at that point to his neutron bombardment treatment, and in uranium suggested that he had possibly created elements with atomic numbers greater than 92. Otto Hahn and Fritz Strassmann reproduced this work in 1938 and in doing so showed by chemical analysis that barium had been produced. Lise Meitner and Otto Frisch correctly interpreted this result as a splitting of the uranium nucleus in 1939, thereby establishing nuclear fission [172, 173].

Uranium has since been most well associated with its role in the nuclear industry. Research into nuclear fission and the development of nuclear weaponry ramped up during the second world war under the Manhattan Project to counter the threat of a rival weapon being created by Nazi Germany [114]. In 1942, Enrico Fermi's team working at the Chicago Pile-1 experimental reactor produced the first self-sustaining nuclear chain reaction [114]. This discovery subsequently resulted in the construction of nuclear reactors that assisted in the production of highly enriched, fissile material that would be used in the weapons used in Japan in August 1945 [116]. Following the war, endeavours to use uranium for peaceful means has drawn substantial investment as civilian nuclear reactors present a low carbon source of semi-sustainable reliable energy.

Though the heaviest primordial element, due to the production of transuranic elements by nuclear reactors and particle accelerators, uranium is no longer the heaviest element known to man. Uranium is now an early member of the actinide series, a collection of elements characterised by the (mostly) sequential filling of the *5f* electron shell. The neutral atom electronic configuration of uranium is [Rn] $5f^3$ $6d^1$ $7s^2$. For the late actinides, americium and beyond, *5f* electrons are localized, and therefore do not play a role in the bonding. This is also the case for the lanthanides (*4f* elements), in which d electrons control the bonding. This causes many of the transition metal characteristics to feature in the lanthanides and heavy actinides. The exceptions are the lighter actinides within which *5f* electrons are itinerant producing low-symmetry phases (body centred tetragonal-Pa, orthorhombic-U, orthorhombic-Np and monoclinic-Pu) in contrast to the close packed structures found in d-bonding elements [235]. Pure uranium possesses three solid phases, α-U, β-U and γ-U before melting at 1132.2 °C and boiling at 4131 °C.

1.1.1 Alpha, α-U

In pure uranium, α-U exists between absolute zero and 668°C [24]. α-U exhibits a particularly unique structure that is not shared by any other known element under normal conditions of temperature and pressure [150]. Under high pressures, early actinides and lanthanides are able to adopt the α-U structure [78, 130]. α-U possesses orthorhombic symmetry with lattice parameters of 2.854, 5.870 and 4.955 Å in the Cmcm (63) space group [127]. Atoms are situated in the *4c* Wyckoff sites at $(x/a, y/b, z/c) = (0, 0.1025, 0.25)$ [247], producing the crystal shown in Figure 1.1.

Additionally, uranium possesses a charge density wave extending up to 43 K. Uranium is the only material to show this characteristic in elemental form [149]. Superconductivity has been reported in the literature multiple times. The presence of this phenomenon in this phase as an intrinsic property is contentious. Recent popular opinion has turned to consider the competing effect of the charge density wave to preclude superconductivity in this phase [102]. Previous observations of the phenomenon are widely considered to be artefacts from impurities for example [102].

The structure is often described as comprising corrugated atomic layers aligned along the (0 1 0) plane as intra-layer atomic distances are shorter than inter-layer distances when viewed in this manner [35, 294]. Projection of atomic positions along the (0 0 1) plane produces a hexagonal configuration. It has been shown that epitaxy is capable of encouraging a hexagonal crystal for thin film single crystals [238]. However, in the bulk α phase, atoms are displaced along the [0 0 1] direction from the (0 0 1) plane.

The complex nature of the structure of uranium additionally impacts the thermal expansion of the lattice which is highly anisotropic. The linear expansion coefficient for the a and c axes are relatively similar for a wide range of temperatures, diverging at low temperatures. Whereas, the linear expansion coefficient for the b axis is negative for a range of temperatures [159]. The vastly different expansion coefficients, in conjunction with crystallographic texture of fuel rods (preferred orientation in the [0 1 0] direction develops in rods rolled at 300 °C) led to dimensional

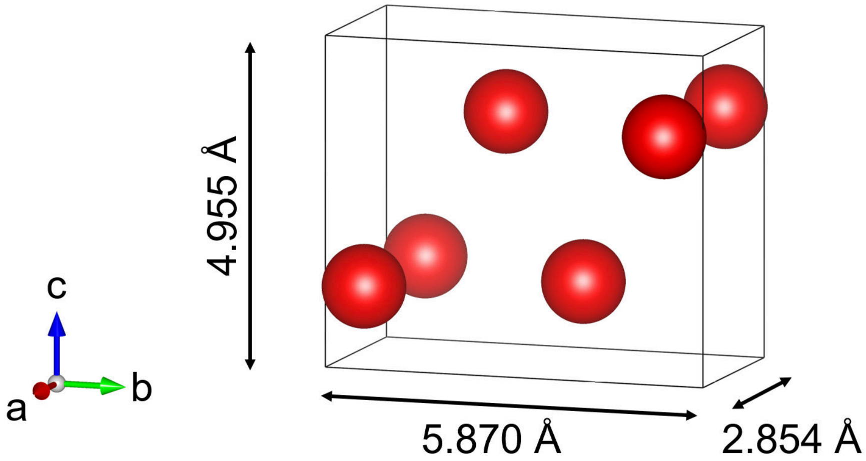

Figure 1.1: Unit cell of the α-U phase based on the lattice parameters and structure identified by Jacob and Warren [127]. This and all subsequent representations of the structures of cells have been produced using the VESTA program [181].

instability of fuel rods during the early years of nuclear power [149]. Despite the favourable high uranium density and a high thermal expansion due to its metallic nature, and substantial efforts to reduce preferred orientation effects to control the instability [90], pure uranium nuclear fuels were sidelined and replaced by uranium dioxide. However, this was not before the UK had made substantial investments into the Magnox reactors that ran on metallic uranium.

Due to the low-symmetry structure of α-U [235], a plethora of mechanical deformation routes including twins, kinks and slip are permitted. Cahn's comprehensive examination of deformation mechanisms showed twinning to be complex with multiple modes frequently observed [35]. In order of prevalence in a polycrystalline material, α-U exhibits $\{1\,3\,0\}$, $\{1\,7\,2\}$, $\{1\,1\,2\}$ and $\{1\,2\,1\}$ twinning modes [35, 54]. The $\{1\,7\,2\}$ and $\{1\,2\,1\}$ modes are type I twins, in which the twinning plane (K_1) and the reciprocal of the twinning direction (η_2) may be expressed by rational Miller indices, $\{1\,1\,2\}$ is a type II twin, where the reciprocal of the twinning plane (K_2) and the twinning direction (η_1) are rational, and $\{1\,3\,0\}$ is compound, meaning that K_1, K_1, η_1 and η_2 are rational.

α-U additionally displays kink bands normal to [100] and slip on the $(0\,1\,0)$ plane along the $[1\,0\,0]$ direction [35]. At room temperature, the slip deformation mechanism dominates [149]. In keeping with most metals, slip acts along the closest packed direction [149]. In uranium, this incurs the shearing of the corrugated planes aligned on the $(0\,1\,0)$ plane.

Despite the use of preparation steps designed to promote a fine-grained and quasi-isotropic structure in uranium metal, insufficiencies in the α structure do not fully stabilise uranium in its pure state [294]. British Magnox reactors used metal fuel but anisotropic swelling and

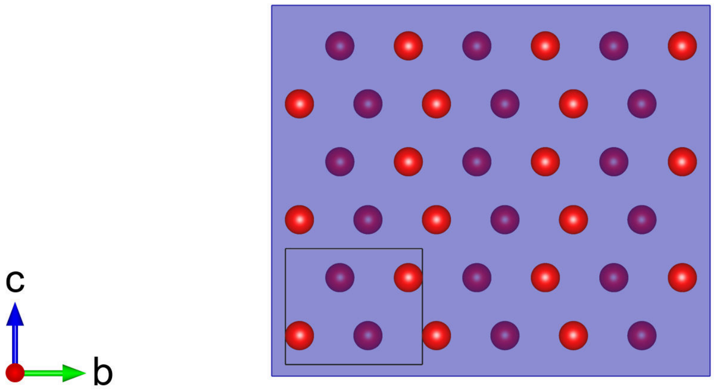

Figure 1.2: α-U viewed along the [1 0 0] direction. The projected hexagonal structure is shown in the (1 0 0) plane with the out of phase atoms separated by the blue plane. The corrugated layers along (0 1 0) planes is also visible in this orientation.

poor irradiation stability greatly inhibited the efficiency of the fuel. Uranium alloys present the possibility of retaining a metallic fuel which possesses superior mechanical and corrosion qualities. Additionally, compared to UO_2, the most commonly used nuclear fuel worldwide, metallic fuels possess higher thermal conductivities and uranium density.

1.1.2 Beta, β-U

In comparison to the α-U phase, the β-U phase is substantially more complex. Several experiments utilising synchrotron facilities and neutron sources have been conducted to collect high quality data capable of solving the structure of β-U [149]. Fitting of the patterns using Rietveld refinement has produced complicated structures with large lattices containing 30 atoms under tetragonal symmetry. Space groups have been identified as the non-centrosymmetric P42nm (102) [68, 239, 263, 269], or the closely related centrosymmetric P42/mnm (136) [48, 153, 239, 270].

Interestingly, the β-U phase of uranium has little resemblance to the intermediary phases of the uranium alloys. Atoms sit in hexagonal planes with smaller hexagons sitting on the (001) plane at $z/c = 0$ and $z/c = 0.5$ (U1, U2, U3 and U4) and larger hexagons at $z/c = 0.25$ and $z/c = 0.75$ (UNb5). Smaller hexagons have inter-atomic distances (edges) averaging 2.95 Å whilst the larger hexagons measure 5.57 Å [48]. The structure of the β-U phase is shown in Figure 1.3.

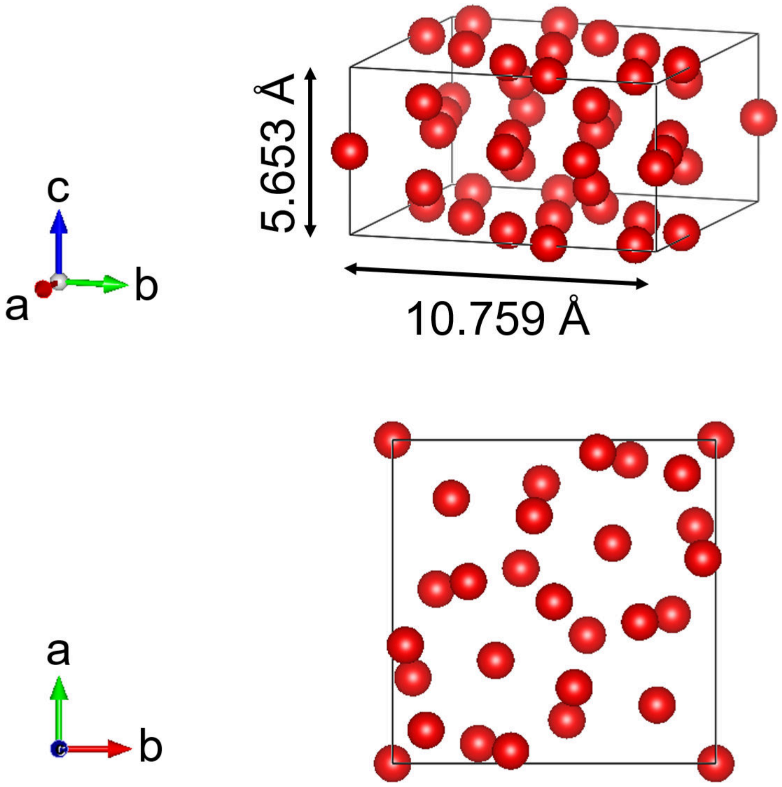

Figure 1.3: Structure of β-U at 722 °C based on the description given by Lawson *et al.* [153]. Top image shows a 3D view of the unit cell, whereas, the bottom image views the β-U phase down the [0 0 1] direction. The two sets of near-hexagonal rings are visible when viewed in this orientation.

1.1.3 Gamma, γ-U

The third allotrope of uranium, γ-U, occurs above 775 °C [24]. Possessing a body centred cubic structure with a lattice parameter between 3.532 and 3.557 Å, γ-U belongs to the Im-3m (229) space group with atoms positioned at the *2a* Wyckoff positions. The structure of the γ phase is shown in Figure 1.4. The *bcc* structure is a relatively common crystal structure featuring in a large number of phase diagrams for the elements, particularly as the phase leading up to the melting point [149]. From a nuclear fuel perspective, the cubic γ phase would be a far more favourable than the α phase. The cubic nature of the γ phase introduces superior mechanical qualities such as malleability and ductility [227, 294], but most importantly, isotropic expansion and strong radiation damage tolerance. Unfortunately, the γ phase cannot be stabilised without

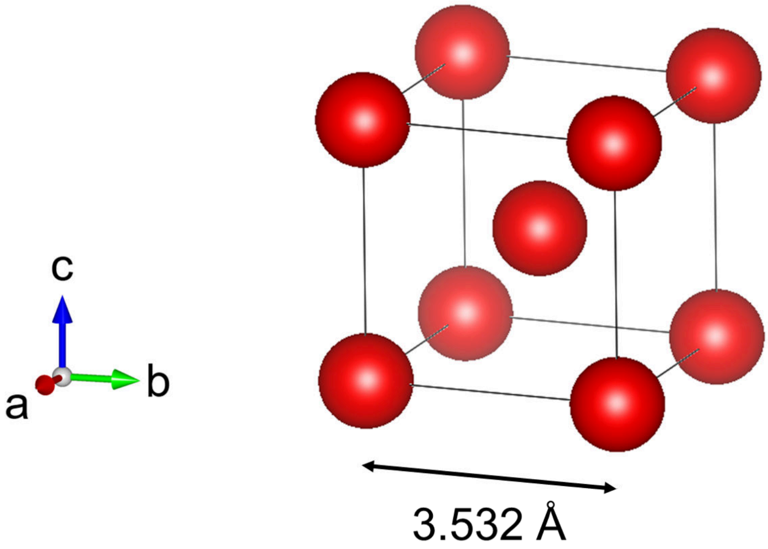

Figure 1.4: Structure of the γ phase based on the observations of Chiotti *et al.*. The lattice parameters shown here relate to a temperature of 773 °C. [48].

alloying additions.

1.2 Niobium

Niobium is a transition metal possessing an atomic number of 41, and with a standard atomic weight of 92.9 [171], is roughly two fifths the mass of a uranium atom. Charles Hatchett discovered the element in 1801, naming it columbium after the mineral, columbite $(Fe,Mn)(Nb,Ta)_2O_6$ from which it had been identified [99]. In the years since, scientists had difficulties in differentiating the element from the chemically similar tantalum. This lead to Heinrich Rose in 1846 to derive another name for the same element, coining the name niobium in reference to Niobe, the daughter of Tantalus after whom tantalum is named [214, 254]. The official name for element 41 was established in 1941 to remove the ambiguity created by the two names [205]. Some early works on the uranium-niobium binary and ternary alloy systems make reference to or explicitly name columbium [91, 200, 212].

Niobium is commonly added to steel to increase toughness and strength [63, 156]. Around 90% of niobium produced is used in low-alloy steels for industries that include oil and gas, automotive and ship building [156]. Niobium is also often a minor component in superalloys which feature in applications such as jet engines [94]. Niobium is also able to be used in the nuclear industry due to its relatively low thermal neutron capture cross section [186, 225]. Although not quite as strong as tantalum, niobium has excellent corrosion resistance, and is impervious to weak acids. [186]. At low temperatures, niobium also becomes a superconductor which has lead to its use in superconducting magnetic coils [156].

Niobium exhibits a *bcc* phase, the same structure as that shown in Figure 1.4, from absolute zero to its melting point at 2477 °C [40, 76, 211]. At 775 °C, the start of the γ phase in uranium [24], the lattice parameter of the niobium is 3.320 Å [76].

1.3 Uranium Alloys

The binary (and some ternary) phase diagrams of uranium and most potential alloying elements were constructed in the 1950's and 60's [216]. Generally, uranium exhibits low miscibility with transition metals, T, at room temperature causing a single phase mixture to be energetically unfavourable. Due to the complex nature of the α-U and β-U phases, other elements cannot easily be added to form a solid solution. Only upon reaching the high temperature γ phase are the Hume-Rothery rules satisfied and *bcc* elements are able to form a solid solution with uranium [103]. Owing to the similar atomic radii [97], uranium typically favours forming substitutional alloys with transition metals, rather than producing interstitial alloys. Towards the uranium-rich end of the spectrum at temperatures below the monotectoid at ~ 650 °C, the stable arrangement is a mixture of the α-U + bcc-T or α-U + hcp-T phases. Unlike some of its neighbours such as plutonium and thorium [47, 79], uranium does not possess an *fcc* phase and so does not alloy with the large number of transition metals that exhibit only the *fcc* structure.

A few elements are capable of facilitating wide ranging mutual solubility, though only at elevated temperatures, where uranium exhibits its high temperature γ phase. These elements belong to the refractory metals and include titanium, vanadium, molybdenum, niobium and zirconium. The alloys of uranium and niobium, titanium and zirconium have complete mutual solubility between the melting point of uranium and around 950-1100 °C, depending on the element. Computational modelling has been applied to these alloys to understand the nature of the bonding and electronic structure [72, 146, 147, 158].

The lack of miscibility between uranium and the transition metals means that slow cooling an alloy from the melt will result in phase separation. Therefore, the most common method of producing usable, single phase uranium alloys is through solution heat treatment in the γ phase prior to quenching in water or oil [7, 52, 252]. Through quenching, decomposition of the γ phase via diffusional mechanisms may be bypassed. Diffusion rates in these systems is relatively low [81], and rates of only $20\,\mathrm{Ks}^{-1}$ or greater are sufficient in avoiding this reaction from dominating [74]. However, quench rate slightly modifies the resulting lattice parameters indicating that some diffusion still occurs at these lower rates [74, 252].

As in the case of steels and a variety of other alloys systems [129, 183], rapid cooling introduces martensitic transformations [38, 85, 122, 237, 274, 276]. When cooled quickly, atoms do not have the possibility of arranging themselves into energetically favourable phases, often requiring distinct regions of different chemical compositions. With diffusion evaded, and now exhibiting a highly thermodynamically unstable structure, the material will undergo a displacive transformation in which the crystal shears to produce a new crystal structure. The martensitic transformation is relatively similar to the process of twinning, with the main difference being the preserved crystal structure in twinning. Atoms collectively move fractions of a unit cell to produce the new energetically favourable structure. Martensitic transformations are mostly commonly observed to occur athermally during a process such as quenching [183], or as a result of applied stress, which has been demonstrated in uranium alloys [31, 38, 276, 301]. Martensitic transformations have also been reported as occurring isothermally [161], though in most cases, the reaction is simulated by a high magnetic field in the case of ferromagnets or at very low temperatures [133, 196, 198, 228]. Isothermal martensitic transitions have also been observed in uranium chromium alloys [268, 288].

Alloying uranium with the early *4d* transition metals is capable of drastically improving both mechanical properties, inferring higher ductilities and strengths in the case of uranium-niobium alloys [49, 199], and corrosion resistance [49], both weaknesses of unalloyed uranium [287]. As well as boosting the candidacy of metallic uranium fuels for nuclear power [176, 233], this has also led to uranium alloys finding use in defence applications [189].

1.3.1 Stable Phases

The binary phase diagram of the U-Nb system is shown in Figure 1.5. At room temperature, there is virtually no solubility for niobium in the α-U phase. This results in a two phase mixture of α-U + γ-Nb as energetically favourable for compositions between 0.5 at.% Nb and 78 at.% Nb. On the niobium-rich end, uranium is soluble in the niobium matrix up to 22 at.%U (78 at.% Nb).

At higher temperatures, there is full solubility in the γ phase. This stretches across all compositions between 950 and 1132 °C. A eutectoid exists between the γ phase and the α-U + γ-Nb two phase mixture at 647 °C and 13.9 at.%Nb (5.9 wt.%Nb) [143, 188]. Either side of this composition, cooling from the γ phase temporarily produces a two phase mixture of either β-U + γ-Nb or γ-U + γ-Nb. The eutectic, the point at which the melting point is minimised, in the U-Nb exists at 100 at.%U.

The phase diagram of the U-Nb system shares a very strong resemblance to that of the Zr-Nb system [2]. Like uranium, zirconium has a larger atomic radius than niobium [231], however, α-U can be considered as very close to a hexagonal structure, the structure of α-Zr until the phase transition to the *bcc* β-Zr at 863 °C [219]. As zirconium is devoid of any other solid phases, the phase diagram is slightly simpler, avoiding the complexity of the β-U contributions. Similarities between the phase diagrams suggest that the bonding between niobium and these two elements is similar, potentially having consequences for the U-Nb-Zr ternary alloy system.

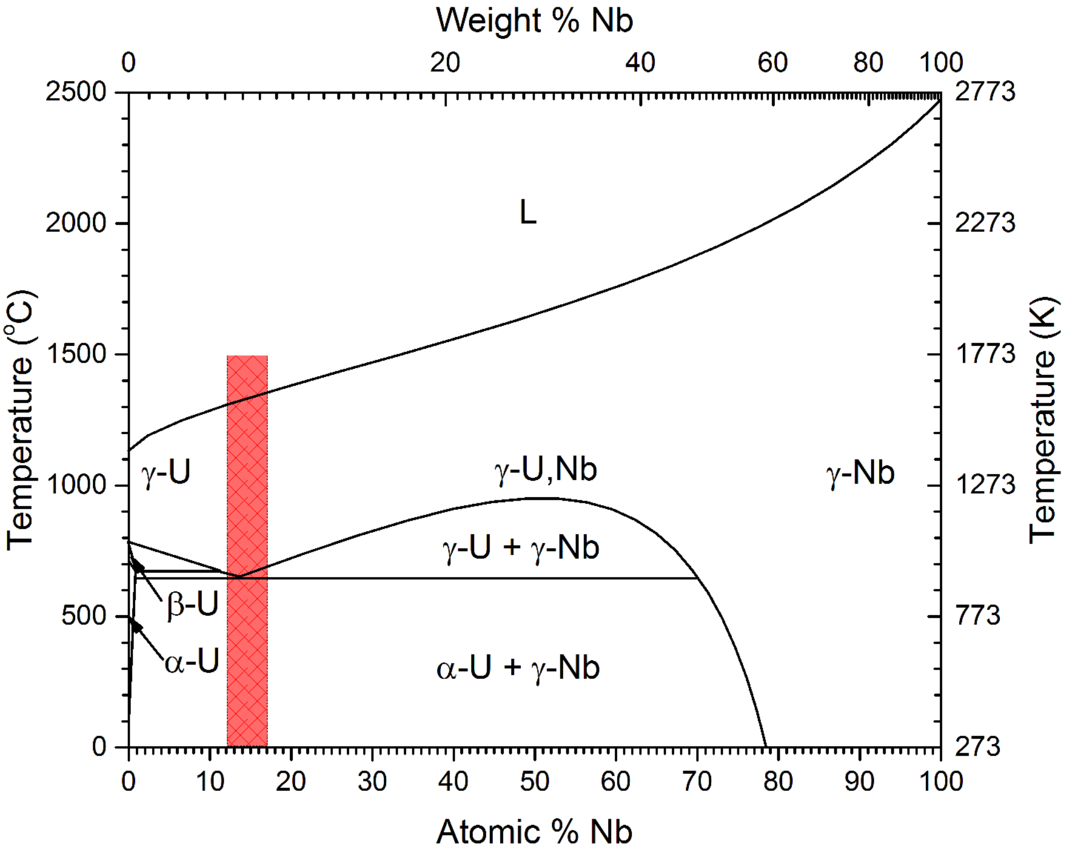

Figure 1.5: Binary phase diagram of the U-Nb system. The red portion of the diagram denotes the region around the eutectoid. The eutectoid compositions present the most advantageous materials when prepared by quenching due to corrosion, irradiation and mechanical property benefits. Image has been redrawn using the data of [143, 158].

1.3.1.1 Intermetallic Phases

No intermetallic compounds are known to exist in the U-Nb system [216]. This has been asserted experimentally and through simulations [143, 158, 188]. Intermetallic compounds such as U_2Mo (Figure 1.6), U_6Fe, U_2Ti and U_6Mn can be created at the uranium-rich end of other systems. Compounds such as UGe_2, URhGe and UCoGe have received a lot of attention for their ferromagnetic and superconducting properties [10].

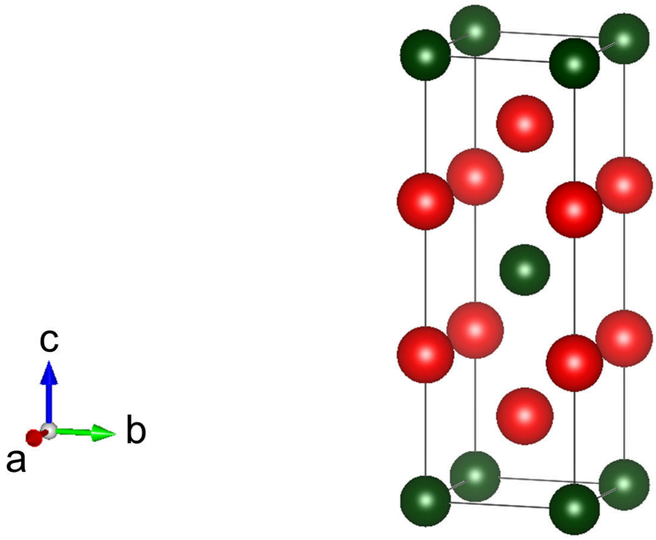

Figure 1.6: Structure of the U_2Mo phase with red spheres denoting uranium atoms and green spheres denoting molybdenum atoms. The U_2Mo phase possesses the I4/mmm space group with the *2a* sites occupied by Mo atoms and *4e* sites occupied by U atoms situated at $z/c = 0.328$.

1.3.2 Metastable Phases

Numerous metastable, martensitic crystallographic phases have been reported for uranium alloys [7, 110, 252, 253]. Owing to the the commonality in the metastable phase between alloys containing elements soluble in the *bcc* γ-U phase, standard nomenclature has been established for the equilibrium and metastable phases in these systems [154]. Given sufficient alloying additions, the γ-U phase may be retained at room temperature via quenching. As this percentage is decreased, the produced phases exhibit features more akin to the α-U phase. The following sections summarise the available literature on the crystallography of these phases to date. Figure 1.7 shows the structures that may be found in the uranium-niobium metastable phase diagram. Comprehensive assessments of the relationship between composition and structure in the U-Nb system has been performed by at least four separate sets of authors with good agreement between [7, 38, 122, 252]. Jackson, and Carpenter and Vandermeer present graphs summarising the results of all four authors [38, 122]. A similar graph is shown later in Figure 4.12.

The list of phases that follows includes only the phases observed in the uranium-niobium system and not phases such as β and ω which are only observed in other systems [111, 268]. Lehmann and Hills provide a complete set of images showing the microstructure created by the metastable phases in UMo alloys [154]. Field *et al.* show a selection of TEM micrographs relating to a range of compositions of the UNb system [85]. All of these are substitutional alloys with random occupancy of elemental species across all atomic sites.

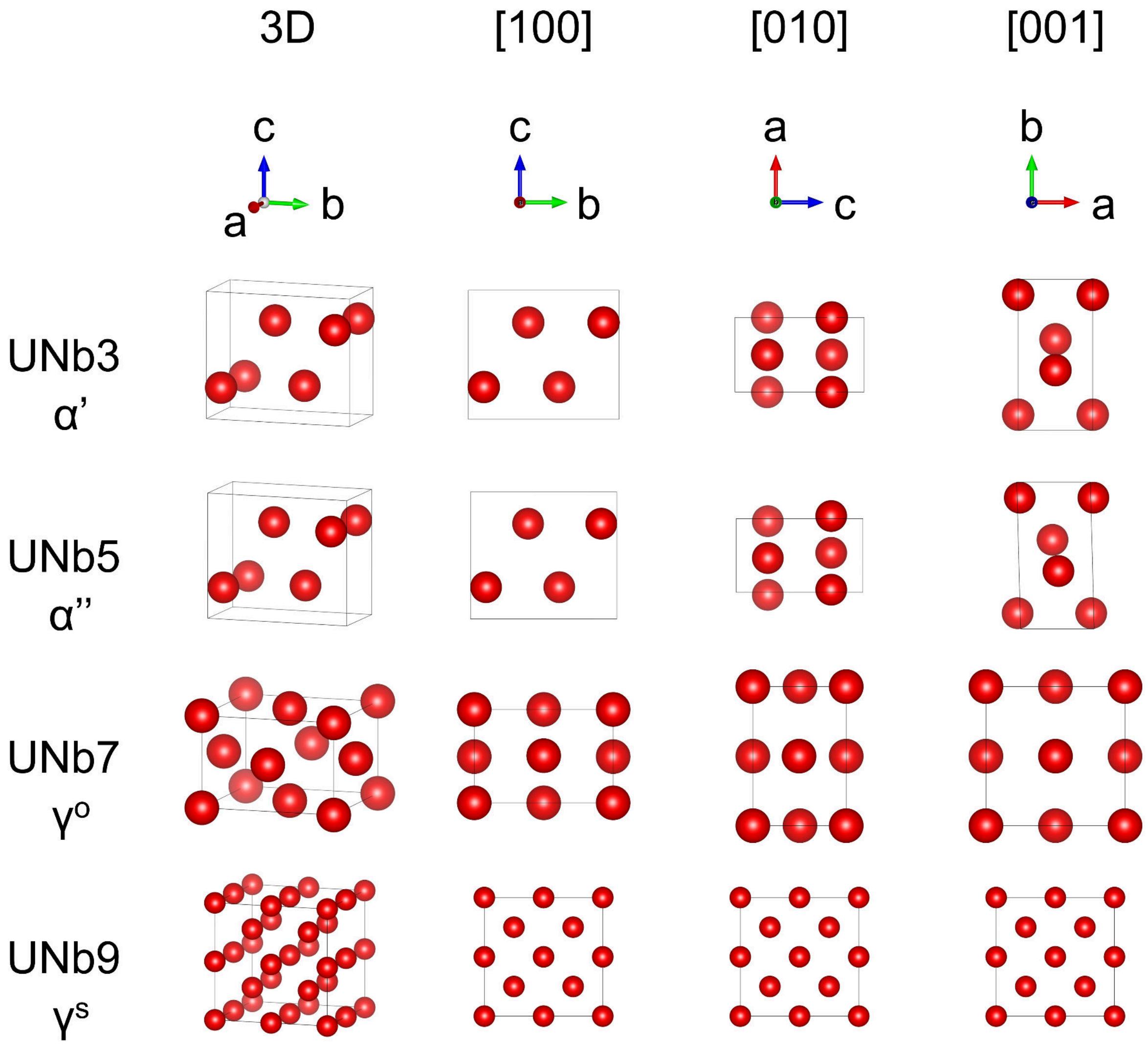

Figure 1.7: Metastable structures of the uranium-rich end of the uranium-niobium binary phase diagram at regular steps of composition in weight percentage. Structures are based on the works of Anagnostidis *et al.*, Tangri and Chaudhuri, and Jackson [7, 122, 252]. Lattice parameters have been interpolated from the three sources where an exact match to to constant-stepped compositions shown here were not present. Lattices are shown in a 3-dimensional configuration as well as parallel to each principal axis.

1.3.2.1 α, 0 - 0.5 at.% Nb

The α phase essentially refers to pure uranium and any composition that falls inside the solubility limit. In the uranium-niobium system, this has been estimated at around 0.5 at.% Nb [143]. The lattice parameters in this situation would be virtually unchanged, essentially those of pure uranium. The microstructure of this phase is also the same as that of pure uranium. The structure for the α phase is shown in Figure 1.1.

1.3.2.2 α', 0.5 - 10 at.% Nb

The α' phase represents the first true metastable phase as the lattice parameters differ to that of unalloyed uranium. The α' phase shares the same symmetries as α-U, maintaining the orthorhombic *Cmcm* space group. The most notable consequence is a decrease in the b axis, however the a and c axis lengths are slightly larger. The microstructure is modified as a result of alloying additions and both acicular and banded microstructures have been reported [154]. The phase is martensitic is nature and heavily twinned with the $\{021\}$ mode displayed most frequently [85].

1.3.2.3 α'', 10 - 16.5 at.% Nb

The α'' phase is the first instance at which a symmetry is broken. With reference to the structure of the α phase, the $\angle\gamma$ deviates from 90 °, breaking orthorhombic symmetry and adopting a monoclinic crystal class. In order to maintain a resemblance with the α phase, non conventional unit cells with unique c axes (rather than b) are most commonly used to describe the structure. Brown *et al.* have suggested the use of $C112_1/m$, a space group that maintains the centrosymmetry present in the α phase [30]. The b cell axis continues to decrease with increasing niobium, with the a and c doing the opposite to a lesser extent. The $\angle\gamma$ is observed to start to deviate from 90 ° at 10 at.% Nb, marking the start of the α'' phase. The α'' is the last phase that is considered α-like with the next phases more closely resembling the γ phase. Between the α and the α'' phase, all changes to lattice parameters have been continuous.

The microstructure of the α'' phase has been shown to vary considerably with 'regular interpenetrating' and 'irregular' bands featured [154]. Herringbone twinning on a variety of length scales is seen frequently in this phase. Field *et al.* established the nature of this ubiquitous twin structure [85], Figure 1.8. Laths on the order of microns contain $(1\bar{3}0)$ twins roughly 20-50 nm in thickness that accomodate the interlath relationship through the (021) and $(1\bar{1}1)$ twin mechanisms [52, 85].

1.3.2.4 γ°, 16.5 - 20 at.% Nb

The γ° phase exhibits a tetragonal structure which was originally designated as having a c/a axial ratio of close to half as the structure was based on the equivalent of 4 *bcc* γ cells $(2 \times 2 \times 1)$

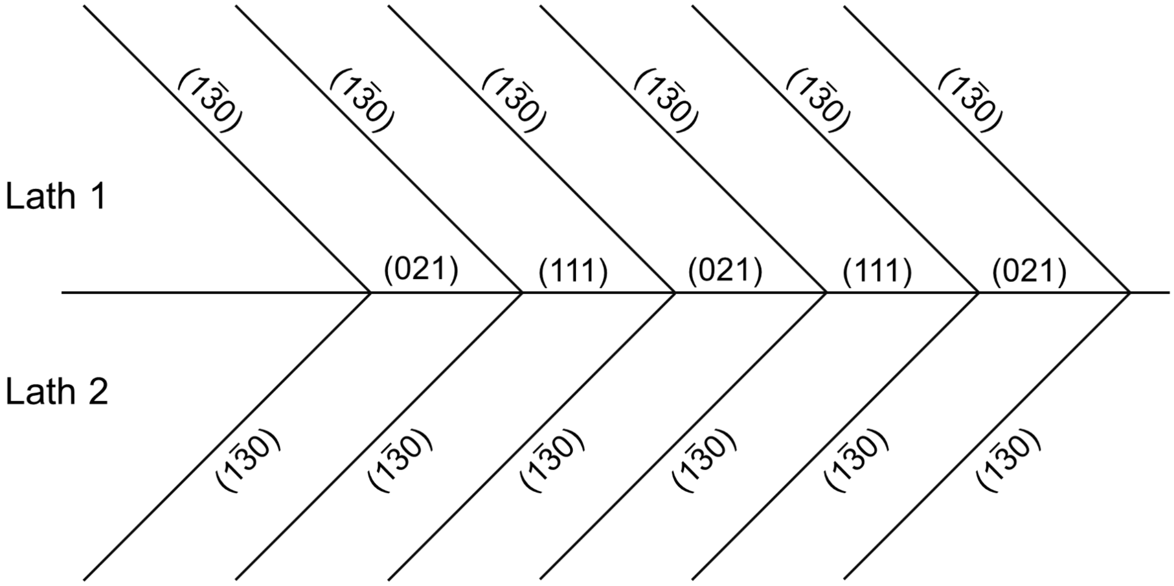

Figure 1.8: Martensitic twins structure observed in the U-13 at.% Nb and deduced by Field *et al.* using selected area TEM diffraction [85]. This image has been reproduced based on the original presented by Field *et al.* [85].

[7, 252]. The atomic coordination is quite close to that of a *bcc* structure. Yakel showed that adequately modelling the anisotropic broadening of the XRD pattern of a 2 hour, 150 °C aged U-16.60 at.% Nb-5.64 at.% Zr (U-7.5Nb-2.5Zr) alloy, required rotating the unit cell and decreasing the a axis by $\sqrt{2}$, halving the volume [293]. The axial ratio under this definition is close to $1/\sqrt{2}$.

Yakel suggested *P4/nmm* as the most likely space group for the γ° structure [293], creating a structure close to that of β-Np [296]. The choice of this cell permitted anti-parallel displacements of the atoms on the $\{100\}$ planes in the $\langle 001 \rangle$ direction. Yakel showed that adding in this capability permitted good simulation of the XRD patterns without the requirement for chemical ordering that had been proposed by Tangri and Williams [253, 293]. Vandermeer established that the γ°, which acts as a precursor to the α'' phase for lower alloy compositions, is produced by displacement ordering of the parent γ phase in the manner described by Yakel [274, 293].

There is a large change in the XRD patterns between the α'' and γ° phase compared to any other neighbouring phases. Carpenter and Vandermeer showed that the transition between the γ° and α'' phases is martensitic and progresses by a discontinuous shearing of the lattice, substantially changing the symmetry of the lattice, much more so than the atomic shuffling that occurs through the rest of the compositional phase space [38].

Examining an 18 at.% Nb alloy using TEM, Field *et al.* observed that the microstructure was composed of numerous domains, within which lamella structure could be observed [85]. Lamellae were established to be around 50 nm in width and related by $\{110\}_{\gamma}$ twinning.

1.3.2.5 γ^s, 20+ at.% Nb

The metastable γ^s phase occurs at the greatest compositions of niobium. As the first phase to form in the quenching process, the γ^s phase most strongly resembles the γ phase. Also using the (unaged) U-16.60 at.% Nb-5.64 at.% Zr alloy, Yakel showed the γ^s phase to be best described by a cubic cell of the $I\bar{4}3m$ (217) space group with axes doubled that of the γ phase's body centred cubic (*bcc*) structure [293]. With increasing niobium content, the lattice parameter has been observed to decrease slightly [122], in keeping with Vegard's law [64].

Yakel and Vandermeer showed atoms situated at the *24g* Wyckoff sites are displaced from (1/4, 1/4, 1/4) positions along the ⟨100⟩ directions to a small degree [273, 293]. To maintain the correct density, the occupancy of the atoms on these sites is 1/3. Yakel also showed that the structure proposed for the UNbZr alloy studied was a better description than that proposed by Tangri for a U-13.9 at.% Mo alloy that relied on chemical ordering [253, 293].

Depending on the context, it may be preferable to work in atomic over weight percentages or vice versa. The conversions between atomic and weight percentage for the U-Nb system are,

$$x_{wt} = \frac{93x_{at}}{93x_{at} + 238(1 - x_{at})} \times 100\%, \tag{1.1}$$

and,

$$x_{at} = \frac{x_{wt}/93}{x_{wt}/93 + (1 - x_{wt})/238} \times 100\%, \tag{1.2}$$

where x_{at} and x_{wt} are the niobium content expressed as percentages.

1.3.2.6 The Metastable Phase Diagram

In the previous section, metastable phases at room temperature as a function of composition were discussed. As in the case of other systems that exhibit the shape memory effect, the phases in these materials are subject to change depending on temperature and applied stress. Figure 1.9 shows the metastable phase diagram for temperature and composition in the UNb system.

The austenitic start temperature, A_s, is located at around 400 °C for the lowest niobium compositions in the range showed in Figure 1.9. A_s falls as the alloying content is increased. The γ phase is stable above this temperature, but below this, the alloy will transform into γ° phase, or, at higher compositions, the γ^s. Eventually, the γ/γ^s phase is stable beyond 18 at.% Nb, at which point, the A_s drops below 0 °C. Vandermeer *et al.* showed the transformation hysteresis, to be very small for reasonable heating rates, < 20 °C, *i.e.* $M_s \approx A_f$ and $A_s \approx M_f$ [274, 276].

The martensitic start, M_s, and finish, M_f, temperatures are much more typical of shape memory alloys. On cooling, the material begins to transform into the α'' phase at M_s and finishes

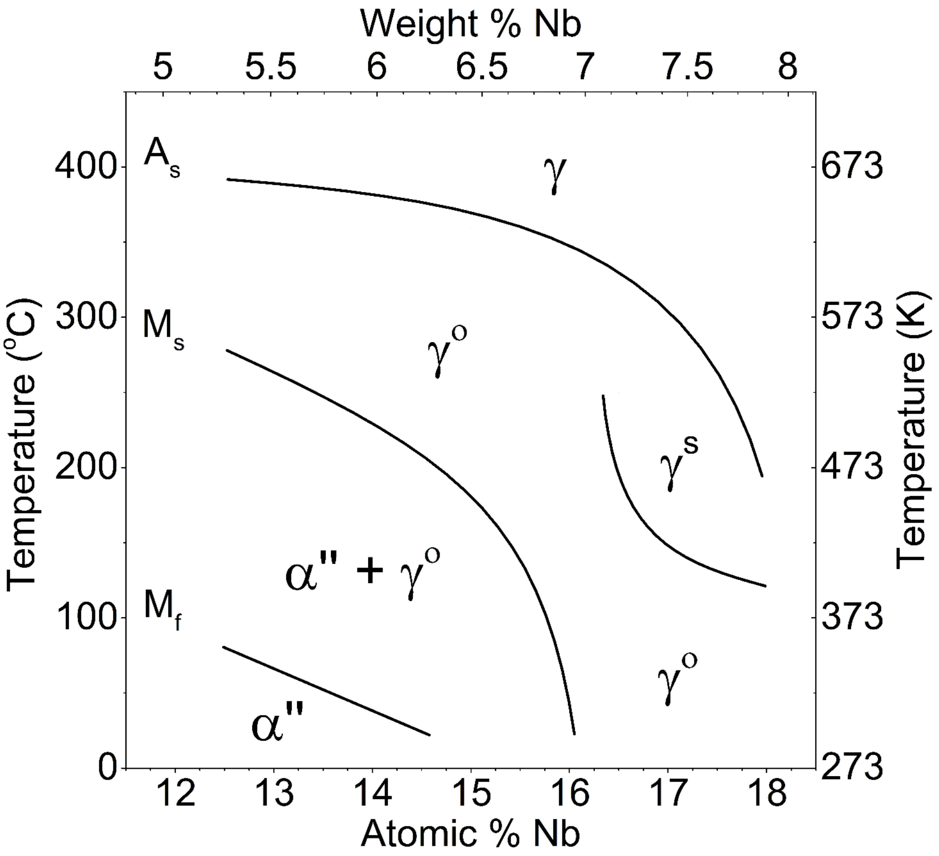

Figure 1.9: Metastable phase diagram for the uranium-niobium system in the region of the eutectoid. Image has been reproduced based on an original constructed by Vandermeer [276].

transforming at M_f. The α'' phase fraction is proportional to the progression of the alloy through the transition. However, the martensitic transformation is not two-way, converting the material back to the γ° can only be achieved by reheating above A_s/A_f to stabilise the γ phase before cooling to below A_s. Compared to the difference between A_s and A_f, the difference between M_s and M_f is very large, around 200 °C.

Vandermeer also investigated the behaviour of the alloys down to room temperature [275], showing that lower temperatures promoted the production of more of the α'' phase as expected but full transformations were not observed in alloys that originally exhibited a mixture of the α'' and γ° phases.

1.3.3 Shape Memory Effect in Uranium Alloys

1.3.3.1 Background to the Shape Memory Effect and Superelasticity

The shape memory effect (SME) and superelasticity (also known as pseudoelasticity) are phenomena exclusive to alloy systems exhibiting the austenite-martensite phase transition [37, 193]. The unique ability for these alloys to transform between the two closely related crystal structures by deformation and recovery of the lattice through applied mechanical stress and heating permits the recovery of shape and size. The shape memory effect and superelasticity are best explained with reference to the theoretical stress-strain curves, Figure 1.10.

Panel *a* shows the stress-strain curve of a typical metal that does not participate in the shape memory effect or super-elasticity. This curve may alternatively represent a material in an austenitic phase but sufficiently far away from the austenite to martensite transition that the martensitic phase is not accessible through applied stress. The curve begins with linear elastic straining in which on the release of the applied load, the lattice reverts back to its original size. This continues until the yield strength, at which point, the material can no longer be strained elastically. Additional (unrecoverable) extension of the material is only possible through plastic deformation. The process of slip facilitates plastic deformation in this region through the production of numerous dislocations; atoms break bonds with their neighbours and reform bonds with new neighbours following a large scale movement of atoms. Strain hardening by plastic deformation continues until the ultimate tensile strength is achieved. At this point, necking starts to occur which sees the cross section of the test piece reduce. The narrowing cross section focuses the stress and eventually the piece fractures.

Panel *b* shows the stress-strain curve of a shape memory alloy at strains less than the yield point. Initially, the alloy is below the martensitic finish temperature, M_f, exhibiting a heavily twinned martensitic microstrcuture. Initially, the alloy experiences elastic straining of the twinned martensitic phase. However, relatively low strains subsequently facilitate the migration of twin boundaries producing a detwinned martensite that is maintained after the removal of the load. Following the complete conversion of the martensite to a detwinned microstructure, the detwinned martensite may continue to be elastically strained to the yield point, after which, true plastic deformation will occur. If the load is removed before the yield point, the alloy will relax, undoing some extension as elastic energy is released. The extension that was evolved throughout the detwinning is not immediately recoverable.

Upon heating, the shape memory effect may be realised. Increasing the temperature above the austenitic finish temperature, A_f, the alloy is converted to the high temperature austenitic phase, taking on the original size and shape of the alloy. Cooling the alloy back to the original temperature converts the lattice back to the martensitic structure but does nothing to alter the macroscopic size and shape of the alloy.

Panel *c* shows the stress-strain curve of a super-elastic material. Superelasticity requires an initially austenitic material, that under applied stresses, converts to a detwinned martensitic phase. Removal of the load returns the material to the original shape and size, without the requirement for subsequent heating. The conversion to the martensitic phase is not permanent, as the phase is only stable under the applied load.

The stress-temperature phase diagram for a shape memory alloy is shown in Figure 1.11. The diagram marks shows the possible transformations that can be produced by either manipulating the temperature or stress in the material.

1.3.3.2 Uranium-Niobium Alloy SME

The shape memory effect was first reported in uranium-niobium alloys by Jackson and Johns in 1970 [126]. Jackson and Johns showed the shape memory effect to be exhibited for compositions in the range of 6 to 21 at.% Nb (2.4 to 9.4 wt.% Nb) between -200 and 400 °C [126], which essentially corresponds to materials exhibiting the α'' and γ°, and mixtures of the two. The effect was observed to be the greatest for 15 at.% Nb (6.5 wt.% Nb) [126], which is an alloy that exclusively shows the α'' phase but is very close to the γ° transition [7, 252].

Vandermeer *et al.* subsequently investigated the SME in compositions spanning the range between 13.9 and 15 at.% Nb [275–277]. A strain induced transformation from the γ° to the α'' phase was observed in a mixed phase alloy (15 at.% Nb) [85, 276]. Otherwise, XRD determined the structures to be unchanged after deformation. Field *et al.* suggests that the unwillingness for the γ° to convert into α'' may be a result of high Nb content uranium alloys instead producing shape memory through realignment of the γ° [85]. The stress-induced martensitic reaction however has been observed by a couple of authors. Carpenter and Vandermeer showed the 6.4 wt.% Nb alloy to undergo a clear γ° to α'' transition by applying progressively up to 3% strain [38]. Zhang *et al.* showed the 5.8 wt.% Nb to lose its γ° component (produced through ageing at 200 °C) as a function of straining [301].

Vandermeer showed that recovery was achieved through a two-step process that was ascribed to successive α'' to γ° and γ° to γ transitions in the low Nb composition, naturally α'' phase alloys. Two step recovery was also observed for higher Nb content alloys naturally possessing the γ° phase which led Vandermeer *et al.* to suggest that in addition to a γ° to γ transition, chemical ordering could be playing a role [276], a conclusion that was refuted by Field *et al.* [85].

Field *et al.* evaluated the microstructure of un-deformed 5, 9, 13 and 18 at.% Nb samples and deformed 13 at.% Nb samples by TEM that included selected area electron diffraction [85]. Comparison between the un-deformed and deformed 13 at.% Nb samples enabled evaluation of the twin structures. As previously stated, the dominant twinning mechanism in the un-deformed is the $\{\bar{1}30\}$ type. In specimens deformed to 3%, the alloy also featured numerous $\{\bar{1}72\}$ twins that had been produced in response to straining. $\{\bar{1}11\}$, $\{112\}$ and $\{012\}$ modes were also discovered but were not as prevalent as the $\{\bar{1}72\}$ and $\{\bar{1}30\}$ twins that together formed the majority of twins. At larger strains (4.5%), the $\{\bar{1}30\}$ twins could not be found and $\{\bar{1}72\}$ represented the majority of all twins. Field *et al.* therefore proposed a model for the shape memory effect in uranium alloys in which deformation was dominated by the production and motion of $\{\bar{1}72\}$ twin boundaries which acted to envelop fine twins and produce single-orientation regions (detwinning). This is shown schematically in Figure 1.12. The $\{\bar{1}72\}$ twins were observed to be capable of crossing pre-existing twins but also, through calculations, were shown to exhibit the low twinning shear.

Both of these characteristics are thought to be responsible for the high mobility shown in these twins.

Clarke *et al.* subsequently used EBSD to study the shape memory effect in the 14 at.% Nb alloys [52]. Clarke *et al.* confirmed that $\{\bar{1}72\}$ along with $\{1\bar{1}1\}$ twins were the dominant species in the deformed alloy. $\{1\bar{3}0\}$, $\{112\}$ and $\{176\}$ twins were also observed. Straining also appears to have effectively induced the production of single-orientation regions that are highly textured in the direction of straining.

Brown *et al.* examined the SME in the 7 wt.% Nb alloy using in-situ neutron diffraction in compression [31]. Study of an alloy initially exhibiting the γ° phase confirmed Vandermeer's observation that the deformation behaviour of the γ° phase is different to that of the α'' phase [276]. Recoverable strain was shown to be accommodated by both the motion of twin boundaries in the γ° and a stress-induced γ° to α'' phase transition. The two processes occur within a very close range of each other with γ° twin boundary movement onset at (-)125 MPa and the γ° to α'' transition commencing at (-)175 MPa. The conversion to α'' phase progresses over roughly 2% on the steeper portion of the curve (region C) up to the start of plastic deformation. Brown *et al.* estimated that only 26% of the material had not been converted to the γ° phase by around 4% total strain. Unloading the alloy caused some reversion on release which is in keeping with SME theory and may explain why previous authors have struggled to confirm the stress-induced γ° to α'' transition previously when not performing the tests in-situ.

Govindjee and Kasper set out the mathematics for the shape memory alloy in the UNb system while also accounting for plastic deformation [96]. Zubelewicz *et al.* had good success in the computational simulation of the stress-strain behaviour of the UNb6 alloy [304].

1.3.4 Phase Transformations in Metastable Uranium Alloys

1.3.4.1 Background to the Phase Transformations in Metastable Alloys

By virtue of the lack of solubility of niobium in uranium at low temperatures, the metastable phases discussed previously would be expected to tend towards decomposing into stable α-U and a niobium rich γ phase [74]. In a large number of alloys used for industrial applications, the desired microstructure is a metastable one, often an intermediate between the initial and equilibrium phases [37]. Phase transformations are therefore frequently induced in metastable alloys to tailor a metal's properties. A strong understanding of the influence of time, and usually temperature, on the stability of phases is therefore required, and isothermal transformation diagrams are often constructed. Such phase transformations are usually thermally activated mechanisms, however, as the last section showed, stress can also be very influential in these polymorphic systems.

Figure 1.13 shows the isothermal transformation diagram, also known as a time temperature transition diagram, for an iron-carbon (steel) alloy of eutectoid composition [37]. In this example, the depicted phases shown here are not accurate, but illustrative of the changes to crystallography and consistent with the conventions of the previous images. Above the eutectoid temperature, A, the austenitic phase is stable. As the temperature is lowered, phase transformations are thermodynamically favourable. Aged at temperatures above the nose of the C-curve, a pearlite microstructure will form. Aged below the nose of the C-curve, bainite will be produced. In this case, the transitions to pearlite and bainite compete over a similar temperature range leading to the appearance of a single C-curve. In other compositions and systems, pearlite and bainite reactions may be further separated by two distinct C-curves. Pearlite and bainite are relatively well related as both are formed by carbon diffusing out of the austenite phase producing spatially separated regions of ferrite, α-Fe, and cementite, Fe_3C. Whereas the terms, austenite and martensite, are used in other alloy systems, bainite and ferrite are used almost exclusively in steels.

The C-curve shape may initially look relatively counter-intuitive as these diffusion mitigated transitions are controlled by Avrami-type kinetics. At constant temperature, this is the case with percentage transformed taking the form of a cumulative distribution function. However, the C-curve shown in Figure 1.13 is produced as nucleation and diffusion have different responses to temperature with nucleation acting faster at low temperature and diffusion more rapid at higher temperatures.

1.3.4.2 Uranium Alloys

Eckelmeyer *et al.* investigated the effects of quench rate on the microstructure, mechanical properties and corrosion behaviour of the UNb6 alloy [74]. Slow rates of quenching, 20 °C/s, were found to be sufficient to force the material into undergoing the martensitic transformation. Common practice is to quench uranium alloys in water with a rate estimated at around 1000 °C/s [252]. Continuous cooling diagrams are often produced for alloys to evaluate the processes and transformations that occur during cooling [37]. In uranium alloys, under normal processing, continuous cooling diagrams are relatively unimportant.

Investigations into the phase transformations of the metastable uranium-niobium alloys have spanned the full temperature range from the temperature of liquid nitrogen up to the eutectoid temperature at 647 °C. The majority of the works in the literature to have investigated the stability of these alloys (and UNbZr alloys) under elevated ageing conditions agree to there being at least two reactions, and isothermal transformation diagrams feature at least two distinct C-curves [39, 61, 273, 274]. Hackenberg *et al.* has established that a third reaction is possible in uranium-niobium alloys [106] and in the uranium-niobium-zirconium alloy, Vandermeer proposed the existence of four distinct reactions [273]. Rates of each reaction is dependent on alloying species and composition, but broadly, the cross-over between the low and high temperature reactions is found at roughly 400 °C for all uranium alloys [199].

Works to have investigated the decomposition of uranium alloy phases has therefore generally been split into two groups; those focusing on high temperatures and those at lower temperatures. The split between has been relatively even with early works mainly focusing on the high temperature reaction [20, 57, 61, 67, 123, 134, 162, 199, 273, 279, 300], but more focus on the lower temperature reaction(s) in recent years as the exact mechanisms responsible remain elusive [20, 30, 51, 104–106, 123, 134, 162, 273, 274, 279, 298, 299, 301]. Jackson has produced a full isothermal transformation diagram for the U-13%at Nb (6% wt Nb) alloy [123]. Hackenberg *et al.* constructed a schematic of the isothermal transformation diagram based on all the available literature [106], which has been reproduced in Figure 1.14.

1.3.4.3 High Temperature Transformations

Literature sources strongly agree the high temperature transformation to be governed by a cellular decomposition style reaction acting to refine a pure α-U and a Nb-rich γ phase in a lamellar structure [20, 57, 67, 74, 123, 199], ocassionally described as analagous to pearlite in steels [123, 199]. Stability is conferred onto these the uranium-niobium alloys with greater alloying additions causing reaction rates to decrease with increasing niobium content [199]. In some cases, reactions can initiate very quickly making in-situ diffraction methods unviable historically. Resistivity, differential thermal analysis and dilatometry measurements have therefore been regularly used techniques to quantify reaction rates as a function of temperature [134, 199, 274], with follow-up, ex-situ metallography and x-ray diffraction best suited to qualifying the changes to the microstructure [123, 124, 134]. Grain boundaries, have been shown as the primary sites of precipitation of the equilibrium phases [67, 123, 140]. Djuric showed the isothermal decomposition of these alloys at high temperatures proceeds by a two step process, in which, a metastable γ phase that maintains a constant composition is initially formed [67]. As the reaction progresses, this metastable phase subsequently separates into the equilibrium α-U + γ-(Nb,U) arrangement. Zhang *et al.* recently studied the high temperature transformation in the 6 wt.% Nb alloy, confirming this two stage reaction progressed by in-situ x-ray diffraction using high energy x-rays [300]. The alloy, initially exhibiting the α'' phase at room temperature was additionally observed to undergo a reverse martensitic transformation, $\alpha'' \rightarrow \gamma^\circ \rightarrow \gamma$, on reheating prior to phase separation.

Isothermal transformation diagrams are specific to each composition. Peterson provides high temperature sections of isothermal transformation diagrams for a small range of compositions [199].

1.3.4.4 Low Temperature Transformations

Low temperature ageing of dilute, metastable uranium alloys has regularly been shown to lead to increases in hardnesses and strength, whilst also incurring losses to ductility [106, 199]. In comparison, ageing the alloys at high temperature leads to a phase separated microstructure resulting in poor corrosion and mechanical properties that are only slightly superior than unalloyed uranium [51, 73]. The low temperature reactions are represented by regions 1 and 2 on Figure 1.14. Hackenberg *et al.* made a distinction between the medium-temperature hardening mechanism, region 2, which involved diffusion to some degree, and the low-temperature hardening mechanism, in which the mechanism is unknown [106].

Low temperature ageing, in contrast to the high temperature reactions, does not incur a loss in corrosion resistance, despite significant changes to mechanical properties [51, 74]. A number of diffusional processes incurring phase separation have been proposed as possible drivers of the low temperature reactions [51]. However, where the effects of diffusion has been observed at temperatures in the 200 - 400 °C degree range [20, 51, 105, 106], it has proved difficult to establish any sources of phase separation at the lowest temperatures [51]. There is still a lack of clarity in the mechanism of the medium-temperature hardening mechanism and it remains to be seen whether the medium-temperature hardening mechanism is a completely separate mechanism, or the same as the low-temperature hardening mechanism but minimally affected by the high-temperature hardening mechanism.

Jackson's 1971 work on the 13 at.% Nb alloy does not make reference to what Hackenberg *et al.* refer to as the low-temperature hardening mechanism [123]. However, the ageing of this alloy at temperatures between 100 and 400 °C is explained as a segregation reaction, but where microscopy fails to observe changes at the lower temperatures. Peterson also stated that it was not possible to follow the course of the low temperature reactions by optical metallography [199]. Jackson's hypothesis of solute segregation is at odds with that of Clarke *et al.* who found very little evidence of chemical redistribution after ageing at 200 °C for up to 70 days [51]. Clarke *et al.* paid special attention to segregation and diffusion of niobium to twin interfaces which was suggested by Jackson as a likely source of strengthening [123]. Clarke *et al.* were also able to rule out spinodal decomposition and ordering at temperatures less than 300 °C from theoretical first principles [51].

Vandermeer's investigations into the phase transformations of the 14 at.% Nb alloys showed that as well as transforming into the α'' phase athermally during the quenching process, the alloy could achieve this state isothermally having been aged at 165 °C above the martensitic start temperature, M_s [274]. Vandermeer also provides indirect evidence for solute segregation that may be influencing the isothermal $\gamma^{\circ} \rightarrow \alpha''$ transition that was believed, as in the case of the athermal reaction, to be martensitic in nature.

An isothermal $\gamma^{\circ} \rightarrow \alpha''$ reaction has also been reported by authors to have investigated phase transformations in the closely related UNbZr alloys [61, 134, 199, 273]. Peterson noticed that the addition of zirconium to uranium alloys sped up the low temperature reactions [199]. In the UNbZr alloy, Vandermeer also expressed the view that solute segregation acts as a precursor to the isothermal martensitic transformation in a U-7.5wt.%Nb-2.5wt.%Zr alloy [273].

Brown *et al.* recently examined the ageing of the 6 wt.% Nb alloy by in-situ neutron diffraction at temperatures up to 300 °C [30]. An initial reversion to the γ° phase was experienced before transitioning back to the α'' phase after several hours. In-situ diffraction was also performed during mechanical loading of the specimens at 200 °C for up to 8 hours, in which microstructural changes were related to macroscopic mechanical changes. The deformation mechanics established by Field *et al.* and Clarke *et al.* were found to be unchanged in form by ageing [51, 85], however the resistance to twin boundary motion greatly increased with ageing. Brown *et al.* attributed the increase in resistance to twin motion to ageing induced rearrangement of twin interfacial structures to lower energy configurations [30]. This was predicted by Brown *et al.* to additionally be responsible for partially stabilising the martenstic structure. Zhang *et al.*, also studying the the low temperature reaction by neutron diffraction, proposed a similar hypothesis, focusing on the migration of defects such as vacancies and dislocations rather than the rearrangement of twin interfaces [298].

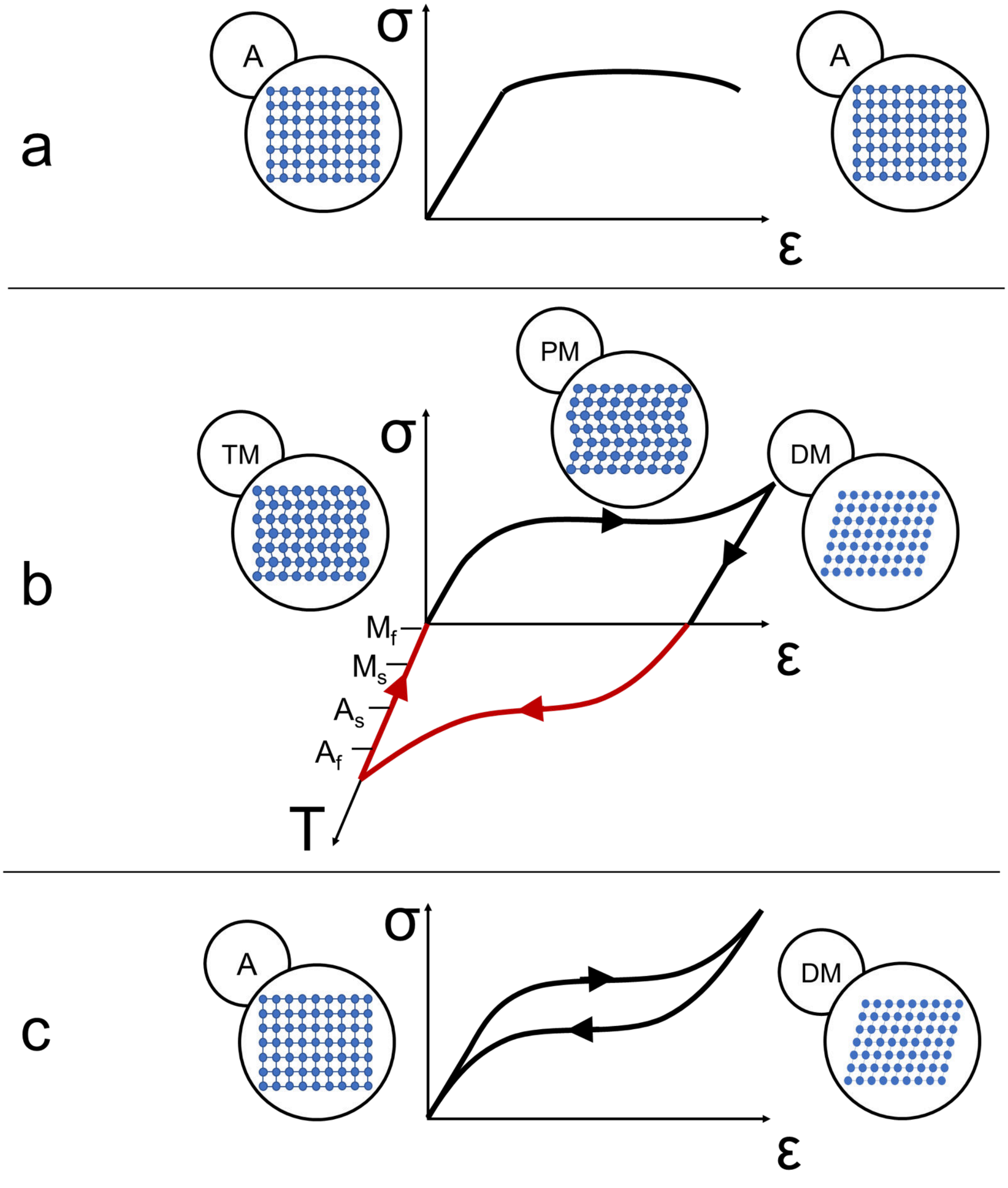

Figure 1.10: Schematic stress-strain curves of, *a* regular metals, *b* shape memory alloys and *c* superelastic alloys. *A* denotes the austenitic phase, *TM* refers to a twinned martensite, *DM* refers to a detwinned martensite and *PM* refers to partially detwinned martensite.

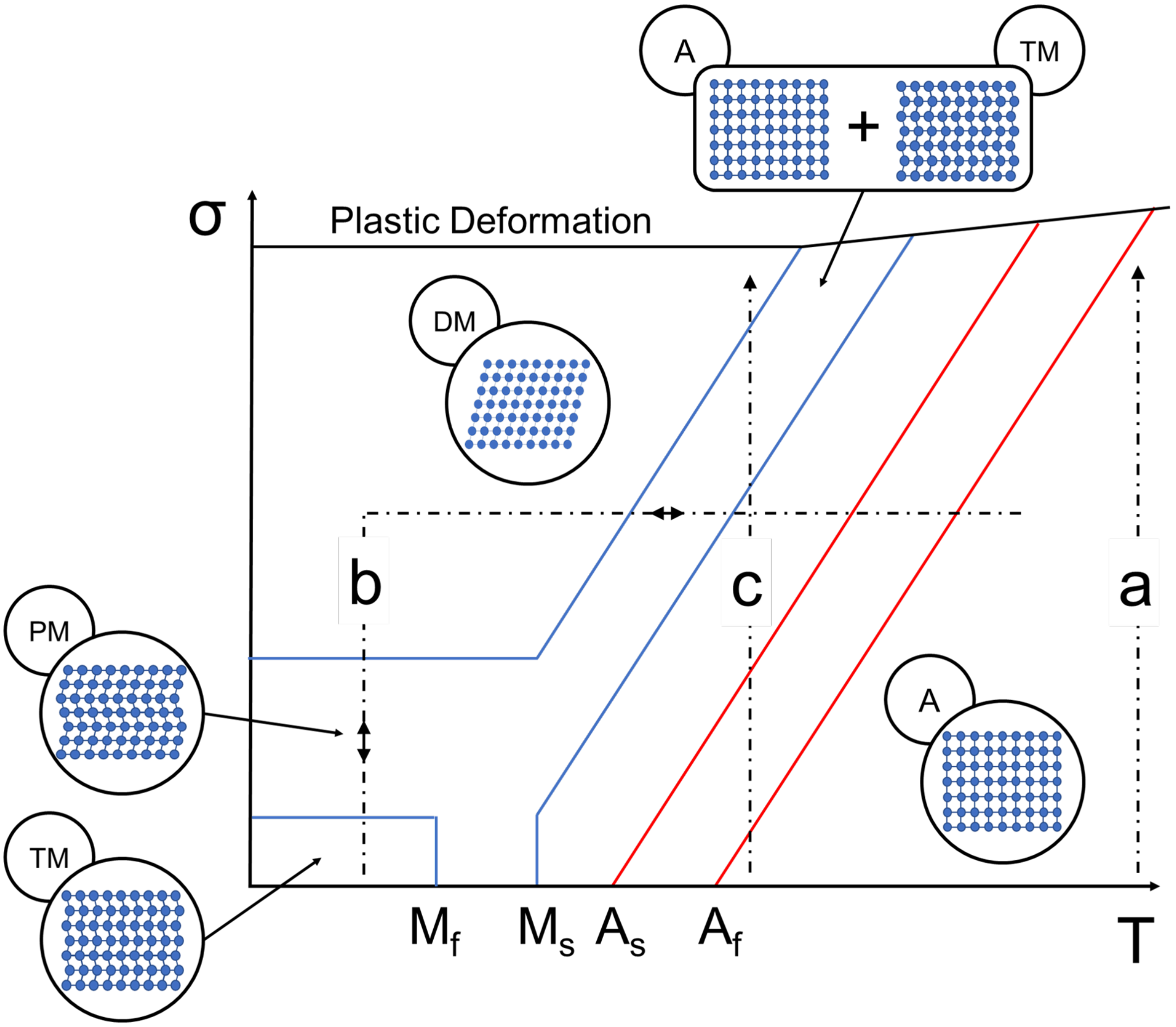

Figure 1.11: Stress-temperature phase diagram of an example shape memory alloy. The paths of the three stress-strain curves shown in Figure 1.10 are annotated on this diagram.

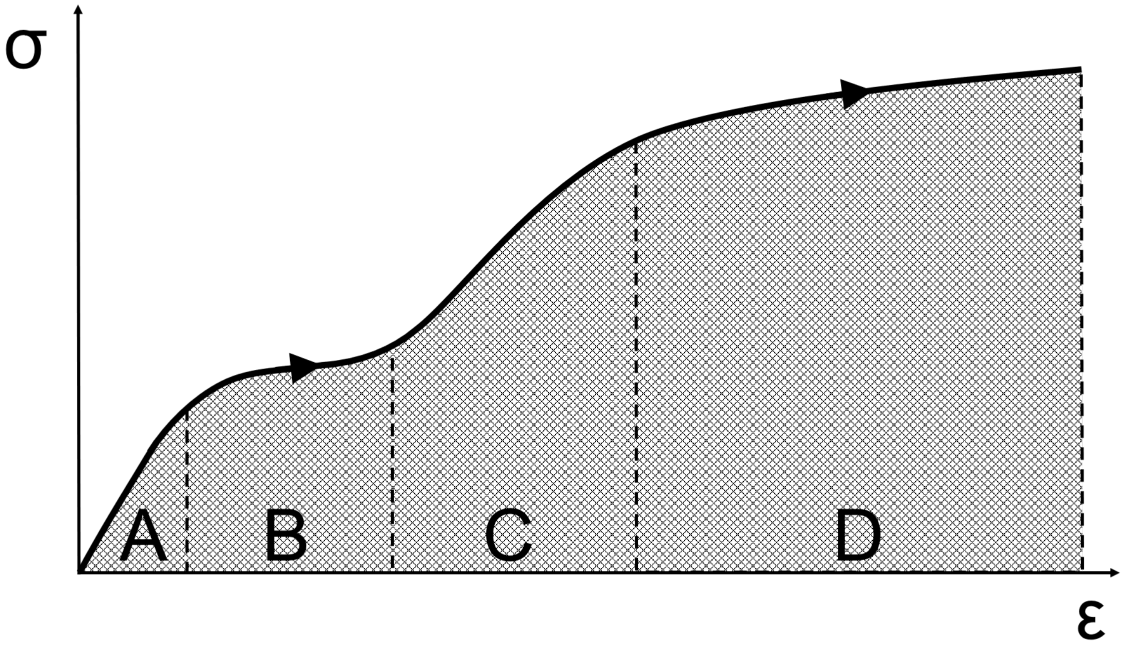

Figure 1.12: A reproduced schematic of the stress-strain curve found in the α'' phase UNb alloys based on an original by Field *et al.* [85]. Field *et al.* suggests the curve can be explained as comprising four distinct regions labelled on the diagram as *A*-*D* [85]. *A* corresponds to elastic straining of the heavily twinned α'' phase martensite. *B* was put to motion of $\{\bar{1}72\}$ twins. In *C*, the cooperative migration of fine $\{\bar{1}30\}$ twins and $\{\bar{1}72\}$ twins was suggested to be responsible for eliminating fine twins producing single-orientation regions. *D* is plastic deformation which is mediated by slip.

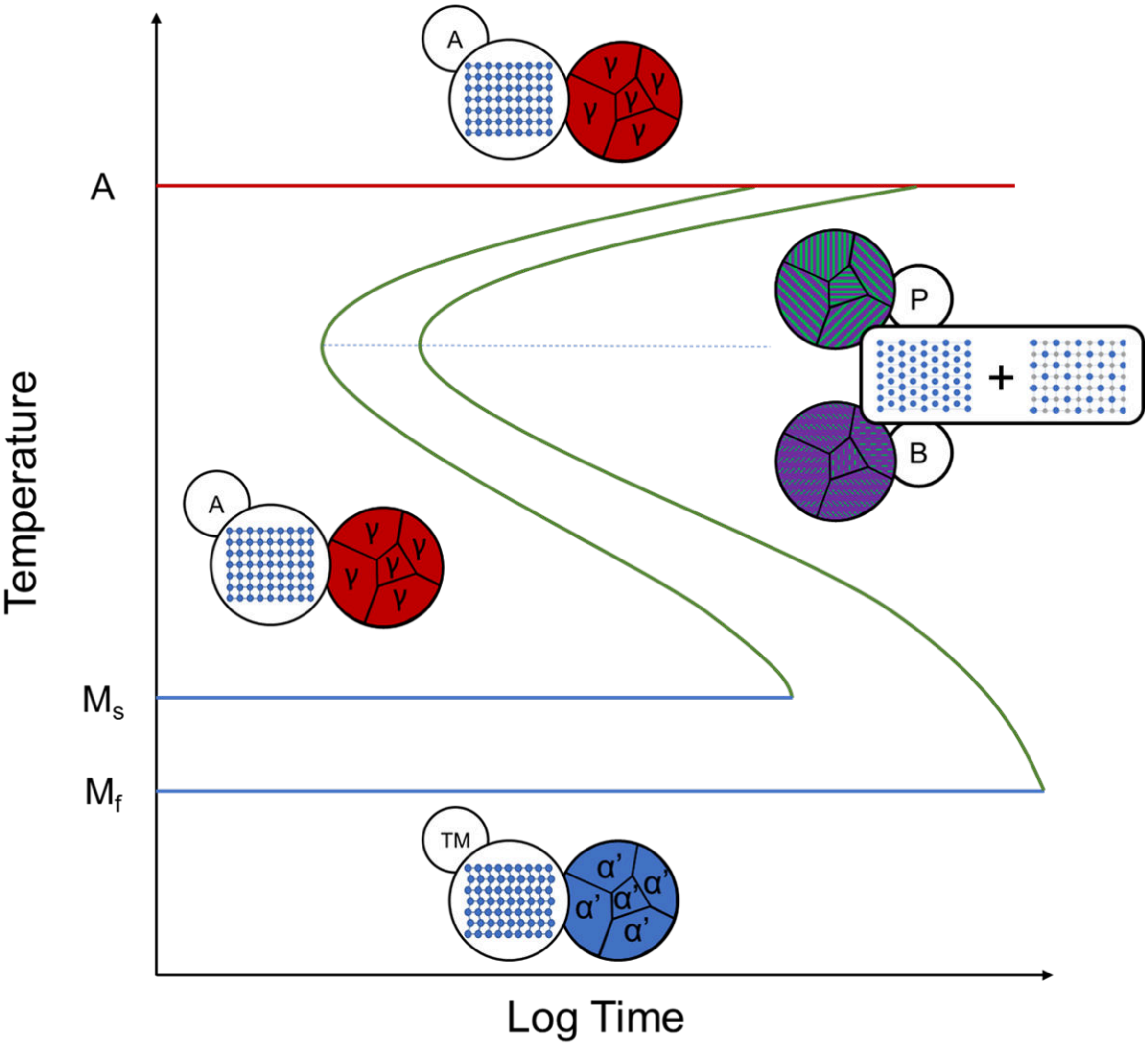

Figure 1.13: Isothermal transformation diagram for an iron-carbon alloy at the eutectoid composition. In addition to the austenite and (twinned) martensite phases already encountered, and denoted by the symbols A and TM respectively, ageing steel also produced the pearlite and bainite microstructures, P and B. Bainite and pearlite are both equilibrium microstructures comprising ferrite, α-Fe, and cementite, Fe_3C. In this example, the transitions to pearlite and bainite are not clearly separated producing a single C-curve. The phases shown here are for illustrative purposes and not necessarily accurate depictions of the true phases.

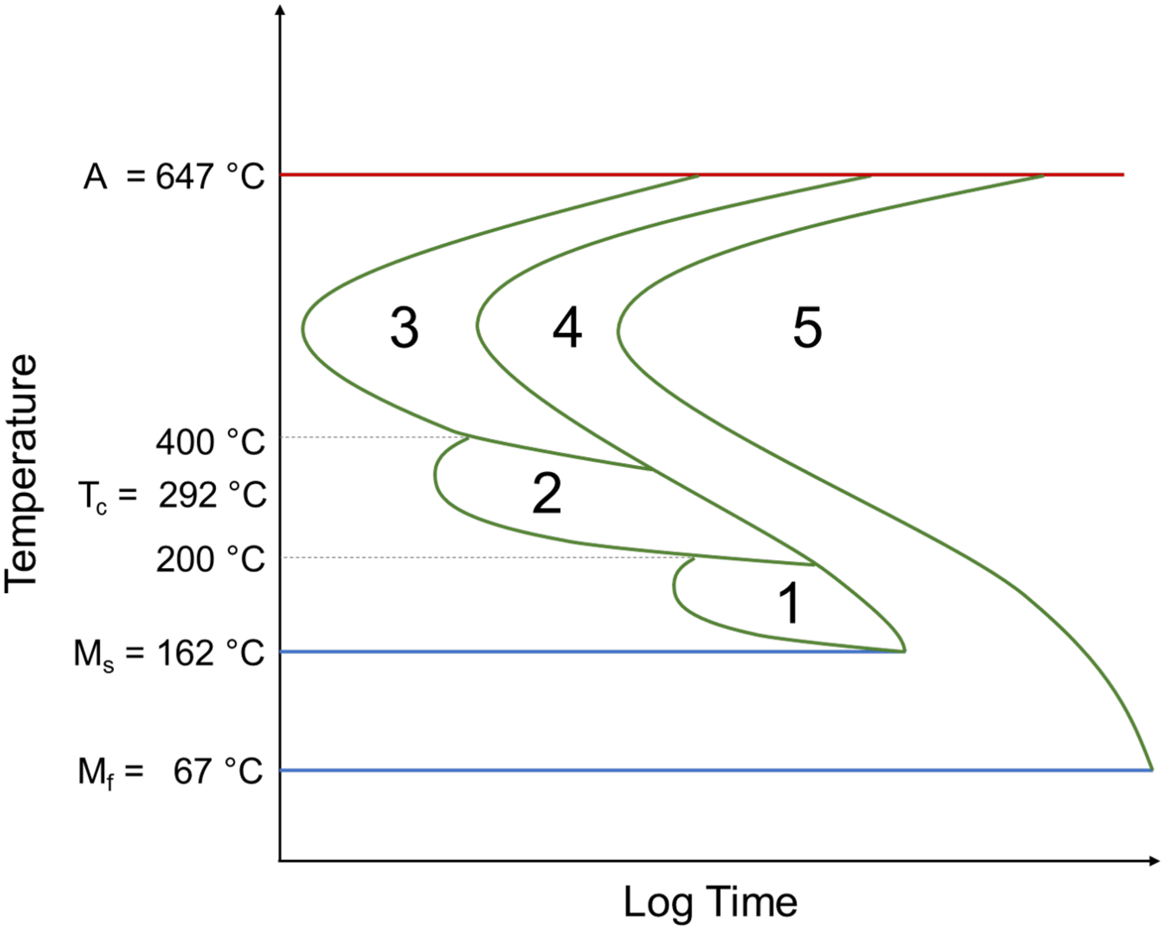

Figure 1.14: Schematic isothermal transformation diagram for the UNb6 alloy based on the original figure produced by Hackenberg *et al.* [106]. Transformation temperatures, evaluated by Vandermeer [274], have been annotated on the diagram to show the martensitic start and finish points, M_s and M_f, as well as the temperature signifying the transition to the γ° phase, T_c. *C*-curves have been labelled using the same convention as that used by Hackenberg *et al.* [106]. The following mechanisms have been labelled as 1 - 5 respectively; low-temperature hardening, medium-temperature hardening, high-temperature hardening, discontinuous precipitation, discontinuous coarsening.

CHAPTER 2

ANALYTICAL TECHNIQUES

Investigations into the crystallography and ageing behaviour of these alloys has, on the most part, made use of five broad classes of analytical techniques. These are electron microscopy, focused ion beam microscopy, x-ray diffraction and atom probe tomography. Additionally, the preparation of alloys by electropolishing has been investigated by electrochemical methods, but these are discussed in Chapter 3. The first four are introduced here with a brief background, theory and the specifics of the experiments performed in this study.

2.1 Electron Microscopy

2.1.1 Introduction

Since its early inception, the electron microscope has been an incredibly important and powerful tool for scientists from a range of fields. Ernst Ruska and Max Knoll constructed the first working electron microscope in 1933 [217, 218]. Ruska was awarded the 1986 Nobel Prize in Physics 'for his fundamental work in electron optics, and for the design of the first electron microscope' [256]. The award was shared in 1986 with the inventors of the scanning tunnelling microscope [262]. Technological advancements, driven by commercialisation of the technique [218], have led to two main variants, the scanning electron microscope (SEM) and the transmission electron microscope (TEM), as well as an effective hybrid, the scanning transmission electron microscope (STEM).

In all variants, electron microscopes utilise the short wavelength of a focused beam of energetic electrons (5-250 keV) to image a specimen at greater resolutions than that capable via light based microscopes. Considering electrons as waves, their wavelengths, λ, can approximation by using the de Broglie equation,

$$\lambda = \frac{hc}{E}, \tag{2.1}$$

where h is Planck's constant, c is the speed of light and E is the energy of the electrons. In this range of energies, wavelengths of the electrons are on the order of Ångströms to picometres. Application of Rayleigh's criterion applied to a circular aperture of diameter, d,

$$\theta = 1.220\frac{\lambda}{d}, \tag{2.2}$$

highlights the increased resolution, θ, that small wavelengths (large energies) achieves.

2.1.2 Electron Gun

Three styles of sources are typically used in electron microscopes, thermionic (hot cathode), field emission (cold cathode) and Schottky (a field assisted thermionic hybrid). Thermionic type guns rely on heating the source causing emission of electrons.

2.1.2.1 Thermionic-emission Electron Gun

Richardson's law describes the emission of electrons from a thermionically heated cathode [207],

$$J = AT^2 e^{\frac{-\phi}{kT}}, \tag{2.3}$$

where J is the current density, T is the temperature, ϕ is the work function of the filament and k is the Boltzmann constant. A is a product of a material-specific correction factor and a number of universal constants. Equation 2.3 shows that electron emission intensity may be controlled by manipulation of the temperature. This in practice is achieved by resistively heating the filament with currents up to a few amperes. Tungsten thermionic cathodes are a relatively cheap and versatile option owing to high melting points and stability in air. LaB_6 sources are more expensive but produce substantially more electrons due to a very low work function, $\phi = 2.7$ eV [192]. Thermionic emission sources suffer from poor resolution and brightness. A schematic of the thermionic-emission source is shown in the left panel of Figure 2.1.

2.1.2.2 Field-emission Electron Gun

Field emission guns (FEG) rely on the stripping of electrons from the source (cathode) purely using a very high electric field applied between the cathode and the anode. Under high electric fields, electrons have sufficient energy to tunnel out of the sharp tip. Moderating the field so that electrons are only capable of escaping from the very tip ensures a high coherency of the beam and a small spot size. Current density for a FEG is governed by the Fowler-Nordheim equation,

$$J = \frac{AE^2}{\phi} e^{\frac{-B\phi^{3/2}}{E}}, \tag{2.4}$$

where E is the electric field and B is a constant.

Field emission guns offer a long lifetime compared to the thermionic emission style. FEGs are commonly made of tungsten though its effectiveness as a field emitter depends on the quality of

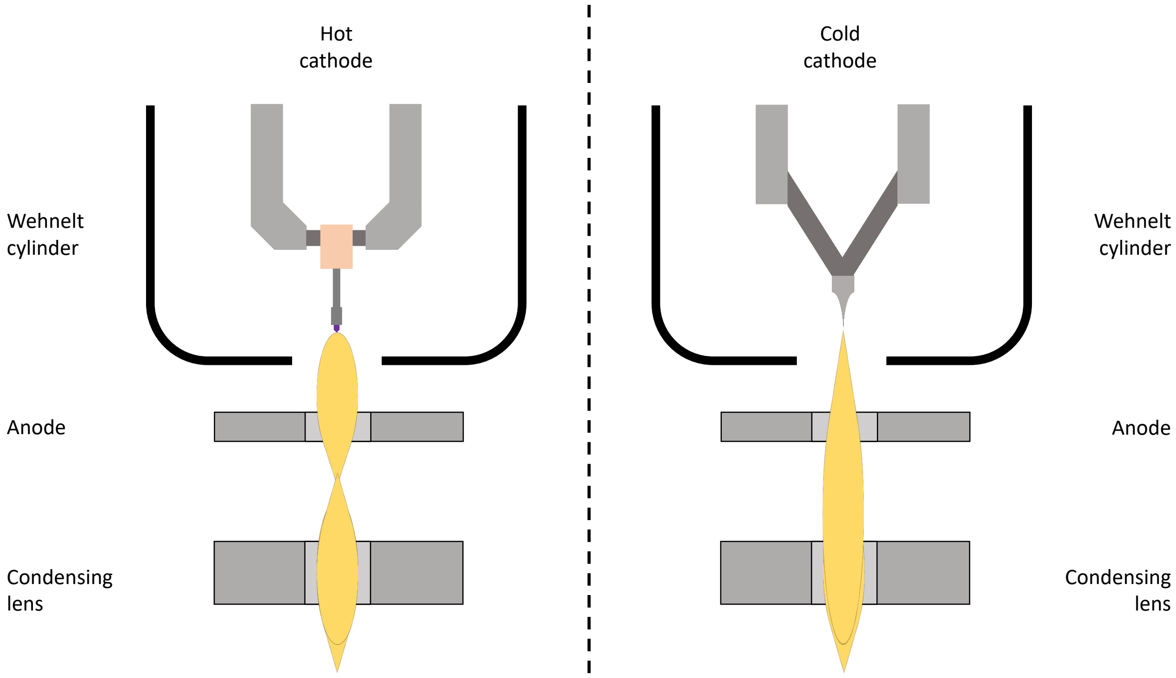

Figure 2.1: Schematic diagrams of thermionic, left, and field emission, right, electron sources.

the surface. High vacuums are required to ensure that the tip remains clean. Cleaning of the source is performed through daily flashing. Despite the limited current, brightness of the beam is high due to small size and low energy spread. A schematic of the thermionic-emission source is shown in the right panel of Figure 2.1.

2.1.2.3 Thermally Assisted Field-emission Electron Gun

The final style, the Schottky emitter, is made of tungsten and coated with zirconium oxide to lower the work function facilitating easier ejection of electrons. The Schottky emitter combines the principles of the thermionic and field emission sources, and such can be thought of a field assisted thermionic source where Richardson's law governs current density but the work function is reduced by,

$$\Delta\phi = \sqrt{\frac{e^3 E}{4\pi\varepsilon_o}} \tag{2.5}$$

where e is the charge on an electron, E is the electric field and ε is the dielectric constant.

The Schottky emitter style produces the most current, however, lifetimes of Schottky emission guns are not as long as cold cathodes, eventually failing when the zirconia reservoir is depleted. Sources are heated to around 1750 K, and, as such contamination is burned off instantly. Schottky emitters are very stable and boast high resolution and beam current.

2.1.2.4 Brightness vs Current

Brightness or current density at the specimen are much more valuable measures of a source than the absolute current. This is principally because thermionic sources produce a large amount of current, however due to the poor beam confinement a lot of electrons are blocked by the aperture for spatial resolution considerations. Brightness is therefore worse for thermionic emitters. Brightness, β, is given by,

$$\beta = \frac{4I}{\pi^2 \alpha^2 d^2}, \tag{2.6}$$

where I_b is the beam current, α is the angle of convergence and d is the spot diameter.

Field emission sources produce typically 100 times less probe current than thermionic sources but due to improved focusing aided by superior spatial and energetic spreads out of the source, brightnesses can be up to 100 times larger than for thermionic emitters [191].

2.1.2.5 Wehnelt cylinder

Within the electron gun exists another electrode known as a Wehnelt cylinder which acts as the first means of focusing the beam. The Wehnelt cylinder sits between the cathode and the anode which together liberate the electrons from the source (cathode). The Wehnelt cylinder is supplied with a couple of hundred (negative) volts that produces a field which acts to condense the electrons into a concentrated beam that passes through the aperture at the base of the source cylinder and into the column of the microscope.

2.1.3 Lenses & Optics

Electron microscopes utilise a combination of electrostatic and electromagnetic lenses to control the shape and path of the beam. Electrostatic lenses are typically used for the acceleration of electron beams down the column rather than imaging as electrostatic lenses incur greater aberrations than electromagnetic lenses. Electromagnetic lenses on the other hand are used to shape the beam, focusing the electrons down to a tight, intense spot. Various electromagnetic lenses are used throughout the column and though configurations and numbers of each type vary with design and model, all electron microscopes will possess at least a condenser lens and an objective lens. Electromagnetic lenses can be either of a quadrupole, sextupole or octupole variety with the higher order configurations typically employed for high end applications such as spherical aberration correction TEMs. Figure 2.2 shows a schematic of an example SEM.

Lenses are constructed from copper wires wound round iron cores. With current flowing, a strong magnetic field is produced, exerting the Lorentz force on electrons moving through the torus. Electrons are accelerated towards the centre of the beam with off-axis electrons experiencing a greater force than those closer to the centre, focusing the electrons into a tighter beam.

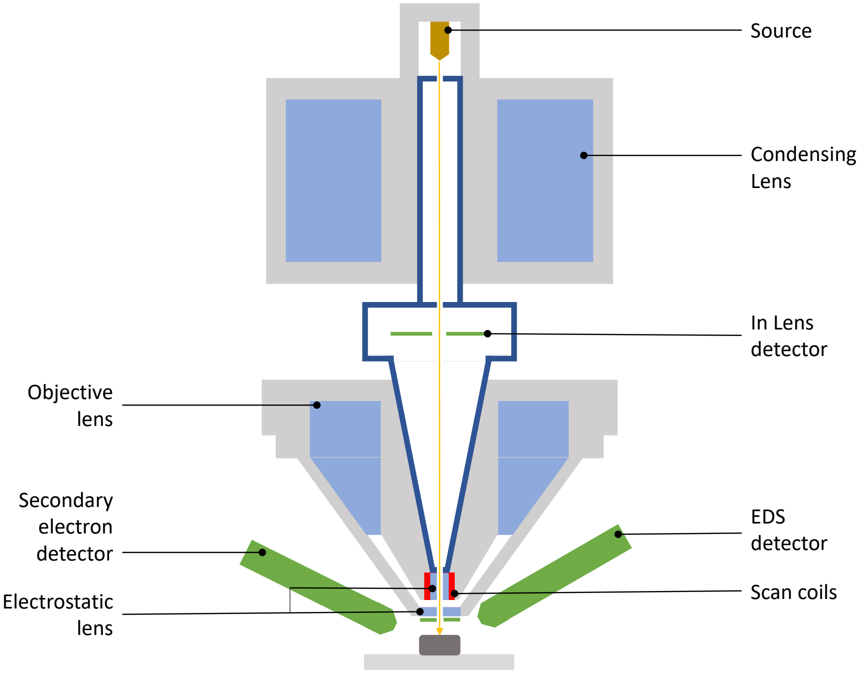

Figure 2.2: Schematic of a SEM. Figure is based on the Zeiss Sigma model which was used to collect the majority of EBSD data [297].

Electron microscopes have two sets of lenses, the condenser and the objective lenses. The condenser lens acts to initially focus the diverging electrons emitted from the source to a spot. The stronger this focusing, the shorter the crossover focal length and the smaller the spot size at convergence. The intensity is low in this scenario but the final probe size will be at a minimum. Stronger probes may be obtained via a weaker lens and a larger spot size but comes at the expense of a less defined electron beam. This intermediary spot size is important in determining the final spot size at the surface of the sample and the number of electrons generated. The objective lens is primarily designed to focus the beam onto the sample surface.

A series of apertures are also available to assist in producing a more coherent electron source. Apertures of varying diameters act to reduce the number of off-axis electrons. An aperture will also correct chromatic aberrations to some extent by removing electrons with energies that are not close enough to the average and are less effectively focused by the lenses. Smaller apertures are more appropriate for high resolution work with low beam currents, whereas larger apertures are useful if a larger beam current is required but suffer from a less defined beam and poorer depth of field.

Scan coils, additional electromagnets close to the end of the column, are used to raster the beam across the sample surface. Detectors operating in real time detect the resulting secondary, transmitted backscattered or x-rays *etc.* produced in the interaction and relate the time of the event to the position of the sample producing an image with contrast relating to physical features.

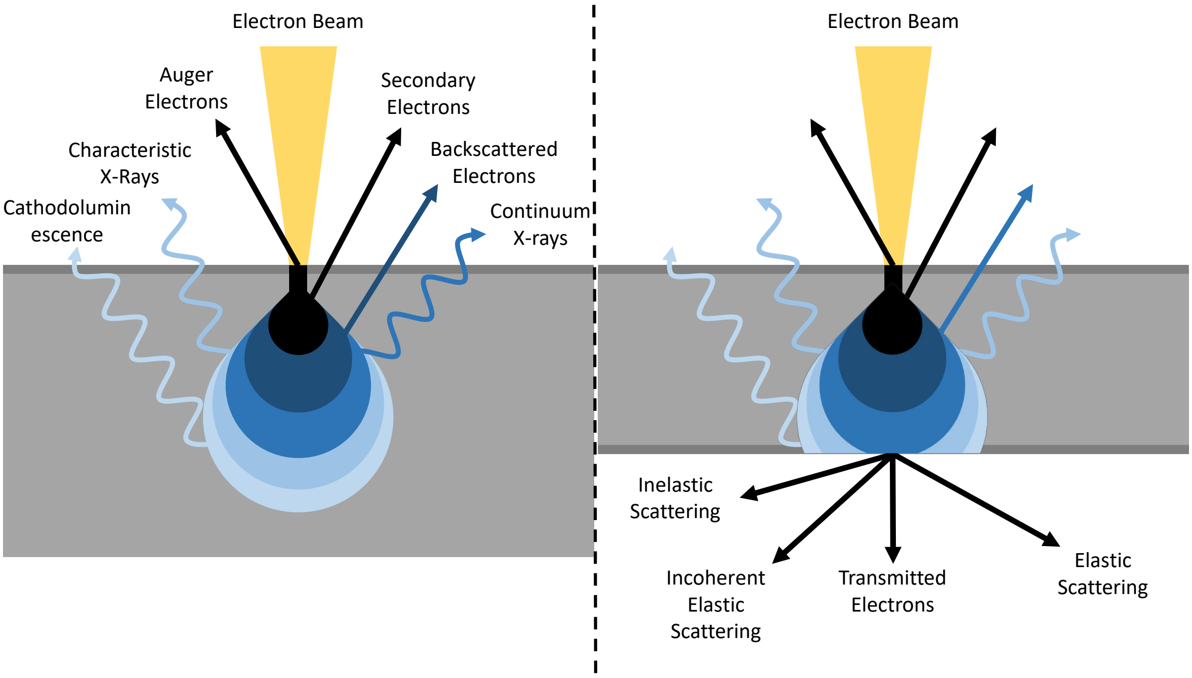

Figure 2.3: Interaction of energetic electrons with matter. Often referred to as the bulb of interaction, the diagram quantitatively shows the origin of the resulting particles and waves. Left hand side shows the case for SEM where the sample is considerably thicker than the penetration depth of electrons. Right hand side shows the scenario for TEM where the penetration depth of electrons exceeds the sample thickness permitting passage of electrons through the sample.

2.1.4 Interaction of Electrons

Energetic electrons incident on a sample can lose energy to Auger or secondary electrons, and characteristic and continuum x-rays, or elastically scatter. Additionally, energy can be dissipated into the system or alternatively electrons can be transmitted through the specimen. Of all of these, secondary, backscattered and transmitted electrons are of most importance in this work. The likelihood of each scenario depends on a number of factors but principally the energy of the beam, the thickness and the density of the sample. Figure 2.3 shows a schematic representation of the possible interactions between high energy electrons and the surface.

2.1.4.1 Secondary Electrons

Secondary electron imaging is the most commonly used method of imaging in a scanning electron microscope [191]. Secondary electrons are produced by the excitation and emission of an electron from an atom near the surface by the primary (incident) beam of electrons. Secondary electrons are typically defined as having energies up to 50 eV [191]. Therefore, only secondary electrons very close to the surface, a few nanometres deep, are capable of escaping the specimen and being detected. Given their high surface sensitivity, secondary electrons provide a very effective means of observing the morphological properties of a material. Additionally, secondary electrons originate from a small area, roughly three times the size of the beam [191], providing strong lateral resolution also.

Image contrast is produced by the fact that yield of secondary electrons is strongly dependent on the morphology of the material. In comparison to flat portions, edges of surface structures permit more secondary electrons to escape and be measured. Other factors such as sample electron density are also capable of contributing to contrast to a lesser extent.

The Everhart-Thornley detector is the predominant type of secondary electron detector installed in electron microscopes. The Everhart-Thornley detector comprises a scintillator located within a Faraday cage. The cage is essentially a metallic mesh onto which a small positive potential is applied. The field generated is sufficient to attract secondary electrons that have escaped the sample. The scintillator is provided with a strong positive voltage which attracts electrons that have successfully made it into the Faraday cage. Electrons striking the scintillator produce photons which are amplified in a photomultiplier tube external to the chamber. Intensity is recorded as a function of time which can be related to the beam's position on the sample.

2.1.4.2 Backscattered Electrons

Electrons may also be elastically scattered in the form of backscattered electrons. In these cases, the kinetic energy of the electrons is mostly preserved. The mass of the electron is so small that despite the high energy of a 30 keV electron, the most probable outcome is an elastic collision in which the velocity of the electron is reversed and that electrons are re-emitted at roughly the same angle as incidence. Most SEMs are fitted with backscatter detector (doped semiconducting silicon) just below the column, so that backscattered electrons may be detected when the sample is positioned normal to the beam. Atoms with a larger atomic number have a greater scattering cross-section, Equation 2.7, leading to increased rates of elastic collisions and backscattered electrons [206]. The elastic scattering cross-section, Q, is given by,

$$Q = 1.62 \times 10^{-20} \times \frac{Z^2}{E^2} cot^2\left(\frac{\phi}{2}\right) \tag{2.7}$$

where Z is the atomic number, E is the energy of the electron beam and ϕ is the scattering angle [43]. Elastic scattering therefore occurs more readily for heavier elements and at lower beam energies. Contrast in the backscatter image is achieved if the sample has regions of varying atomic densities; larger average Z numbers will be brighter than regions of low average Z number.

In addition to imaging, backscattered electrons can also be used to understand crystallographic properties about the sample. In the previous case it was irrelevant whether backscattered electrons were scattered coherently or not. For the purposes of obtaining crystallographic data, electrons are required to be coherently diffracted.

Electron backscatter diffraction (EBSD) is a very powerful technique that enables the determination of the local crystallographic structure of crystalline specimens. Distributions of crystal phases, orientations, defects such as twin and slip boundaries, and strain may be determined using EBSD. EBSD has several key advantages over the measurement of crystallographic texture by x-ray role figures [220]. The most significant advantage, EBSD delivers a microstructural picture of the sample. Additionally, x-ray pole figures can be difficult to set up without incurring undesirable biases, EBSD offers higher angular resolutions and EBSD observes all orientations so does not rely on implied data; many reflections are not observed in XRD due to the structure factor.

Backscattered electrons produce a Kikuchi pattern, which in the context of EBSD is most commonly referred to as an electron backscatter pattern (EBSP). EBSPs can be considered as a gnomonic projection of the crystal at the point that the electron beam impinges on the sample [220]. An example is shown in the left hand potion of Figure 2.4. The sample is typically tilted around 70 ° to the incident beam to increase the intensity of Kikuchi patterns. EBSP patterns in practice consist of a regular arrangement of parallel bright bands which intersect creating zones. The width of bands are related to the interplanar spacing, d_{hkl}, given by Bragg's law,

$$2d_{hkl}sin\theta_{hkl} = n\lambda \tag{2.8}$$

where θ_{hkl} is the angular separation of a band, n is an integer representing the order of diffraction and λ is the wavelength of the electrons. By small angle approximations, the width of Kikuchi bands, w_{hkl}, in the vicinity of the patterns centre is,

$$w_{hkl} \approx 2l\theta_{hkl} \approx \frac{nl\lambda}{d_{hkl}} \tag{2.9}$$

where l is the distance from the sample to the pattern centre. To first approximations, this simplification works, but for high resolution and advanced indexing techniques it is important to realise that the EBSD is subject to the dynamical theory of electron diffraction [290].

The detector usually comprises a phosphor screen, lens and a CCD camera. The detector is positioned at 90° to the pole piece. Due to the tilting of the sample to 70°, the sample is effectively rotated back 20° with respect to the detector. Electrons striking the phosphor screen cause it to produce photons that illuminate the screen, which is captured by the camera.

Although lower accelerating voltages promote elastic scattering, drawbacks of operating at low voltages include the possibility of the beam being affected by stray magnetic fields, low efficiency of the phosphor screen and susceptibility to surface preparation artifacts [220]. Despite the high accelerating voltages often used (30 kV), the information depth in EBSD is often estimated at roughly 20 nm [220]. For heavy elements like uranium, this is likely to be only a few nm, though the literature is lacking in this area. Large beam currents (and crucially brightness) are desired to increase counts in diffraction pattern without sacrificing spatial resolution. In the best case scenario, lateral resolutions of around 20 nm can be achieved [220].

Similar to the production of a secondary electron image, an EBSD maps is created by the rastering the beam over a portion of the sample. However, instead of recording the intensity of the signal at the detector at each step, a pattern is collected, processed and indexed.

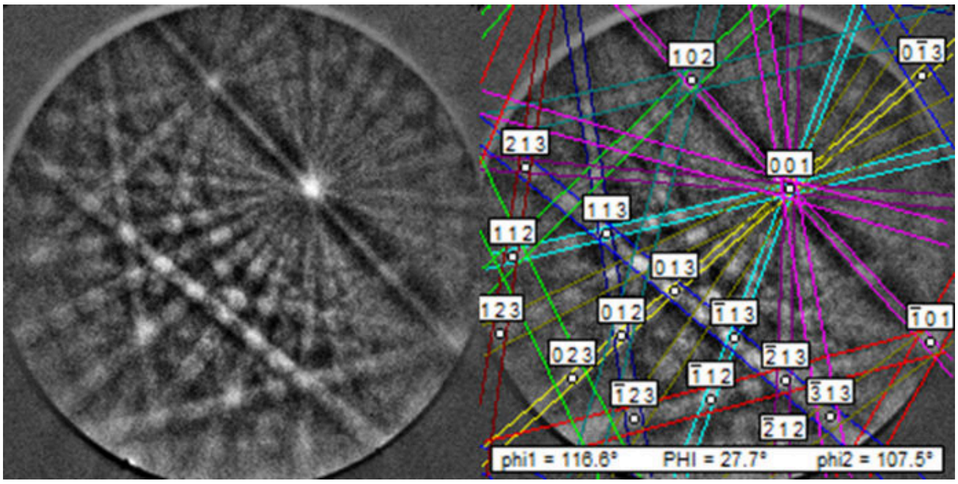

Figure 2.4: Kikuchi/electron backscatter pattern that was collected from an unaged UNb5 sample. Left side shows a pattern that has had a background subtraction applied. Right side shows the result of indexing the pattern with a material file representing the UNb5 α'' phase. Labelled positions refer to zone indexes.

Indexing of EBSD patterns relies on feature detection and image analysis techniques. The EBSD maps shown in this thesis have not required advanced indexing treatments, and so a brief qualitative description is provided. The reader is directed to Schwarzer *et al.* for a full treatment of EBSD indexing [220]. Indexing EBSD patterns requires the positions and widths the bands to be extracted with a high accuracy. An EBSD pattern is unique to the crystal's structure and orientation [220]. Extracting the position and rotation of the pattern (as expressed in Euler coordinates) is important in order to determine the orientation of the crystal, whereas the width of bands gives the lattice parameters. The strategy employed is therefore to use the Radon or Hough transform to detect the position of the bands and reconstruct the pattern based on simulations given the expected crystal structure [62, 120]. A major benefit that this method possesses is that intensity of bands does not require modelling [220].

2.1.4.3 Transmitted Electrons

Transmission of electrons requires extremely thin specimens. Even at normal operating TEM energies of 100-300 keV, sample thicknesses of less than 100 nm are required for adequate transmission. TEMs have developed a plethora of complementary analytical tools to combine imaging, diffraction and spectroscopy using all the various types of scattered (and un-scattered electrons), Figure 2.3.

Transmission electron microscopy is generally performed with the use of one of two variations on the transmission electron microscope, the conventional transmission electron microscope (CTEM) and the scanning transmission electron microscope (STEM). CTEMs and STEMs are similar instruments that are most clearly defined by the method by which they form an image.

Like an SEM, a STEM rasters the beam, which has been focussed to a fine spot, across the specimen in a raster pattern. There is no rastering of the beam in a CTEM, as such, an image is formed instantaneously from a parallel beam that is at least as wide as the features that are desired to be captured in the image. To enable this, the STEM features scanning coils, thereby making the construction of the STEM similar to an SEM. The main differences are that in a STEM, the lower objective lens features after the specimen and the scan coils are advanced ahead of the upper objective lens.

TEM images presented in this work originate from a STEM, details are listed below. CTEMs were not used to collect the original data presented in this thesis. Of all the companion STEM techniques that may be used to analyse a material, only imaging and electron dispersive x-ray spectroscopy (EDX/EDS) were used. EDX, a technique that enables mapping of elements based on their characteristic x-ray excitations, however provided inconclusive evidence and so the data is not shown. Therefore, a description of the imaging capabilities of a STEM is provided.

STEM imaging detectors may be split into two categories, bright-field (BF) and dark-field (DF). Bright field detectors are placed in the path of the transmitted beam and are sensitive to differences in 'mass-thickness'. Assuming that the sample is flat, bright-field imaging is essentially showing average density. In comparison, dark-field imaging is more complex and several versions of the dark-field detector exist. The instruments used in this project featured an annular dark field (ADF) or a medium angle annular dark field (MAADF) and a high angle annular dark field (HAADF) detector. ADF/MAADF detectors make use of diffraction contrast, i.e. signal that has been scattered off axis due to a fulfilment of the Bragg condition, Equation 2.10. These images can therefore highlight crystallographic features, such as crystallite orientations or defects, that are present in the sample. Dark-field imaging also excludes the bright-field beam which produces images with low noise and a reduced susceptibility to mass-thickness effects. However, ADF/MAADF is also influenced by incoherent (Rutherford) scattering of atoms which is proportional to average atomic number, Z. HAADF detectors regularly feature in STEMs to separate the effects of Bragg and Rutherford scattering. HAADF detectors are placed at very large angles with respect to the transmitted beam so to prevent Bragg scattering from contributing to the signal. A comparison of the two dark field imaging capabilities (MAADF/HAADF) is shown in Figure 2.5. The off-axis annular detectors permit the simultaneous collection of dark-field data alongside simultaneous, complementary bright field, EELS or EDX data.

Despite only using imaging capabilities, information regarding the density of the sample, thickness, structural defects or crystallographic defects may be acquired. However, investigations into the crystallography of specimens on the nanometre scale is possible by TEM diffraction with a small adjustment to the optical setup. Generation and interpretation of zone axis patterns can enable the crystallographic relationships of small regions to be interrogated. TEM diffraction patterns have not been used in this project. The reader is however directed to Andrews *et al.* for a full treatment of the analysis of TEM electron diffraction patterns [8].

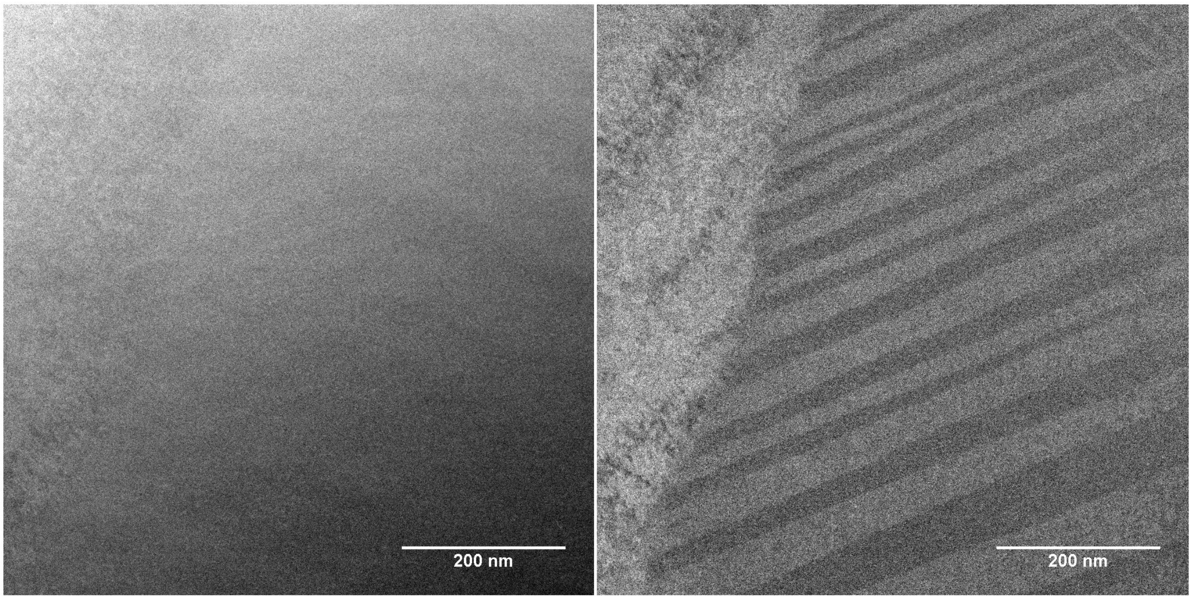

Figure 2.5: HAADF and MAADF of 5000 hr aged UNb7, assumed to be alternating γ° phase twin variants bound by a grain boundary. Significant contrast in the MAADF image indicating structural inconsistencies, yet almost no contrast in the HAADF image confirms that the structural effects observed here are not related to compositional differences.

2.1.5 Instruments

Four instruments were used to perform electron microscopy on samples for the work included in this thesis. Two dedicated SEMs, a Zeiss SigmaHD and a Zeiss EVO MA 10, situated in the School of Physics, University of Bristol were used to perform SEM and EBSD. A FEI Helios NanoLab 600i dualbeam was used to examine foils via the STEM technique and was also used for its FIB capabilities. A JEOL ARM200F situated at the Department of Materials, University of Oxford was used for the study of foils previously crafted by the dualbeam. Atomic resolution imaging was possible using the spherical aberration corrected JEOL ARM200F [121]. The JEOL STEM was operated by Dr Ian Griffiths.

2.2 Focused Ion Beam Microscopy

Focused ion beam (FIB) microscopy shares numerous similarities with scanning electron microscopy [278]. The two techniques are mostly separated based on their choice of probe. Where SEM uses electrons, FIB uses ionised atoms. As such, the sources are an entirely different technology and electrostatic lens polarity is reversed.

Focused ion beams have been historically developed for, and used extensively in the semiconductor industry [278]. However, FIBs are also widely used in a more general materials science capacity and are capable of performing a number of tasks such as imaging, sectioning, depositing certain materials and preparing samples for further analysis [95]. This thesis uses all of these capacities for different applications. Though, FIB can be used to image surfaces in the same way as SEM if the beam current and accelerating voltage is sufficiently low, FIBs present the greatest utility by embracing sputtering [4].

Whereas SEM is a non-destructive technique, with the only detrimental effect being carbon contamination of the surface [202], the FIB technique by nature is destructive. The interaction of energetic ions on a solid is best explained by the concept of the collision cascade model [229, 278]. In this model, energy is lost by the gallium atom by a series of independent, binary collisions. If sufficient energy has been transferred to the target atom, it will be displaced from its original site, producing a vacancy and potentially creating further collisions. The gallium ion and displaced sample ions will continue to undergo collisions until they come to rest, having dissipated all of their kinetic energy into the system. A displacement collision that occurs close to the surface has the potential to liberate a sample atom and allow it to pass into the vacuum, sputtering. This short-lived process can lead to; emitted particles, ion and secondary electrons which are used for imaging; electromagnetic radiation; sample heating; gallium implantation and ion beam damage, for example by the production of point defects.

In the case of uranium and its alloys, being metals with modest thermal conductivities and exhibiting no solubility for gallium in any of their crystallographic phases [216, 294], the most important mechanism here is ion beam damage. Through careful milling using glancing angles and low accelerating voltages, it is possible to significantly reduce the effects of ion beam damage [17]. Amorphisation of surface by ion beam damage is particularly problematic for TEM sample fabrication. Damage is estimated to extend on the order of tens of nanometres into most materials at 30kV [278]. Due to the density of uranium, TEM foils are required to be around 100 nm thick, and so care must be taken to ensure that damage is minimised.

FIB and SEM techniques can be combined in the same instrument, often referred to as a dualbeam. A dualbeam instrument combines an electron beam column, positioned vertically, and an ion beam with a substantial angular offset. Both columns converge at the same point, the eucentric height, permitting the study of the same region of the sample with both FIB and SEM technologies concurrently.

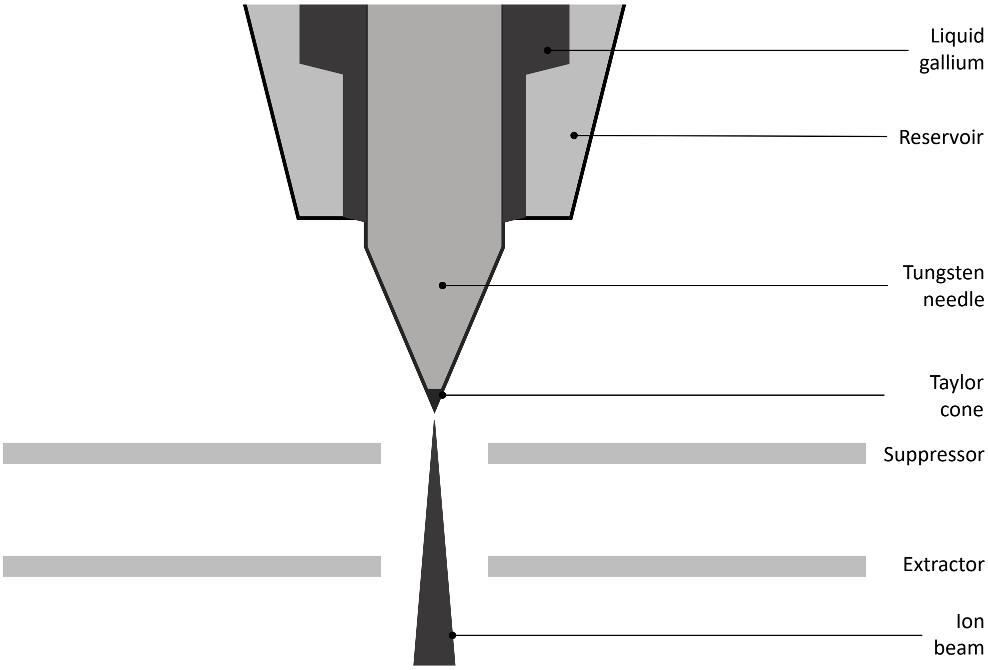

Figure 2.6: Diagrammatic representation of the liquid metal ion source used in focused ion beam (FIB) instruments.

2.2.1 Sources

The majority of FIBs employ a liquid metal ion source (LMIS) which provides elemental gallium ions [203]. In a LMIS, gallium is held in a reservoir that surrounds a tungsten needle possessing a radius of a few microns at the tip. Gallium has a very low melting temperature of 30 °C [236], permitting conversion to molten state with light heating and wetting of the tungsten needle. With a large electric field applied (in excess of $10^8\,\mathrm{V\,cm^{-1}}$), the electric field overcomes the surface tension forces permitting ionisation and emission of gallium atoms at the tip forming a Taylor cone in the process. The source current is maintained by capillary action of the gallium at the source. A representation of the LMIS is displayed in Figure 2.6.

2.2.2 Sample preparation

FIB has been used to prepare TEM specimen foils, cross section trenches and slice and view 3D reconstructions enabling a visualisation of the microstructure of uranium alloys at various points throughout this project. A standard lift-out procedure that has been well documented in the literature was used to craft TEM foils [95, 152]. This method essentially involves the production of a thin lamella, revealed by cutting two trenches very close to each other, Figure 2.7, cutting it free and attaching it to a TEM grid using deposited platinum as a ‘weld’. A Kleindiek MM3A-EM micromanipulator enables the foil to be temporarily affixed to a needle and transferred between the original specimen and the grid. An example of a TEM foil that has been attached to the Cu

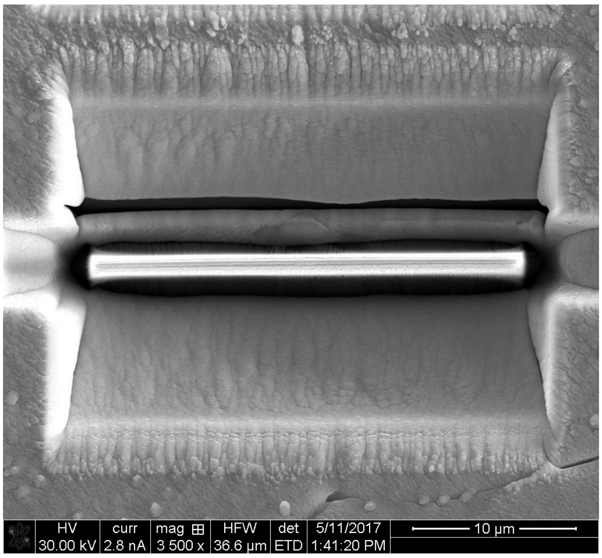

Figure 2.7: Free-standing TEM lamella that has been cut out of the sample using staircase cross sections. The lamella will be subsequently bonded to the macromanipulator needle before being cut free of the sample at the base and transferred to the Cu grid.

grid and subsequently thinned to a thickness of around 150 nm is shown in Figure 2.8.

Slice and view, and cross sections are produced in a similar manner to the first half of the process for the production of TEM foils. In both cases, a stair-step trench is cut to produce a straight edge that may be viewed at an angle when rotated with respect to the beam. Cleaning of this face using a low beam current is often necessary to mitigate the effects of uneven milling, curtaining. The cross section may then be viewed and an image taken. In the case of slice and view reconstructions, an iterative process of image acquisition and cleaning of the face to remove around 100 nm produces a 3D dataset which may be reconstructed using 3D visualisation software. Figure 2.9 shows an image of two frames in the slice and view process.

2.2.3 Instruments

A FEI Helios NanoLab 600i dualbeam (DB) situated in the School of Physics, University of Bristol was used for the production of STEM, atom probe, cross-section trenches, and slice and view data sets. A FEI Strata 201 FIB also situated in the School of Physics, University of Bristol was also used for investigations where the electron beam was not also required. Cross-section trenches were cut using the FIB and the instrument was also used to investigate the effectiveness in preparing the surface for EBSD analysis.

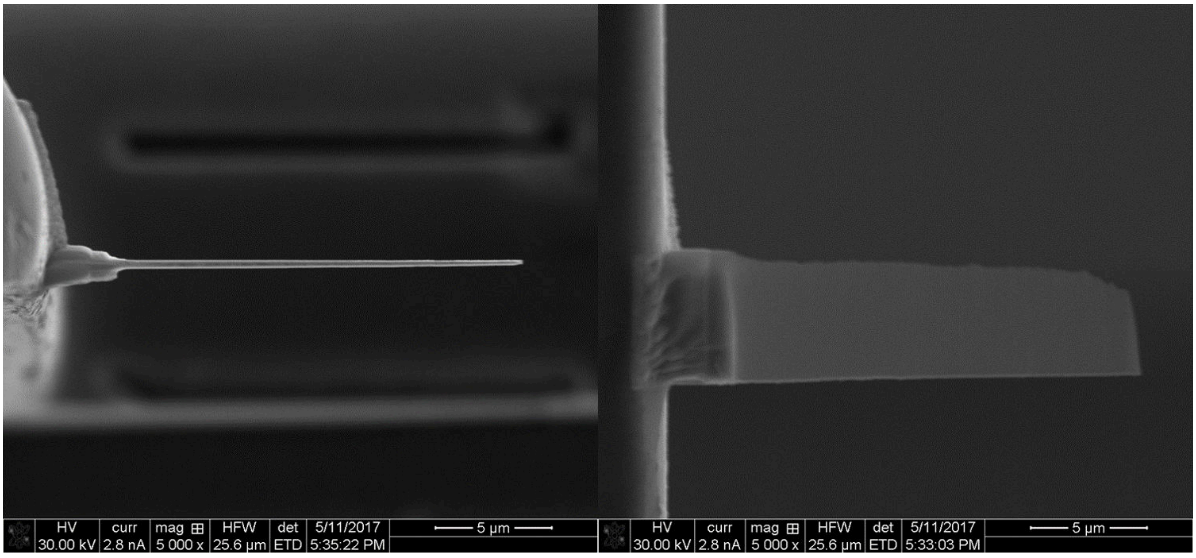

Figure 2.8: TEM foil affixed to the Cu grid as viewed edge-on, left, and side-on, right. The platinum adhesive may be seen on the left of the images. The foil will subsequently require a low kV polish at glancing angles to remove the final tens of nanometres.

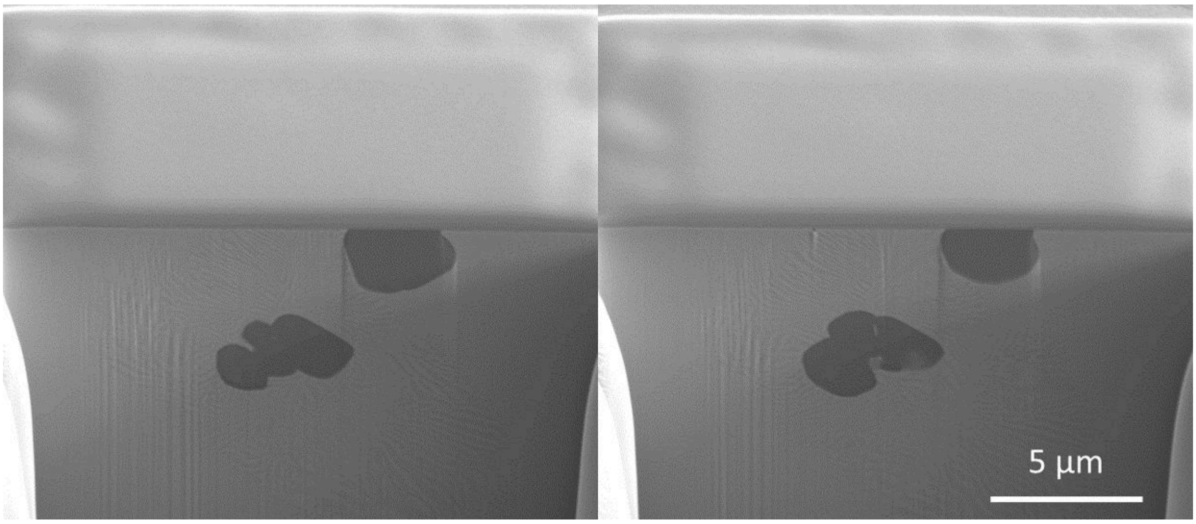

Figure 2.9: Slice and view cross sections produced from a UNb7 sample aged to 350°C for 2 hours. The two frames are separated by 500 nm. Small levels of curtaining can be seen to have developed due to differences in densities bewteen the homogeneous alloy and portions that have experienced fine-scale phase separation around carbide inclusions.

2.3 Atom Probe Tomography

Atom probe tomography is a technique capable of producing near atomic resolution 3-dimensional elemental maps [177]. Atom Probe Tomography has evolved out of the field ion microscope however, the modern APT instrument has more in common with a time-of-flight mass spectrometer [177]. Essentially, APT computes mass to charge ratios of ions evaporated from a specimen and attributes them to an original position. With knowledge of the chemical makeup of the system, mass to charge ratios can be assigned to elements and a 3D reconstruction of the original sample may be obtained [178].

Needle shaped samples with a tip radius of around 50-100 nm are required for atom probe tomography [178]. Production of a small sample tip is commonly achieved through FIB milling or electropolishing [138]. A small sample tip enhances the electric field applied between the specimen and the detector and promote field evaporation of specimen atoms. The process is often controlled by ultra-fast laser pulses which provide the additional energy required to overcome this threshold [178]. Evaporated ions are accelerated towards the detector which records their position and time of flight. Position of an atom in the sample can be reconstructed from the position on the detector whereas time of flight, as in the case of a SIMS instrument, is converted into a mass/charge ratio.

Pulse duration is controlled such that an average of less than one evaporation per cycle is achieved, as such the laser pulse time period is required to be on the order of hundreds of kHz. The detection of single atoms that have travelled undisturbed for up to a metre with a reasonable detection rate (>50%) requires an ultra high vacuum. Cooling the sample to cryogenic temperatures is essential to limit thermal vibrations in the system and therefore, the uncertainty in atomic positions [226].

2.3.1 Preparation of APT Samples

APT samples were prepared using the FEI Helios Nanolab 600i dualbeam. Preparation was performed using a very similar method to that employed by Thompson *et al.* [264]. The first stage of the sample preparation involved laying down a protective platinum strap over an area of roughly 20 x 10 μm^2. Samples would be obtained from the material beneath this layer so platinum was often laid down to intersect a grain boundary or triple point to maximise the chances of finding chemical segregation. The sample would subsequently be tilted to 15° relative to the ion beam and a triangular prism milled out using the ion beam, Figure 2.11. A deep wide cut is required to completely free the prism and preclude redeposited material causing it to reattaching during milling. High beam currents at the high beam energies is used for this rough cut to speed up the process. One end would be milled free so that the prism is held only at one end.

The Kleindiek nano-manipulator would subsequently be brought in close to the free end of

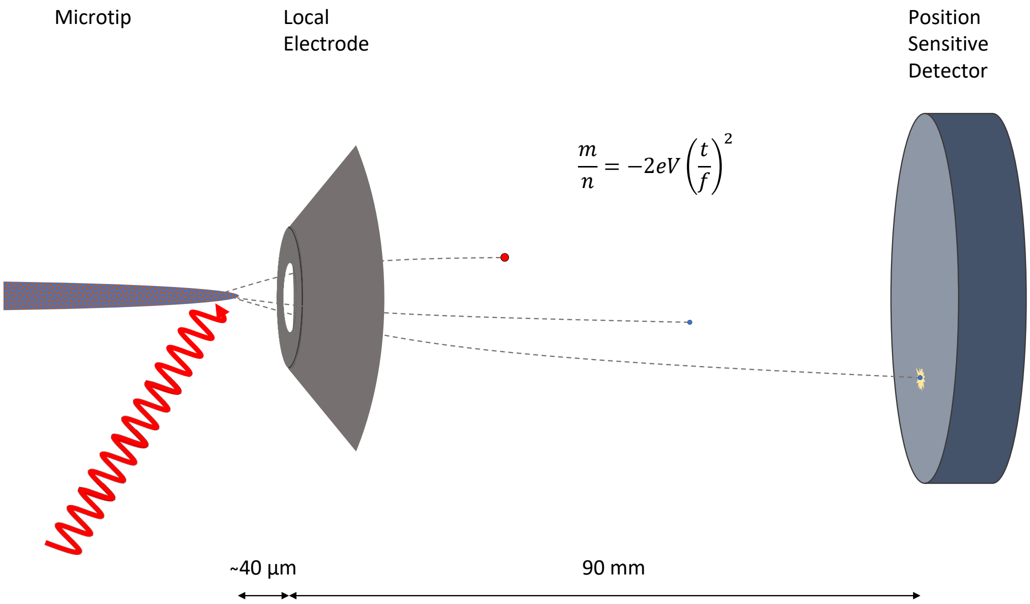

Figure 2.10: Local Electrode Atom Probe Tomography Layout. In this example, three ionisation events have occurred in the same cycle. The evaporated, doubly charged niobium ion escapes the sample and travels towards the detector with the highest velocity, v, striking it at time T. A singly charged niobium ion, accelerated to a lesser extent by the local electrode, travels at $1/\sqrt{2}\,v$, reaching the detector at $\sqrt{2}$T. A singly charged uranium ion travels at $0.44\,v$, reaching the detector at $2.29\,T$.

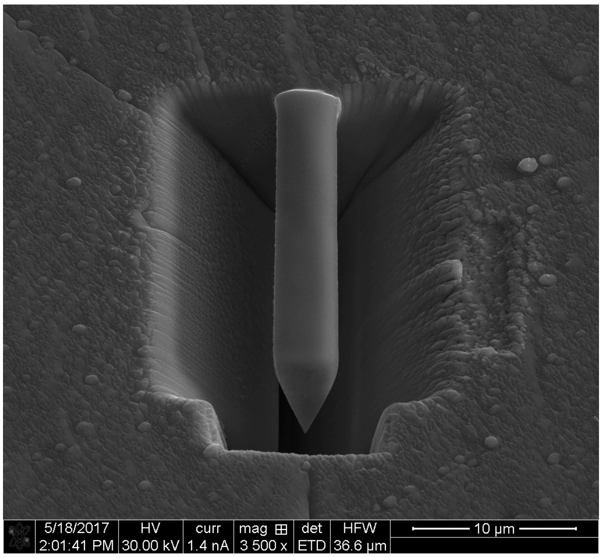

Figure 2.11: The first stage of APT sample preparation involves excavating a prism by digging wide trenches either side of the region of interest. The prism is 5μm wide, 10μm tall and 20μm long, and has been placed to intersect a triple point.

the prism and with contact made, the manipulator would be attached to the prism by depositing a patch of platinum. Once secure, the other end of the prism may be cut free from the rest of the alloy. With the prism now only attached to the manipulator, it is now taken to the APT stub and attached to a silicon post. Cutting behind the attachment leaves a small amount of material, Figure 2.12 that can be fashioned into a APT microtip, Figure 2.13.

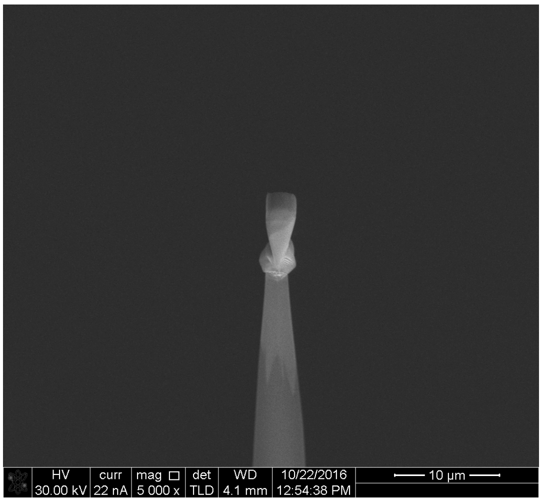

Figure 2.12: A portion of the lifted-out wedge, roughly 2μm deep has been affixed to the silicon tip by deposited platinum.

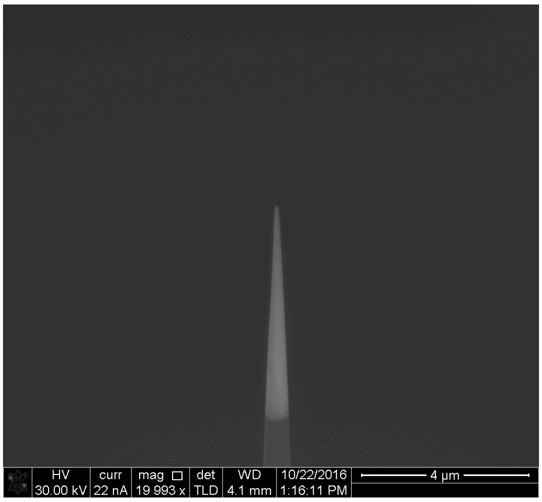

Figure 2.13: Needle is subsequently sharpened through annular milling to a fine point with tip radius around 100 nm. All platinum has been removed from the needle.

Turning the wedge in Figure 2.12 into the microtip in Figure 2.13 is achieved by annular milling with progressively smaller radii from the zenith of the microtip. As the radii are decreased, beam current is lowered to moderate the speed of thinning. Beam energy is also stepped down to reduce beam damage and limit gallium implantation as the microtip becomes thinner. The final polish should be conducted at the lowest possible beam energy, in this case 5 keV, when the tip radius is approximately 100nm.

2.4 X-Ray Crystallography

2.4.1 Introduction

The crystal structure of a solid is intrinsically linked to a large number of its physical traits. This includes electrical, thermal and mechanical properties for example. Knowledge of the crystal structure is therefore of key importance for the understanding of the behaviour of materials from a physical and chemical standpoint, and the tailoring of qualities from a materials science perspective. X-ray crystallography is the study of the atomic structure of a material by the use of diffraction and other scattering techniques.

From a materials science perspective, it is important to determine the deviation from a perfect ordered structure. For this, it is important to study the real structure of the material. Real structure often considered as violations of perfect periodicity of the crystal [234]. For single crystals, lattice defects (impurity atoms, vacancies, interstitials and dislocations) are the main contributors to the real structure. Polycrystalline materials additionally introduce distributions of sizes and orientations of grains, and grain boundaries. Diffraction patterns are only weakly affected by the real structure so analysis by diffraction is inherently very complex. X-ray diffraction analysis of real structures consists of evaluating the diffraction line profiles and intensities [234].

The phenomenon of x-ray diffraction is capable of being described by the dynamical or the kinematic theories. The dynamical theory can be considered the purer form, but only comes into play for near-perfect crystals. Otherwise the kinematic theory works well. A detailed derivation and description of the the dynamical theory of x-ray diffraction may be found in Authier *et al.* [13]. However, given that the work here deals with polycrystalline materials, and ones that exhibit a large number of intra-granular defects such as twinning, slip and kinks, the kinematical theory of diffraction is the most suitable theory to discuss [234].

X-rays incident on a crystal are scattered by the electron cloud of the atoms and a spherical wave of equal energy is produced in the elastic interaction. Destructive interference would be the most likely outcome, however, the reciprocating nature of a crystal enables waves to interfere constructively in some certain circumstances.

Bragg's law provides the conditions for constructive interference,

$$2d\sin\theta = n\lambda, \tag{2.10}$$

where d is the inter-planar distance, θ is half the difference in angle between the incoming and diffracted beams (2θ), n is an integer and λ is the wavelength of the radiation. From Bragg's law it is clear to see that a full range of angles, θ, may be utilised when the wavelength, λ, is on the same order of magnitude as the inter-planar distances, d. Since first order atomic plane spacings are usually on the order of 1-10 Å, x-rays possess the most suitable wavelengths when compared to the whole electromagnetic spectrum.

The structure factor, F_{hkl}, determines the amplitude of reflections from each crystal lattice plane as described by its Miller indices, $(h\,k\,l)$. F_{hkl} is given by,

$$F_{hkl} = \sum_j f_j exp[2\pi i(hx_j + ky_j + lz_j)], \tag{2.11}$$

where f_j is the scattering factor of the j^{th} atom, x_j, y_j and z_j are the fractional coordinates of the j^{th} atom in the unit cell. The intensity of a reflection depends on the location of each atom (and therefore electron cloud) of the unit cell.

Given details of the crystal, namely the lattice symmetry, dimensions and basis, it is possible to use Bragg's law and the structure factor to simulate the position and intensity of all reflections permissible: the crystal's powder diffraction pattern. Equally, given the diffraction pattern and some knowledge of the sample, the crystal structure may be solved.

2.4.2 Geometries

Although Röentgen was the first to discover x-rays [213], von Laue takes the credit as the first to utilise them in investigations into crystal structures [75, 281]. In 1912, he and his co-workers exposed a single crystal of copper sulphate hydrate to white x-ray radiation [6]. They observed a diffraction pattern of spots with each one corresponding to a coherent scattering condition. von Laue's method fixes the crystal position with respect to the x-ray beam. The continuous nature of the wavelengths in white light therefore acts as the independent variable scanning criteria for constructive interference in Bragg's law, Equation 2.10.

Since the initial works over 100 years ago [26, 27, 281], that only a couple years hence resulted in von Laue and the Braggs being awarded Nobel prizes [260, 261], setups for x-ray diffraction have become substantially more sophisticated. A major shift towards monochromatic sources has necessitated a change in the way diffraction data is collected. Using monochromatic radiation has a few major advantages over the Laue method; monochromatic radiation means that the intensity of each peak is calculable not susceptible to the quality of white light; peaks are spatially separable; determination of the quality of a crystal is more rigorous and polycrystalline samples may be measured.

The two dominant setups used today are the Bragg-Brentano and the Debye-Scherrer geometries. In the Bragg-Brentano geometry, x-rays are reflected off the sample. The setup either sees the source fixed and the sample rotated by θ and the detector by 2θ, or the sample fixed and the source rotated by θ and the detector also by θ. In either method, the sample can be considered at the centre of the focusing circle which the source and the detector travel around on in opposite directions, at the same rate, Figure 2.14.

In the Debye-Scherrer geometry, a collimated x-ray beam is transmitted through the sample and diffracted onto stationary detectors. The Debye-Scherrer method produces cones that fall on the detector as rings, Figure 2.15. Azimuthal integration of these rings returns the 1-dimensional patterns observed in Bragg-Brentano geometries. Key benefits of using the Debye-Scherrer over

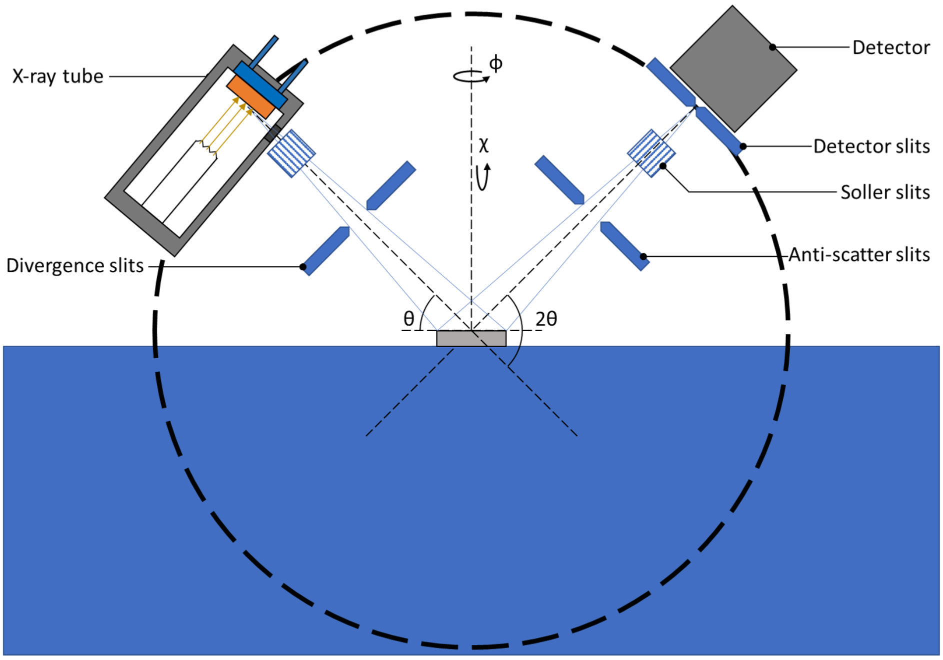

Figure 2.14: Schematic representation of the Bragg-Brentano geometry used by the laboratory diffractometer. The dashed line represents the focusing circle on which the source and detector travel.

the Bragg-Brentano geometry are that this method is comparatively easy to use, peak profiles are less complex, hazardous and air-sensitive materials can be measured from sealed capillaries and sample effects such as preferred orientation can be minimised. The main disadvantage, particularly for materials with high average atomic numbers is that producing sufficiently thin samples to enable transmission can be difficult.

2.4.3 X-ray sources

Laboratory based x-ray diffraction instruments use the x-ray tube source in the production of x-rays [6]. Whilst tube sources are widely available, relatively inexpensive and adequate for the measurement of samples in an ex-situ situation, particularly using the Bragg-Brentano geometry, tube sources have a fixed wavelength and poor flux. Synchrotron sources offer much more versatility permitting non-standard diffraction experiments and opening up a range of additional experimental techniques that would be otherwise impossible to carry out using a conventional lab source. Both laboratory diffractometers and synchrotron sources have been used in this work. The key concepts of each are discussed below.

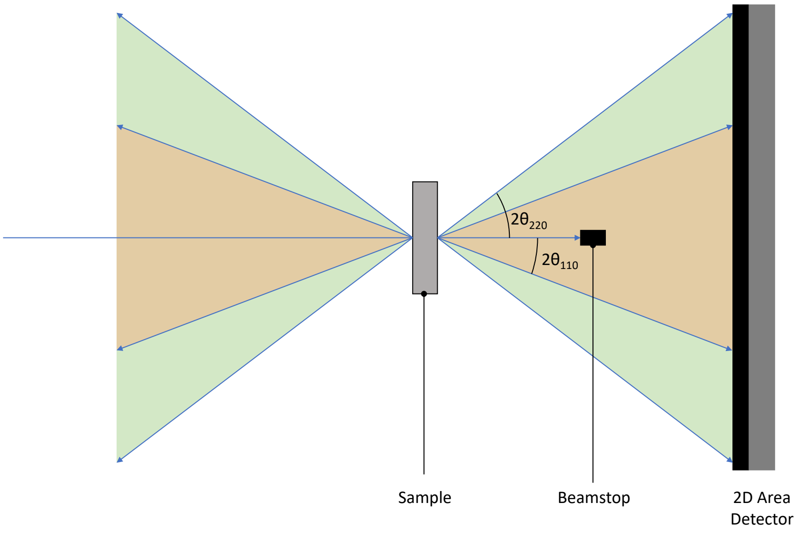

Figure 2.15: Schematic representation of the Debye-Scherrer geometry that was used during the high temperature experiment conducted at Diamond on the I12 beamline.

2.4.3.1 Tube Sources

In an x-ray tube, electrons are accelerated from a heated tungsten filament (cathode) towards the anode by a strong electric field [6]. The tube is evacuated to preclude interaction of electrons with air molecules. Upon striking the anode, electrons rapidly decelerate and lose their energy to heat and Bremsstrahlung radiation. A schematic representation of the tube source is shown in Figure 2.16. In addition to Bremsstrahlung radiation, characteristics x-rays are also generated by electrons dropping down to the K shell to replace those knocked out in collisions. These characteristic lines possess small spreads in wavelength and are on the order of Ångströms making them suitable for probes of crystal lattices, which have similar periodicities.

However, the majority of the energy is lost to heat rather than the production of x-rays [248]. Water cooling of the anode is required to militate against overheating of the anode. A rotating anode additionally reduces the effects of heating as instantaneously, only a small portion of the anode being struck by electrons.

Bremsstrahlung radiation and additional characteristic x-rays can be mostly removed by filters or monochromators. A nickel filter is particularly adept at filtering out the Kβ lines of a copper source as the absorption edge resides between the Kα (unattenuated) and Kβ (attenuated) lines. Two lines remain for copper sources, Kα_1 and Kα_2. The Kα_2 has a difference in wavelength of 3.83×10^{-3}Å and half the intensity of the Kα_1 and cannot be filtered out without expensive optics. The two lines are only resolvable in highly crystalline samples when measured with high resolution beam settings.

The majority of laboratory x-ray tubes use sources fitted with either a Cu or Mo anode (target), however other target materials such as Cr, Fe, Ti, Co and Ag are occasionally used. These

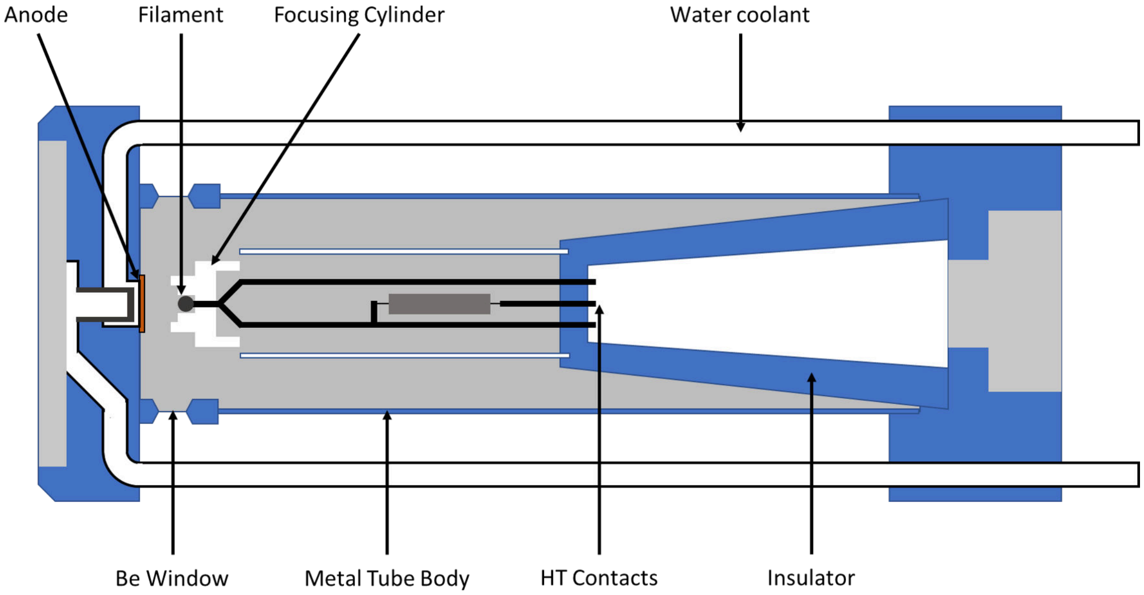

Figure 2.16: Schematic of a modern x-ray tube source. This image has been modelled on the Philips Empyrean source, the x-ray tube used in the Panalytical X'Pert Pro MPD [201].

elements can be used to give a discrete set of seven x-ray wavelengths ranging between 0.56 and 2.75 Å for the extremes of Ag and Ti respectively [65].

2.4.3.2 Synchrotron Sources

Synchrotron light source facilities present a means of carrying out a large variety of experiments that would otherwise be impractical or even impossible using conventional sources [232]. Synchrotrons permit higher fluxes, tunable beam energies, a wider range of spot sizes, higher resolution and polarisation options [6]. The modern synchrotron is a complex particle accelerator in which electrons are used to produce energetic x-rays that beamlines employ to conduct experiments.

A synchrotron (but specifically Diamond Light Source) will include an electron gun, producing electrons through thermionic emission; a linear accelerator, which accelerates the electrons from 90 keV to 100 MeV with radio frequency cavities; a booster synchrotron, which brings the electrons up to an energy of 3 GeV and the main storage ring [6, 46, 232]. The main storage ring comprises many straight sections that are joined by bending magnets that curve the beam between straight sections. On changing momentum at the bending magnets, electrons emit Bremsstrahlung radiation, photons with wavelengths extending from high energy x-rays down to the infra-red. Insertion devices are arrays of magnets that are 'inserted' into straight sections of the storage ring. Insertion devices facilitate the tuning of beam energies and by doing so, decrease the spread of energies, thereby increasing spectral brightness compared to bending magnets.

Insertion devices come in two varieties, wigglers and undulators [6, 32]. Wigglers cause the electrons to oscillate in a sinusoidal path in the plane of the beam, generating light in wide cones with a broad spectrum of x-ray energies. Wigglers are effective means of producing high energy x-rays that are useful for penetrating deep into dense objects. The I12 beamline uses a 4.2 T super-conducting wiggler that is capable of producing photon energies of between 53 and 150 keV [69]. Whereas the periodicity of the wiggler is fixed, the magnet array separation in an undulator is tunable. This enables undulators to produce much higher spectral brightnesses over a wide range of energies.

2.4.3.3 Instruments

With the exception of the measurements made at the Diamond Light Source, all XRD measurements were made on the Panalytical X'Pert Pro Multi-Purpose Diffractometer (MPD) situated in the School of Physics, University of Bristol. The X'Pert Pro is a versatile instrument capable of performing a range of scan types such as a conventional specular scans, texture and stress measurements. These scan types are possible as the instrument has a four-circle Eulerian cradle as standard and employs a vertical goniometer measuring θ-θ scans. ϕ and χ angles are therefore additionally accessible in addition to the standard θ and ω angles. Different sized samples are accommodated by an adjustable height stage.

The X'Pert Pro was fitted with a copper anode source and a Ni β filter. Without a monochromator, both the Kα_1 and Kα_2 x-ray lines with wavelengths of 1.540598 and 1.544426 Å are produced [117]. Filtering out the Kα_2 line can be done with expensive optics but reduces the intensity considerably and little gain would be achieved by doing so as diffraction peaks in the materials used in this work are relatively broad.

0.04 rad Soller slits were used to limit the divergence of the beam in the direction perpendicular to the scan axis. Divergence and receiving slits were set to be fixed at 0.5 ° with detector height also set to 0.5 mm. These settings were found to be optimal for maximising counts through illumination of an area approximately the same size as samples, whilst not incurring any artificial peak broadening from poor resolution settings. Fixed slits are required to ensure that a constant volume is maintained throughout the scan, essential for fitting of a diffraction pattern through Rietveld refinement.

The diffractometer was fitted with a proportional Xe, point source detector which requires relatively long scans given that each point has to be stepped through and the poor crystallinity of the samples in this work. Scans would be run over a wide range, usually 25-120° with the tube at 40 kV and 40 mA.

The I12-JEEP (Joint Engineering, Environmental, and Processing) beamline situated within Diamond Light Source, Oxfordshire, UK, was used to conduct the high temperature experiments. A complete detailed description of the beamline has been set out by Drakopoulos et al. [69]. To avoid the uranium K-absorption edge and promote transmission, 112 keV x-rays were used for the experiments at I12. The beam was monochromated using a Si (111) cryo-cooled double bent Laue crystal. The beamtime was mainly used to take diffraction data but tomographic scans were also collected using the beamline's bespoke imaging system. Slit sizes were set such that, at their widest, no more than $0.2 \times 0.2\,\mathrm{mm}^2$ of the sample was exposed to the beam. A Pilatus3 X CdTe 2M detector was used for the collection of x-ray diffraction data. Acquisition times as short as 2 s per frame were used to measure time dependent processes.

2.4.4 Analysis of Diffraction Patterns by Rietveld Refinement

Rietveld refinement is a diffraction pattern fitting technique which models the entire pattern rather than each peak individually, treating the process as a least squares problem. Originally conceived by Hugo Rietveld in 1966-1967 [208, 209], the Rietveld refinement technique has revolutionised powder diffraction and crystallography.

The major strengths of the technique are that overlapping peaks can be easily deconvoluted and that contributions from crystal structure and instrumental profile were modelled together. The techniques has been hugely successful, adapting and expanding over the years since to a point such that thousands of publications use Rietveld refinement every year [113].

Rietveld refinement uses the crystal structure to generate a model of an x-ray diffraction pattern with which the experimental data is compared. However, Rietveld refinement does not encompass structure determination, *i.e.* finding space groups. With each iteration, the goal is to make small adjustments to the crystal structure, changing the simulated pattern in a way that better models the received data and reduces the residual.

Rietveld's formula essentially breaks the entire profile into a handful of parameters. For a single phase in the pattern [295], its contribution may be written as,

$$y_i = S \sum_{hkl} L_{hkl} |F_{hkl}|^2 \phi(2\theta_i - 2\theta_{hkl}) P_{hkl} A + c_i \tag{2.12}$$

where S is the scale factor; L_{hkl} represents the Lorentz, polarization, and multiplicity factors; F_{hkl} is the structure factor for the $(h\,k\,l)$ reflection; ϕ is the profile function which takes the position of the $(h\,k\,l)$ reflection, $2\theta_{hkl}$, and the angular position of point i, $(2\theta_i$, as arguments; P_{hkl} is the preferred orientation of the $(h\,k\,l)$ reflection; A represents the absorption and c_i is the background at step i.

In analogy with other least squares problems, the objective during the fitting is to minimise,

$$M = \sum_{i}^{n} w_i (y_i^{obs} - y_i^{calc})^2 \tag{2.13}$$

where M is the function to be minimised, w_i is the weighting at point i based on the intensity, y_i^{obs} is the value of the observed pattern at point i and y_i^{calc} is the value of the calculated pattern at point i which is function of m parameters, p, *i.e.* $y_i^{calc} = g(p_1, p_2, p_3, ..., p_m)$.

The quality of a powder pattern fit is often quoted in terms of the weighted pattern factor, R$_{wp}$,

$$R_{wp} = \sum_i^n \left(\frac{w_i(y_i^{obs} - y_i^{calc})^2}{w_i(y_i^{obs})^2} \right)^{1/2} \times 100\% \tag{2.14}$$

which can be seen to closely resemble M, the function to be minimised. Essentially M has been normalised and converted into a percentage where lower values are better. However, R_{wp} is quite sensitive to experimental factors such as the quality of data; a R_{wp} of around a couple % should be expected from synchrotron or neutron data whereas around 10% is acceptable for laboratory sources [170].

Additionally, it is common to report a Bragg residual for each phase included in the fit,

$$R_{Bragg} = \sum_i^m \frac{|I_j^{obs} - I_j^{calc}|}{\sum_i^n I_j^{obs}} \times 100\% \tag{2.15}$$

in the chapters to follow this will be written as R_{γ° or $R_{\alpha''}$ for example.

The goodness of fit, χ, is also often reported,

$$\chi^2 = \sum_i^n \frac{(y_i^{obs} - y_i^{calc})^2}{n-p}, \tag{2.16}$$

which also summarises the quality of the fit as a whole, by comparing R_{wp} to the expected R value in the form of a ratio. A value of 1 is regularly cited as a good value where the quality of fit is equal to that expected given the statistics. However, like R_{wp}, χ^2 can also be affected by the quality of data [170]. When comparing qualities of fit, it is therefore important to ensure that the source of the data is considered.

2.4.4.1 Broadening Function

Given the intrinsically complex microstructure of the metastable phases in uranium alloys, the diffraction patterns would not be expected to be simple. The most significant contributor to the peak profile shapes from the perspective of the sample properties is the twinning which not only introduces crystallite size effects but also anisotropic strains.

To account for these effects, the formulation for anisotropic broadening derived by Stephens and incorporated in GSAS-II has been used in the fitting of XRD patterns throughout this project [240, 266]. In Stephen's model the Gaussian component of the peak profile is given by,

$$\Gamma_G = [U tan^2\theta + V tan\theta + W + (1-\zeta)^2 \Gamma_A^2(hkl)]^{1/2} \tag{2.17}$$

where the first three terms are the same as in the Caglioti formula [34], and a final term has been added to account for anisotropic broadening. Whereas, the Lorentzian component is given by,

$$\Gamma_L = X tan\theta + Y/cos\theta + \zeta \Gamma_A(hkl). \tag{2.18}$$

Sample microstrain broadening will be shown later to be best modelled with Lorentzian contributions, *i.e.* $\zeta = 1$. The formula for the anisotropic broadening half-width, Γ, is defined as,

$$\Gamma_A = [\sigma(M_{hkl})^2]^{1/2} tan\theta / M_{hkl} \tag{2.19}$$

where M_{hkl} is related to the lattice spacing by,

$$M_{hkl} = 1/d_{hkl}^2. \tag{2.20}$$

The variance, σ^2, of M_{hkl} can be written as the sum of up to 15 independent variables that together describe the distribution of strain,

$$\sigma^2(M_{hkl}) = \sum_{HKL} S_{HKL} h^H k^K l^L \tag{2.21}$$

for $H + K + L = 4$.

For example, in the triclinic case,

$$\begin{aligned} \sigma^2(M_{hkl}) = & S_{400}h^4 + S_{400}k^4 + S_{400}l^4 \\ & + 3(S_{220}h^2k^2 + S_{202}h^2l^2 + S_{022}k^2l^2) \\ & + 2(S_{310}h^3k + S_{103}hl^3 + S_{031}k^3l + S_{130}hk^3 + S_{301}h^3l + S_{013}kl^3) \\ & + 3(S_{211}h^2kl + S_{121}hk^2l + S_{112}hkl^2). \end{aligned} \tag{2.22}$$

Cubic, tetragonal, orthorhombic, monoclinic and trigonal cases can be derived from the above equation by identifying zero and non-zero components. Additionally, so that reflections can be easily compared, the anisotropic broadening half-width can be normalised by dividing through by $tan(\theta)$. So for example in the monoclinic case, the full formula is given by,

$$\Gamma_A = \frac{(S_{400}h^4 + S_{400}k^4 + S_{400}l^4 + 3(S_{220}h^2k^2 + S_{202}h^2l^2 + S_{022}k^2l^2))^{1/2}}{\frac{h^2}{a^2} + \frac{k^2}{b^2} + \frac{l^2}{c^2}}. \tag{2.23}$$

A physical interpretation of these parameters in terms of actual strain for each reflection can be obtained by applying the following scale factor,

$$\frac{\delta d}{d} = \frac{\pi[\sigma^2(M_{hkl})]^{1/2}}{18000 M_{hkl}}. \tag{2.24}$$

2.4.4.2 Texture Analysis

Texture analysis (and preferred orientation corrections) were used in the modelling of powder diffraction data throughout the previous chapters. Von Dreele incorporated the model set out by Bunge [33], when writing the original GSAS program [280].

Textural intensity corrections is governed by the even component of the orientation distribution function,

$$A(h,y) = 1 + \sum_{L=2}^{N_L} \frac{4\pi}{2L+1} \sum_{m=-L}^{L} \sum_{n=-L}^{L} C_L^{mn} k_L^m(h) k_L^n(y) \tag{2.25}$$

$k_L^m(h)$ represents crystal symmetries whilst $k_L^n(y)$ represents sample symmetry terms.

Sample symmetries incorporated in GSAS-II include cylindrical, 2/m, mmm and no symmetry. The choice of different sample symmetries affects the coefficients that may be called upon. For 'no symmetry', there are no restrictions on the terms, whereas for cylindrical symmetry, $k_L^n(y)$ terms are non-zero and the rest can be neglected, hence the texture can be expressed as the set of C_L^{m0} coefficients. Cylindrical sample symmetries was used in the texture fitting of the data sets used.

As the data collected in these chapters for full texture fitting are derived from a 2D flat panel detector without using any sample rotations a large amount of sample symmetry information is lost resulting in the ability to construct inverse pole figures, but not pole figures as peak intensity distributions along the rolling and transverse directions would need to have been measured.

Texture magnitude is conveniently expressed as,

$$J = 1 + \sum_{L=2}^{N_L} \frac{1}{2L+1} \sum_{m=-L}^{L} \sum_{n=-L}^{L} |c_L^{mn}|^2 \tag{2.26}$$

with $J = 1$ representing a perfectly untextured sample. J may not take a value less than 1 so greater values represent increased texture.

2.4.4.3 Texture Visualisation

Pole figures and inverse pole figures (IPF) are convenient means of visualising crystallographic texture within a sample. A pole figure is a stereographic projection of the crystallographic orientations of grains or crystallites in the sample. The axes of the pole figure are aligned with the specimen and relate to real space. In comparison, an inverse pole figure assumes a single sample direction such as the normal, ND, or directions parallel to the surface (rolling direction, RD, or transverse direction, TD). The inverse pole figure has the benefit that identical crystallographic directions (e.g. $[1\,0\,0]_{bcc}$ and $[\bar{1}\,0\,0]_{bcc}$) can be folded onto the same position and used to construct texture contours. All IPFs shown in this work have been constructed in relation to the normal direction (ND) coordinate axis.

CHAPTER 3

PREPARATION OF URANIUM AND URANIUM ALLOYS AND ANALYSIS OF SURFACES

This chapter investigates the process of preparing high quality, oxide-free surfaces from uranium and alloys. Particular attention is paid to electropolishing, often the final step in preparing metallic specimens for microscopy techniques and as a finishing step for industrial applications. A three electrode cell has been used to conduct electrochemical measurements aimed at elucidating the polishing process. Surfaces are subsequently examined by XRD to characterise residual stresses. The polishing methodology described in this chapter proves to be capable of producing surfaces with minimal residual stresses, removing those imparted in mechanical polishing, and enabling high quality EBSD maps that show the microstructure in fine detail.

The work presented in the first half of the chapter was supported by Dr James Darnbrough, as it was recognised that there was substantial cross-over with a complementary post-doctoral project examining the effects of hydriding on stresses within unalloyed uranium. A MATLAB script written by Dr Darnbrough was used to analyse some of the stress analysis data.

3.1 Introduction

Uranium based materials are particularly sensitive to preparation methods owing to strong scattering of x-rays, electrons and ions by high electron densities. Many common lab and large scale facility techniques rely on electron and x-ray probes. Strong scattering results in a short mean free path, low penetration and ultimately sampling of only the surface. Very high energies are required to penetrate an appreciable distance into the material where the true bulk state exists and is completely unaffected by surface effects. Beam energies for lab based diffraction techniques such as XRD and EBSD are comparatively a lot lower and as such require excellent surface preparation.

As is the case for many metals, standard practice for the polishing of uranium and its alloys is to use a two step process of mechanical polishing followed by electropolishing [136, 137]. Many preparation routines for metals have now also evolved to incorporate vibration polishing steps [187]. A variety of polishing solutions and conditions have been reported in the literature [9, 52, 136, 137], however, there has been a dearth of information supplied on the reasoning for some of the decisions made with often circumstantial evidence provided for suitability.

Various electrochemical experiments including linear sweep voltammetry, cyclic voltammetry, chronoamperometry and electro impedance spectroscopy (EIS) may be utilised to understand the mechanisms at play in electropolishing [88]. Performing these experiments is essential in order to inform ideal conditions and develop the preparation process. Carried out poorly, preparation by electropolishing is capable of imparting deleterious effects onto a surface; preferential etching of grain boundaries, inclusions, secondary phases or twin boundaries and excessive oxidation (anodisation) can negatively affect the resultant surface [180]. The benefit of electropolishing though include a smooth surface free of mechanical deformation and stresses. From a commercial perspective, electropolishing also produces a smooth and brilliant finish that improves aesthetics whilst also fulfilling functional requirements such as deburring metallic components [180].

Application of standard electrochemical experiments using a three electrode cell has been used to dictate polishing conditions. Ex-situ analysis of the surfaces is equally important in characterising the effects of polishing. Stresses have been characterised by x-ray diffraction (XRD) and morphology by scanning electron microscopy (SEM) and electron backscatter diffraction (EBSD). An ultimate goal is to be able to refine the process to produce high quality EBSD patterns of uranium alloys, for which there are very few examples in the literature [52, 83]. Pure uranium metal is initially used as a surrogate as collection of EBSD maps from this material is easier than in the alloys given superior crystallinity. Additionally, there are numerous examples of pure uranium EBSD maps in the literature with which to compare [21, 84, 141, 167–169, 224, 303]. The techniques used to produce pristine surfaces, from which high quality EBSD maps from pure uranium have been produced, were reapplied to the uranium alloys.

3.2 Experimental Details

3.2.1 Materials

Cast and rolled low carbon depleted uranium coupons provided by AWE Plc were used to perform polishing experiments on to complement the uranium alloys study. Samples measured 10 × 10 × 0.75 mm but were cut into thirds to minimise the number of original pieces used. At approximately 3 × 10 × 0.75 mm, the coupons of pure uranium used were roughly the same size as the uranium alloy equivalents.

3.2.2 Mechanical Polishing

Samples were set in Clarocit epoxy resin, purchased from Buehler, and subsequently polished with SiC grit papers ranging from P180 through to P4000 on a Struers TegraPol 5. Samples were rinsed with water in between each step to remove any dislodged SiC abrasives. Polishing using P4000 paper would produce a mirror finish, however, scratches are still ubiquitous on the micron scale length. To make the effects of electropolishing as noticeable as possible, mechanical polishing was concluded at this step for the initial investigations. Once the effects of polishing potential and durations had been investigated and production of the best quality maps were on the agenda, mechanical polishing also included polishing with 6, 3, 1 and 1/4 μm diamond paste grades.

Samples were cleaned in a beaker of acetone in an ultrasonic bath and broken out of resin before electropolishing. Any further grease was removed by rinsing the sample in water, acetone and methanol and allowed to air dry.

3.2.3 Electrochemical Configuration

Solutions containing phosphoric acid have been the most commonly reported choice for the electropolishing of uranium metal and alloys [9, 136, 137, 169, 294]. Additionally, phosphoric acid is also a widely used electrolyte for the polishing for a variety of other metals such as aluminium [15], copper [71, 175] and steel [163, 166]. A commonly used solution of 45 % ethanol, 27 % ethylene glycol and 27 % phosphoric acid (85 % assay) by volume was used for the electropolishing of pure uranium [9, 16, 50, 84, 93, 132, 167–169, 224]. For the more electrochemically impervious uranium alloys [292], solutions consisting of just phosphoric acid and water are reported as being suitable with 5 - 50 % H_3PO_4 apparently being equally strong choices [137].

A three electrode cell, shown schematically in Figure 3.1, was used to perform electropolishing and electrochemical tests. A Ag/AgCl reference electrode was used as the reference electrode and platinum wire as the counter electrode with the sample forming the working electrode. The counter electrode and working electrode are the equivalent of the cathode and anode in a conventional setup. The reference electrode provides an accurate measurement of the potential between the surface of the working electrode and the solution, independent of other sources of potential difference that may vary between setups. Values of the potential are quoted relative to the Ag/AgCl reference electrode which has a fixed relation of + 0.230 V *vs* the standard hydrogen electrode. As samples were not necessarily the same size, values presented have generally been converted to a current density with units of mA/cm^2. Solutions were stirred throughout electrochemical experiments and electropolishing by a magnetic flea driven by a Fisher Scientific stirrer operating at 900 rpm.

Samples would be rinsed with water once electropolishing had been concluded to remove all traces of the polishing solution. Samples would be wiped with alcohol moistened blue-roll and allowed to dry in air.

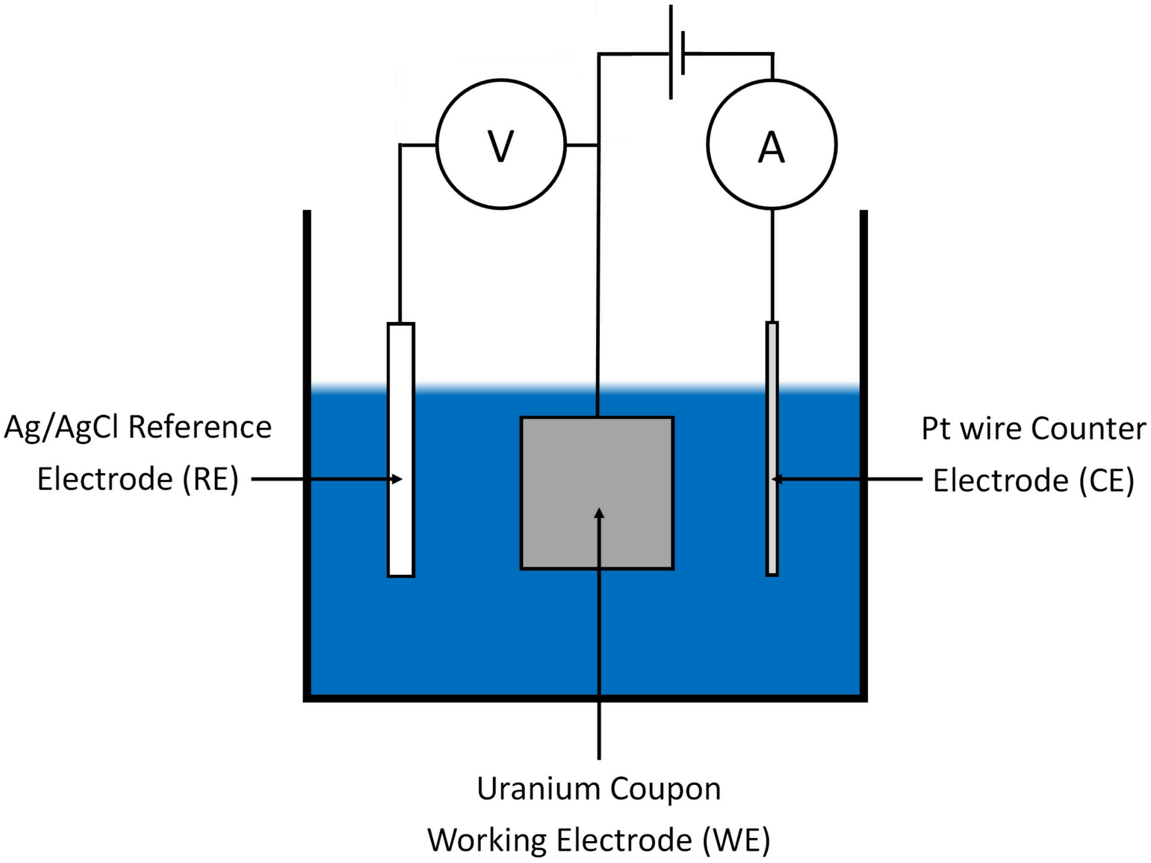

Figure 3.1: A schematic of the experimental configuration used during electropolishing. The three electrode cell comprises a reference electrode, a counter electrode and the working electrode. The potentiostat was used to control all experiments by applying a potential between the reference and working electrodes and measuring the current via the counter electrode.

3.2.4 Characterisation

EBSD maps of the pure uranium samples were collected using a Zeiss EVO MA10 scanning electron microscope fitted with a LaB_6 source operating with an accelerating voltage of 30 kV. EBSD maps of the uranium alloys were collected using a Zeiss SigmaHD scanning electron microscope fitted with a FEG source and also operated at 30 kV. The SigmaHD was used instead of the EVO as the FEG source offered greater stability and brightness which was essential for assessing the uranium alloys, which required very time consuming scans (approximately 12 hours).

EBSD pattern confidence indices were used as the primary metric for the analysis of ideal polishing conditions. Microscope and image processing settings were kept constant for the collection of scans to ease comparison of polish quality. Two patterns, each with an exposure time of 0.05 s were collected for each point of an EBSD map. Maps of pure uranium measured at least 100 μm × 50 μm. Additionally the image processing routine was kept constant with background subtraction, dynamic background subtraction, normalised intensity histogram and median smoothing filter functions used.

XRD scans were performed on a Philips X'Pert Pro multi-purpose diffractometer fitted with an Empyrean Cu-Kα tube source operated at 40 kV and 40 mA. The diffractometer was fitted with 0.04 radian Soller slits. 1/2 ° divergence and receiving slits were used as these settings were assessed to introduce instrumental peak broadening insignificant when compared to the sample microstrain whilst also providing strong beam intensity. Scans were typically run between 25 and 140 °.

XRD was used to assess stresses and strains in the materials by two complementary techniques. The well established Williamson-Hall method was used to assess strains and coherent crystallite domain sizes [289]. A similar form of this analysis is also present in full pattern fitting techniques such as Rietveld refinement. Sin$^2\psi$ tests were also carried out to establish stresses present on select samples [286]. In a Bragg-Brentano geometry, the sin$^2\psi$ method measures the same Bragg peak at varying sample tilts. The effective sampling depth, τ, is provided by,

$$\tau = \frac{sin^2\theta - sin^2\psi}{2\mu sin\theta cos\theta} \tag{3.1}$$

where θ is half the diffraction angle (2θ), ψ is the angle between the surface normal and diffraction vector and μ is the x-ray absorption coefficient. In uranium, 8 keV x-rays produced by a Cu-Kα source produces an absorption coefficient of 5760 cm^{-1} [184].

The (1 3 5) peak, the reflection relating to the smallest d-spacing measured (0.845 Å), permitted the greatest permissible value of sin$^2\psi$ (0.8). Based on this reflection and using Equation 3.1, a minimum information depth for sin$^2\psi = 0.8$ can be determined to be 67 nm, which equates to fewer than 800 planes of this orientation. In a specular scan, the same orientation will access in excess of 9000 layers. As a single peak is examined during each sin$^2\psi$ scan, centred 2θ scans with a range of 4 ° with a step size of 0.02 ° were conducted. Positive tilts were used to ensure that the beam footprint did not exceed the size of the sample at high values of sin$^2\psi$.

XRD Williamson-Hall and sin$^2\psi$ data were fitted with pseudo-Voigt peaks by MATLAB scripts that used the M-fit least squares fitting routine produced by the Institut Laue-Langevin [108]. Full powder pattern fitting was performed by GSAS-II and enabled an accurate measure of lattice parameters, texture and a secondary value of strain in the material [266].

3.3 Results

3.3.1 Uranium

3.3.1.1 I-V Curve Characteristics

A linear sweep of uranium in the 45 % ethanol, 27 % ethylene glycol and 27 % phosphoric acid polishing solution is shown in Figure 3.2. The scan was swept between -2 V and +6 V at a rate of 50 mV/s. Bubbles, presumed to be hydrogen, were observed to form readily on the working electrode in the cathodic region. As the potential is increased, this reaction is no longer supported, current returns to zero as the open circuit potential is achieved and the production of bubbles on the working electrode drops. In the anodic section of the curve, the activation polarization for the polishing reaction is achieved at around +0.5 V. The curve briefly experiences an exponential rise, region 1, before an extended linear rise, region 2. The curve subsequently experience a turning point, region 3, before the current falls back to the mass-transport limited plateau between regions 4 and 5. The current density limit under this steady state can be observed to equal around 25 mA/cm^2.

Current can often be observed to increase again at high potentials curtailing the plateau [1, 70, 71, 115, 175]. This is often explained as the onset of oxygen evolution at the working electrode (generally accompanied by visible bubble formation) or Joule heating [42, 70, 265]. The high acidity and minimal water in the solution is thought to be precluding oxygen evolution whilst the ethylene glycol improves viscosity aids in heat transfer [1]. The plateau extends to at least +10 V. Limitations in the potentiometer used preclude assessment of the curve beyond +12 V.

Linear sweep curves were found to not be constant with scan rate, as might be expected. Increasing scan rates caused the total current produced to increase but also cause the peak to shift to higher potentials. This behaviour is relatively peculiar and combines a mixture of what appears to be fast kinetics as observed from the increasing current density with scan rate and the slow electron transfer kinetics as evidenced from the moving peak position. Cyclic voltammetry showed that the current density at the mass-transport controlled portion of the curves at anodic potentials increased slightly between the first and second cycles as a response to the time delay in achieving a steady state. Reactions are confirmed to be irreversible using cyclic voltammetry; there appears to be no affinity for stripped uranium species to redeposit on the working electrode at cathodic potentials in a region which is dominated by H_2 gas evolution.

3.3.1.2 Chronoamperometry

Samples were electropolished under chronoamperometry conditions. Figure 3.3 shows an example of the response produced with the system under constant potential conditions. The black curve shows the data plotted against linear time. The same data has also been plotted against the square root of time and against logarithmic time, red and blue curves respectively. Current

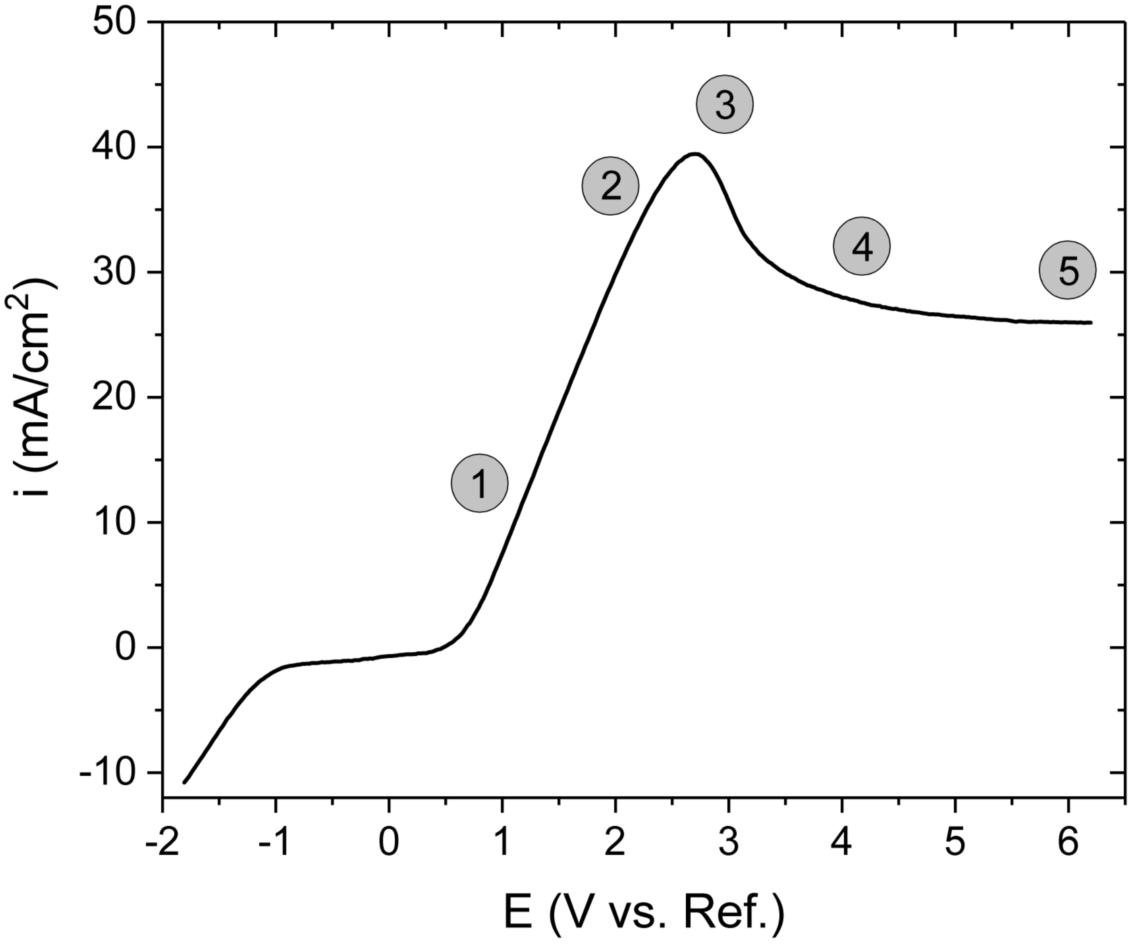

Figure 3.2: An example linear sweep curve obtained from a uranium sample in the 3-part polishing solution. This data set was collected with a scan rate of 50 mV/s. Key features have been annotated on the graph and are discussed in the text. The potentials of the annotated points have subsequently been used in chronoamperometry scans to evaluate the effects of potential on polishing quality.

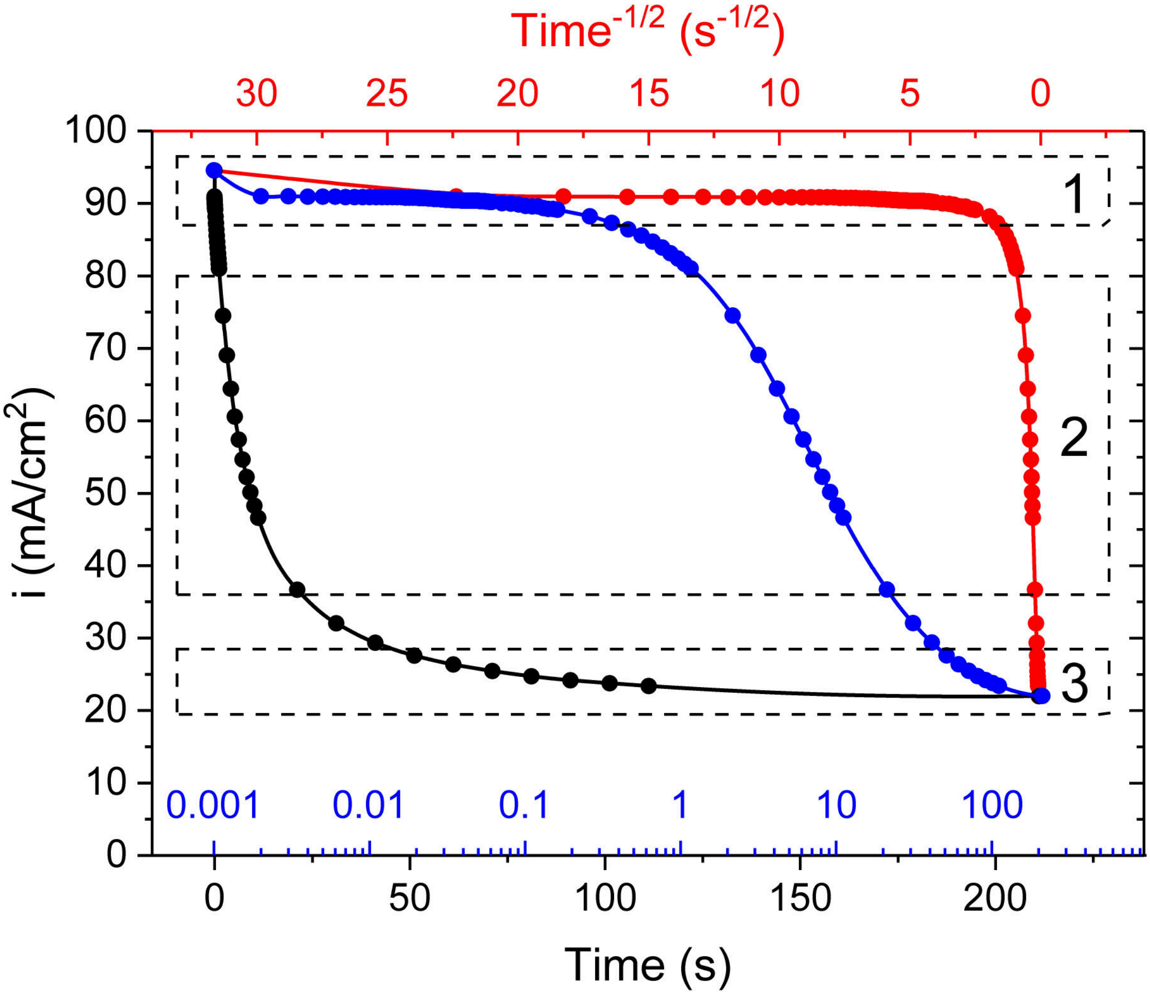

Figure 3.3: Data from a chronoamperometry scan conducted at a potential of 7.0 V plotted on three x axis scales. Current density as a function of time is plotted on a linear scale (black curve), logarithmic scale (blue curve) and on a square root scale (red curve). The Cottrell plot, i vs $t^{-1/2}$ (red curve) permits the easy identification of diffusion controlled processes as linear sections on this axis.

density is initially very large, close to 100 mA/cm^2, but this only lasts for around ~0.1 s, region 1. Current subsequently decreases rapidly between 1 - 20 s, region 2, in a regime characterised by a straight line on the Cottrell plot (i vs. $t^{-1/2}$). A final region which emerges at times beyond 200 s may be seen to be present from the blue logarithmic curve.

Diffusion coefficients of each regime may be extracted from the gradients of the Cottrell plot. The Cottrell equation can be written by,

$$i = \frac{nFc\sqrt{D}}{\sqrt{\pi t}} \tag{3.2}$$

where i is current density, n is the number of electrons involved in the oxidation reaction, F is the Faraday constant, c is the concentration of the analyte, D is the diffusion constant and t is time. Since there are relatively large errors and unknowns involved in this equation, the ratios between the diffusion coefficients may be a better comparison. Region 1 has a diffusion coefficient $(1.0 \pm 0.3) \times 10^7$ times larger than that of region 2. Region 1 is expected to relate to the transfer of charge through the near surface layer whereas region 2 belongs to the diffusion of ions away from the working electrode. Region 3 could be a response to a changing solution chemistry or the growth of a thin oxide layer.

3.3.1.3 Polishing Potentials

Five samples cut from the same original batch were used to investigate the results of polishing under different electrochemical potentials for a constant time. From the linear sweep of Figure 3.2, five distinct points were chosen to investigate the optimal polishing potential. The resultant EBSD maps, after a constant polishing time of 210 s, are shown in Figure 3.4. Average confidence index is maximised for the sample polished at +4.0 V.

Conventional thinking on ideal polishing potentials based on the linear sweep curve would appear to agree well with Figure 3.4 [283]. At potentials below the peak, polishing is ineffective with an insufficient volume of material removed after 210 s resulting in poor EBSD patterns. The production of quality EBSD patterns may be additionally be hampered by the formation of pores at low potentials, pitting has been established as favourable when below the limiting current [151]. With larger potentials, the polishing reaction is more effective and the average confidence index in the EBSD maps increase. There is appreciable variety in the confidence indices for the maps of Figure 3.4. This is thought to be mainly due to grain orientation effects and unexpected previous sample history as there appears to be substantially more twins in panel *e* than panel *d*. Despite this, samples polished at +4.0 V and +7.0 V were indexed effectively within the entire map region. The complementary chronoamperometry scans are provided in Figure 3.5. Despite instantaneous currents proportional to the applied potential, the stable polishing potentials of +2.7, +4.0 and +7.0 V were found to converge on a steady current density of approximately 20-25 mA/cm^2 at 210 s. Using a similar solution, 30 mA/cm^2 has previously been reported as optimal [9].

3.3.1.4 Polishing Durations

The effect of polishing time was subsequently investigated by a series of samples polished at +5.5 V, as was found to be suitable in the previous section, for varying durations. Figure 3.6 shows the EBSD maps generated from this study.

As in the previous section, the levels of twinning appears to differ between samples. Confidence indices can again be seen to be highly dependent on the grain orientation. For example, panels *e* and *f* show the orientations close to the [0 0 1] direction (red grains of panel *f*) produce

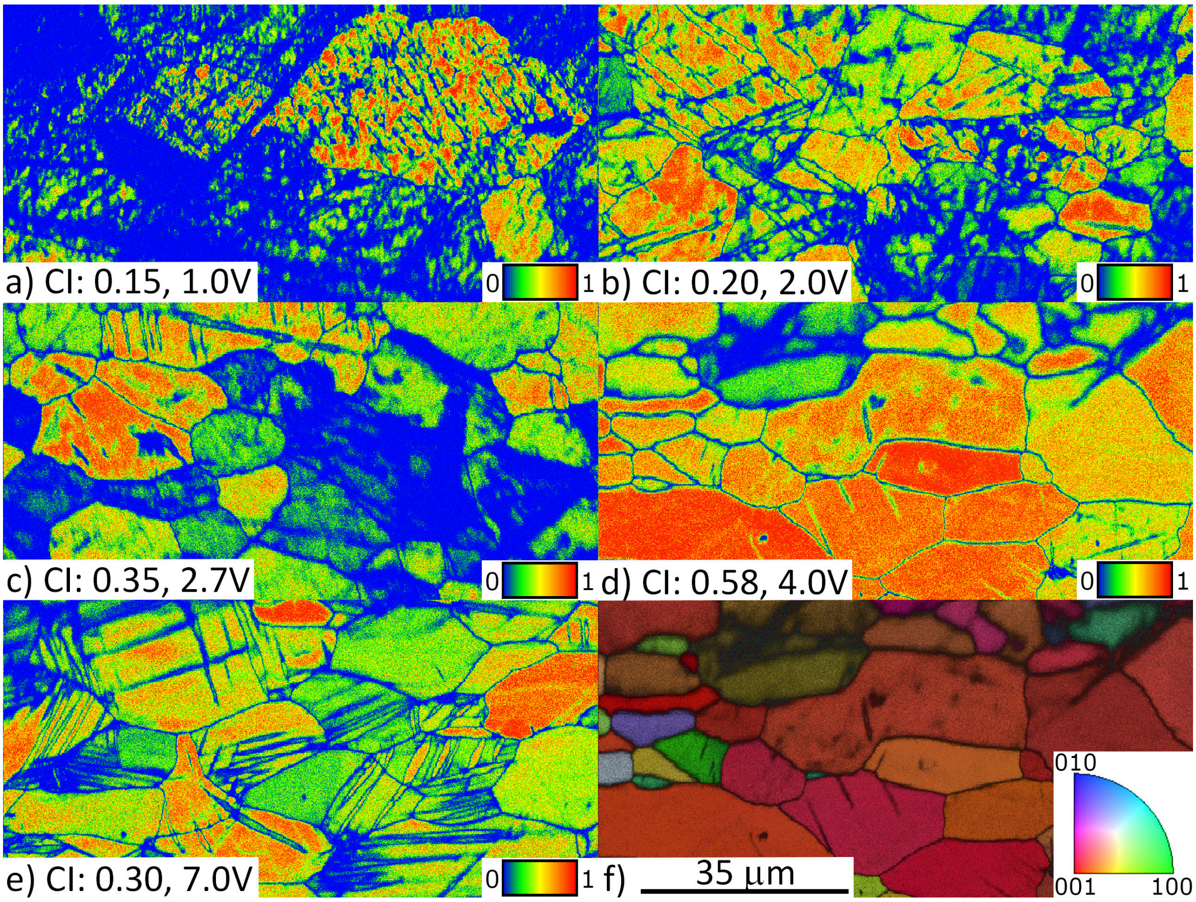

Figure 3.4: EBSD maps of specimens that were all been polished for equal durations, 210 s, but at varying potentials. The potentials used for polishing were based on the positions of features in the linear sweep curve of Figure 3.2. Panels *a* through *e* show confidence ranging from blue to red on the colour scale. Panel *f* shows a conventional EBSD map of the same area as panel *d*, with crystallographic orientation on the colour scale and image quality on the greyscale. In each instance, maps are 100 x 50 μm in size and the scale bar serves each panel.

higher average confidence indices than others. This might be due to an orientation's propensity for electropolishing [139, 151, 155], the thickness of oxide that will have formed subsequently during transportation to the microscope or the number of lattice planes contributing to the scattering of electrons in each crystallographic orientation. The density of strong Kikuchi bands crossing the detector given a grain's orientation is likely also having a strong effect, particularly given uranium's unconventional crystallographic structure.

Electropolishing is occasionally reported to induce roughening with extended and lengthy polishing durations impacting the quality of EBSD patterns [215]. Since the initial state of the material in this case was quite rough, having been finished mechanically by P4000 grit paper, the surface has been smoothed substantially by the electropolishing as evidenced by strong EBSD patterns and maps that generally improve with polishing duration.

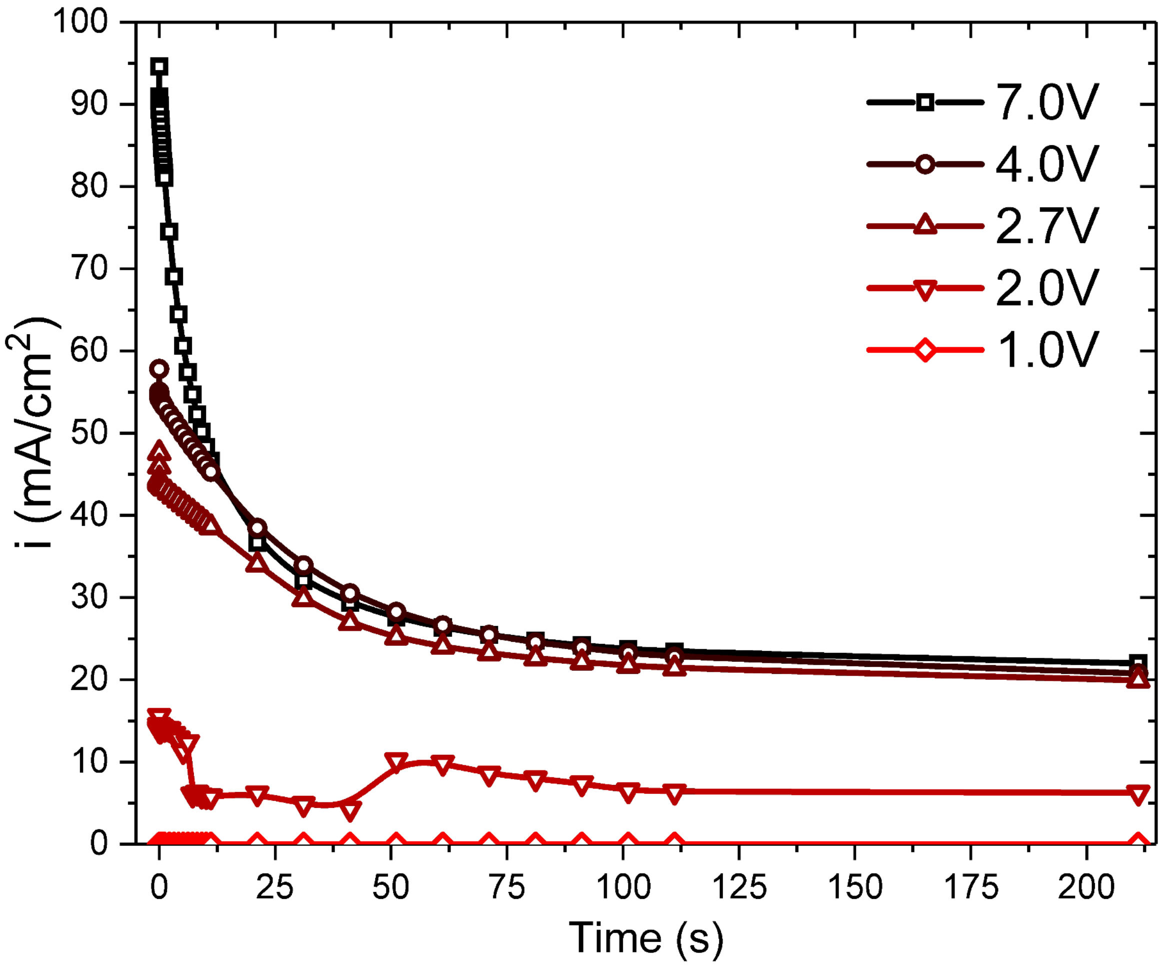

Figure 3.5: Chronoamperometry scans showing the relationships between current density and time for the five polishing potentials used to investigate the effect of polishing potential. At potentials greater than the activation potential, current is limited to around 23 mA/cm^2 after the initial, instantaneous response to the change in potential. The lower potentials of 1.0 and 2.0 V did not produce effective polishing, which is assumed to be linked to the fact that current limiting polishing was not achieved. Data points are connected by spline curves to add clarity.

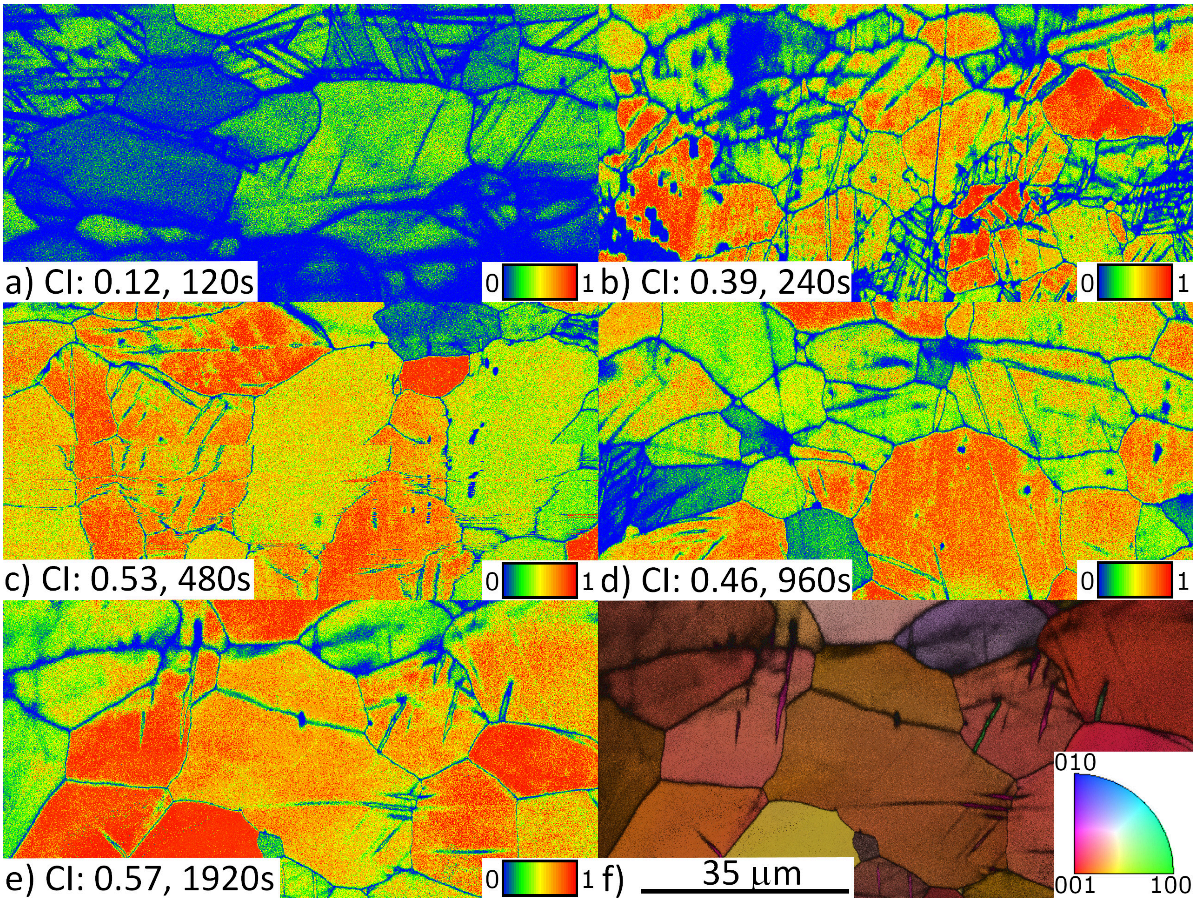

Figure 3.6: EBSD maps of the specimens polished at 5.5 V for exponentially increasing durations. Panels *a* through *e* show confidence ranging from blue to red on the colour scale. Panel *f* shows a conventional EBSD map of the same area as panel *e*, with crystallographic orientation on the colour scale and image quality on the greyscale. In each instance, maps are 100 x 50 μm in size and the scale bar serves each panel.

3.3.1.5 Evaluation of Residual Stresses

Following the successful preparation of samples in the previous two sections, a final sample was prepared from which residual stresses would be measured. In order to extract the best possible EBSD patterns, mechanical polishing additionally included 3 and 1 μm diamond pastes which minimised the number and size of scratches prior to electropolishing which was performed at 5.5 V for 600 s. An EBSD map of many grains surrounding a cluster of carbide inclusions is shown in Figure 3.7. Most of the carbides have been stripped or polished out during the electropolishing process leaving pits that are not easily indexed. However, in some cases, there is enough remaining carbide material at the bottom of sufficiently shallow pits to enable indexing.

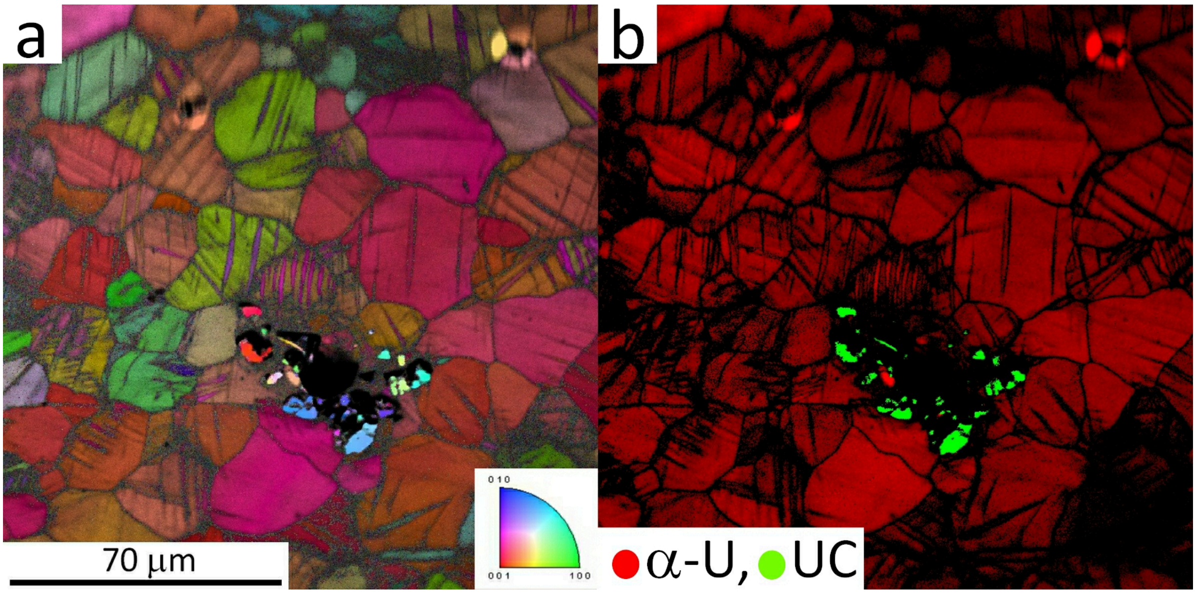

Figure 3.7: EBSD maps of the surface of the optimally prepared uranium sample in a preparation routine that included diamond paste polishing. Panel *a* shows a conventional map where crystallographic orientation is shown on the colour scale and confidence index is incorporated in as the greyscale. Panel *b* shows a map of the phases on the colour scale and confidence index on the greyscale. A carbide cluster is shown clearly in this figure, however, much of the carbide material has been etched away through polishing leaving pits and resulting in much of the cluster going un-indexed.

Non-metallic inclusions have been shown to display a tendency preferentially removed from the surface [151]. Confidence indexes were found to be higher in the vicinity around carbides. This can be seen in a couple of cases at the top of Figure 3.7. Landolt *et al.* suggests that inclusions disrupt the Helmholtz double layer, dissolving preferentially or perturbing local current transfer [151].

Figure 3.7 shows the microstructure of this sample to be dominated by twinning, with the (130) mode featured particularly frequently, in keeping with literature expectations [294]. The confidence index distribution is broadly Gaussian in this sample with a mean of 0.36 and a standard deviation of 0.22 with much of the variation attributable to the effects of grain orientation. A large EBSD map collected from the same sample is shown in Figure 3.8. The large scale of the map requires a sacrifice in resolution which makes identification of the narrow twins more difficult. However, the numerous grains accessed from such a large map enables the modelling of the texture within this sample which points towards a preference for the [001] direction oriented normal to the surface.

A fitted x-ray diffraction pattern of the optimised sample is shown in Figure 3.9. Rietveld refinement was used to determine lattice parameters for use in the EBSD material file and fit the texture of the sample. An equivalent Inverse Pole Figure generated from the XRD data is inset in Figure 3.9 and broadly agrees with that obtained by EBSD. The XRD IPF however, suggests a

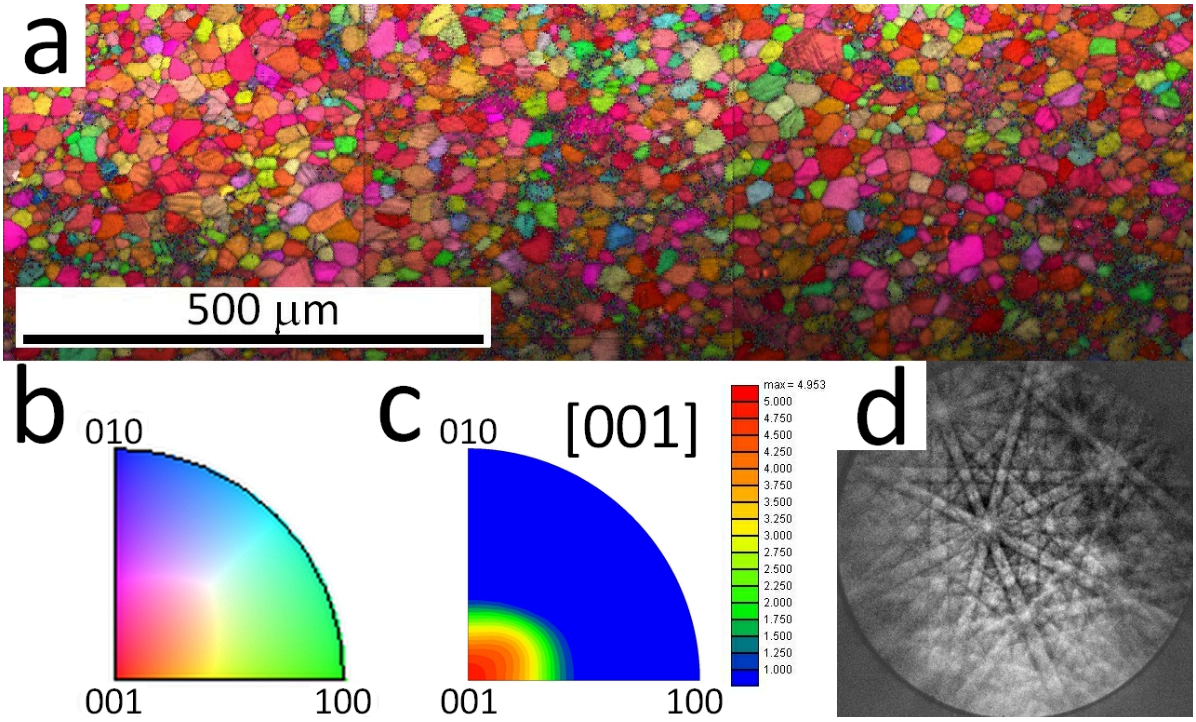

Figure 3.8: Panel *a* shows a large EBSD map of the optimally prepared uranium sample with an inverse pole figure legend, texture plot and example Kikuchi pattern shown in panels *b* to *d* respectively. The Kikuchi pattern in panel *d* has been collected with 1 x 1 binning to evaluate the potential of performing cross correlation EBSD on this material using a similar preparation method.

maximum for the [2 0 1] direction. This does not relate to an observed reflection in the powder pattern and is most likely an artefact of the texture fitting which may need refinement.

3.3.1.6 Williamson-Hall Method

A mean crystallographic strain was obtained by applying Williamson-Hall peak analysis on the specular XRD powder pattern of Figure 3.9. Increasing peak widths with increasing diffraction angles is an indicator of strain in the material. Fitting the Williamson-Hall plot, Figure 3.10, produced a very small gradient, $< 1 \times 10^{-3}$, illustrating minor deviations in the periodic structure within the sampled volume. Inherent features of the bulk material, such as grain boundaries and twins have the potential to induce strain in the material.

A version of the Williamson-Hall formula is given by,

$$\beta_{hkl}\, cos\theta = \frac{K\lambda}{D} + \frac{\sigma_{hkl}\, sin\theta}{E_{hkl}} \tag{3.3}$$

where β_{hkl} is the peak width, D is the particle size, K is Scherrer's constant and E_{hkl} is the in-plane elastic modulus. In this scenario, an isotropic stress, σ_{hkl}, is evaluated for each

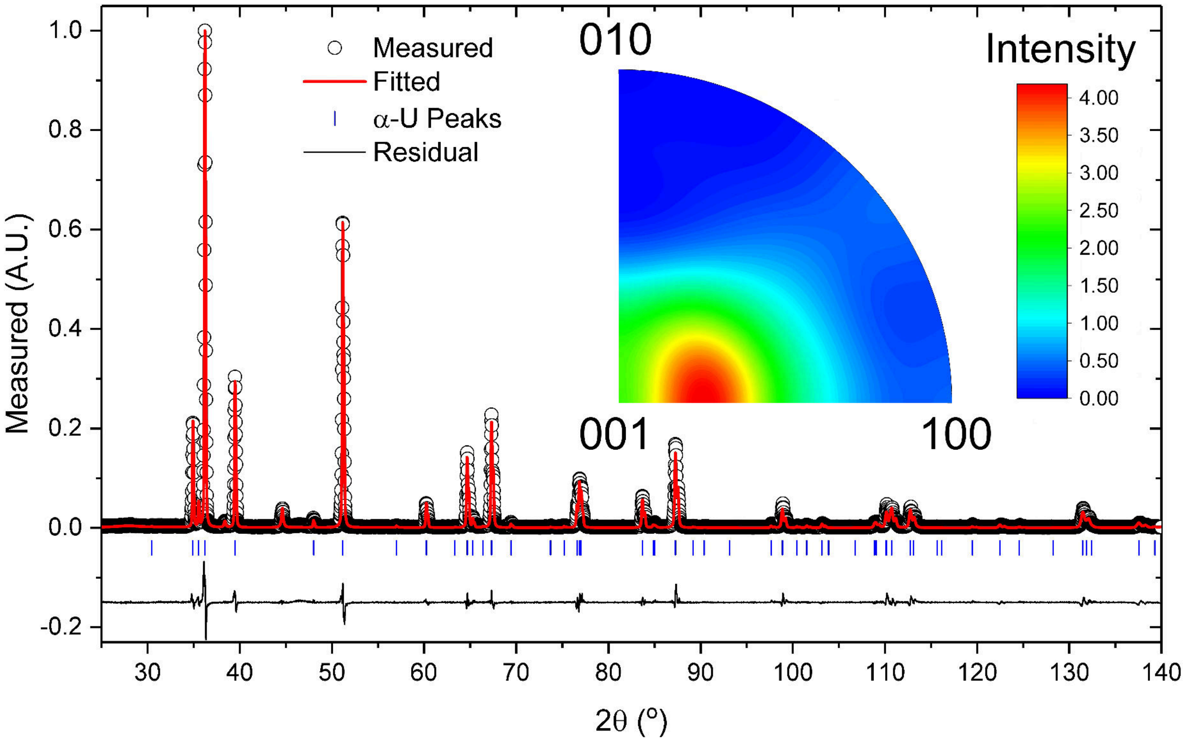

Figure 3.9: XRD pattern fitted by Rietveld refinement. A preferred orientation model based on spherical harmonics was included in the fit which resulted in the inset texture plot.

reflection. However, this relies on the in-plane elastic modulii which are provided by,

$$\begin{aligned}(E_{hkl})^{-1} =& n_1^4 s_{11} + n_2^4 s_{22} + n_3^4 s_{33} \\ &+ n_2^2 n_3^2 s_{44} + n_1^2 n_3^2 s_{55} + n_1^2 n_2^2 s_{66} \\ &+ 2n_1^2 n_2^2 s_{12} + 2n_1^2 n_3^2 s_{13} + 2n_2^2 n_3^2 s_{23}\end{aligned} \tag{3.4}$$

where n_i are the Euler angles between reflections and the principal axes, s_{ij} are the inverse of the elastic stiffness moduli, c_{ij}, ($s_{ij} = c_{ij}^{-1}$) obtained from Fisher and McSkimin [89]. Individually modifying each reflection based on the calculated in-plane elastic modulus increased the stress and the error, -83 ± 33 MPa, compared to the equivalent, using the mean elastic modulus of 201 GPa [11], -45 ± 9 MPa. Both results indicate compressive stresses but the material is best described by the uniform treatment of reflections and orientations. The model may potentially be improved upon by employing the Warren-Averbach method or accounting for the numerous deformation pathways such as twinning and slip that exist in uranium [35, 284].

3.3.1.7 Sin$^2\psi$ Method

Stresses in this sample were also directly measured using the sin$^2\psi$ method. The relationship between the interplanar spacing and sine^2 of the tilt is shown in Figure 3.11. Progressively larger

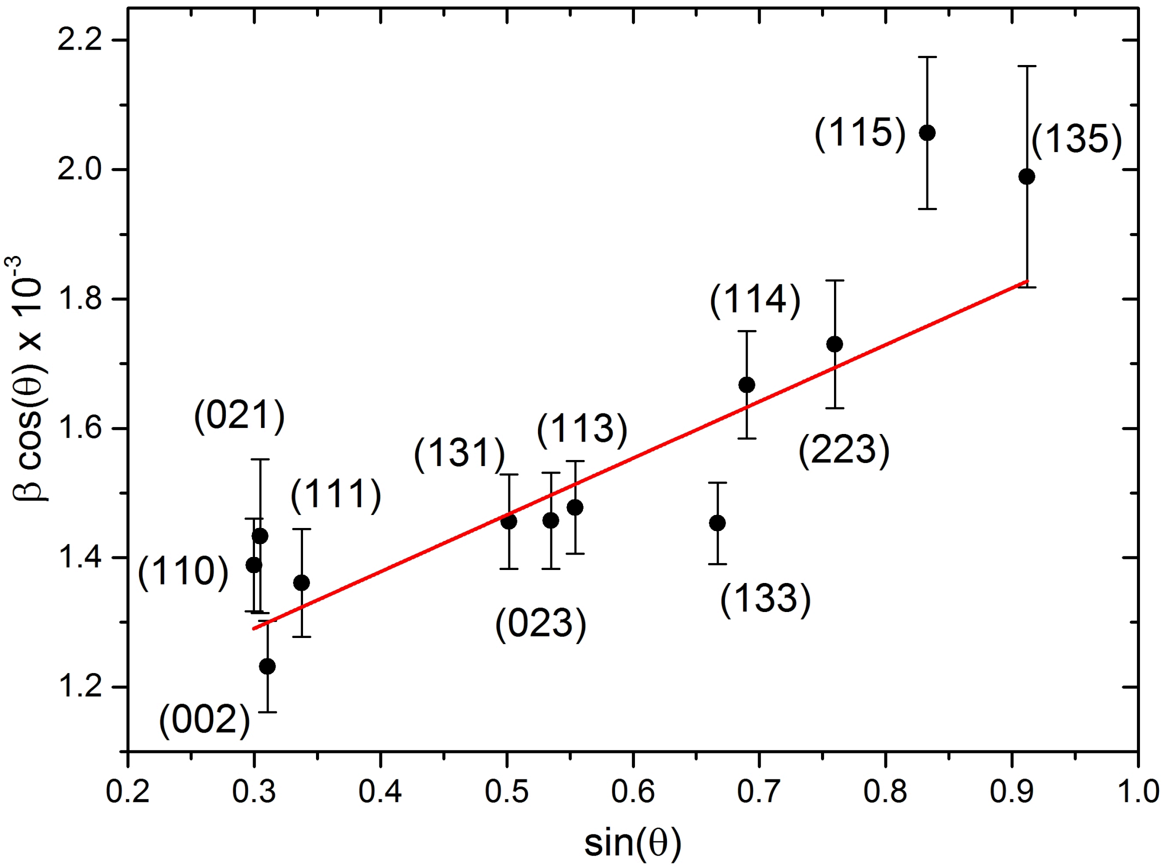

Figure 3.10: Fitted Williamson-Hall plot produced from single peak data extracted from Figure 3.9. The gradient of the the linear best fit line was evaluated as (8.8 ± 1.9) × 10^{-4}. Error bars do not completely account for the scatter in the data away from the line of best fit, which may suggest that the complex deformation pathways of uranium may be independently affecting reflections.

tilts caused inter planar distances to decrease by thousandths of Ångströms, agreeing with the expectation that the majority of crystal orientations are compressed by mechanical working. Particularly at high tilts, the $\sin^2\psi$ method is only able to access the very top few layers.

As the last section showed the suitability of the averaged elastic modulus compared to the resolved in-plane equivalent, stresses were calculated from the gradients of the curves of Figure 3.11 using a mean elastic modulus,

$$\sigma_{hkl} = \frac{E}{1+\nu}\frac{d\epsilon}{d(sin^2\psi)} \tag{3.5}$$

where ν is Poisson's ratio for uranium, 0.23 [11], and ε is the strain between the ideal and measured peak position, based on a Rietveld fitting of the entire pattern.

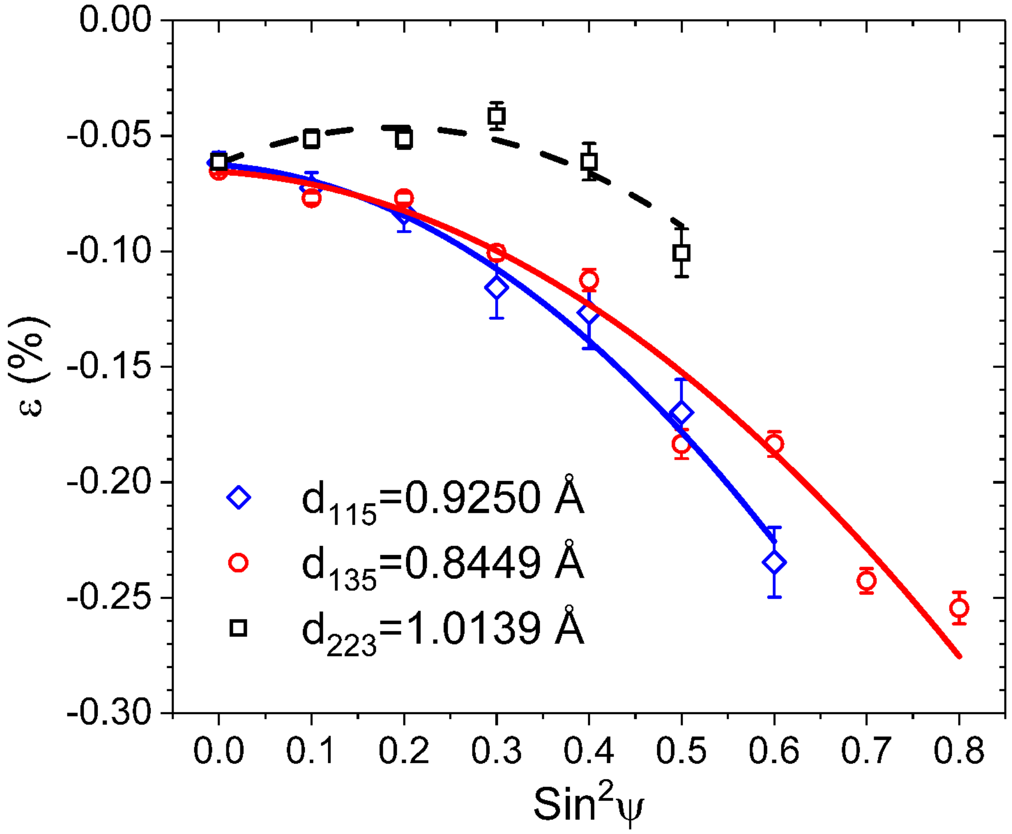

Figure 3.11: $\mathrm{Sin}^2\psi$ plot for the (115), (135) and (223) reflections. Data was collected in positive tilt (of the ω-axis) mode to ensure that the beam footprint did not exceed the size of the specimen. These reflections were chosen as intense peaks at high angles in 2θ are required to access and be able to detect peaks at high values of $\sin^2\psi$.

Uniform stresses would conventionally produce a linear relationship [286]. The data shown in Figure 3.11 is better described by parabolic curves which would indicate an inhomogeneous stress profile that increases towards the surface. The curves have been differentiated analytically and evaluated at their maxima to provide an upper estimate for the stress at the surface. Stresses in each of the reflections shown in Figure 3.11 were σ_{115} = -841 ± 156 MPa, σ_{135} = -815 ± 168 MPa and σ_{223} = -448 ± 227 MPa. The result for the (223) reflection comes with a large error as a result of the few values of $\sin^2\psi$ that are accessible using this geometry. Tracing the curves back to $\sin^2\psi = 0$, where the geometry is the same as that of the Williamson-Hall tests, produces a stress of -44 ± 44 MPa (as averaged between the (115) and (135) reflections), a figure that agrees with that determined previously by Williamson-Hall analysis. The compressive yield strength of uranium is roughly 750 MPa [294], meaning that plastic compression would be limited to only the top few layers.

3.3.2 Uranium Alloys

3.3.2.1 I-V Curve Characteristics

A linear sweep voltammogram of the UNb6 alloy in the 85 % phosphoric acid polishing solution is displayed in Figure 3.12. The curve shares many features with the uranium equivalent in the previous section, Figure 3.2, and those expected suitable for polishing. As before, in the cathodic region, there is a significant reaction that occurs beyond -1 V which is linked to a production of hydrogen bubbles at the working electrode. A plateau which encompasses the open circuit potential thereafter follows before the anodic polishing reaction which is initiated at approximately +0.7 V. Following a peak at around +1.9 V, the current appears to initially attempt to trend towards a mass-transport controlled plateau. However, this is temporary as the current increases again beyond +3 V. The production of a large number of oxygen bubbles is assumed to by linked to the current increase [42, 70, 265], masking the true nature of the polishing current [151].

Scan rate was also investigated with Figure 3.13 showing the results of five different sweep speeds. The response to scan rate is slightly different to that of uranium in the 3-part solution. Like the polishing of uranium, as the scan speed is increased the peak position may be observed to shift considerably to higher potentials. Whereas, in the polishing of uranium, the gradient leading up to the peak remained the same irrespective of scan rate, a softening of the gradient occurs in the case of the alloy. The curves presented in Figure 3.13, are more typical of an irreversible electron transfer reaction [88]. Increasing total current with scan rate is usually indicative of fast, reversible reactions, however it is assumed that the reaction relating to the evolution of oxygen is primarily responsible for the increases to current. Lower scan rates are more typical of the system under steady state conditions as the diffusion layer has sufficient time to equilibrate. It would therefore seem sensible that a polishing potential of +2 - 2.5 V would permit mass-transport limited polishing without undesired oxygen evolution that is undoubtedly altering the chemistry of the polishing solution.

UNb7 alloy samples were polished with both the 3-part and the phosphoric acid polishing solutions separately to examine the effectiveness of each. Clarke *et al.* advocated the serial use of both solutions in their polishing routines [52]. Kelly *et al.* reported the use of a 5-10 % oxalic acid as a secondary ‘electroetching’ step in their polishing procedure [136, 137]. With the same amount of surface area exposed, the phosphoric acid polishing solution produces roughly ten times the current of the 3-part solution. Peak positions appear relatively unchanged suggesting the same reactions feature. EIS conducted on this specimen using both solutions shows the spectra to be similar in both cases with the most obvious differences being in the frequencies of features in the Bode plots. A complete model of the EIS spectra has proven to be difficult to extract and so the results have been omitted.

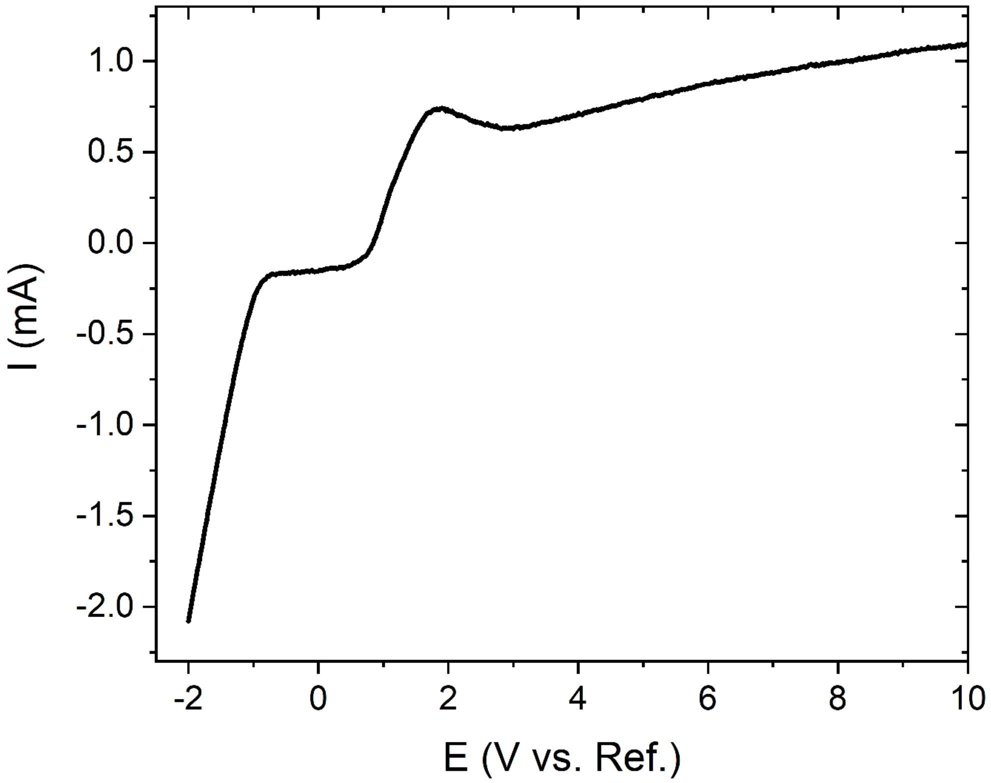

Figure 3.12: Linear sweep voltammogram of the UNb6 alloy in the 85% phosphoric acid solution conducted with a scan rate of 50 mV/s. The cathodic section of the curve is shown of the left at negative potentials and the anodic section on the right at positive potentials. The plateau at high anodic potentials was affected by oxygen evolution to a greter extent than the uranium equivalent, Figure 3.2.

3.3.2.2 Chronoamperometry

A typical chronoamperometry scan collected from the UNb7 alloy is shown in Figure 3.14. Under a constant potential of +1.9 V, the system shows expected behaviour with a roughly $i \propto \mathrm{t}^{-1/2}$ form [53]. The current density settles on roughly 16 mA/cm^2 following the relaxation of the system to steady state polishing. Large errors in the effective polishing area (due to inadvertent polishing of the specimen sides and reverse) mean that it is difficult to be absolutely certain of the the current density. However, current density is of the same magnitude as that obtained using pure uranium and the three part solution.

After an extended period of polishing, beyond 15 mins, the solution would start to exhibit a faint yellowish tinge as released uranium ions complex and accumulate in the solution. By 45 mins, a yellowing of the solution is particularly noticeable. Despite changing chemistry in

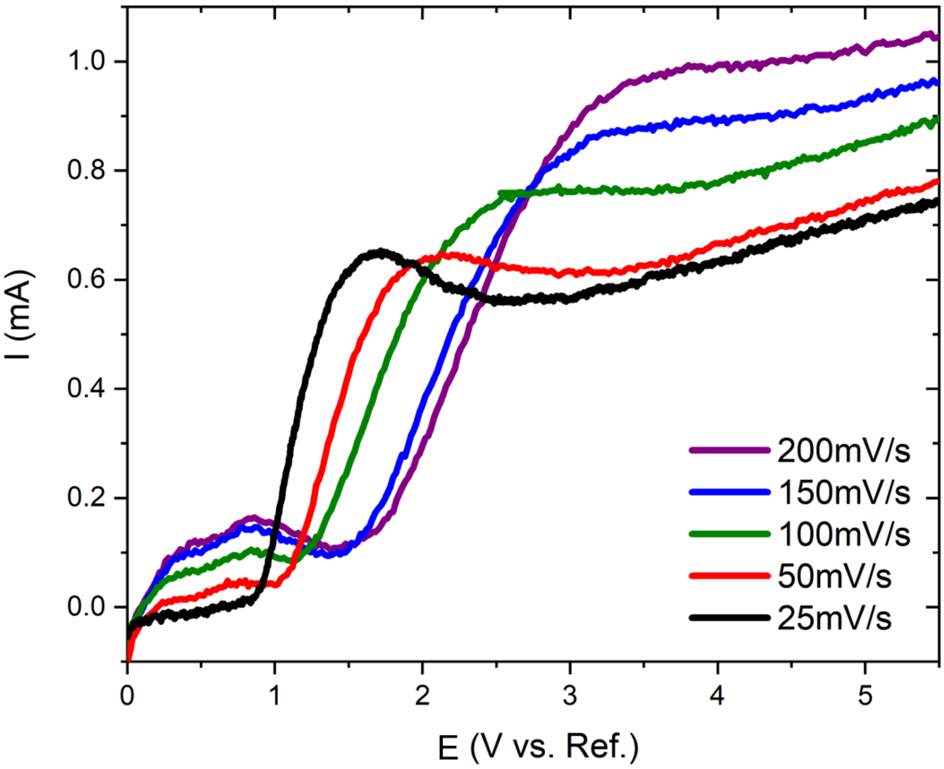

Figure 3.13: Linear sweep voltammograms of the UNb6 alloy in the 85% phosphoric acid solution for a range of scan rates. A constant surface area was used for each run to minimise errors. Additionally, the same solution was used for each scan rate, albeit with a suitably long incubation time between each run to allow the solution to return to a steady state.

the system, chronoamperometry and linear sweep curves do not show significant changes under lengthy polishing treatments.

A build-up of an oxide layer during electropolishing is evidenced by a yellowish tinge developing on the surface of the alloy. Zhang *et al.* also reported a thin oxide to have formed as a result of polishing at high potentials (12 V), but was able to remove it using a lower voltage (3 V) for a few seconds [301]. Here, the colour was not observed to grow a deeper yellow suggesting that the layer can not continue to grow indefinitely. This observation backed up by the EIS measurements (which show constant solution resistance, increasing polarization resistance and decreasing capacitance under increasing potentials [265]), complement the compact film model of electropolishing described by Grimm *et al.* and Matlosz *et al.* [100, 101, 166]. There has been some disagreement in the the literature over the nature of the anodic compact film with some in the support of a solid oxide film and others proposing anhydrous films [151]. In this case, if

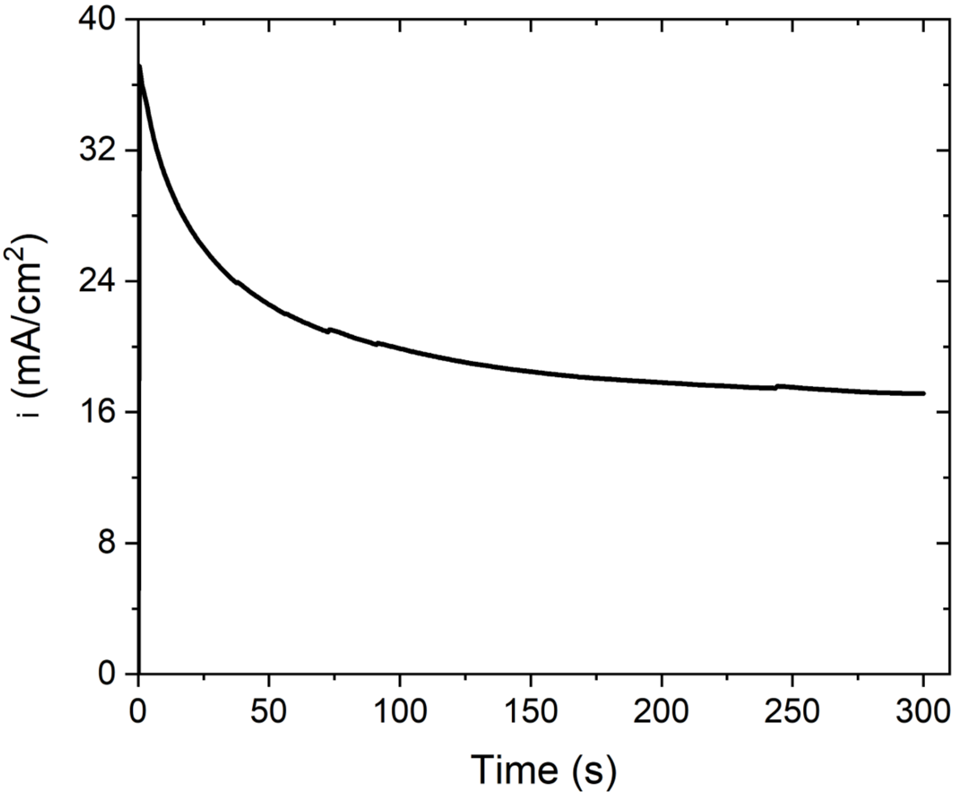

Figure 3.14: Chronoamperometry curve of the UNb7 alloy in the 85% phosphoric acid solution under a constant potential of 1.9 V. A steady-state current density of 17-18 mA/cm^2, slightly less than that observed in the case of uranium polishing, Figure 3.3, was observed at longer polishing times.

removed from the solution quickly, the anodic layer could be preserved. However, leaving the sample in the solution for roughly a minute or polishing at low potentials (~ 0.5 V) would be effective in dissolving the layer and returning the surface to the metallic, silvery colour. In some cases, a linear sweep conducted after electropolishing under chronoamperometric conditions would result in a noisy scan assumed to be due to the formed oxide film. Allowing the film to dissolve into solution permitted the collection of a linear sweep voltammogram complementary to the initial state.

A long electropolishing treatment was applied to the UNb6 alloy to assess the stability of the polishing process. Figure 3.15 shows the linear sweep voltammogram and chronoamperometry scan of a 45 min section of an hour long electropolish. The linear sweep curve showed an extended current limited plateau which enabled polishing of the alloy at 5 V without a large contribution from oxygen evolution. The chronoamperometry scan is relatively stable (apart from when the

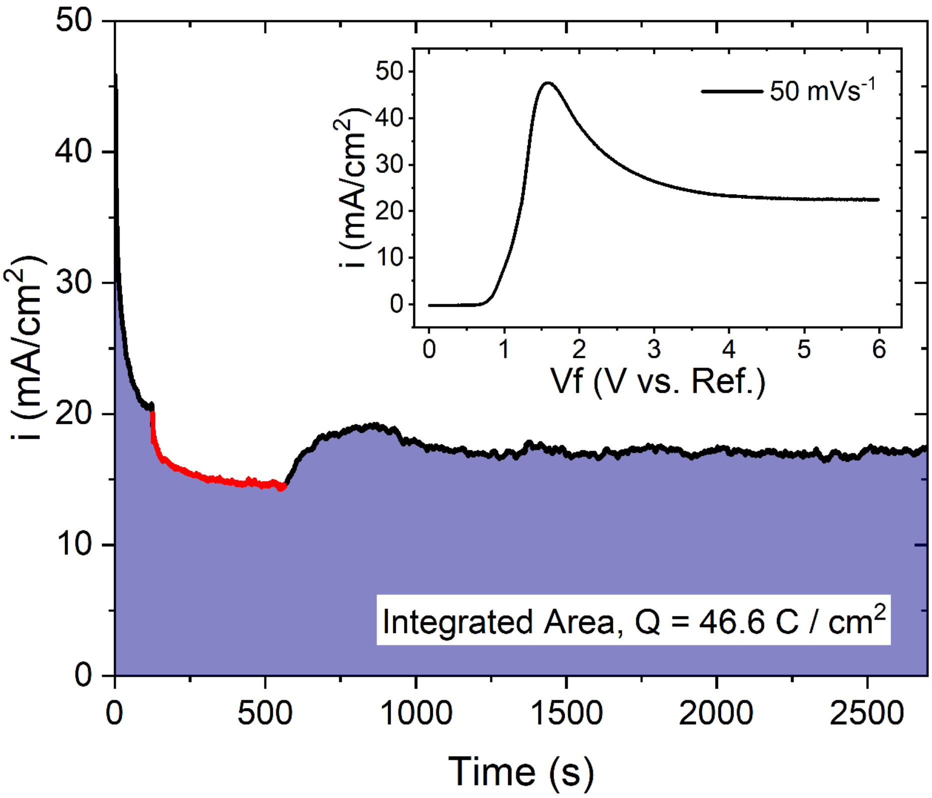

Figure 3.15: Linear sweep voltammogram (inset) and chronoamperometry scan of the UNb6 alloy polished at 5 V for 45 mins. The red portion of the curve was caused by increasing the stirrer rate from 90 to 180 rpm. Excessive agitation of the solution resulted in a decreased effectiveness of electropolishing until the previous stirring rate was restored.

stirring rate was changed) with the current density converging on 17 - 18 mA/cm^2. There is a small amount of noise in the data which is presumed to be due to a small amount of oxygen bubble evolution.

The long electropolishing treatment also permitted an estimation of the rate of mass removal. Without knowledge of the valency of the metal ion and efficiency of the system, it is difficult to estimate the polishing rate. A feature formed at the boundary of the meniscus is shown in Figure 3.16. Imaged at a variety of angles using the FIB, the height difference between the un-polished and the polished section of the alloy can be estimated at approximately 20 μm, equating to a polishing rate of 1/3 μm per minute. Weighing the specimen is an alternative and more usual method of obtaining an estimate of the polishing rate [58, 92, 144]. However a slightly different setup, where only the face is exposed, would be required as the edges and reverse appear to also be polished creating ambiguity over the effective surface area.

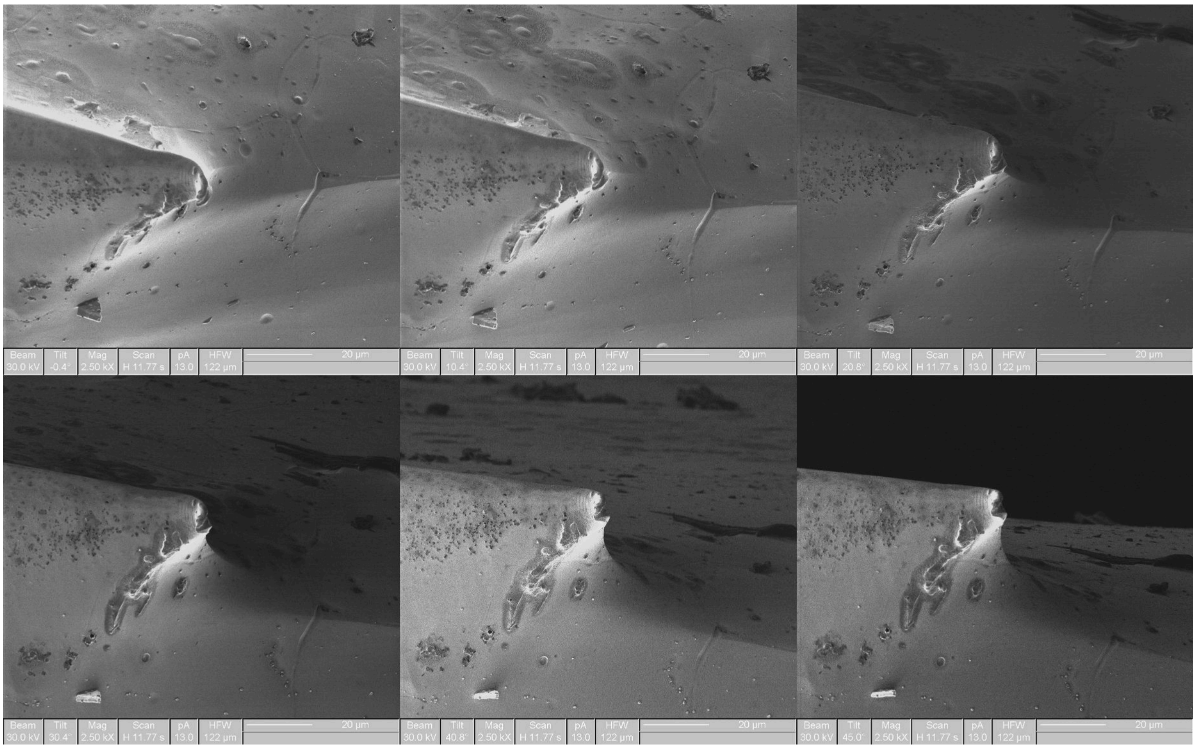

Figure 3.16: Feature produced by the polishing of the UNb6 alloy for 1 hour at 5 V. A miniscus formed on the sampe leaving an outcrop that was not immersed in the solution and therefore not polished. From this feature and a similar one on the other side of the sample, it is possible to estimate that approximately 20 μm has been polished away at roughly 1/3 μm per minute.

An image of the polished surface of the UNb7 alloy imaged at 70 ° using the SEM along with a complementary EBSD map is shown in Figure 3.17. Polishing is effective in producing a relatively flat surface free of mechanical abrasion artefacts. Microstructural defects such as grain boundaries and twin variant interfaces have been etched preferentially.

Carbides on the other hand show one of two behaviours. NbC/Nb$_2$C inclusions are mainly found to have been retained, protruding from the surface. Uranium rich inclusions on the other hand are mostly polished away leaving behind a pit. In the UNb6 alloy, electron probe microanalysis (EPMA) evidence (not shown) found the uranium based inclusion particles to be mainly UN with NbC/Nb$_2$C veins and a roundish uranium oxide centre. A slice and view image of one of these carbides collected using the dualbeam is shown in Figure 3.18.

Figure 3.19 shows images of the inclusion particles found in the UNb6 and UNb7 alloys. The distribution of inclusions appears to be different for the UNb6 and the UNb5 and UNb7 alloys, possibly due to differences in manufacture which have resulted in the banded microstructure of the UNb6 that is not reciprocated in the other two alloys [107]. This can be seen by the bumpy surface of the UNb6 alloy which is due to differences in alloy concentration throughout the material [136, 222]. The UNb6 alloy shows some regular, often square pits which is where UN/UC

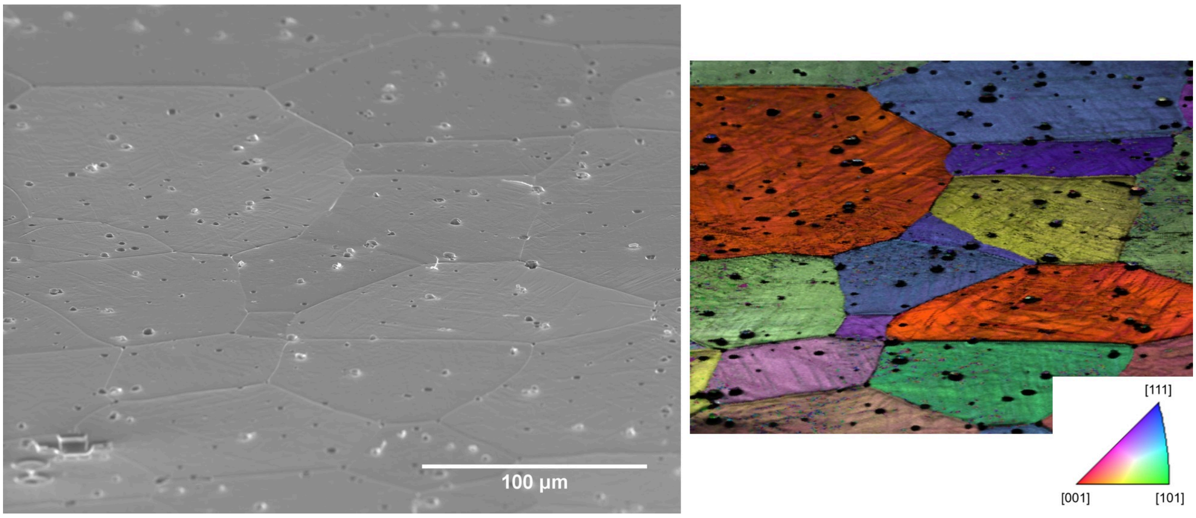

Figure 3.17: Left, surface of the UNb7 alloy following 20 mins of electropolishing at 1.9 V imaged by SEM. Right, sample is imaged at 70 ° for EBSD mapping, right. Scale is correct only for horizontal distances. The surface features a mixture of etched and proud carbides. Based on their morphology, the brighter carbides are thought to be the Nb_2C inclusions whereas the dull and etched away carbides are predicted to be UC. The bottom left of the image shows a fiducial marker.

inclusions have been etched out but the sporadic clusters of Nb_2C inclusions are much more prevalent. In contrast, the weighting is more even in the UNb7 alloy and Nb_2C carbides appear to take on a much more regular form. The retained niobium carbides, particularly in the UNb5 and UNb7 alloy, also present an opportunity to estimate the polishing rate. The top right image of Figure 3.19 shows a carbide around 2 μm high where the top surface is likely to be very close to the original height of the material. Given a total polishing time of 20 mins, a rate of roughly 0.1 μm per minute would be expected, quite a bit lower than that estimated from the features created by the meniscus.

3.3.2.3 XRD

To further illustrate the requirement for electropolishing, Figure 3.20 shows the XRD patterns arising from the UNb7 alloy given different stages of the preparation process. The pattern arising from the freshly cut specimen displays a highly strained bcc (γ phase) pattern with a small amount of oxide also present. Mechanical polishing appears to reveal an additional phase to be present in the patterns. It is only after the electropolishing step that the γ° phase can be determined to dominate the XRD pattern.

In a similar manner to that performed for the pure uranium samples, $\sin^2\psi$ stress testing was performed on electropolished uranium alloys. Unfortunately, given the poor peak intensity inherent in these patterns $\sin^2\psi$ testing did not produce satisfactory counting statistics to yield reliable results in the alloys. Additionally, efforts to assess the crystallographic texture in

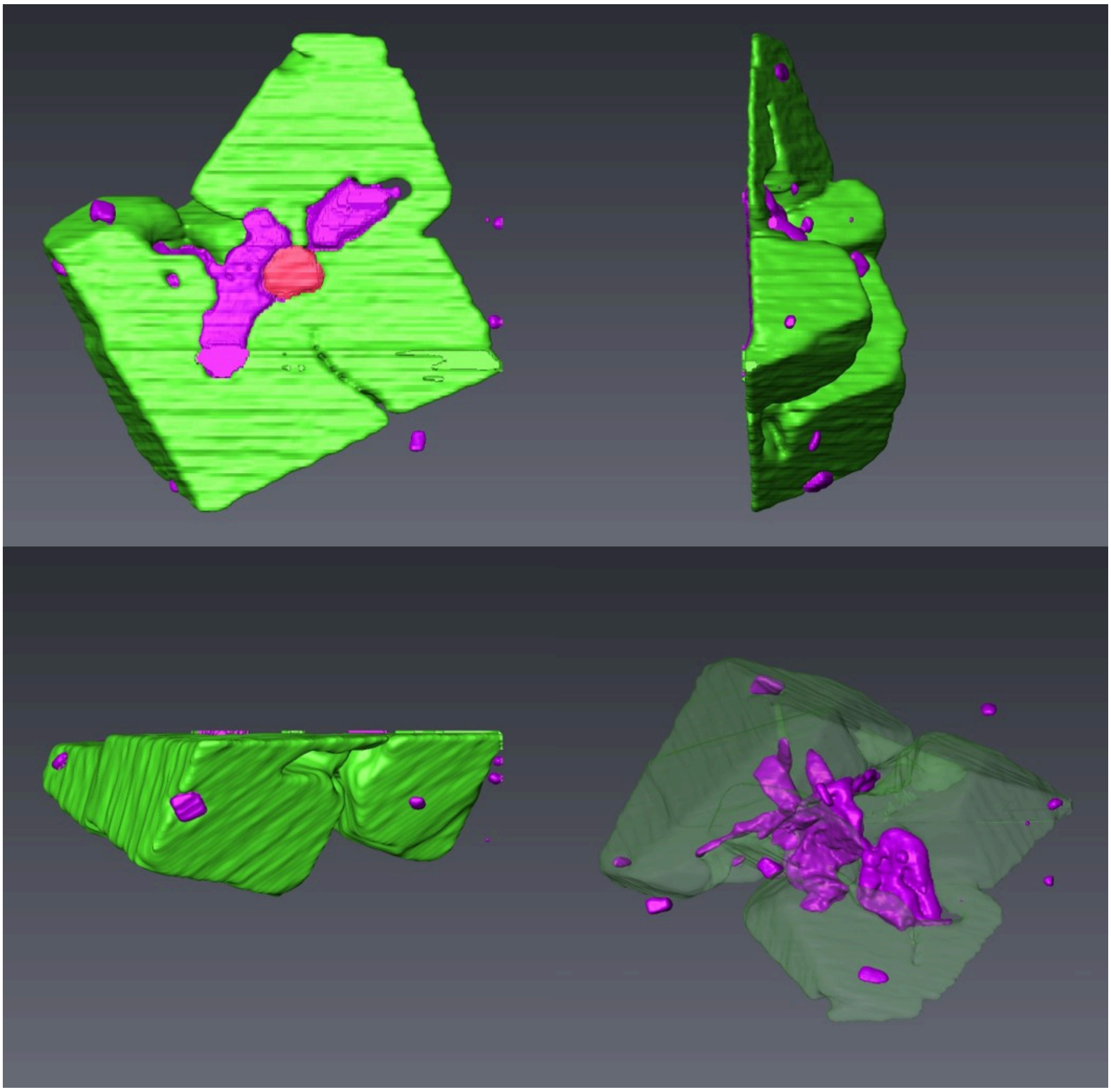

Figure 3.18: Reconstructed inclusion particle cluster from the UNb6 alloy examined using the slice and view technique on the dualbeam. Pink regions denote the Nb_2C phase, green regions denote the UN phase and red denoted the UO_x phase.

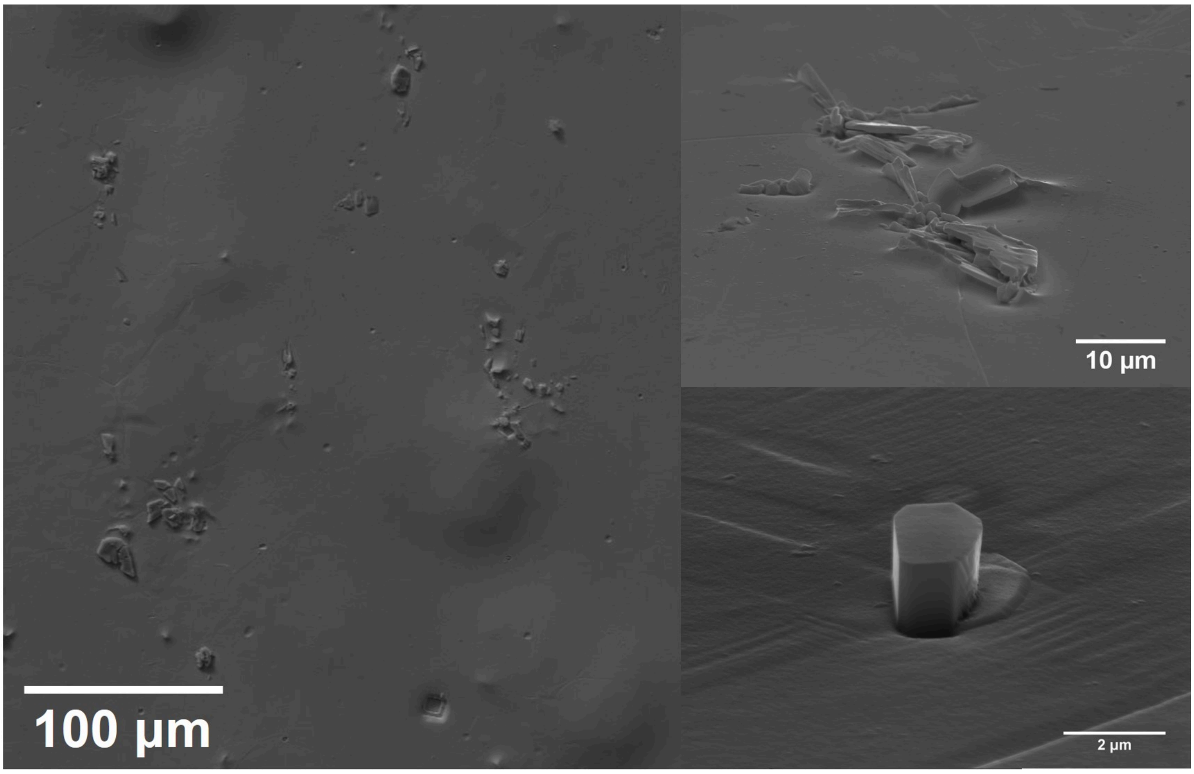

Figure 3.19: Left, surface of the UNb6 alloy following 60 mins of electropolishing at 5 V. Top right, Nb_2C carbide cluster in the UNb6 alloy viewed at 70°. Bottom right, carbide of the UNb7 alloy following 20 mins of electropolishing at 1.9 V viewed at 70°.

this material was unsuccessful using XRD due to poor intensities. Pure and low alloy content uranium generally has high levels of texture originating from manufacture [294]. Due to the alternative preparation route for these alloys, culminating in a quench from high temperature, crystallographic texture is expected to be minimal.

3.3.2.4 EBSD

One of the main goals of this chapter was to increase the quality of EBSD maps so that the microstructure of the alloys could be better visualised and understood. The detailed crystallographic relationships that exist within the grains as a result of athermal martensitic transformations during a quench are incapable of being captured by optical microscopy. EBSD maps of the uranium alloys produced by the preparation steps listed previously are shown in Figures 3.21 - 3.25. Maps had previously only been achievable at the University of Bristol through electropolishing followed by extensive FIB milling at grazing incidence angles [221, 223]. Whilst throughout this work, EBSD patterns could be collected from samples that had experienced only mechanical and electropolishing treatments, patterns and maps were far superior when also lightly polished by an argon ion beam. The maps of alloys shown in this chapter have been etched using an argon ion

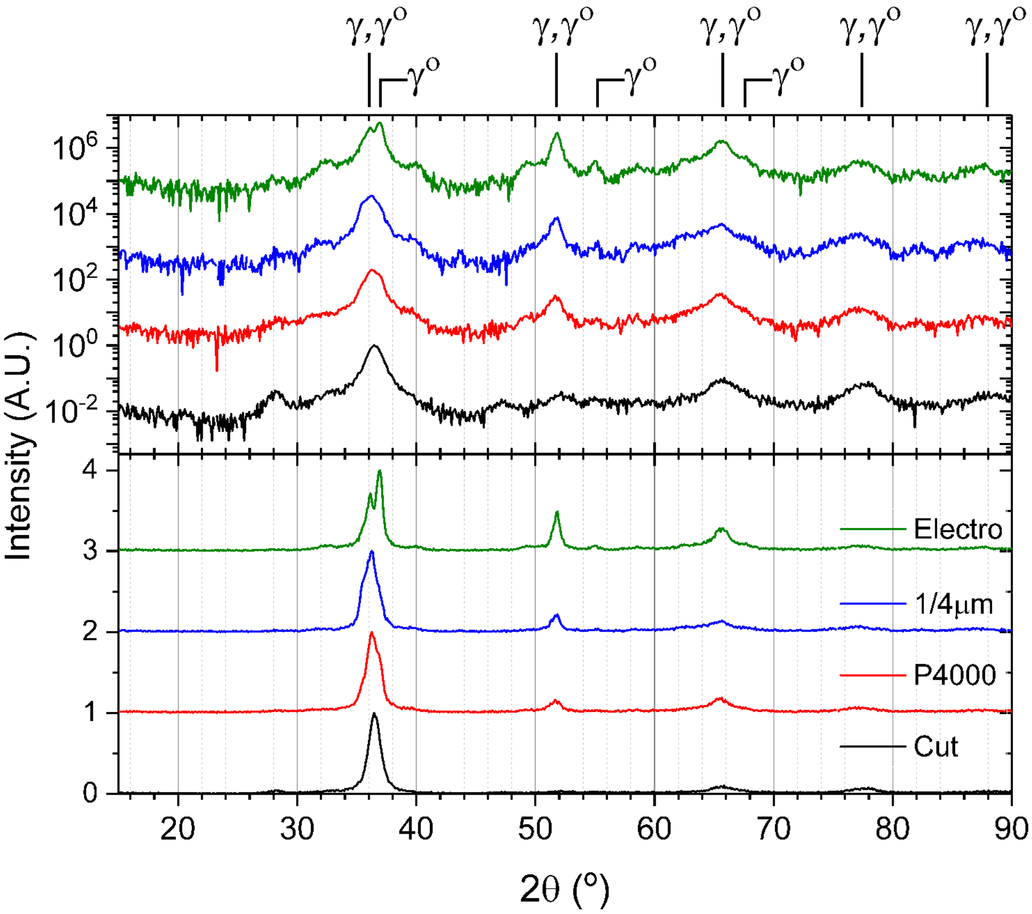

Figure 3.20: X-ray diffraction patterns of the UNb7 alloy throughout the polishing process. The data has been presented twice on different axes with the linear scale shown in the lower panel and a logarithmic scale on the upper panel. The phase resembles a *bcc* structure immediately after cutting using an Accutom-5 fitted with an alumina cutting wheel. With progressive polishing the characteristic γ° phase expected in this material is observable. Weak, higher order γ° peaks, indistinguishable from the background, have not been labelled.

beam operating at 1.5 keV for 30 mins. This low energy ion sputtering was performed to enable XPS measurements of the metal (not shown) having removed away the surface oxide layer.

Carbide inclusions have proved very difficult to successfully map owing mainly to substantially different polishing rates compared to the metal. With UC/UN carbides being etched out and Nb_2C carbides sitting proud, the morphology of the carbides do not lend themselves towards strong indexing, despite high crystallinity producing strong diffraction. However, carbides can be identified in the patterns by the black spots. Identifying the species of carbide is possible by manually controlling the beam onto a flat section of the carbide.

Figures 3.21 and 3.22 show the point of intersection of three or four grains in the UNb5 and UNb6 alloys respectively. Although the α'' phase is the only crystallographic phase in each of these alloys and the mean compositions of the alloys are relatively similar, the microstructure of the two are slightly different with the UNb5 alloy displaying a much more ordered approach to twinning with regular periodicity of twin variants and a high density of secondary twins.

Figure 3.23 shows an EBSD map of the UNb7 alloy. Much larger maps may be produced from this alloy due to the tetragonal γ° phase. Due to the higher crystallographic symmetry compared to the α'' phase, the γ° phase has more of the pattern intensity is confined to fewer Kikuchi bands. The more intense bands permit higher scan rates allowing the quicker collection of maps. However, due to a c/a cell length ratio of close to unity, the γ° phase suffers from the pseudosymmetry problem inducing a detrimental effect on the quality of patterns [185, 291]; the software is unable to properly discern between similar orientations of the γ° phase, e.g. [1 0 0] and [0 0 1]. Instead, the UNb7 alloy has been indexed with the *bcc* γ phase which removes this ambiguity and produce maps that show the microstructure clearly. However, indexing with the γ phase impacts the fidelity of the maps. Figure 3.23 appears to feature many low angle boundaries within grains, suggesting kinking. If indexed successfully using the γ° phase, these intra granular defects would appear as twins (which can produce kinking as viewed by some orientations).

The large EBSD maps of the UNb7 alloy enable an assessment of crystallographic texture in these alloys. From the map shown in Figure 3.24, an IPF showing a relatively even spread of orientations may be constructed, in agreement with neutron diffraction measurements conducted by Brown *et al.* [30]. Though it has not been possible to generate an equivalent IPF for the UNb5 and UNb6 alloys, the mostly common preparation methods suggest that the other two alloys also exhibit minimal textural effects.

Figure 3.25 shows two more examples of EBSD maps obtained from the UNb6 alloy. Despite being of completely different orientations, the microstructures featured appear relatively dissimilar. It is assumed that the slightly different preparation route for the UNb6 alloy which results in chemical banding on the order of roughly 100 μm is contributing to the variety in microstructures [107, 136]. Although not confirmed with EDX or differential interference contrast (DIC) microscopy, it is expected that the left image represents a region with a slightly higher local niobium content than the right image which shares resemblances with the UNb5 alloy map, Figure 3.21.

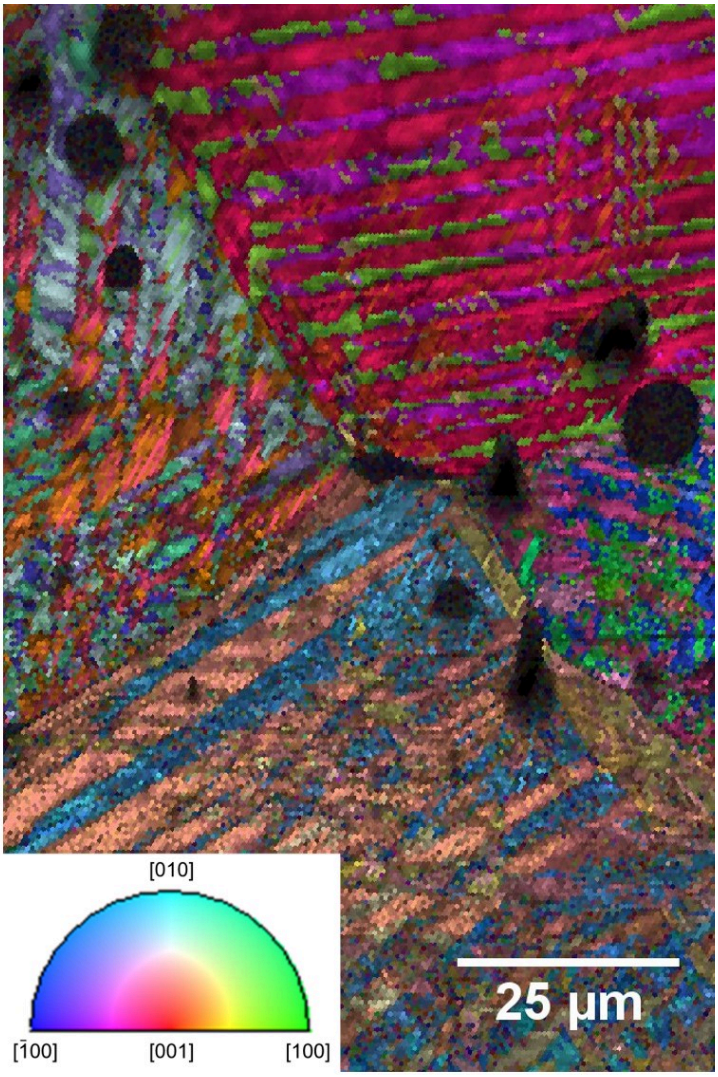

Figure 3.21: EBSD inverse pole figure orientation map of the UNb5 alloy polished at 3.5 V for 20 min. Black spots are un-indexed carbides or pits created by their removal during the electropolishing process. Patterns have been indexed using the ‘unconventional’ phase description as detailed in Chapter 4.

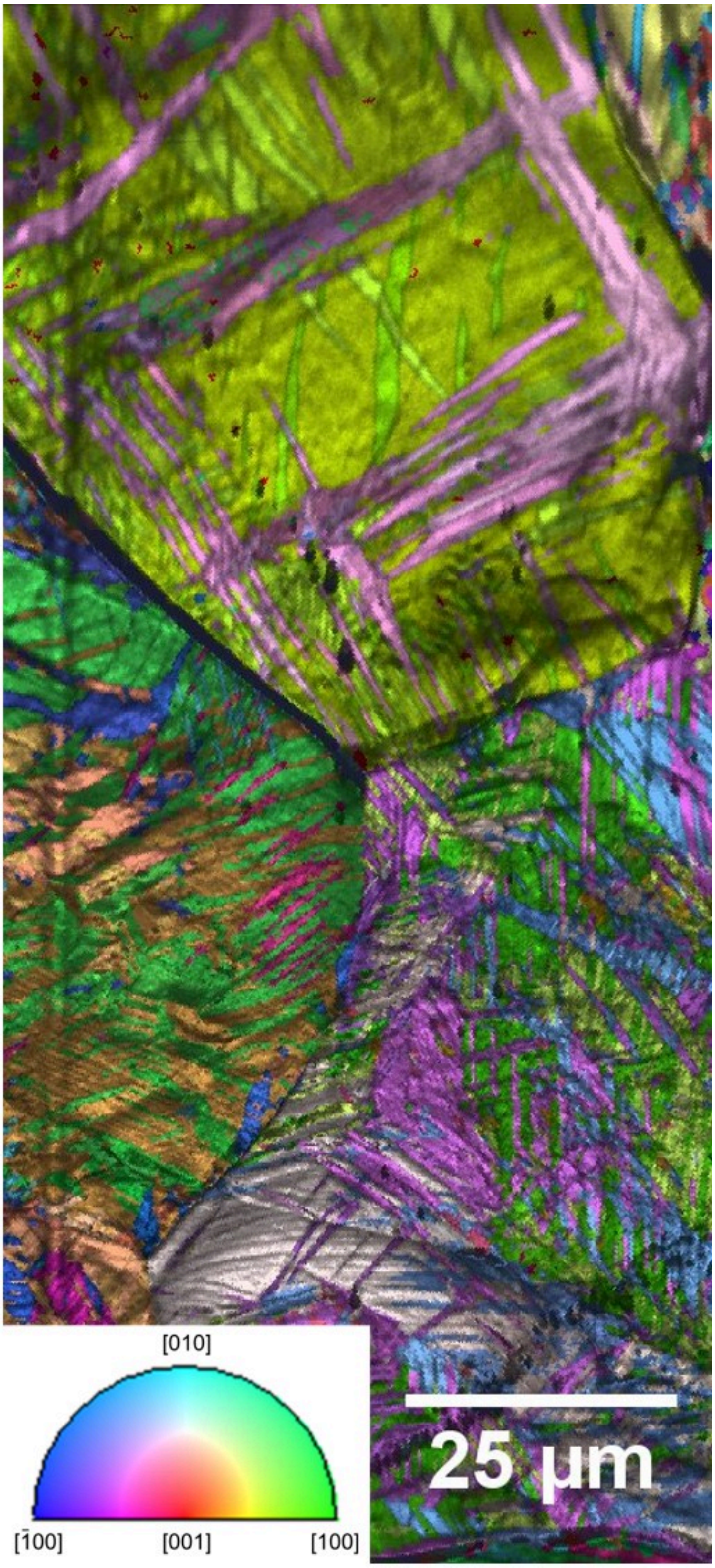

Figure 3.22: EBSD inverse pole figure orientation map of the UNb6 alloy polished at 3.4 V for 60 min. Patterns have been indexed using the 'unconventional' phase description as detailed in Chapter 4.

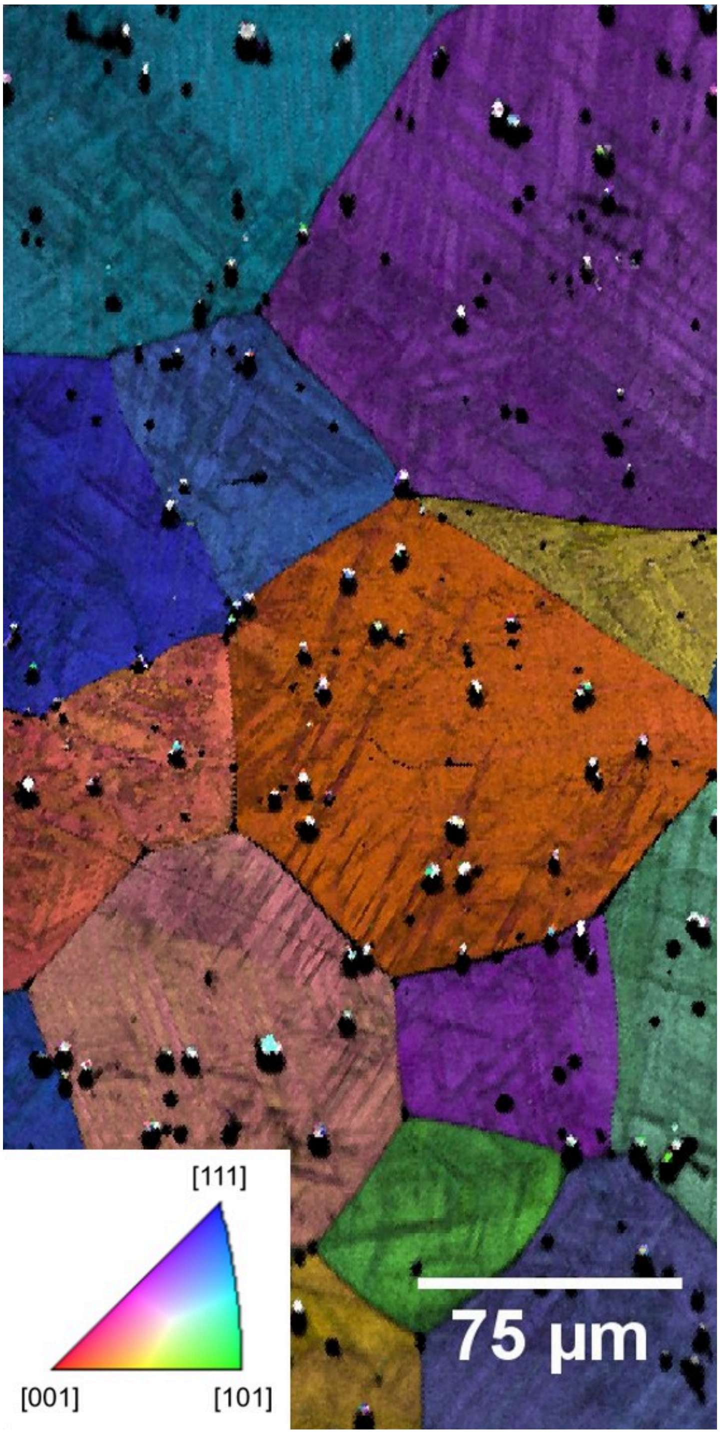

Figure 3.23: EBSD inverse pole figure orientation map of the UNb7 alloy polished at 3.1 V for 20 min. Patterns have been indexed using the γ phase due to negative pseudo-symmetry effects. The result is a map that shows microstructural features more clearly at the expense of intra-granular crystallographic relationships.

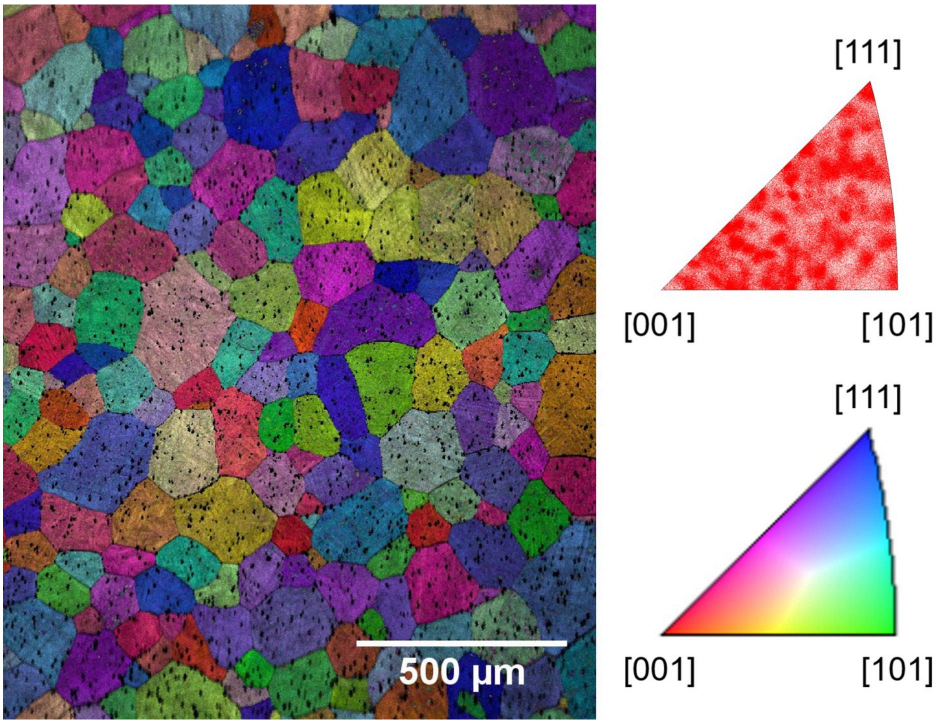

Figure 3.24: EBSD inverse pole figure orientation map of the UNb7 alloy covering a large area. Although the grain sizes are large and only around a couple of hundred grains have been indexed, the inverse pole figure shows a lack of dominating texture.

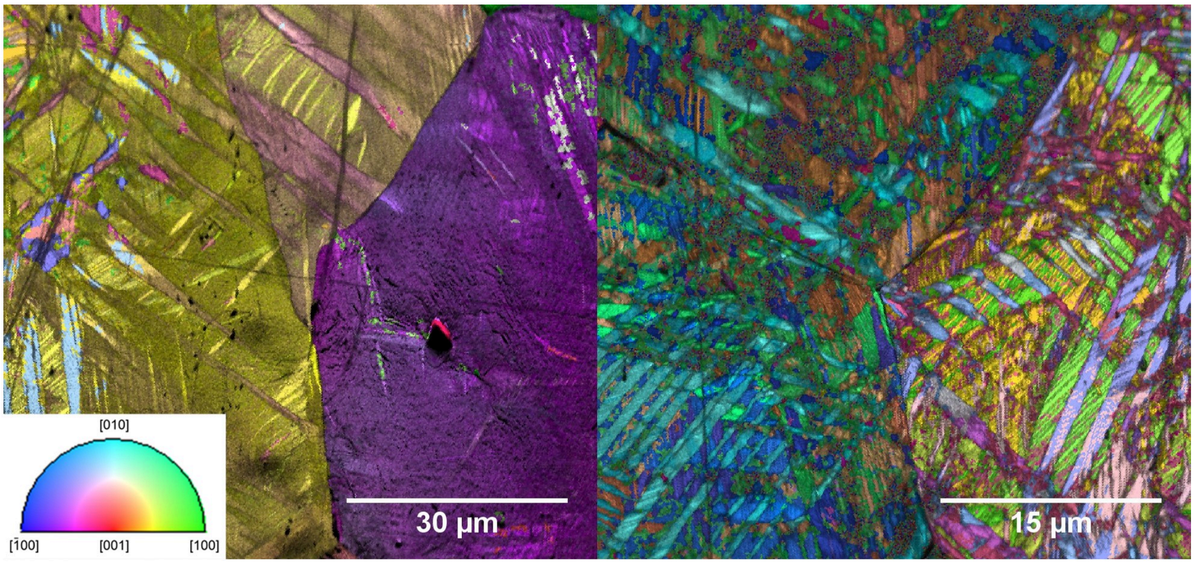

Figure 3.25: Two additional EBSD inverse pole figure orientation maps of the UNb6 alloy showing the apparent heterogeneity in microstructure as a result of crystal structure. The maps have been indexed using the 'unconventional' phase description as detailed in Chapter 4.

3.4 Discussion

3.4.1 Uranium

Analysis of the linear sweep curve and subsequent investigations into chronoamperometric scans at varying polishing potentials showed at least 3 V to be an appropriate polishing potential for this system. Unsatisfactory results were obtained with polishing potentials significantly less than 3 V. The linear sweep curve suggests that the anodic polishing reaction occurs at around 2.75 V, though this is dependent on scan rate. Due to the slow kinetics of the system, chronoamperometry scans teamed with EBSD maps were essential in confirming the suitability of potentials greater than 3 V. At potentials significantly less than 3 V, polishing is not current limited and the treatment is ineffective.

EBSD patterns showed no substantial gains in quality at potentials above 3 V. Higher potentials would be expected to lead to a greater oxide layer and evolve more oxygen bubbles and should therefore be discouraged [151, 164]. It has been shown for other systems that potentials above that required to evolve oxygen can introduce severe pitting [139]. An alternative strategy might be to use chronopotentiometry/galvanostatic conditions, in which, a constant current is applied and the potential is permitted to vary. 25 mA/cm^2 was found to be the limiting current for all potentials above the onset of the anodic polishing reaction, in accordance with previous observations [9]. The potential downside of galvanostatic scans is that changing chemistry or build-up of an oxide layer may lead to large jumps in the potential [42]. Galvanostatic tests were not performed during this study but should be considered as a worthwhile expansion along with the examination of the effectiveness of different solutions.

Despite the formation of a thin oxide layer as part of the polishing process, allowing the dissolution of the layer following the cessation of polishing minimised the residual oxide. However, a very thin oxide layer may still be present on the surface following the dissolution treatment. To compare with the uranium alloys, a pure uranium sample was electropolished and also etched under the argon ion beam. The map generated was excellent following this treatment, Figure 3.26, and pattern quality was substantially higher in regions that had been sputter cleaned compared to those that hadn't. However, the ion beam sputtering may have also been effective at removing an oxide layer that had built up during transit of the sample.

XRD was able to confirm the lack of gross oxide and measure the texture of the metal. Williamson-Hall analysis confirmed relatively low strain present within the material. EBSD shows a variety of microstructural defects which may account for many of the sources of strain in the material. Sin$^2\psi$ data reinforced the notion of small stresses in the bulk that increase towards the sample surface. Since the sin$^2\psi$ method samples a very small gauge volume in uranium at high tilts, the region of increased stress only relates to a small thickness that may be affected by an oxide layer. Non-linear sin$^2\psi$ plots may also be produced by textural effects or shear stresses which induce ψ-splitting behaviour [286]. To investigate these effects would require a much more exhaustive study that would be impracticable given the combination of the sample and equipment to hand. Sin$^2\psi$ testing is efficiently performed on synchrotron and neutron beamlines and would guarantee measurements are independent of the surface state [60, 174, 194]. Performing such a study on uranium however would be a relatively interesting exercise in itself due to its complexity in the crystallographic structure and deformation pathways. Generally, for the purposes of conventional XRD and EBSD experiments, the surface can be seen to be representative of bulk material.

The low-stress surfaces are most noticeable via the high quality EBSD patterns that have been produced in this notoriously difficult-to-prepare material [137, 169]. It has been possible to collect high quality maps on the millimetre length scale, a favourable result given strong texture and large grain sizes [294]. Additionally, relatively rapid scan rates (possible through good EBSD patterns) enable quick collection of sizeable maps that ought to open the door to real-world corrosion and mechanical deformation experiments.

Kikuchi patterns obtained from the uranium specimens in this work are strong with a typical example shown in Figure 3.8. It is expected that it would be possible to perform Cross-Correlation EBSD on similarly prepared samples using the state of the art equipment with optimised settings. Cross-Correlation EBSD would permit the interrogation of stresses around the numerous microstructural features such as twins and grain boundaries.

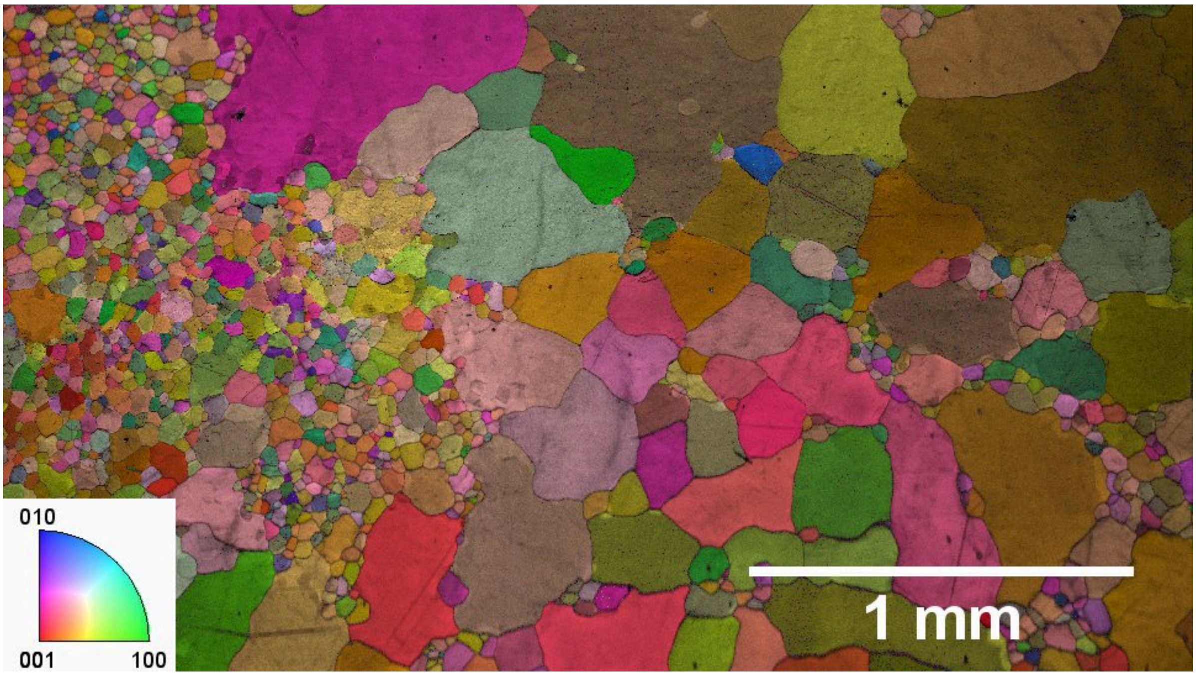

Figure 3.26: EBSD map of a pure uranium sample that has experienced localised annealing resulting in the considerable growth of some grains. This map was collected on the FEG-SEM following electropolishing and argon ion sputtering.

3.4.2 Uranium Alloys

Efforts to better understand and control the electropolishing process in the uranium alloys has resulted in better EBSD patterns than previously producible. There are few examples of UNb alloy EBSD maps in the literature [52, 83]. Currently, the only known examples for the UNb5 and UNb7 alloys have been produced by Scott *et al.* [221, 223]. Though EBSD patterns can be generated following just mechanical and electropolishing, argon ion beam polishing significantly improves the quality. A small layer of oxide is still present on the surface of the alloy as a result of either electropolishing or transfer in air. Avoiding the ion beam polishing step would be preferable as ion beam damage may incur local heating [182] and disruption of local crystal structures [142]. However, 1.5 keV argon ions will have a much reduced effect than the 30 keV gallium ions previously used so this method ought to represent a substantial improvement. Maps may still be improved further through a more thorough diamond polishing step to remove the scratches still present in some of the EBSD maps. Additionally, advancements would include enabling indexing with the true γ° phase and using the conventional setting of the α'' phase.

Ideal linear sweep curves, Figure 3.14 supply evidence for the suitability of the alloy polishing solution. However, it also appears that this combination is more susceptible to oxygen evolution than the pure uranium equivalent, Figure 3.12. There has been no effort to drastically alter the polishing solution, nor explore the oxalic acid based polishing solutions recently reported in the literature [136, 137], in an attempt to extract the compositional dependencies. Given the little information provided on the choice of these solutions it would seem prudent to examine alternatives using the techniques set out here and EIS, which has been briefly discussed. From an environmental viewpoint the uranium alloy solution is preferable to the pure uranium version which includes the toxic ethylene glycol which presents a problem for disposal [137].

Only a handful of electrochemical techniques have been employed in this study creating potential to expand the investigations further. Despite this, the work presented here has succeeded in developing a methodology to assess acceptable polishing conditions. Further experimentation might additionally be benefited by the adoption of the rotating disk electrode (RDE), a standard configuration in electropolishing experiments [190]. The setup used here has permitted much more insight in to the process of electropolishing than would be achievable using previous practises.

It has not been possible to assess stresses in the alloys as was done for the pure uranium samples however, production of high quality EBSD patterns suggests the surfaces produced are mostly free of mechanical deformation. XRD measurements show that electropolishing is capable of removing damage produced by mechanical work and return the surface to a state very close to that of the bulk.

3.5 Conclusions

Initially, using uranium as a surrogate, the electropolishing mechanism of an established solution was investigated. Ideal polishing conditions were assessed to exist beyond 3 V with strong EBSD patterns achievable after 5 - 10 mins of polishing. Large maps covering significant portions of a sample have been produced from samples that were prepared with a quite initially rough surface. XRD was subsequently used to characterise stresses in the surface and confirm the effectiveness of the electropolishing treatment.

The protocol, established using the easier to work with pure uranium samples, was applied to the uranium alloys. Using this setup, some of the most detailed EBSD patterns to date have been produced permitting assessment of the detailed microstructural features inherent within these alloys. The production of strong EBSD maps suggests stresses are minimised using this polishing routine and subsequent studies on the evolving crystallographic features in these alloys are not influenced by preparation.

CHAPTER 4

ASSESSMENT OF THE CRYSTAL STRUCTURES OF THE METASTABLE URANIUM ALLOYS, α'' AND γ^{o}

This chapter examines the crystal structures of the metastable uranium-niobium alloys in the vicinity of the eutectoid composition. A wide range of complex structures manifest themselves over this relatively narrow compositional range and many require further work for a complete characterisation. A full pattern fitting, Rietveld approach has been implemented with the specific objectives of generating suitable space groups that define these phases and describe changes to crystal structure that occur throughout ageing. Another key benefit of this approach is the information relating to atomic coordinates that may be extracted; observing the shuffling of atoms through these transitions is crucial to understanding the driving forces for breaking of symmetries. The work presented in this chapter originates from measurements made on a lab-based diffractometer at the University of Bristol and also the I12 beamline at the Diamond Light Source.

4.1 α'' Phase

4.1.1 Introduction

Uranium possesses fascinating crystallographic structures in its α-U and β-U allotropes. Equally, uranium-rich alloys containing refractory elements, quenched from the high temperature bcc γ phase, produce a continuum of phases, lying between γ-U and α-U. Adding progressively more alloying content, α-U may be modified to adopt metastable orthorhombic (α'), monoclinic (α''), tetragonal (γ°) or cubic (γ^{s}) structures [7, 252]. Quenching by-passes the β-U phase, a tetragonal structure with a very large unit cell and a unique basis, comprising 30 atoms [153].

Lattice parameters of metastable uranium alloy phases have been studied extensively [7, 122, 252]. However, space groups have received much less attention. In 1966, Stewart and Williams were able to generate atomic positions (treating uranium and molybdenum in this case equally) and thereby offer an explanation towards the γ° and α'' phase relationship. Though no space group was proposed, the atomic positions that they determined (particularly that of all atoms sitting on z/c of either 0.250 or 0.750) implied the non-conventional C 1 1 2_1/m space group which Dabush *et al.* and Chakraborty *et al.* have been able to apply to UMo alloys [41, 55]. The author is unaware of any examples in the uranium-niobium binary alloy system where the fits are adequately reported.

This section is focused on determining a model for the structure of the monoclinic α'' phase in the UNb5 and UNb6 alloys. Additionally, there still exists some ambiguity with regards to potential chemical ordering and atomic shuffling within these phases [51, 119, 299]. A full pattern fit can be used to draw conclusions on the possibility of chemical ordering.

The metastable phases share resemblances to high pressure modifications of early lanthanides [14, 45, 160]. Under hundreds of GPa these elements experience a dramatic volume collapse and adopt the α-U structure; behaviour that has been attributed to delocalisation of the $4f$ shell electrons. Existing at room temperature, α-U is the prototype of the orthorhombic Cmcm structure, an arrangement that itself has been attributed to itinerant $5f$ electrons. In the case of neodymium, the transition is continuous, resulting in the adoption of an intermediary monoclinic C2/m phase [45]. Formalising the space group and atomic sites hopes to assist in determining whether the effect of introducing an early transition metal (i.e. partially filled d shell) has the same effect as exerting great pressure on the lanthanides, i.e. delocalizing outer f electrons.

4.1.2 Experimental

A uranium-niobium alloy containing 5.1 %wt Nb (UNb5) was cast and solution heat treated under UHV at 1000 °C for 2 hours. The alloy was held at 850 °C for 30 minutes to promote formation of the high temperature γ phase before being quenched in water to room temperature. Alloys were hot rolled to 50 % of the original thickness before the heat treatment process was repeated. Impurities in this alloy have been estimated as 153±28 wt ppm C, 42±4 wt ppm O and <4 wt ppm N [223]. Results from the UNb5 alloy were compared to those obtained from a UNb6 alloy which displayed the same crystallographic phase, α''.

X-ray diffraction was performed using Cu-Kα radiation on a Philips X-Pert Pro multipurpose diffractometer. The x-ray tube was operated at 40 kV and 30 mA with $\theta/2\theta$ scans conducted between 25 and 90 ° with a step size of 0.025 °. Instrumental broadening was accounted for by calibrating the diffractometer against a LaB_6 standard.

Data were analysed using Rietveld refinement, conducted using GSAS-II [266]. 3D visualisations of the crystal were produced using VESTA [181].

4.1.3 Results

4.1.3.1 UNb5 Alloy

Compared to α-U, the $\angle\gamma$ is observed to open in these alloys with progressively more alloying additions [7, 122, 252]. It is therefore desirable to use a non-conventional space group to allow for a non-90° $\angle\gamma$, rather than the usual $\angle\beta$, and maintain a resemblance to the α-U. Stewart and Williams effectively proposed C 1 1 2_1/m, however a more general structure would be P 1 1 2_1/n as equivalent positions are (x,y,z), (-x,-y,-z), $(\frac{1}{2}+x, \frac{1}{2}+y, \frac{1}{2}-z)$ and $(\frac{1}{2}-x, \frac{1}{2}-y, \frac{1}{2}+z)$. Essentially, this permits the positioning along the c axis to assume values other than z/c=0.25.

Figure 4.1 shows the results of the fitted powder pattern using the P 1 1 2_1/n space group. Similarities between Figure 4.1 and the pattern of α-U may be found in the positions of reflections [148]. However, due to atomic positioning within the cell, intensities of peaks weakly correlate. The pattern shares a likeness with the bcc γ phase, displaying strong peaks at interplanar distances of 2.50, 1.79, 1.44 and 1.25 Å. These peaks are remnants of the structure of the original γ phase pre-quench. There is however no indication of any β-U or γ-U phases present within the alloy.

The weighted residual on the entire pattern (R_{wp}) was minimised at 15.6 %. For the α'' phase, the weighted Bragg factor (RF^2) was minimised at 5.46 % and the un-weighted Bragg factor (RF) equated to 2.77 %. A small amount of surface oxide, UO_2, was present, for which the residuals RF^2 and RF were calculated to be 6.59 % and 3.17 % respectively. Table 4.1 displays the results of the fit. The z/c parameter has been fitted as 0.250(1) which might suggest that the atoms are locked into this quarter position. The data was therefore refitted using the C 1 1 2_1/m structure as has been suggested by a variety of authors [41, 55, 299]. Fitting statistics are almost identical using this configuration with $R_{wp} = 15.6\,\%$, $RF^2 = 5.52\,\%$ and RF = 2.73%. A schematic of the unit cell produced in the refinement is shown in Figure 4.3. The relationship between the α'' and α-U phase is shown in Figure 4.4.

Reducing these statistics was aided by fitting peak broadening using the generalised microstrain model. Besides possessing relatively low crystal symmetry, the α'' phase is inherently martensitic and possesses many crystallographic defects such as twins, kinks and slip. The effect of these deformations is the production of stacking faults along affected directions and a range of peak breadths. Field *et al.* analysed the twin structure of a U-13%at.Nb, and found evidence of $(\bar{1}11)$, (112) and (012) twins [85], with the $(1\bar{7}2)$ and $(1\bar{3}0)$ twins found to be the dominating species. It would therefore be expected that the microstrain distribution is not trivial. Modelling the broadening as an ellipse, using uniaxial terms with a unique axis chosen based on known twinning orientations proved to be insufficient. The resultant microstrain distribution using the generalised model is shown in Figure 4.2. Microstrain can be seen to be relatively constant along the z-direction or c-axis with a relatively uniform value of around 20000. In comparison, microstrain peaks for the $[1\bar{2}0]$ direction and to a lesser extent, the $[110]$ direction. The $[1\bar{2}0]$ direction roughly equates to the $(1\bar{3}0)$ plane (twins). A minimum exists for the $[100]$ direction,

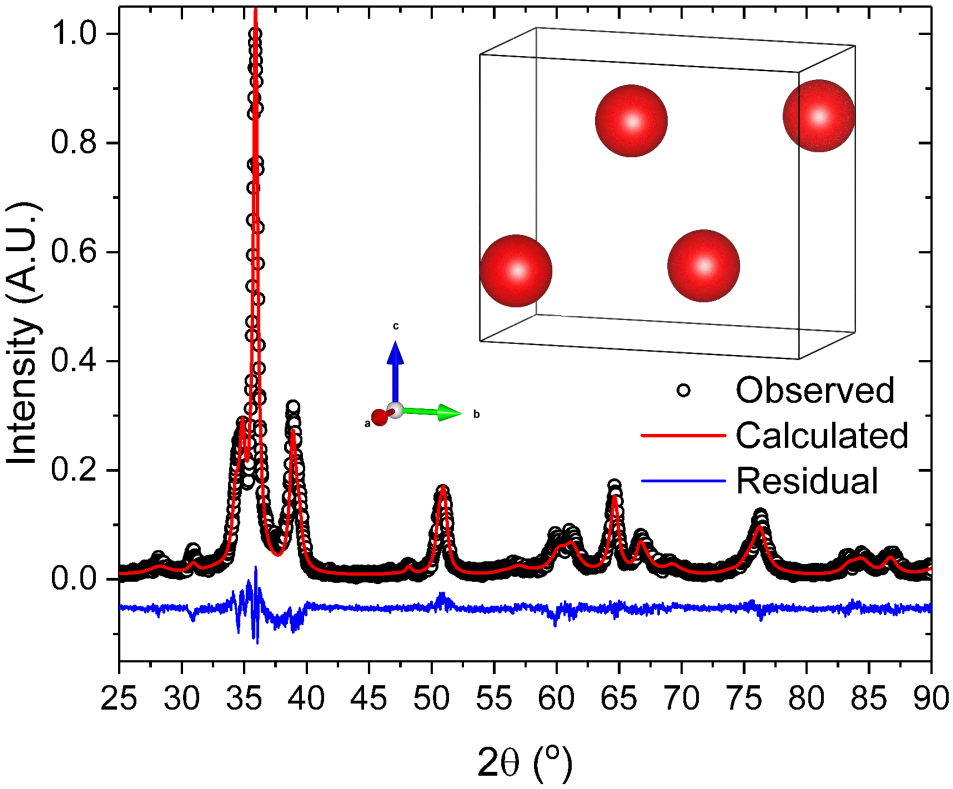

Figure 4.1: Rietveld fitted x-ray diffraction pattern of the UNb5 alloy with the structure shown inset. Lattice parameters were derived to be a = 2.891(4) Å, b = 5.755(8) Å and c = 4.984(7) Å with $\angle\gamma = 91.054(1)\,^\circ$. The pattern has been fitted with anisotropic microstrain and without the requirement of preferred orientation corrections.

suggesting that the a axis is the most stable of the three. The average microstrain for the entire fit is 25900 ($\varepsilon = 2.59\,\%$).

Modelling crystallite domain sizes only was attempted. Axes propagating perpendicular to twin habit planes were approximated as $[13\,\overline{10}\,0]$ and $[6\,\overline{21}\,7]$ for the $(1\,\bar{3}\,0)$ and $(1\,\bar{7}\,2)$ respectively. Both produced plate like shapes best estimated by an equatorial size of 26 ± 2 nm and an axial size of 18 ± 2 nm. Though crystallite size modelling produced a similar pattern residual, R_{wp}, the phase residuals were significantly worse than using the microstrain model.

Additionally, atomic disorder scattering factors, U_{ij}, were modelled anisotropically. These were found to be dominated by U_{11} and to a lesser extent, U_{33} and U_{12}. Respectively, these were 0.036(3), 0.012(2) and 0.015(2) with the others equalling zero. These values are large when compared to a single crystal of α-U, 0.0083(2), 0.0063(5), 0.0069(3) [148], but probably to be expected, given the extremely stressed crystal environment present in the material. The

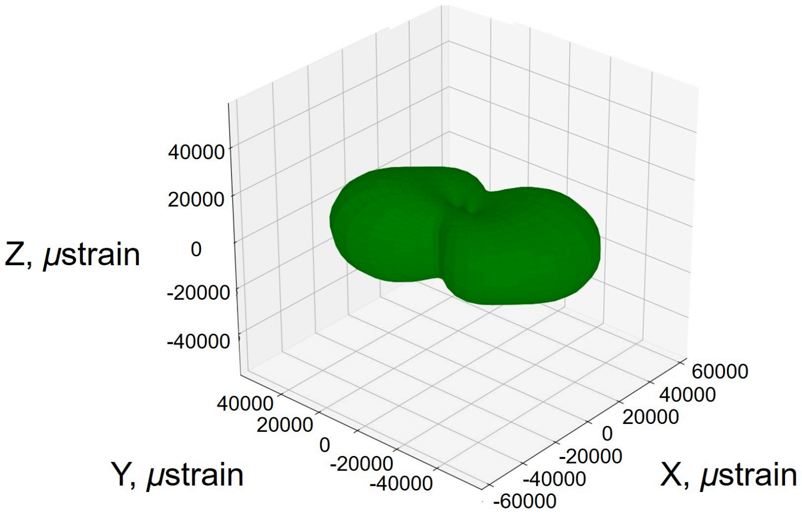

Figure 4.2: Microstrain profile of the UNb5 alloy as derived from the fitting of Figure 4.1. The surface is defined by the unit cell vectors so for instance the x and y axes shown here are bisected by the [1 1 0] vector and the microstrain for that point is plotted.

covariance matrix suggested that the fitting of anisotropic microstrain and atomic disorder concurrently had little effect on each other. The P 1 1 2_1/n solution found the U_{13} and U_{23} to be negligible contributors. The slightly higher symmetry of the C 1 1 2_1/m phase automatically defines these parameters to be zero which is quite strong evidence that this is the correct space group as the atoms are locked in at $\frac{1}{4}$ sites.

Given the non-conventional P 1 1 2_1/n space group, the structure of the most basic conventional unit cell would be useful in many cases. Converting to the P2_1/c space group altered the cell lengths to a = 2.891(4) Å, b = 4.984(7) Å and c = 6.397(8) Å. b becomes the unique axis with $\angle\beta = 115.8(1)^\circ$. Since this cell is effectively doubled along the c axis, the cell may be halved at $c/2$. The reduced cell may be rewritten as in the P 2_1/m space group with a doubled z/c. The parameters of this unit cell are shown in Table 4.1.

4.1.3.2 UNb6 Alloy

The same P 1 1 2_1/n and C 1 1 2_1/m models have been applied to the UNb6 alloy. The result of the P 1 1 2_1/n fit may be seen in Figure 4.5. The pattern of UNb6 strongly resembles that of UNb5 with the most noticeable difference being the further separated $(\bar{1}10)$ and (1 1 0), and $(\bar{1}11)$ and (1 1 1) reflections, resulting from a wider $\angle\gamma$, and a reduction in intensity of higher order peaks.

The pattern and phase residuals were quite similar to those obtained for the UNb5 alloy. The weighted pattern residual, R_{wp}, was 13.1% and the Bragg factor residuals were 5.80 and 2.83% for RF and RF^2 respectively. UO_2 was not detected in any significant quantities to warrant application of it as a refineable phase. A key difference between the UNb6 and UNb5 alloys is

	U	UNb5 (1)	UNb5 (2)	UNb5 (3)
a/Å	2.854	2.891(4)	2.8903(5)	2.891(4)
b/Å	5.870	5.755(8)	5.757(2)	4.984(7)
c/Å	4.955	4.984(7)	4.9828(8)	3.198(4)
$\angle\beta/^\circ$	90	90	90	115.79(1)
$\angle\gamma/^\circ$	90	91.054(1)	91.060(1)	90
x/a	0	0.965(1)	0.966(1)	0.860(1)
y/b	0.1025	0.1065(4)	0.1063(4)	0.250(1)
z/c	0.25	0.250(1)	0.25	0.7848(4)
R_{wp}/%	-	15.6	15.6	-
RF^2/%	1.6	5.46	5.52	-
RF/%	1.3	2.77	2.73	-
S.G. No	63	14	11	11
Setting	Cmcm	$P\,1\,1\,2_1/n$	$C\,1\,1\,2_1/m$	$P\,2_1/m$

Table 4.1: Results of the fitting of Figure 4.1 using a Rietveld refinement fitting procedure. Values for α-U are taken from Lander *et al.* [148]. Fitting statistics have not been reported for UNb5 (3) as the structural parameters shown here have been derived from UNb5 (1) via symmetry operations.

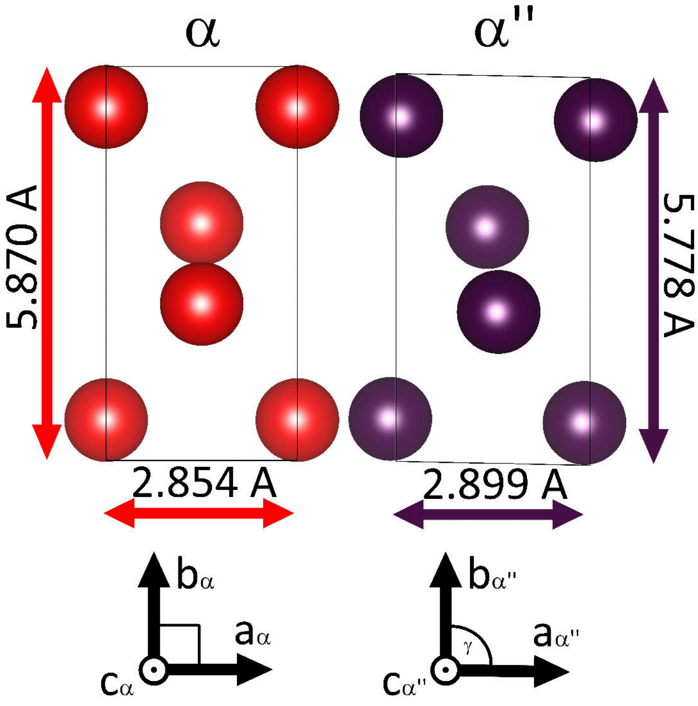

Figure 4.3: Crystallographic structure of the α and α'' phases viewed down the [0 0 1] directions. As uranium and niobium atoms are in solution without any ordering, both atomic species are coloured the same colour (purple) for clarity.

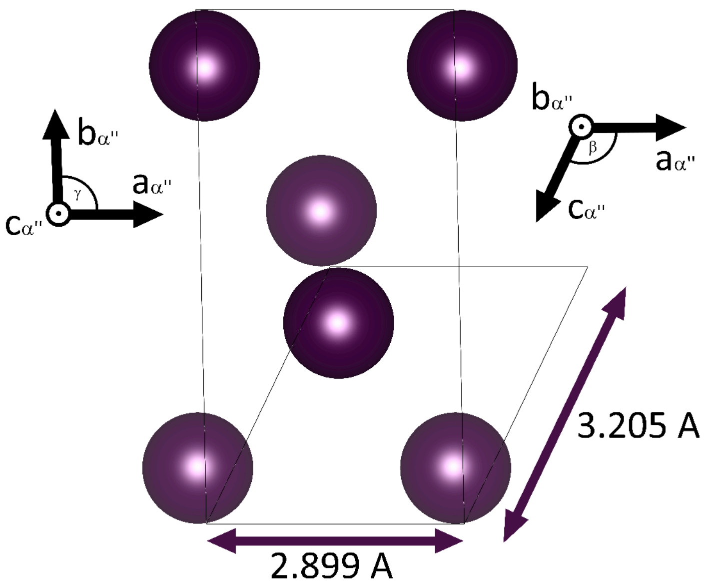

Figure 4.4: Comparison of the crystallographic structure of the α'' phases in each of the two space group definitions.

that when fitting using the P 1 1 2_1/n approach, the z/c parameter was fitted to 0.244(3), not 0.25 as was the case in UNb5. Though the difference here is small, this may suggest that the C 1 1 2_1/m is not the correct description in this case and with compositions closer to the γ° boundary. The residuals were slightly worse as a result of pinning the atoms to $\frac{1}{4}$ sites using the C 1 1 2_1/m description, $R_{wp} = 13.1\,\%$, $RF^2 = 6.50\,\%$ and $RF = 4.46\,\%$.

Likewise for this sample, the pattern was fitted with anisotropic microstrains which manifested themselves in a distribution shown in Figure 4.6. Consistent between the two samples is the large microstrain along the $[1\bar{2}0]$ direction which has previously been attributed to $(1\bar{3}0)$ twinning. However, there are additionally, large contributions in the [0 0 1] and [1 1 0] directions. There are reasons to suggest that these may not necessarily be genuine observations, the [0 0 1] corresponds to the (0 0 2) reflection which overlaps significantly with the (0 2 1) peak. The (0 2 1) peak has been fitted with a much narrower peak, and since both have similar integrated intensities it appears as if the program has used the two reflections to generate its own 'pseudo-Pseudo Voigt profile'. Additionally, the [1 1 0] direction closely corresponds to the (2 1 0) peak which is an un-allowed peak in this space group setting. Geometrically, the closest peaks are the (2 1 1) and $(\bar{2}11)$ reflections, which are comparatively weak and located in the high density of similar intensity peaks between 65 and 70°. Average microstrain is 30000, 16% higher than the UNb5 alloy. Using C 1 1 2_1/m, the equivalent was 35800 which represents a 38% increase.

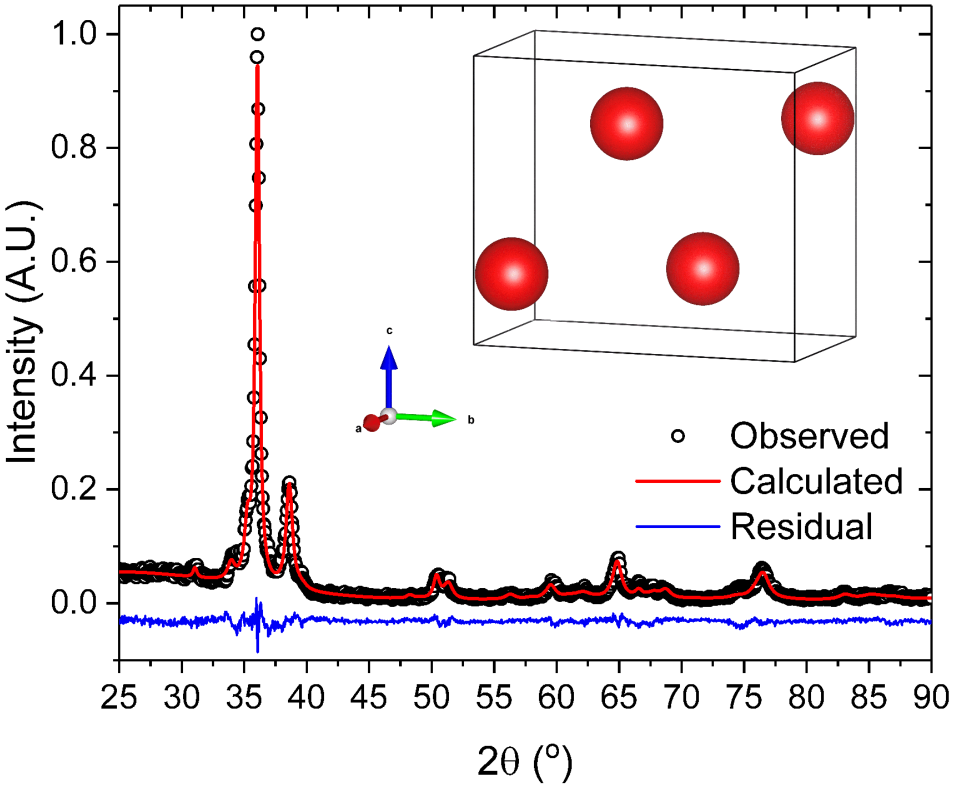

Figure 4.5: Rietveld fitted x-ray diffraction pattern of the UNb6 alloy with the structure shown inset. Lattice parameters were derived to be a = 2.900(1) Å, b = 5.755(2) Å and c = 4.975(2) Å with $\angle\gamma = 92.6034(1)\,°$. The pattern has been fitted with anisotropic microstrain and without the requirement of preferred orientation corrections.

4.1.4 Discussion

Residuals resulting from the fit point towards a good estimation of the structure, which is ultimately limited by the material's poor crystallinity and the quality of data. Fitting was successful without the requirement for the modelling of texture. It is common practice to reheat worked uranium to the β-U or γ-U phase before quenching to remove texture [294]. This alloy was heated to 850 °C before quenching which should have removed all preferred orientation. Given that the effective sampling area can be estimated at about ~0.5cm^2 and the grain size is typically 100-200 μm in diameter, roughly 3000 grains will have been sampled. Given that each grain is subdivided by numerous sub-grains, the number of coherent crystallites effectively rises dramatically.

Adequate fitting of the pattern with no additional, unaccounted-for peaks indicates no evidence of chemical ordering or secondary phases that have sometimes been suggested in the

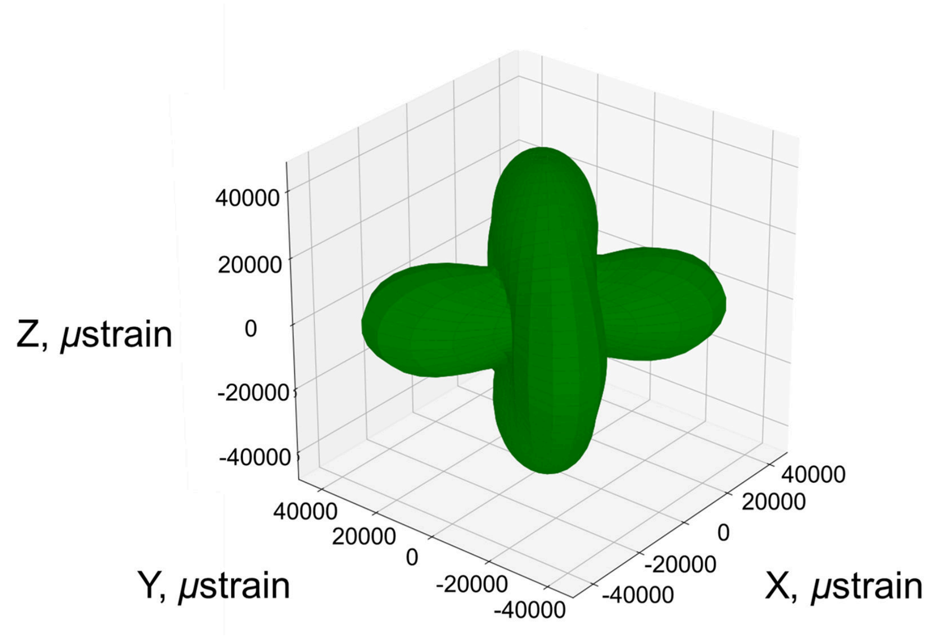

Figure 4.6: Microstrain profile of the α'' phase of the UNb6 alloy as derived from the fitting of Figure 4.1.

literature [119, 299]. The pattern has been modelled using a completely random distribution of constituent elements in a substitutional arrangement.

Confidence in the fitting of microstrain may be derived from knowledge of the twinning mechanisms permitted in the material. The fact that microstrain is maximised for the $(1\bar{3}0)$ plane is promising, though this is not also seen for the $(1\bar{7}2)$. The $(1\bar{7}2)$ reflection exists at unreachable values of 2θ and the closest planes producing intense reflections may be incapable of effectively capturing the broadening. The $(1\bar{3}0)$ plane in comparison is represented in the pattern and is the only significant peak in its vicinity at 57.1°. Field *et al.* suggested that the $(1\bar{7}2)$ twins are secondary and form within $(1\bar{3}0)$ twins [85]. It may be that in this material they are not very prevalent or contributing to a smaller extent, or that the bulge created by the $(1\bar{3}0)$ reflection is hiding the broadening of the $(1\bar{7}2)$ reflections. The use of the microstrain model meant that information regarding the crystallite sizes was difficult to extract. As both have similar effects on the shape of peaks (Lorentzian broadening, where size is constant with angle and strain increases with angle, in the isotropic cases), the two sets of fitting parameters influence each other. In this case, as the microstrain model produced a better fit and literature provides estimates on the coherency of the microstructure, crystallite size was not modelled to prevent over-fitting of the data.

Lattice parameters obtained in this study complement Jackson's findings for 5 and 6 wt.%Nb alloy [122]. Examining a 10 at.%Mo alloy (5.2 wt.%Mo), Stewart and Williams determined that atoms sit at fractional coordinates of (0.964, 0.102, 0.25) [241]. Based on the y/b parameter, this

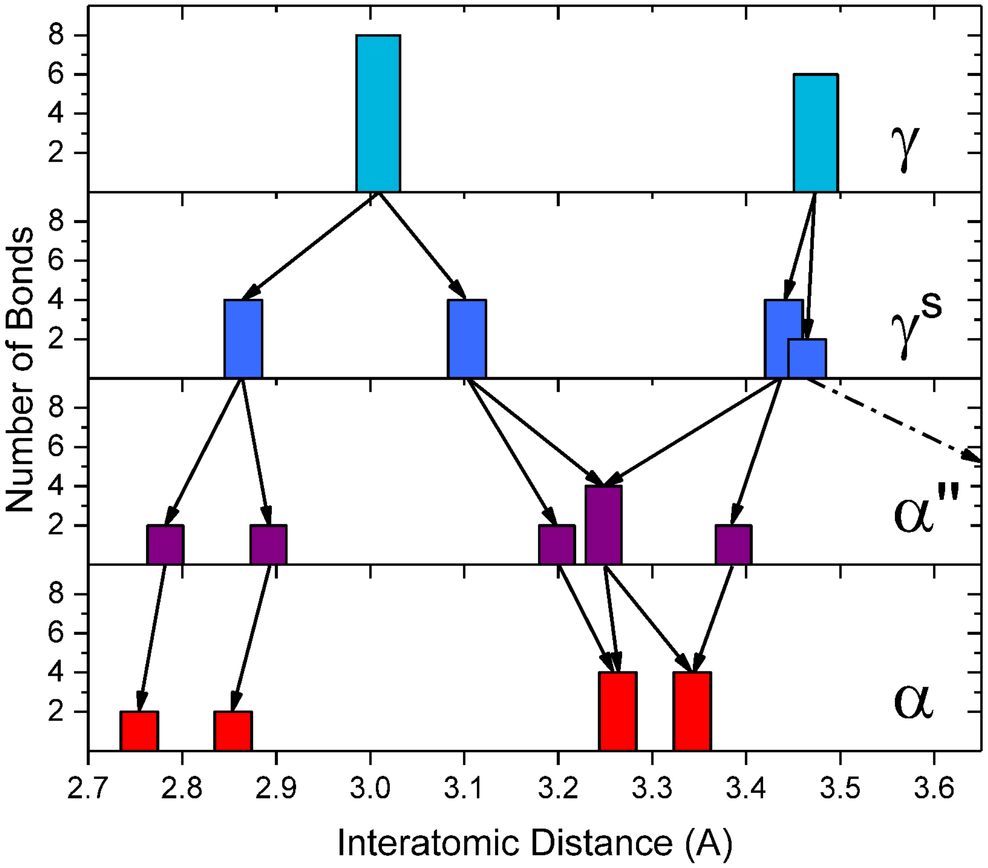

Figure 4.7: Interatomic distances of α'' phase nearest neighbour atoms with equivalent data for α [148], γ^s [293] and γ [122] phases as detailed in the literature, displayed for comparison.

suggests that the 5.2 wt.%Mo alloy is further from the α-U structure than that of the 5 wt.%Nb alloy. This is to expected as it is known that Mo is superior to Nb in stabilising the metastable phases. The fit in this study yields a better RF than previous works (RF = 15.2%) [241]. The ability to obtain a better fit may have been limited by the anisotropic distribution of peak widths.

Given that z/c was found to be extremely close to 1/4, it is probable that the atoms have locked into these quarter sites, at least in the case of the UNb5 alloy. Whether this is also true for the compositions closer to the γ^o phase boundary remains to be seen. It may well be that 1/4 sites are characteristic of the phase and the C 1 1 2_1/m space group may be used, as Brown *et al.* have done [30]. Presently however, the conservative P 1 1 2_1/n space group permits the alteration of this parameter without disrupting the atomic density, thereby offering more flexibility.

Figure 4.7 suggests a continuous progression in the interatomic distances of nearest neighbours. The formation of the α phases sees a nearest neighbour of the γ phase, shuffle sufficiently to become a next-nearest neighbour. The shortest bond length is observed to increase, in contrast to β-U, which retains a very short bond of 2.78 Å. This may give credence to the notion that the 5*f* states, which feature heavily in the bonding of uranium, are likely to tend towards localization with increasing alloying content.

4.1.5 Conclusion

The P 1 1 2_1/n space group has been determined to be the preferable space group convention for the UNb5 alloy. This space group should be extended to all uranium alloy systems where a substitutional arrangement is favourable and the α'' phase is exhibited. This work has additionally shown that there is no evidence for chemical ordering in these alloys.

4.2 γ° Phase

4.2.1 Introduction

Literature is in good agreement that the tetragonal γ° phase starts in this system at roughly 16 % at. Nb (6.9 % wt. Nb). Aided by the results of Anagnostidis and Tangri, Jackson showed that 21 % at. Nb is the onset of the metastable γ phase with cubic symmetries [7, 122, 252]. Within this range, the γ° unit cell is described as a 'supercell' structure comprising 4 γ-like cells that have been compressed in the *c* direction and experience shuffling of the centred atoms. The effect of this is weak-'super lattice' reflections emerging at otherwise unallowed positions. Jackson does not take the opportunity to estimate the magnitude of the shuffling of these atoms [122].

A year earlier though in 1969, working on a U-16.60 at% Nb-5.64 at% Zr alloy aged at 150 °C for 2 hours, Yakel also noticed these diffuse reflections and decided to redefine the γ° unit cell [293]. Increasing the *a* and *b* axes by $\sqrt{2}$ with respect to the *bcc* unit cell was shown to be sufficient to account for the weak 'super-lattice' reflections. Yakel's alloy had lattice parameters of $a = 4.948(5)$ and $c = 3.371(2)$ Å. Referring to Figure 4.12, this puts the alloy very close to the γ° to α'' transition. Additonally, Yakel was able to suggest a space group, P4/nmm, and calculate the atomic positions from peak structure factor intensities. Yakel was additionally able to discount chemical ordering in this phase as it had been suggested as a possibility for this phase a few years previously by Tangri. The resultant structure is shown in Figure 4.8.

In the years since, the majority of authors have adopted Tangri's definition of the $\sqrt{2}$ expanded γ° phase. However, Yakel's phase shown in Figure 4.8 is slightly strange. Owing to the 2 different atomic sites, the structure effectively has two different atomic environments depending on their positions within the cell. Atoms on the *ab* faces exhibit much more order than those half a unit cell displaced along the c axis.

Few studies which include the crystallography of this phase have used quantifiable fitting. Fewer still have fully reported their results when using a technique such as Rietveld refinement. Many of the early works on this topic were published around the time of Rietveld's seminal

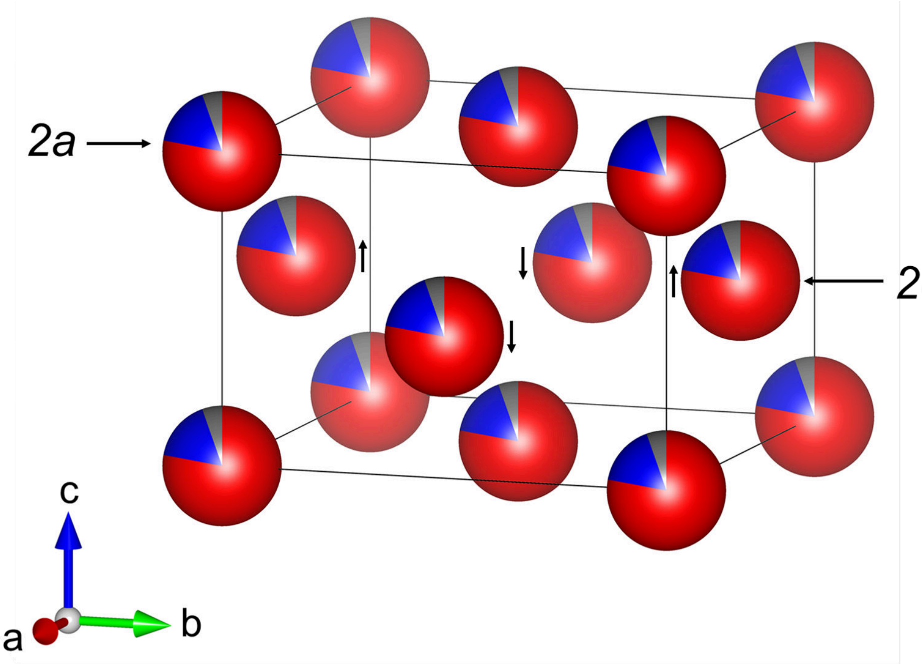

Figure 4.8: Structure of Yakel's U-16.60 at% Nb-5.64 at%Zr alloy [293]. There is no chemical ordering in this structure, atoms are randomly distributed. Atoms are coloured to reflect the constant probability of finding uranium (red), niobium (blue) and zirconium (grey) at any position. *2c* atoms on the (100) plane have been displaced by $z/c = 0.05$ along the c direction whereas the atoms (011) plane are anti-correlated and are displaced by the same magnitude in the opposite direction. Coordinates of the *2a* and *2c* Wyckoff positions are (0, 0, 0) and (0.5, 0, 0.5-z/c).

article on full pattern fitting in 1969 and so at the time, the technique was not very widespread or developed. This section seeks to investigate the UNb7 alloy using the Rietveld technique to obtain information regarding lattice parameters, atomic positions and microstrain so that the material may be initially characterised and the effects of ageing may be understood.

4.2.2 Experimental

A uranium-niobium alloy containing 7.1 %wt Nb (UNb5) was cast and solution heat treated under UHV at 1000 °C for 2 hours. The alloy was held at 850 °C for 30 minutes to promote formation of the high temperature γ phase before being quenched in water to room temperature. Alloys were hot rolled to 50 % of the original thickness before the heat treatment process was repeated. Impurities in this alloy have been estimated as 153±28 wt ppm C, 42±4 wt ppm O and <4 wt ppm N [221].

Data from the I12 beamtime was used for the initial characterisation and assessment of space groups for the UNb7 alloy. Since UNb7 has the potential to be work-hardened and crystallographically deformed during mechanical polishing, the bulk-sensitive transmission data obtained using 112 keV x-rays in a Debye-Scherrer geometry was used. This mitigated against

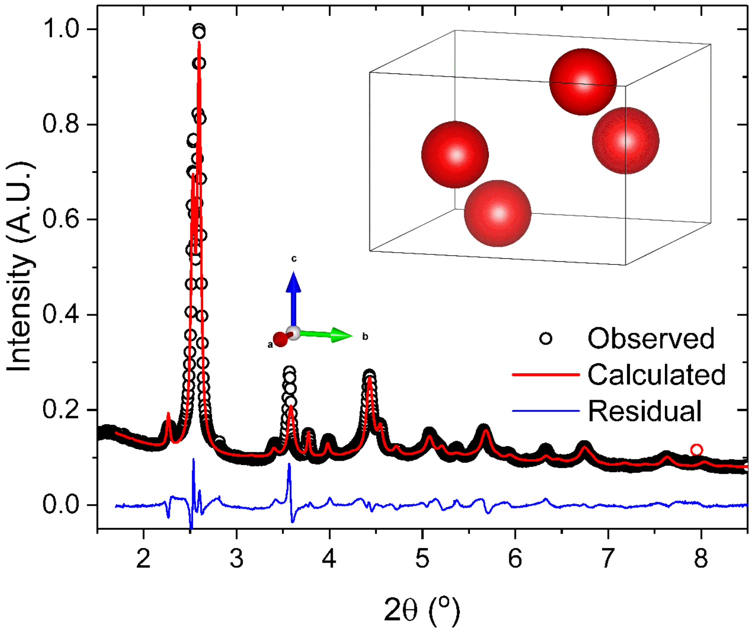

Figure 4.9: Fitted pattern of the UNb7 alloy using the P4/nmm space group. The cell is represented in the inset using the $P\bar{4}m2$ centering convention, thereby differing from Yakel's original model.

any possibility of preparation negatively affecting the results. Additionally, the data is collected on a 2D detector enabling visualisation of preferred orientation in the sample. Since the widest reliable slit settings available were 200 × 200 μm, a large grid was scanned over and frames summed to make an effective area of 2 × 2 mm.

4.2.3 Results

Fitting the UNb7 powder data with the P4/nmm space group suggested by Yakel produced a reasonable estimation of the lattice parameters. The suitability of a few other space groups based on the 4/mmm point group were trialled for this phase. These included $P\bar{4}m2$ and $I\bar{4}m2$ as these are the tetragonal derivatives of the $I\bar{4}m3$ space group that Yakel proposed for the γ^{s} phase.

Fit statistics were $R_{wp} = 5.92\,\%$, $RF^2 = 8.70\,\%$ and $RF = 5.70\,\%$ using the P4/nmm space group, whereas the $P\bar{4}m2$ phase produced slightly better fit statistics of $R_{wp} = 5.37\,\%$, $RF^2 = 6.67\,\%$ and $RF = 4.61\,\%$. Both fits used the same suite of variables and degrees of freedom, which included preferred orientation corrections, though the effects proved to be minimal. Using the generalised microstrain model, the distribution was relatively isotropic, in each case producing a mean value of around 29500 ($\varepsilon = 2.95\,\%$). The results for the fitted lattice parameters were quite close for each phase, although there was minor discrepancy that was not accounted for by the calculated errors.

The benefits of using the $P\bar{4}m2$ space group are extra otherwise unallowed reflections in the

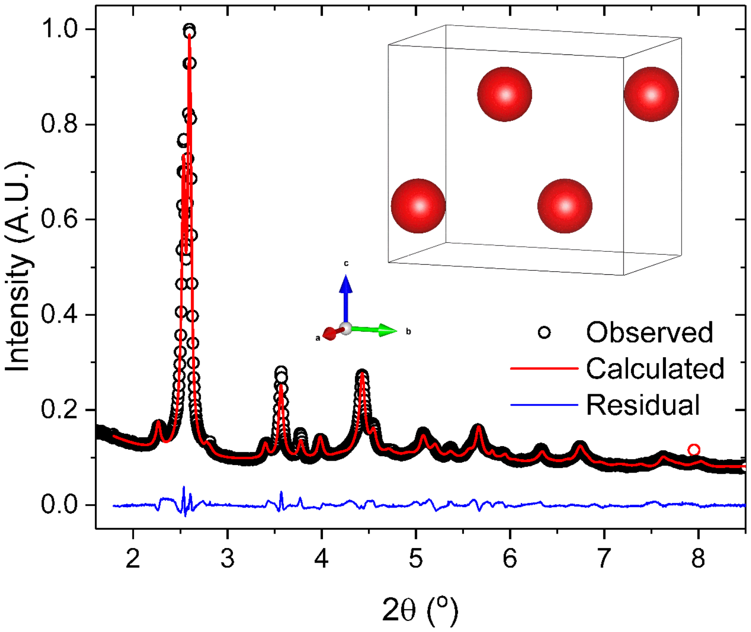

Figure 4.10: Fitted pattern of the UNb7 alloy using the P112$_1$/n space group.

case of P4/nmm and degrees of freedom in atomic displacement parameters. Notably, the P$\bar{4}$m2 space group permits the (210) reflection to manifest in the pattern, albeit rather weakly. In the scale of the pattern shown in Figure 4.9, this reflection exists at a 2θ position of 2.82°, forming the right hand shoulder of the initial doublet that is poorly accounted for using the P4/nmm structure. Both solutions produced very similar estimates of the displacement to Yakel's *2c* atom. P$\bar{4}$m2 produced z/c = 0.4457(23), whereas for P4/nmm using the conventional setting as shown in Figure 4.9, z/c was 0.0534(18), corresponding to 0.4466(18) using Yakel's definition.

The P$\bar{4}$m2 fit generated a value of U_{11}= 0.156(11) for the *2g* atom (*2c* in Figure 4.8) and U_{33}= 0.250(28) for the *1b* atom (the base centred *2a* atom in Figure 4.8. In comparison, the P4/nmm produced U_{33}= 0.139(14) for the *2a* atom. All other values for the remaining atoms in each of the space groups were very close to zero when errors were considered. The large disorder along the *a* axis for the *2g* atom is a direct consequence of the inclusion of the (210) reflection. The P4/nmm structure is not driven to affect this variable in the same way without this peak.

Attempts to fit a model that did not exhibit the two layer structure, as in the case of P4/nmm, were unsuccessful. The I4$_1$ space group could be used to generate a similar structure to Yakel's, but it was unable to generate the diffuse superlattice reflections required. Using the P4 space group, no improvement could be made over the P4/nmm and P$\bar{4}$m2. In fact, due to the numerous reflections with intensities that were essentially zero, the phase statistics were very poor.

As a test, the pattern was also fitted with the α'' phase. Fitting with the P112$_1$/n α'' phase pro-

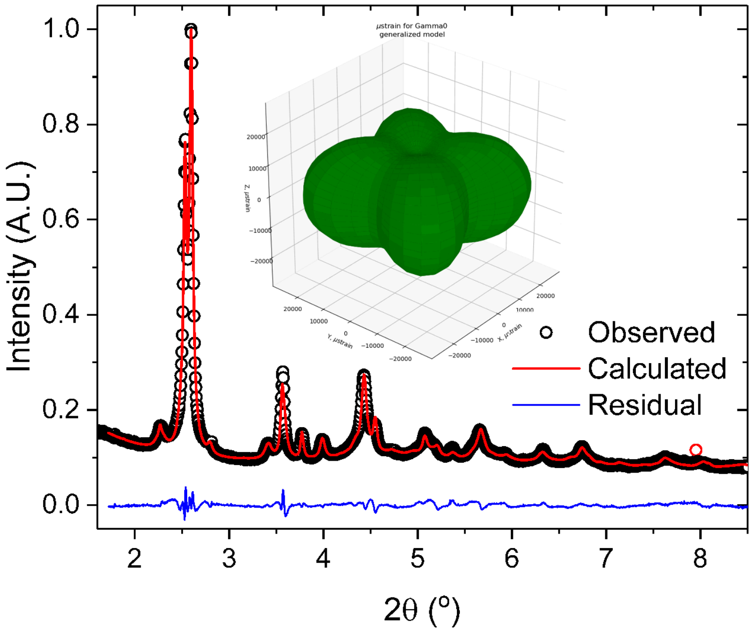

Figure 4.11: Fitted pattern of the UNb7 alloy using both the α'' and γ° phases. Plot inset shows the microstrain distribution for the dominant γ° phase.

duced statistics of $R_{wp} = 4.85\,\%$, $RF^2 = 7.06\,\%$ and $RF = 5.96\,\%$. This is shown in Figure 4.10. The lattice parameters produced using the α'' phase fit were $a = 3.040(2)$, $b = 5.6370(6)$, $c = 5.0055(7)$ and $\angle\gamma = 97.13(4)$ and are shown in dark green on Figure 4.12. Fitting with both phases produced the best overall result with $R_{wp} = 3.51\,\%$, $RF^2_{\alpha''} = 10.54\,\%$, $RF_{\alpha''} = 5.72\,\%$, $RF^2_{\gamma^{\circ}} = 6.66\,\%$ and $RF_{\gamma^{\circ}} = 4.06\,\%$. The fit of this scenario is displayed in Figure 4.11. The weight fraction of the α'' phase was determined to be 36.4 % which would explain why the phase statistics for this phase have worsened. The lattice parameters produced using both phases were $a_{\alpha''} = 3.007(3)$, $b_{\alpha''} = 5.704(5)$, $c_{\alpha''} = 4.986(5)\,\text{Å}$, $\angle\gamma_{\alpha''} = 95.67(5)^{\circ}$, $a_{\gamma^{\circ}} = 4.9875(6)$, $c_{\gamma^{\circ}} = 3.3510(5)\,\text{Å}$. The lattice parameters for both phases are shown in light green in Figure 4.12. Using the α'' phase caused the mean microstrain of the γ° to be reduced to 20400, whilst for the α'' this rose to 43100.

4.2.4 Discussion

The mixed phase solution of $\gamma^{\circ} + \alpha''$ produced what appears to be the strongest result. No attempt to fit the pattern solely with a γ° phase was able to reproduce some of the more subtle aspects of the data, such as the shoulder at $2\theta = 2.87\,^{\circ}$. The α'' phase was calculated to be the secondary phase in the pattern, which is promising, as the pattern can easily be identified by inspection as predominantly γ°.

Although the UNb7 sample had been fabricated in 2007, it is thought that no ageing has

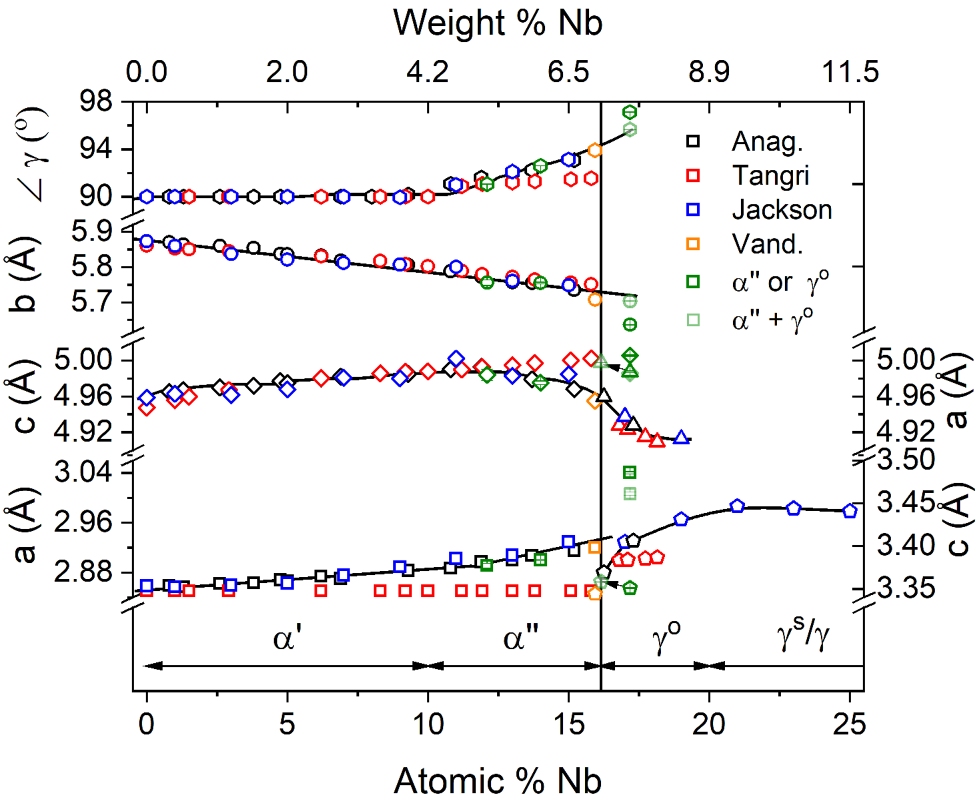

Figure 4.12: Composite plot of the variation of lattice parameters in the uranium-niobium alloy system as drawn from the sources of Anagnostidis *et al.*, Tangri and Chaudhuri, Jackson and Vandermeer [7, 122, 252, 275], and the values obtained in this chapter for the UNb5, UNb6 and UNb7 alloys.

been applied in this time. This would imply that either the sample has progressed to a two phase mixture over time, as according to the majority of the literature, this composition should be fairly safely within the γ° phase, or that original works in the literature failed to detect the α'' phase without the developed tools of Rietveld refinement and anisotropic microstrains. This in turn would suggest that the γ° to α'' phase boundary is not sharp but a smoothed out transition.

Vandermeer's 1985 report detailing the behaviour of this system below room temperature took 9 alloy compositions between 6.4 and 7.2 % wt. Nb and determined $\alpha'' : \gamma^\circ$ phase fractions using a 'peak unfolding procedure'. Vandermeer showed that between 5.8 and 7.0 % wt. Nb, the γ°:α'' phase fraction rose linearly at room temperature. The result here would be complementary to Vandermeer's study, however, not completely consistent, as compositions do not predict the same phase fraction. For example, Vandermeer would predict that the UNb6 alloy contains 16 % γ°, whereas the previous section showed that this alloy can be described as entirely α'' phase.

Reasons for the discrepancy may include manufacturing practices, impurities, ambient ageing or fitting sensitivity: Vandermeer looks to have used a relatively basic approach to widths and fixed structure factor constants, thereby not permitting atomic positions to vary. However, Vandermeer agrees that the relationship between composition and crystallographic phases is not characterised by a discontinuous boundary.

Lattice parameters derived from these fits for the UNb5 and UNb6 alloys are consistent with the literature, particularly the Anagnostidis and Jackson data. Variation between Tangri and other sources may be explained by the fact that Tangri did not permit the axis to change in his fitting routine, and the a and c axes' fitted results are highly dependent on each other. At first glance, this success is not shared in the case of the UNb7 alloy, especially when fitted with either the α'' or γ° phase. However, when fitted with both phases, the α'' phase lattice parameters adopt values closer to the literature and can be seen to be consistent with overall trends. Even after the two phase fit, the γ° parameters appear to be quite far off the trendlines. Considering that the α'' phase has formed out of the γ° phase, it could be argued that the γ° parameters would have shifted to the phase's theoretical lower limit. This is shown by black arrows on Figure 4.12.

It would be very instructive to essentially repeat a study of the phases as a function of composition if more information, concerning the phase fractions and inherent strains in the samples were desired. It is clear from the pattern alone that the UNb7 alloy has a large amount of stress residing within it. The mean microstrains calculated from the fits are relatively large. This appears to be the first fit of the γ° phase where an example of the fitted pattern and the fit statistics are included. Additionally, the full microstrain distribution shown here also appears to be the first of its kind, as previous works to estimate this quantity have been limited by a narrow range of d spacing values.

One obvious limitation in the work that has been done here is the equal treatment of uranium and niobium atoms. The x-ray atomic form factor (scattering amplitude of x-rays) increases with atomic number, Z. Uranium has roughly $2\frac{1}{4}$ times the number of electrons than niobium, and since niobium only forms 17% of the atoms, the uranium atoms are responsible for approximately 99.4% of the total signal. For this reason, any attempt to extract information about the local environment of niobium atoms will always be very challenging. Neutron diffraction appears more promising as the neutron form factor, on the other hand, depends on the neutron scattering length, which varies between isotopes but is relatively similar for ^{41}Nb and ^{238}U, 7.054 and 8.402 fm respectively.

However, the EXAFS technique is probably the most promising in being able to determine local atomic coordination of the niobium atoms. Valot et al. performed a study on the U-Nb system as a function of composition [272]. When compared to the nearest neighbour distances determined for this work, the α'' phase (13 at % Nb) shown in Figure 4.13 shares a relatively strong resemblance to their 15 at % Nb data. However, by the authors own admission, the fitting might need some refinement. The peaks observed at 2.4 Å are striking as not only does this disagree with these Rietveld fits, the interatomic uranium distance is far below that of α-U. In addition, the 5 at % Nb and 15 at % Nb share a strong resemblance, as the 10 at % Nb and 20

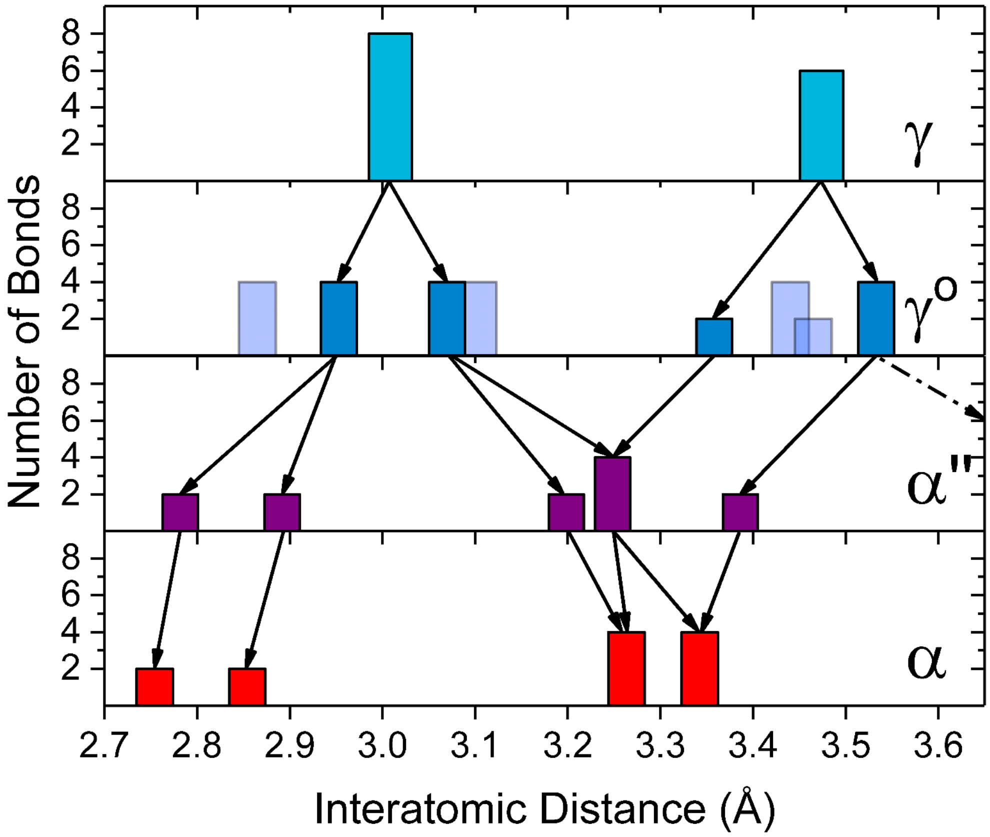

Figure 4.13: Interatomic nearest neighbour distances for the γ° and α'' phases with equivalent data for α [148], γ^s [293] (shown in transparent blue) and γ [122] phases as detailed in the literature, displayed for comparison.

at % Nb also share resemblances. In contrast though, the radial distribution function for the niobium atoms shows noticeable differences compared to the uranium atoms. This is probably not unexpected as from very simple arguments the ionic radii of the elements are slightly different. Uranium could be seen to generally fit that of the data presented here, whereas Nb is very different.

Considering just the uranium ions, the atomic positions from the Rietveld fits may be seen to generate a relatively continuous transition from the γ through to the α phase. The γ^s phase as reported by Yakel [293] is also shown but does not fit with the trend suggesting that some of the atomic positions may not be particularly accurate. Yakel's results would suggest that four of the nearest neighbour distances contract, expand and contract once again en route from the γ to the α phase.

Attempting to definitively confirm the exact space group of the γ° phase from this data would be too ambitious. Ideally a new sample with possibly a slightly higher alloy content would be required. A range stretching between 16 and 20 % at Nb (6.9 and 8.9 % wt Nb) would be preferable.

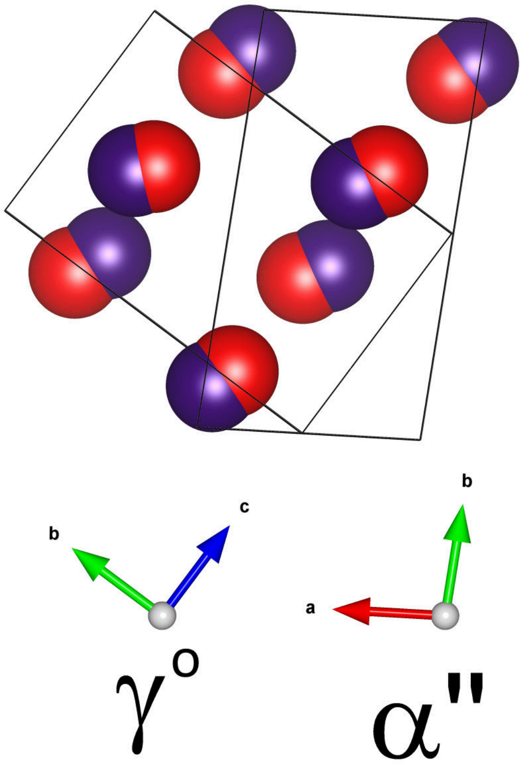

Figure 4.14: Relationship between the γ° and α'' phases. Purple atoms show the atomic positions of the α'' phase, whereas, the atomic sites of the γ° phase are shown by the red atoms. The figure is essentially the same as that proposed by Carpenter and Vandermeer [38], apart from a translation in the plane that has been applied to the cells to account for the 'non-conventional' setting for the γ° phase.

Neutron diffraction and EXAFS should be considered as important tools for obtaining further information on the crystallography of these materials.

4.2.5 Conclusion

A mixture of $\gamma + \alpha''$ phases was found to be the best solution to the UNb7 alloy diffraction pattern. The P4/nmm space group was used for the γ° phase with the previously confirmed P 1 1 2_1/n space group used for the α'' phase. Microstrains and uranium local coordinations have been determined for the phases in this alloy which will be instrumental in assessing the evolving crystallographic properties through ageing.

CHAPTER 5

LONG TERM INVESTIGATIONS INTO THE LOW TEMPERATURE AGEING OF THE UNB5, UNB6 AND UNB7 ALLOYS

This chapter examines long-term low-temperature ageing behaviour of the metastable uranium-niobium alloys in the vicinity of the eutectoid at high temperatures. This work builds on previous reports produced by the University of Bristol for AWE Plc. A range of commonly used materials science analytical techniques such as XRD, EBSD, SEM, TEM, APT and EDX have been used to characterise changes observed in these alloys as a result of extended ageing and relate them to the alterations observed in the mechanical properties of the alloys. The majority of the work was performed in-house at the University of Bristol with TEM and APT conducted at the University of Oxford.

5.1 Introduction

Low-temperature ageing is known to induce changes to the mechanical properties of uranium alloys near the eutectoid composition where the shape memory effect is the strongest [106]. Despite the well-characterised response to low temperature ageing, ambiguity exists over the responsible mechanism with multiple diffusionally mediated possibilities suggested, such as spinodal decomposition [107, 118, 123, 274, 279], chemical ordering [118, 119, 302] and clustering of niobium at defects [123, 125]. Hackenberg *et al.* conducted a study into the effects of long term ageing on mechanical properties as assessed by stress-strain curves [106]. Ageing at temperatures between 100 and 200 °C induced dramatic losses in ductility and increases to the first yield strength, second yield strength and ultimate tensile strength. Volz *et al.* showed an increase in hardness as a function of time for both the UNb5 and UNb7 alloys, but particularly for the UNb7 alloy [279]. Higher temperatures were shown to accelerate these changes in both cases. Hackenberg *et al.* also report an initial age-softening in banded UNb6 alloys at very low temperatures [106].

Materials and particularly metallic structural components with a high strength are generally favourable for the majority of applications. There are a few methods commonly employed to strengthen metals, however, most also incur a loss of ductility [37]. Strengthening is virtually always achieved by restricting the movement of dislocations, requiring greater mechanical forces to induce plastic deformation. However, plastic deformation relies on the motion of dislocations on bulk, which, under strengthening mechanisms, are hindered from doing so, reducing total plastic deformation or ductility. It is important for the safety of structural components to incorporate at least some ductility. A brittle component will fail if load exceeds the yield stress, whereas, a ductile component will likely continue to strengthen through strain hardening and though displaying wear will deform to accommodate the stress. Additionally, some metals lose ductility as the temperature is lowered.

The University of Bristol produced two reports on the ageing of UNb5 and UNb7 alloys in 2012 and 2013 [221, 223]. Based on observations made from TEM images, these reports came to the conclusions that spinodal decomposition was occurring on a very fine scale, following ageing times of up to 5000 hours at 150 °C, echoing Hsiung *et al.*'s conclusions [118]. This effectively assigned the hardening mechanism as connected to precipitation hardening. In addition to the impact that such a reaction would have on mechanical properties, a consequence would include the production of regions of progressively less alloyed uranium with an increasing propensity to corrosion.

However, Clarke *et al.* showed that spinodal decomposition was an unlikely mechanism in the low-mid temperature ageing of the UNb6 alloy by APT and calculations [51]. Whilst clear phase separation into regions of high and low niobium content was observable in materials aged to 300 °C, only very subtle changes to niobium concentration could be extracted at low temperatures. Additionally, it is debatable whether the fine-scale segregation reported by Scott *et al.* and Hsiung *et al.* [118, 221, 223], and the indirect observations by Volz *et al.* and Vandermeer *et al.*, is capable of producing the rather dramatic changes to the stress-strain curves [274, 279]. Brown *et al.* studied the low temperature ageing phenomenon by in-situ neutron diffraction and proposed rearrangement of defects within the twin structure to be responsible for strengthening the alloy. Additionally, Brown *et al.* were able to discount chemical processes by evaluation of peak widths which limited the redistribution of niobium to a maximum of 0.2 weight percent.

This chapter seeks to investigate the source of strengthening in this alloy system, paying attention to microstructural changes to uranium-niobium alloys exhibiting the shape memory effect.

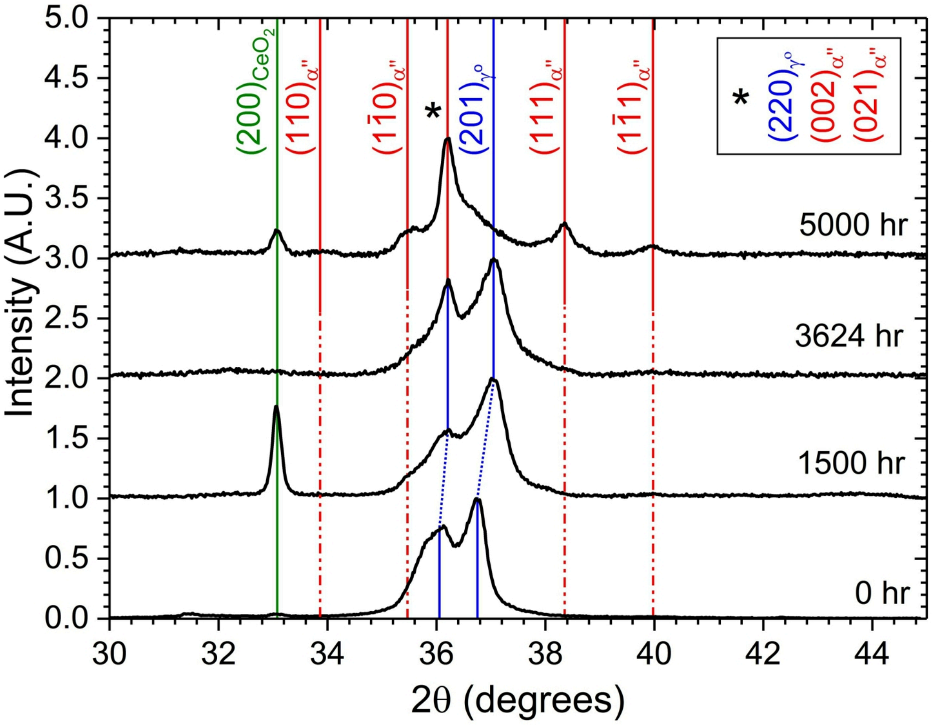

Figure 5.1: XRD patterns of the UNb7 alloy throughout ageing at 150 °C. Performing an accurate Rietveld refinement where microstrain dominates on a limited 2θ range is challenging, however, the patterns appear to show the γ° phase replaced by the α'' phase. This data presented here was previously reported in Scott *et al.* but has been replotted and annotated [221].

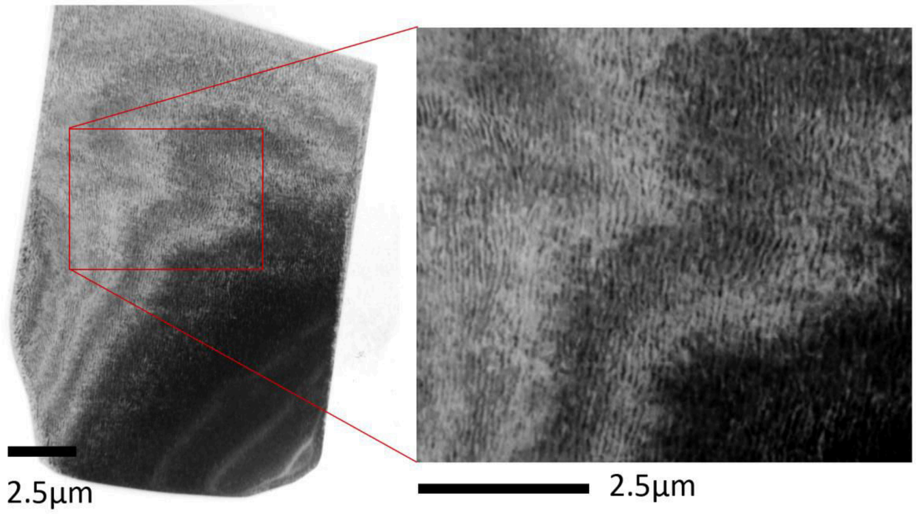

Figure 5.2: TEM micrographs of the unaged UNb7 alloy which was described as 'showing the presence of nano-scale banding ascribed to subtle chemical segregation'. This figure presented here was originally reported in Scott *et al.* [221].

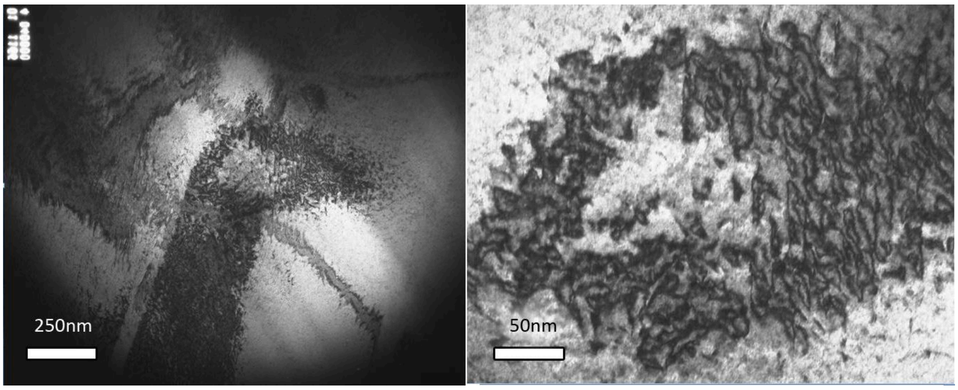

Figure 5.3: TEM micrographs of the 5000hr aged UNb7 alloy which was described as '[having] evolved further than spinodal decomposition, developing angular nanoscale platelets assumed to be the α'' phase'. This figure presented here was originally reported in Scott *et al.* [221].

5.2 Experimental

UNb5 and UNb7 samples received from AWE Plc that had been pre-aged at 150 °C for ageing times of 1500, 3624 and 5000 hr were used in this work. These samples had been studied prior in a commercial report produced by the University of Bristol for AWE Plc [221, 223]. Figures 5.1, 5.2 and 5.3 originate from these reports, as well as the hardness data inset in Figures 5.5 and 5.6. Selected samples were re-examined by SEM, EBSD, TEM and XRD, and further investigated by APT. Tensile stress-strain data from sister samples has been provided by AWE Plc and were measured using an Instron 5885 in extensometry to failure.

Further ageing was carried out on UNb5, UNb6 and UNb7 alloys at temperatures of 55, 75, 100, 125, 150 and 200 °C for cumulative ageing periods of 10, 20, 40, 80 and 160 days. These ageing temperatures were chosen to span the range established to be responsible for the low temperature ageing phenomenon [106]. Five logarithmically separated ageing periods of up to 160 days (and unaged data) were employed to complement the ageing of the received samples (up to 5000 hours which equates to 208.33 days). Efforts to extend the ageing of these samples to beyond 160 days was hampered by excessive oxidation of the samples.

XRD was performed on a Philips X'Pert Pro MPD located in the School of Physics, University of Bristol. Data was fitted using a similar methodology as in the case of Chapter 4. Due to the inherently poor quality of data obtained from a lab source compared to that from a synchrotron source, the isotropic strain model was used in favour of the anisotropic model used in the Chapter 4. Whilst the anisotropic strain model is superior in describing the distribution of strain in the material, relatively high quality data that is free of peaks in the background and minimal texture are required. The isotropic model ensures that a constant fitting procedure may be applied to each sample, from which a mean microstrain may be extracted and compared against samples of different ageing treatments.

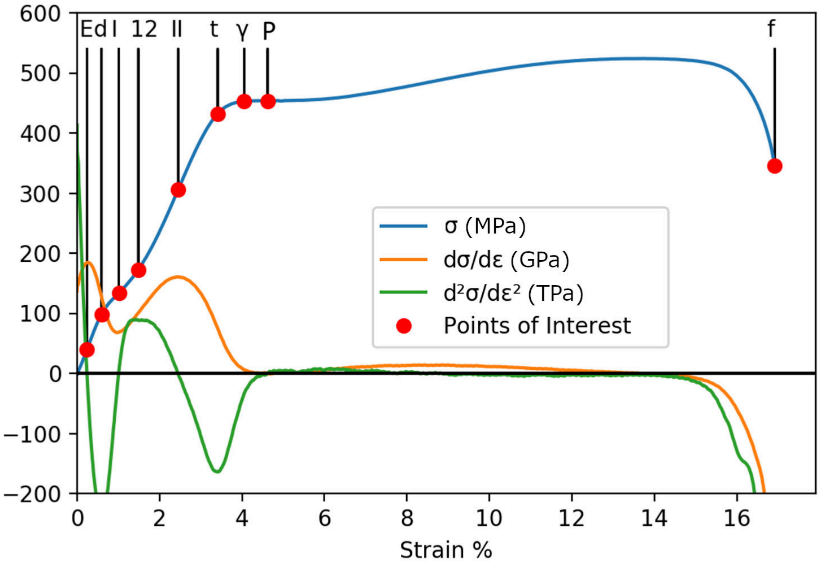

Figure 5.4: An example of a stress-strain curve that has been analysed using the code presented in Appendix C. Points of interest identified by analysis of the gradient of the data have been annotated onto the curves.

EBSD was performed on a Zeiss SigmaHD using the phases extracted from the Chapter 4. Dr Ian Griffiths assisted by Dr Xander Warren produced the TEM lamella that were taken to Oxford and subsequently examined on a JEOL ARM200F by Dr Ian Griffiths. Figures 5.2 and 5.3 shown here as a comparison were obtained from a Philips EM430 housed in the University of Bristol. Hardness data was originally reported by Scott *et al.* [221, 223].

Stress-strain charts were analysed with a bespoke computational program written in Python (using numpy, pandas and scipy packages) to employ a uniform methodology. The code is included in Appendix C. The behaviour of the stress-strain charts shown are not trivial but are full of information that can be extracted. This is particularly the case for the UNb5 and zero-age UNb7 alloy curves where detwinning behaviour is clearly identifiable. Analysing the curves using conventional analysis (0.002 strain offset method [37]) of the curves using secant moduli would be insufficient. The tangent rather than secant moduli have been evaluated due to the necessity in evaluating these constantly changing curves, Figure 5.4. This method is also useful for analysing regimes which are short lived, for example the elastic strain of the unaged UNb5 alloy. In this case, the secant modulus does not produce a vastly different result but it would only be useful in determining the Young's modulus, E, and not other portions and features of the curves.

The regions of elastic straining (E), easy flow strain hardening (I), more difficult flow strain hardening (II) and plastic flow (P) have been identified as regions where the gradient ($\frac{d\sigma}{d\varepsilon}$) of the stress-strain curve is at a maximum (E and II) or minimum (I and P). These points are therefore determined as when $\frac{d^2\sigma}{d\varepsilon^2} = 0$. The gradients are most important parameters for these points (E, θ_I and θ_{II}). Between these regions, inflection points are worth examining. These are defined as; the onset of detwinning (d), boundary between easy flow and more difficult flow strain hardening regimes (12), and start of yielding (t). Additionally, the fracture point is important. Key parameters for describing these points are the strain and stress at each point ((ε_d, σ_d), (ε_{12}, σ_{12}), (ε_t, σ_t)). These are defined as the points at which $\frac{d^3\sigma}{d\varepsilon^3} = 0$.

Vandermeer *et al.* identified the γ point as a weak, diffuse maximum prior to large scale plastic deformation [276]. This was a point at which necking was not observed, before the start of work hardening. To ensure that the allocation of the γ point was repeatable, the γ point was defined here as the point at which the stress-strain curve and the tangent extending back from the point on the curve at which its second differential crossed zero for the fourth time differed by less than 0.5%.

Toughness of samples was also evaluated by integrating the stress-strain curve between zero and the fracture point. Despite increasing upper tensile strengths, toughness decreases owing to the dramatic loss in ductility. Resilience, the integral within the elastic limit, on the other hand increases as the yield point barely changes but stresses increase.

5.3 Results

5.3.1 Mechanical Testing

Stress-strain curves of the UNb5 and UNb7 alloys as a function of ageing at 150 °C are shown in Figures 5.5 and 5.6. Hardness plots are also shown as insets of each figure. Table 5.1 shows the key values extracted from stress-strain plots.

Both the unaged UNb5 and UNb7 alloys exhibit quintessential shape memory alloy behaviour featuring double yielding that is often ascribed to the production of detwinned martensitic crystallites [37]. The entirely martensitic UNb5 alloy is capable of being strained to a greater extent, both up to the yield point, ε_γ, and to fracture, ε_F. Between the yield point and fracture, the unaged alloys exhibit significant work hardening under additional straining (also known as strain hardening). After the first ageing treatment, the ability for work hardening is lost in both alloys and the fracture point decreases significantly.

The two unaged curves share a resemblance owing to both alloys' closeness to the austenite-martensite transition. Under a classical SMA description, the 'martensitic' material (UNb5) would be expected to initially exhibit elastic straining of the twinned martensite (I) before undergoing detwinning throughout the flatter portion (12) and subsequently recommencing elastic straining of the detwinned martensite (II). On the other hand, the 'austenitic' material (UNb7) in the vicinity of the martensitic transition would be expected to elastically deform (I) before undergoing a strain induced martensitic reaction to detwinned martensite (12). This would also be followed

	Ageing	ε_{12}	ε_{γ}	ε_F	σ_{12}	σ_{γ}	σ_{UTS}	θ_I	θ_{II}	E	Hardness	Toughness
	hr	%	%	%	MPa	MPa	MPa	GPa	GPa	GPa	Hv	MPa
UNb5	*0*	*2.5(1)*	*6.4(2)*	*26.39*	*188(8)*	*546(1)*	*714*	*9.8(4)*	*16.4(3)*	*27.3(43)*	255(14)	-
	1500	2.24(4)	5.47(8)	12.5(9)	446(19)	672(15)	721(13)	5.0(3)	10.0(2)	36.0(13)	287(14)	73.9(58)
	3624	2.48(6)	5.64(1)	12.4(5)	486(22)	690(12)	726(5)	4.0(2)	9.1(3)	35.8(4)	299(7)	74.5(22)
	5000	2.35(8)	5.62(35)	10.7(26)	504(14)	714(22)	735(7)	4.0(2)	9.1(5)	37.8(3)	278(12)	64.8(179)
	21600	2.57(5)	5.10(33)	6.72(60)	584(1)	716(27)	719(26)	2.5(8)	6.9(7)	41.5(5)	-	37.9(50)
UNb7	0	1.44(4)	3.83(9)	16.8(3)	177(9)	455(4)	529(4)	7.7(8)	16.0(7)	18.6(2)	147(5)	73.3(15)
	1500	-	3.52(28)	8.4(9)	-	635(1)	638(1)	-	3.3(5)	34.1(6)	233(23)	44.6(60)
	3624	-	3.57(16)	8.2(5)	-	657(1)	660(1)	-	2.5(4)	34.8(3)	258(13)	45.3(31)
	5000	-	3.55(23)	7.2(15)	-	669(4)	670(4)	-	2.3(6)	35.2(9)	262(9)	39.2(101)
	21600	-	3.99(14)	6.4(2)	-	698(6)	700(6)	-	1.6(3)	37.1(3)	-	35.9(20)

Table 5.1: Results of the stress-strain tests of UNb5 and UNb7 alloys aged at 150 °C. Standard deviation is based on 3 measurements of 3 different samples. In the case that a sample failed prematurely, the standard deviation becomes half the range between the mean of the two successful tests. The unaged data has been sourced from Volz *et al.* [279], using Engauge digitizer [179].

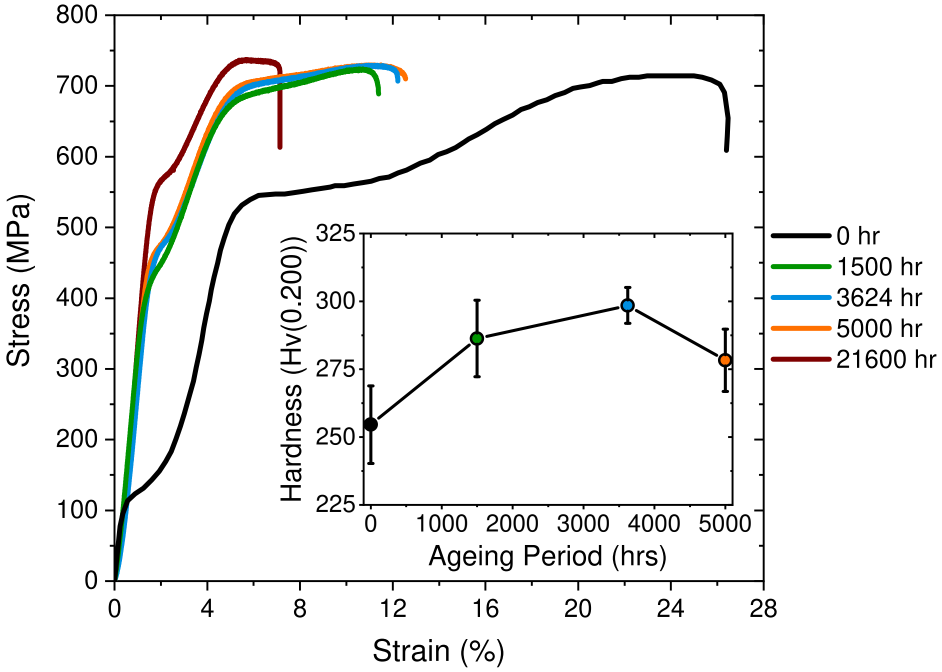

Figure 5.5: Engineering stress-strain charts of the UNb5 evolving through isothermal ageing at 150 °C. The unaged data has been sourced from Volz *et al.* using Engauge digitizer [179]. Otherwise, the data were provided by AWE plc.

by elastic straining of the detwinned martensite (II), as in the case of the initially martensitic material.

In the UNb5 alloy, detwinning and yield stresses, σ_{12} and σ_{γ}, increase sharply between the unaged and first ageing period. The onset of detwinning and the yield point, ε_{12} and ε_{γ} are only slightly affected by ageing. The ultimate tensile strength however, remains relatively unchanged between ageing periods. It is probable that the UNb5 is still capable of cycling through the SME though greater stresses indicate that rearrangement of the twin boundaries to achieve a detwinned state becomes increasingly difficult with ageing. Increased stresses may have an effect on the total strain recoverable but as all samples were tested until fracture with no unloading, this was not examined.

The unaged UNb5 alloy displays near perfect plastic deformation between 5 and 10 %. Strain hardening subsequently takes over until eventual necking and fracture. In the 1500, 3624 and 5000 hr aged samples, the ability for strain hardening is lost. In the 21600 hr aged sample, the plastic yielding section is also truncated. Integrating the curves shows decreasing toughness with ageing.

The Young's modulus of the twinned α'' phase in the UNb5 alloy is observed to increase slightly

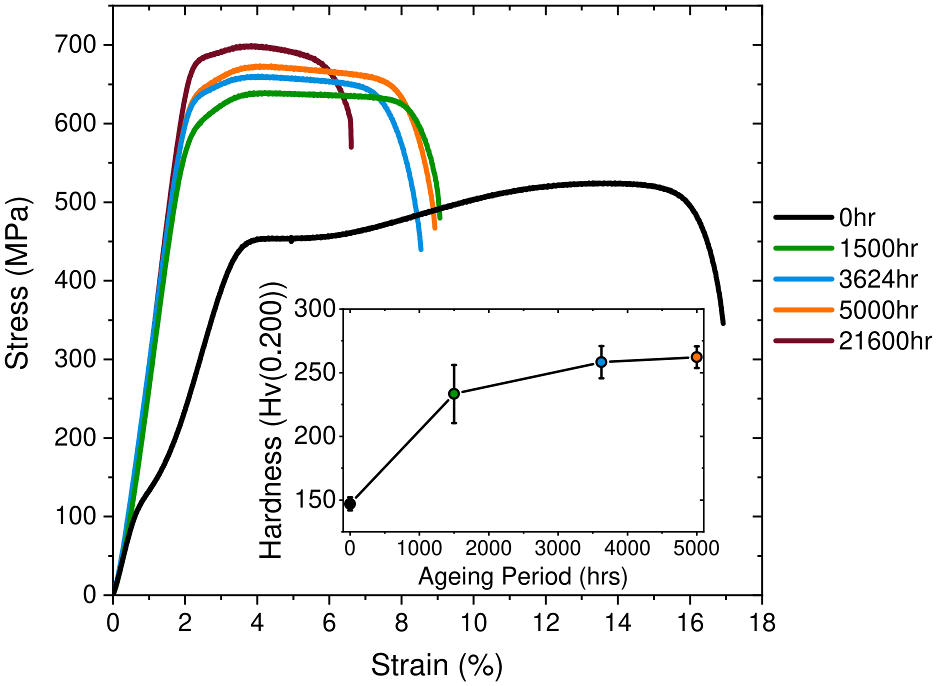

Figure 5.6: Engineering stress-strain charts of the UNb7 evolving through isothermal ageing at 150 °C. The data were provided by AWE Plc.

with ageing, whereas the detwinning gradient, θ_I, and the gradient of the elastic straining of the detwinned α'' phase decrease.

The behaviour of the the UNb7 alloy is slightly more complicated as the double yielding behaviour is seemingly lost by the first ageing treatment. Figure 5.6 shows the Young's modulus extending to around 2 % in all aged samples with a more gradual transition to the yielding portion of the curve. Within this relatively flat section, it is difficult to immediately identify whether any production of detwinned martensite is possible. Beyond 3.5 %, the gradient of the curves decrease to roughly zero. In the case of the aged materials, the gradient turns negative indicating that necking has probably started. Like the UNb5 alloy, the UNb7 material loses the ability to strain harden by the first ageing treatment and fracture occurs at decreasing strains with ageing. This also results in a decreasing toughness despite increasing ultimate tensile strengths. The Young's modulus in the unaged UNb7 is significantly lower than in subsequent ageing treatments.

Overall, both alloys can be characterised as strengthening whilst losing ductility throughout ageing. Despite this, over this ageing period, specimens stayed above 5% elongation, an often used threshold for brittle materials [37].

Hardness testing also shows the material to strengthen and resist plastic deformation with ageing. In the case of the UNb7 alloy, this trend is seen very clearly, particularly as the unaged state is relatively soft with a hardness of 147 ± 5 Hv. In the UNb5 alloy, a fully martensitic material, the hardness is initially high yet shows a small increase with ageing. Errors are large using this method and statistical as a result of the heterogeneity of the microstructure. Hardness and ultimate tensile strength can often be shown to be related by a linear relationship [37]. The relationship between these two parameters is shown in Figure 5.7. The gradient is determined to be $0.75 \pm 0.04\,\mathrm{MPa}^{-1}$. In comparison, the same relationship for steels using the closely related Brinell scale has a gradient of $0.290\,\mathrm{MPa}^{-1}$ ($(3.45\ \mathrm{MPa})^{-1}$) [37].

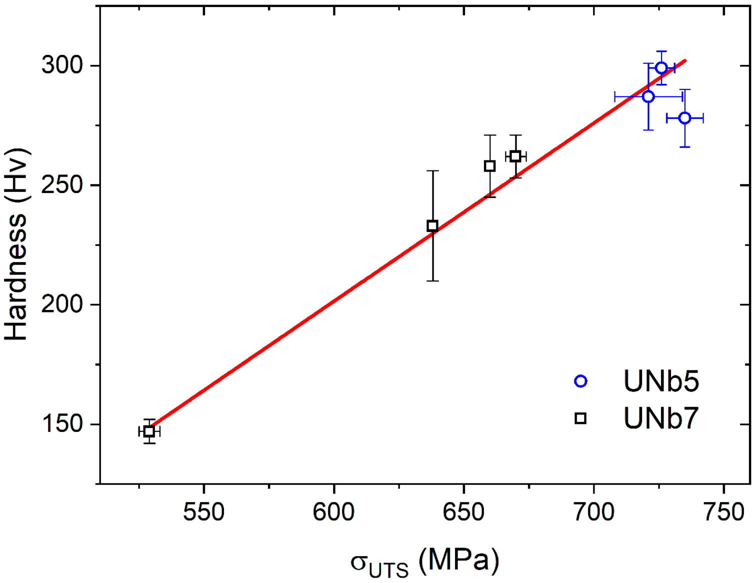

Figure 5.7: Relationship between the hardness and upper tensile strength of unaged and aged specimens. High adjusted R-squared value of 0.982 suggests a strong link between the two parameters as would be expected. Plotting with axes inverted and converting to the Brinell scale [12, 25] for easier comparison with literature sources gives a gradient of 1.27 ± 0.14 MPa.

5.3.2 XRD

Figures 5.8 and 5.9 show the evolution of (isotropic) microstrain in the UNb5 and UNb6 alloys throughout ageing at temperatures ranging between 100 and 200 °C. The samples aged at temperatures below 100 °C were not observed to produce any noticeable differences in XRD patterns. Microstrain in the α'' phase of the UNb5 and the UNb6 alloys can be observed to initially decrease after the first ageing treatment. In the case of the UNb5 alloy, microstrain appears to be relatively unchanged with ageing thereafter and not overly reliant on ageing temperature. The UNb6 alloy on the other hand shows a trend of increasing microstrain with further ageing. Chapter 6 showed that instantaneous heating of the alloys significantly reduces microstrain but following the reaching of temperature, microstrain is re-established. In the UNb6 alloy, it appears microstrain builds slowly between 100 and 150 °C, but at 200 °C, there is a significant amount of microstrain produced by the first ageing treatment. Microstrain of the α'' phase in the UNb6 alloy appears to trend towards approximately 19000, whereas in the UNb5 alloy it is lower at around 14000.

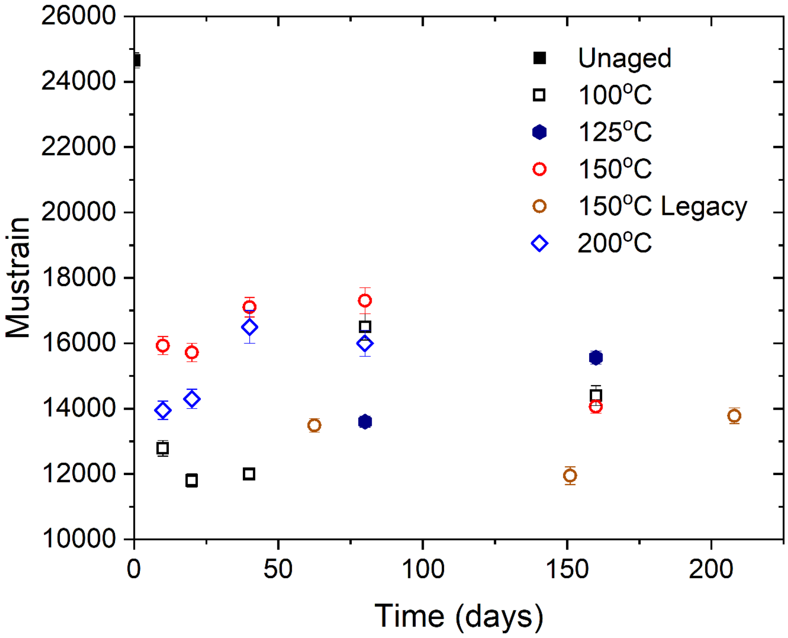

Figure 5.8: Microstrain of the α'' phase of the UNb5 alloy throughout ageing at temperatures up to 200 °C.

Figures 5.10 and 5.11 show the corresponding evolution of microstrain in the UNb7 alloy through ageing at temperatures of up to 200 °C. Figure 5.12 shows the evolution of the α'' phase fraction under ageing. Microstrain in the γ° phase drops for the 100 and 150 °C aged samples but remains high for the 200 °C aged samples. In all cases, fitting of the XRD patterns suggests that the fraction of the material belonging to the α'' phase increases along with increasing microstrain in this phase. Temperature appears to be an important parameter with samples aged at higher temperatures producing higher microstrains and greater amounts of the α'' phase.

XRD results obtained for the UNb7 alloy are not consistent with those presented by Scott *et al.* [221]. The XRD patterns originally measured for these previously aged samples suggested a complete transition to the α'' phase by 5000 hours. A rudimentary Rietveld refinement applied to the limited range pattern showed the α'' phase to be capable of producing a good fit without the need for additional phases. In contrast, the patterns measured of the newly aged specimens

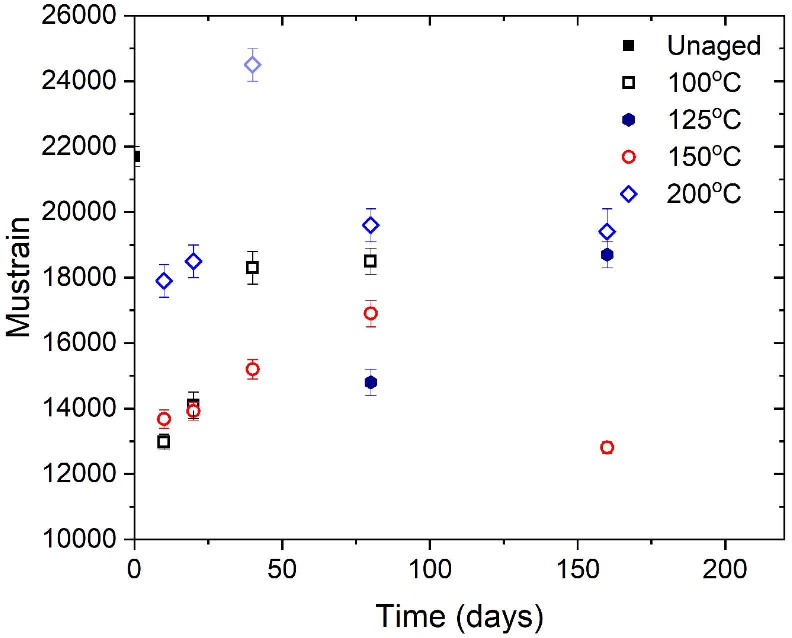

Figure 5.9: Microstrain of the α'' phase of the UNb6 alloy throughout ageing at temperatures up to 200 °C.

showed the γ° phase to, on the whole, remain the dominant phase, Figure 5.12. Due to inconsistency between the legacy data and that received from the additional ageing treatments and limited range of the legacy data, the legacy XRD data was remeasured. Figure 5.13 compares the XRD data extracted from the newly aged samples and those received in an aged state from AWE.

The two sides of Figure 5.13, though both relating to the same set of samples with no additional ageing having been applied between measurements, seem incompatible. Whilst the 0, 1500 and 3624 hr aged samples appear to feature the γ° phase dominating the pattern, peak width is higher in the originally measured aged samples data. Additionally, multiple shoulders in the legacy data set imply that secondary phases are present to a greater extent. The greatest difference is observed in the 5000 hr aged sample in which the originally measured data is best fitted by the α'' phase. In comparison, the remeasured data resembles the γ° phase better and based on a full pattern fitting is estimated to contain $33.6 \pm 2.7\,\%$ α'' phase.

The legacy 5000 hr aged UNb7 alloy data, Figure 5.13, strongly resembles a pattern received from a poorly prepared unaged UNb7 sample, Figure 5.14. The poorly prepared sample was found to have not been supplied with a sufficiently adequate electrical connection during electropolishing. The high potential across the surface of the sample that would have resulted from a poor electrical connection is theorised to have induced a transformation of the surface to the α'' state. It was subsequently found that mechanically polishing away the surface of the specimen

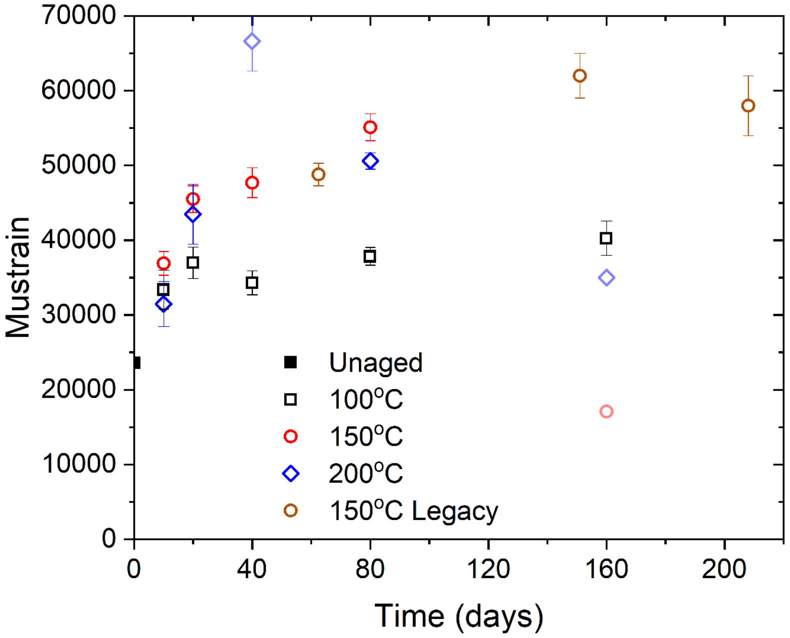

Figure 5.10: Microstrain of the α'' phase within the UNb7 alloy throughout ageing at temperatures up to 200 °C.

permitted the measurement of the γ° phase again when adequately electropolished.

The results of the fitting of the remeasured data of Figure 5.13 as well as the additionally aged samples are shown in Figures 5.10, 5.11 and 5.12. The remeasured data can be seen to agree relatively well with the data collected from the additionally aged samples, particularly with the repeated 150 °C ageing measurements. There is some variation to be expected as the data from the additionally aged specimens relate to the same samples remeasured between ageing treatments, whereas the legacy data comes from 3 entirely different samples.

Figures 5.8 - 5.12 feature some results that have been identified as likely to be anomalous. The preparation of samples is highly influential on these measurements as was shown in Chapter 3. For example, in the case of the 200 °C aged samples, microstrains for the UNb6 and UNb7 alloys appear overly exaggerated for the 40 days aged data, Figure 5.9. Discrepancies has been attributed to inconsistencies in preparation of this batch of samples, likely from a less effective electropolishing step. All samples required diamond and electropolishing to remove oxide built up during ageing. 160 day aged data also suffers from poor reliability but this is attributed to excessive oxidation due to a low purity environment that samples were sealed in as a result of glovebox contamination. Oxidation caused many samples, particularly those aged at the higher temperatures to lose a substantial amount of metal to oxide making it difficult to enable effective polishing in the already small samples.

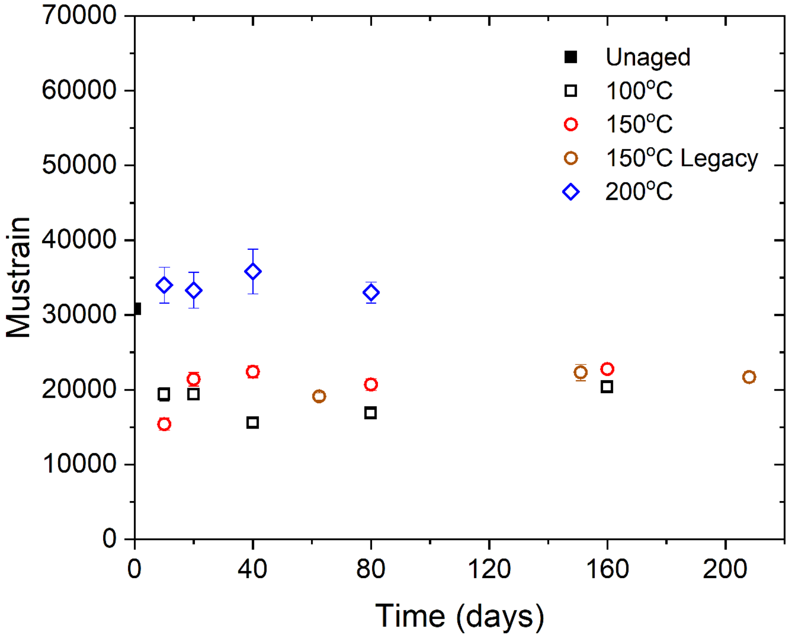

Figure 5.11: Microstrain of the γ° phase within the UNb7 alloy throughout ageing at temperatures up to 200 °C.

Figure 5.15 displays the fitted patterns of the unaged alloy and a heat treated alloy example to show the differences in the patterns and the quality of the fits. Fitting of the data is generally reasonable but wouldn't be considered exemplary. The difficulty in producing a high quality pattern fit arises from two similar overlapping XRD contributions, broad diffraction peaks and complexities in the profiles of each phase due to

The weighted residual for the aged pattern shown in Figure 5.15 was $R_{wp} = 8.44\,\%$ and phase residuals were $RF^2 = 3.896\,\%$ and $RF = 2.509\,\%$ for the α'' phase and $RF^2 = 2.957\,\%$ and $RF = 2.855\,\%$ for the γ° phase. The phase residuals are quite good however the pattern residual is relatively high and has been artificially lowered by background peaks that have been subsequently removed. These fits were achieved without the use of preferred orientation effects. Fitting used an isotropic microstrain model in conjunction with reasonable atomic displacement parameters to make minor adjustments to peak widths based on crystallographic directions.

Despite the few spurious results, some trends may be observed in the UNb7 alloy data. As in Chapter 4, the unaged UNb7 alloy was found to be best modelled by a mixture of the γ° and α'' phases. The starting α'' phase fraction is lower than in Chapter 4 owing to the choice of microstrain model used here. Through ageing, the phase fraction and microstrain of the α'' phase increases. Microstrain in the γ° phase was not observed to change significantly with ageing apart from in the initial step in which it decreased at ageing temperatures of 100 and 150 °C but

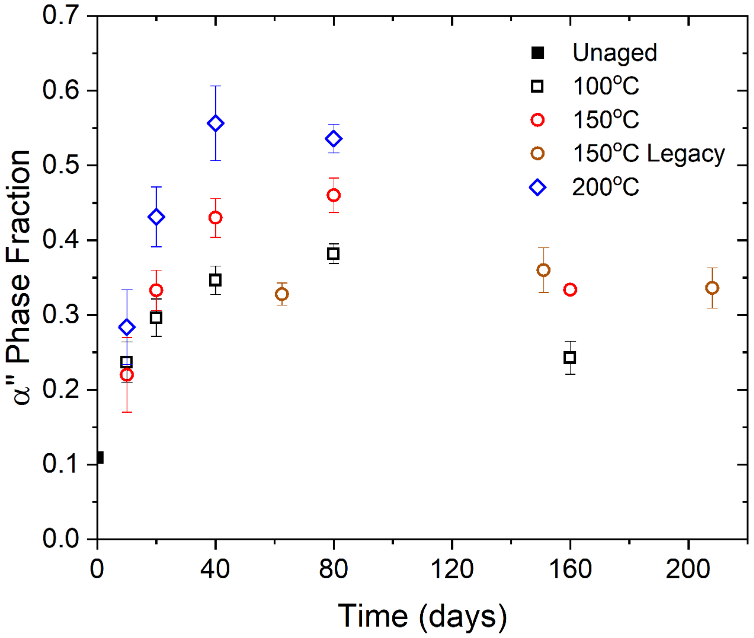

Figure 5.12: Phase fraction of the α'' phase within the UNb7 alloy throughout ageing at temperatures up to 200 °C.

increased slightly at ageing temperatures of 200 °C.

5.3.3 EBSD

EBSD maps were collected from the UNb5, UNb6 and UNb7 alloys aged at 150 °C for 160 days (the culmination of the ageing treatments), Figures 5.16, 5.17 and 5.18 respectively. The right panel of Figure 5.18 shows an unaged example of the UNb7 alloy where the orientation of the grains featured are very similar to those in the aged alloy of the left panel of Figure 5.18.

Given the immense heterogeneity of the microstructure of the α'' phase alloys and the difficulty still present in acquiring large, accurate EBSD maps of these alloys, it is difficult to draw any meaningful results from the maps of aged samples presently. Figure 5.16 shows a very regular pattern of twins, within which a multitude of secondary twins have formed. It would be desirable to perform counting statistics on the type and density of twins, however presently it is impractical to collect the large, yet high resolution maps required to draw significantly statistical results. Likewise, the EBSD map of the aged UNb6 alloy, Figure 5.17, shows a few incredibly distressed grains frequented by numerous sources of microstructural defects. It has been more difficult to obtain good quality EBSD patterns from the aged UNb6 than the unaged equivalents.

The UNb7 alloy presents the best opportunity to examine any meso-scale changes to the microstructure with ageing. Large, high quality EBSD maps are most easily collected from

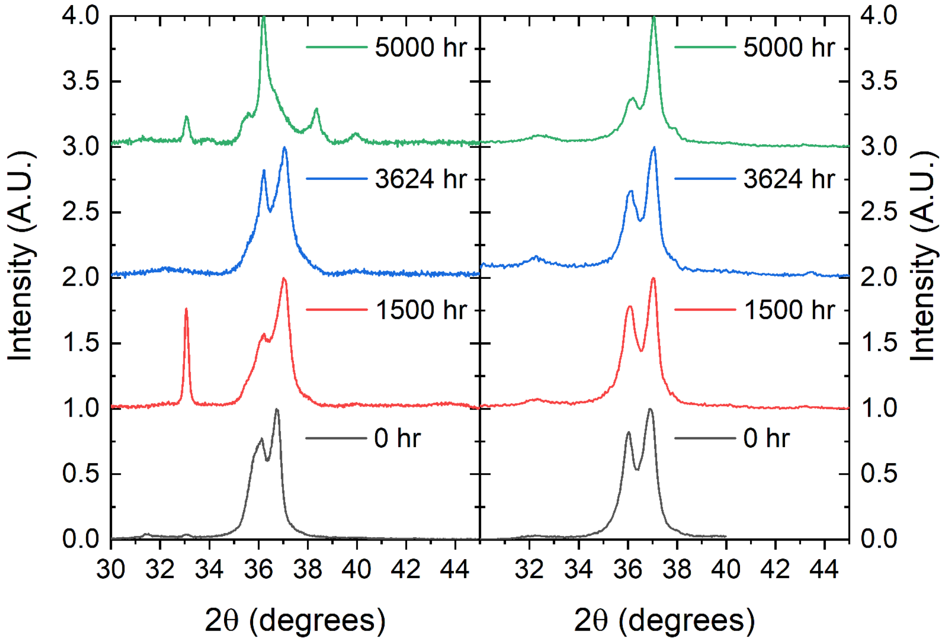

Figure 5.13: XRD patterns of the UNb7 alloys received from AWE Plc in an aged state. Left side shows the original XRD measurements originally reported by Scott *et al.* [221], right side shows the remeasured data. Full scans were recorded when remeasuring the alloys, a limited range is displayed here for comparison.

the UNb7 alloys for the reasons discussed in Chapter 3. The unaged and aged comparison EBSD maps, Figures 5.18, each show grain orientations relatively close to the [001] (pink), [101] (green) and [111] (purple) directions. Both maps show a small intragranular crack that is assumed to be a rarely occurring feature originating in manufacture. The microstructure of the [111] grains appears to be constant between the unaged and aged samples. Similarly, the [001] grains also show the twin morphology to be consistent with ageing but potentially the density of twins is greater in the unaged case, the pseudosymmetry problem causes twins to appear more like kink bands and the issue is further complicated by the slight offset in grain orientations. The [101] orientations appear to be too greatly separated to draw meaningful conclusions, the microstructures displayed do not appear to be commensurate. Generally, EBSD shows the alloy to have not undergone vastly different changes through ageing on this scale.

5.3.4 TEM

TEM specimens were extracted from the 1500 and 5000 hour aged alloys and examined using an atomic resolution microscope, Figures 5.19 - 5.24. Unfortunately, a zero aged specimen was not used for comparison but examples of TEM images for similar compositions exist in the literature

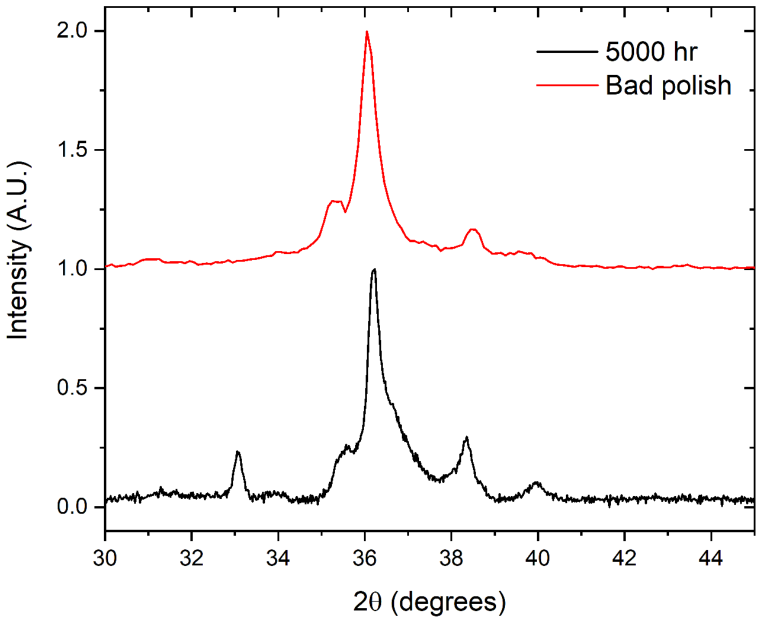

Figure 5.14: Comparison between the XRD pattern of the 5000 hr aged UNb7 alloy in Figure 5.13 and the pattern from a poorly prepared sample in which it was discovered that there was a poor electrical connection to the sample during electropolishing. Data quality is worse for the poorly prepared sample which only received a cursory investigative scan.

[85]. EDX maps were produced to complement the micrographs collected by 3 different imaging detectors. In no instance did EDX show significant variation in niobium content that might be linked to a diffusional process.

Figure 5.19 shows a pair of complementary dark field images collected from the 1500 hr aged UNb7 alloy. It would be tempting to suppose the bands observed relate to the spinodal decomposition mechanism suggested by some in the literature. Whilst the morphology and contrast in the mass thickness sensitive HAADF image might lend itself to such a conclusion, EDX maps would be expected to display differences between these relatively large bands. An alternative explanation might be offered by considering the left portion of Figure 5.20. The foil produced from the 1500 hr aged UNb7 alloy does not appear to be particularly well prepared with regions much thinner than others and bending of the foil. It is expected that a combination of these two effects are responsible for the features observed in Figure 5.19. Streaks observed in the left side of Figure 5.20 can be seen to be on the same scale as those in Figure 5.19. Alternatively, these may be representing complex stacking faults or shear bands [112]. Moiré patterns are considered to be unlikely due to their morphology and the large length-scales over which these bands are formed. A high resolution TEM image of this same sample is shown on the right side

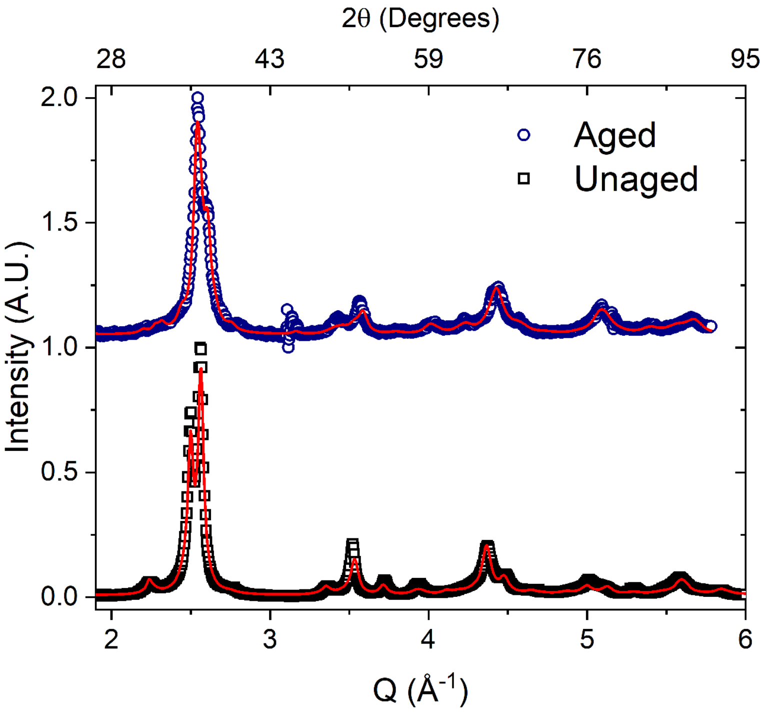

Figure 5.15: Comparison between the XRD patterns of the unaged UNb7 alloy and a UNb7 alloy coupon heated at 200 °C for 80 days. As two different wavelengths were used in collecting these datasets (synchrotron and copper source), the data has been plotted with the scattering vector, Q, on the x axis with the equivalent 2θ scale for a copper source ($\lambda = 1.54$Å) shown above.

of Figure 5.20. In agreement with the results from fitting XRD patterns, the 1500 hr aged UNb7 alloy displays poor crystallinity with coherent crystallites only extending over tens of nanometres.

An example of twinning in the UNb7 alloy is shown in Figure 5.21. Within twins it is possible to observe the effects of stacking faults, Figure 5.22. In these images, contrast is dominant in the MAADF images, showing features much more clearly than HAADF counterparts. MAADF images are much more sensitive to structural and diffraction features, whereas, HAADF images excel in detecting sources of mass thickness. The features shown here are all crystallographic in nature. The contrast observed in HAADF images is likely to be attributable to the detector's imperfect exclusivity of crystallographic and structural (MAADF) sources.

Figure 5.23 shows an example of twinned martensite found in the 5000 hr aged UNb7 alloy. The morphology of the twin and secondary twinning is consistent with that commonly observed in the α'' phase [85]. The irregular habit plane separating the lath of α'' phase from the γ° matrix gives additional evidence that the martensite has formed by twinning mechanism rather than slip. Speckling within the α'' lath shows signs of dislocations within martensite twin variants. Speckling is unlikely to be connected to chemical segregation because one would expect the HAADF image to show this clearly and the diffraction pattern would show faint rings.

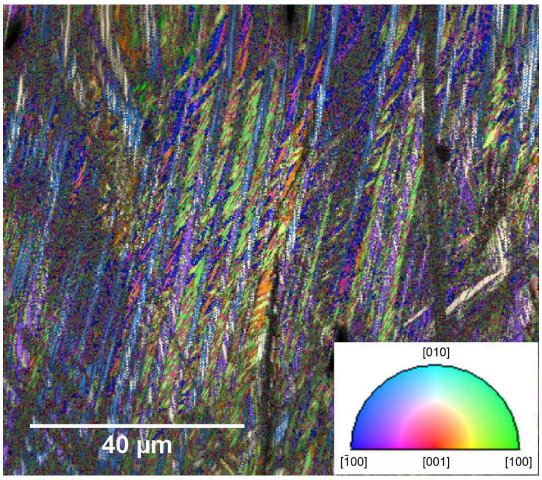

Figure 5.16: EBSD map of the UNb5 alloy aged for 160 days at 150 °C. An example of the unaged UNb5 alloy can be found in Figure 3.21. It has not been possible to acquire an EBSD map of like orientations given the difficulties in collecting EBSD data from this alloy and the low symmetry of the crystal structure.

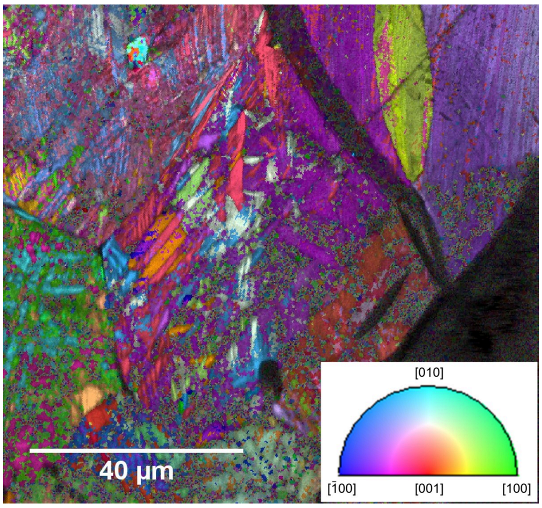

Figure 5.17: EBSD map of the UNb6 alloy aged for 160 days at 150 °C. An example of the unaged UNb5 alloy can be found in Figure 3.22. It has not been possible to acquire an EBSD map of like orientations given the difficulties in collecting EBSD data from this alloy and the low symmetry of the crystal structure.

Uncertainty over the scale of the SAED images mean that a detailed analysis of the diffraction pattern would require substantial deductive work. An additional reason to believe that the feature in Figure 5.23 belongs to the α'' phase may be drawn from an analysis of the angles in the SAED image. Angles between the spots are not 90 ° as would be expected of the tetragonal γ° phase but 89 and 91 °, the same as the $\angle\gamma$ in the α'' phase implying that the zone axis has been aligned along the c axis.

An overview of the foil extracted from the 5000 hr aged sample is shown in Figure 5.24. Despite the foil being perforated in the course of thinning, this TEM sample appears to have been better prepared than that cut from the 1500 hr aged sample. A relatively large section sufficiently thin for strong TEM measurements and a minimal thickness gradient has enabled the imaging of various nanoscale structures in this alloy with no areas found to resemble the structures shown in Figure 5.19.

A high resolution image is shown in the right half of Figure 5.24. Though the microstructure of this alloy (even in its natural state) is incredibly heterogeneous, the crystallite domains are very poorly ordered, possibly less so than the in the equivalent of the 1500 hr aged sample equivalent, Figure 5.20. Loss of crystallinity and the inherent introduction of lattice defects as a result may explain the increases in microstrain observed in Figures 5.10 and 5.11.

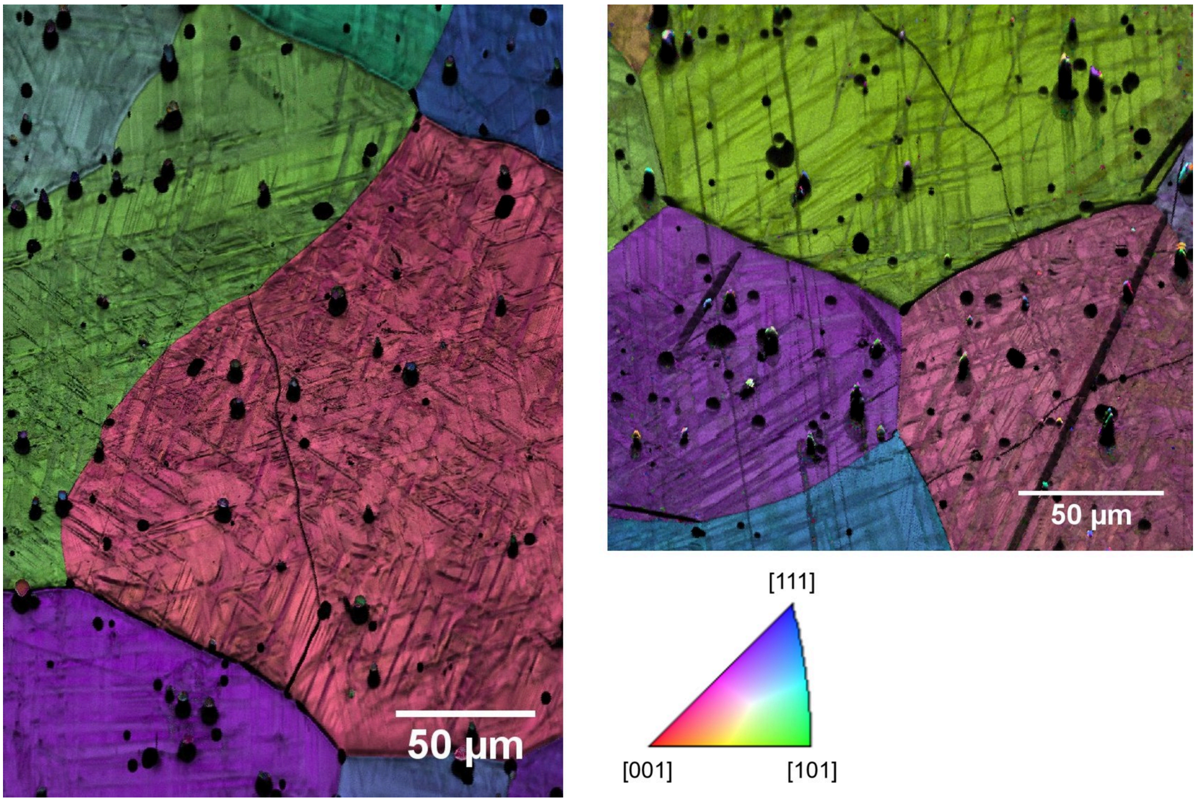

Figure 5.18: Left, EBSD map of the UNb7 alloy aged for 160 days at 150 °C. Right, EBSD map of the unaged UNb7 alloy showing similar grain orientations as to that seen in the 160 day, 150 °C aged UNb7 alloy.

5.3.5 APT

Atom probe tomography needles were extracted from the unaged, 1500 and 5000 hr aged samples. Samples were extracted from both the interior of grains and at the boundaries where chemical segregation would be expected to occur most rapidly. In no samples that were assessed by atom probe tomography was an appreciable separation of the alloy observed. Figure 5.25 shows a representative needle extracted from the 5000 hr aged sample. The reconstructed needle has been produced three times with the populations of uranium, niobium, and both uranium and niobium as separate instances of the same sample. The sample can be clearly observed to have not separated into distinct phases of niobium rich and niobium depleted zones as would be expected from a spinodal decomposition or cellular decomposition reactions.

Figure 5.26 shows the distribution of niobium nearest neighbour atoms extracted from the needle shown in Figure 5.25. The distribution of niobium atoms (and therefore also uranium) is almost exactly in keeping with that expected from a perfectly random distribution.

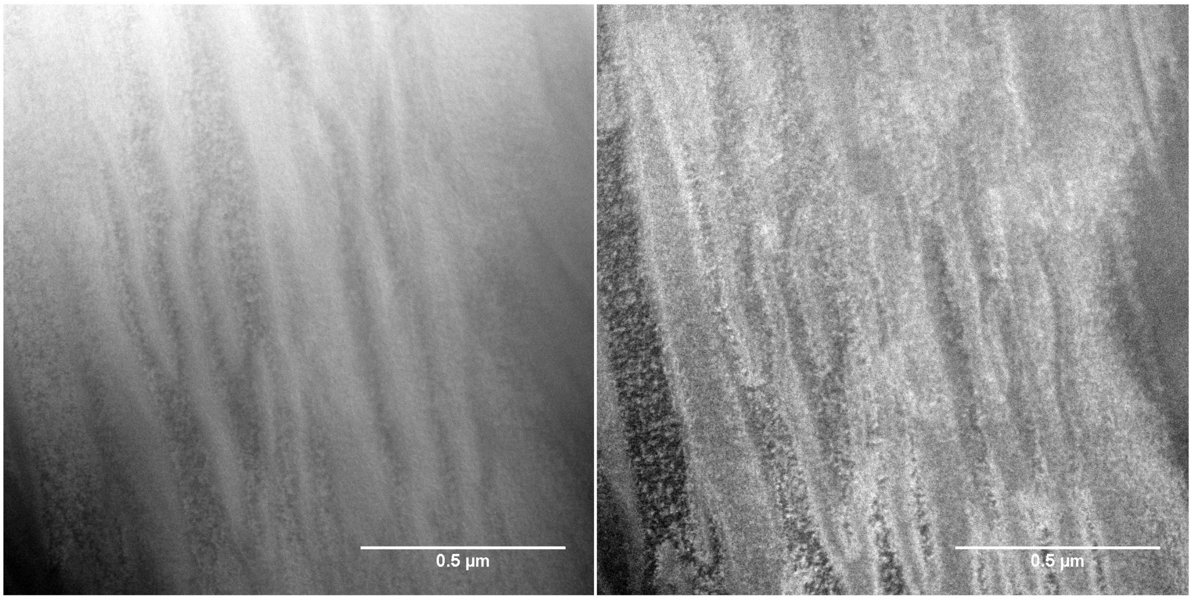

Figure 5.19: Complementary HAADF and MAADF images of the UNb7 alloy aged at 150 °C for 1500 hrs.

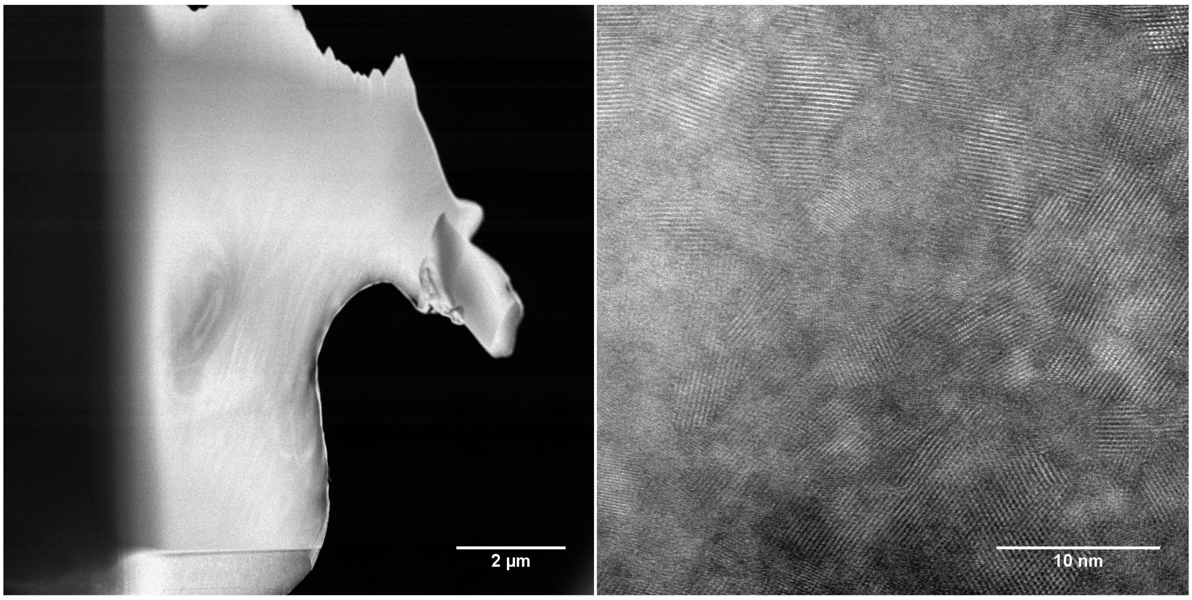

Figure 5.20: MAADF overview and HAADF atomic resolution TEM image of the UNb7 alloy aged at 150 °C for 1500 hrs.

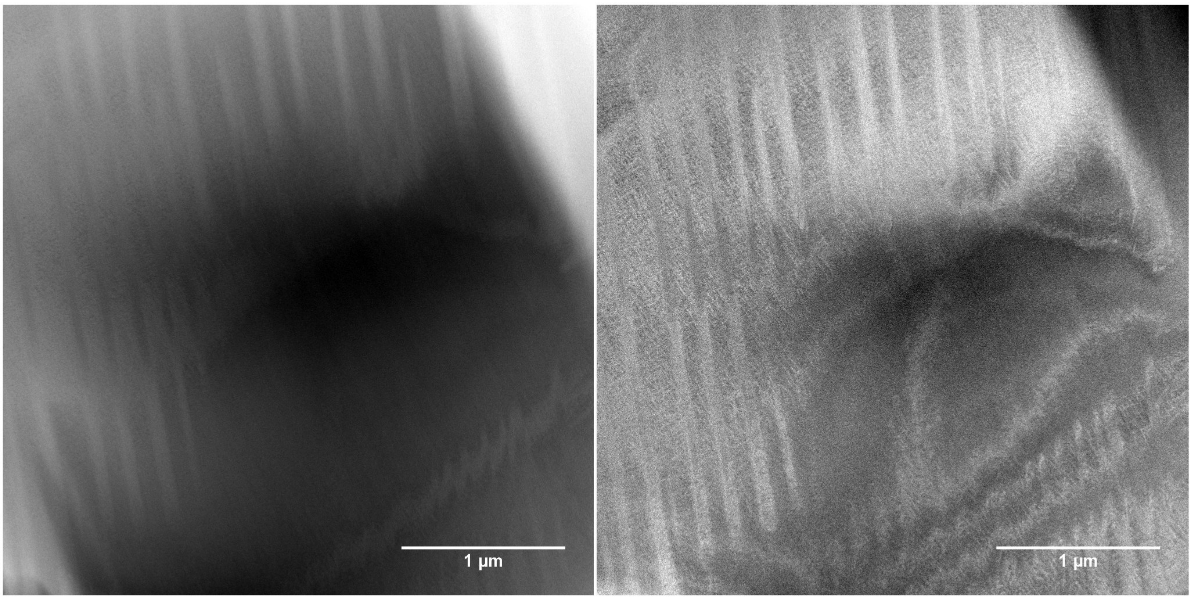

Figure 5.21: HAADF and MAADF, left and right respectively, TEM images showing twinning in the 5000 hr aged UNb7 sample.

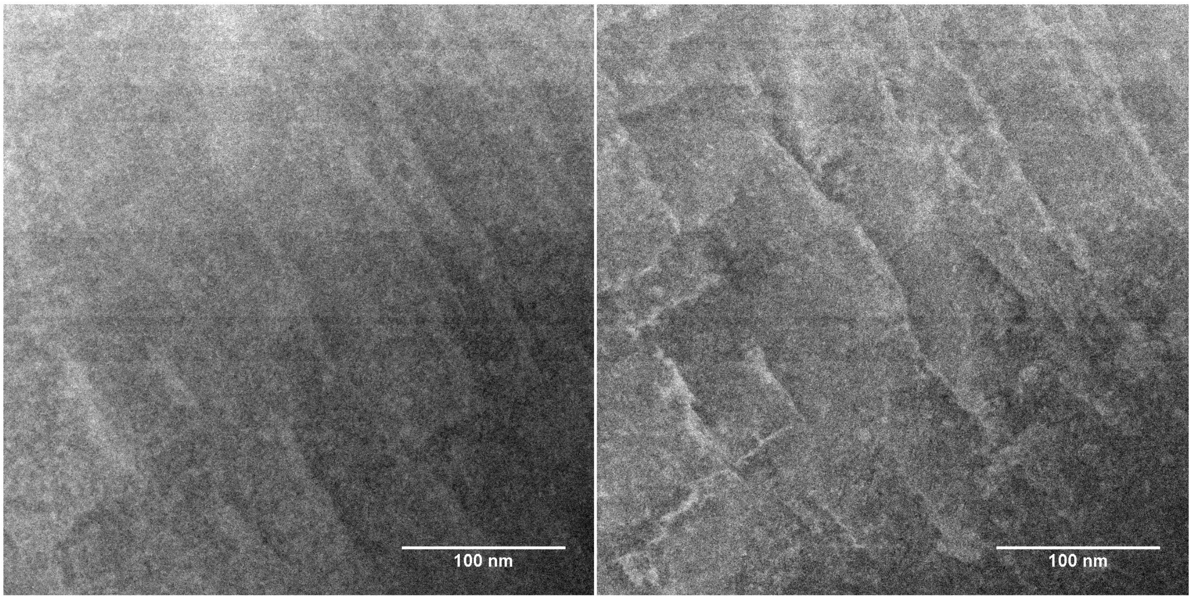

Figure 5.22: HAADF and MAADF, left and right respectively, TEM images showing stacking faults in the 5000 hr aged UNb7 sample.

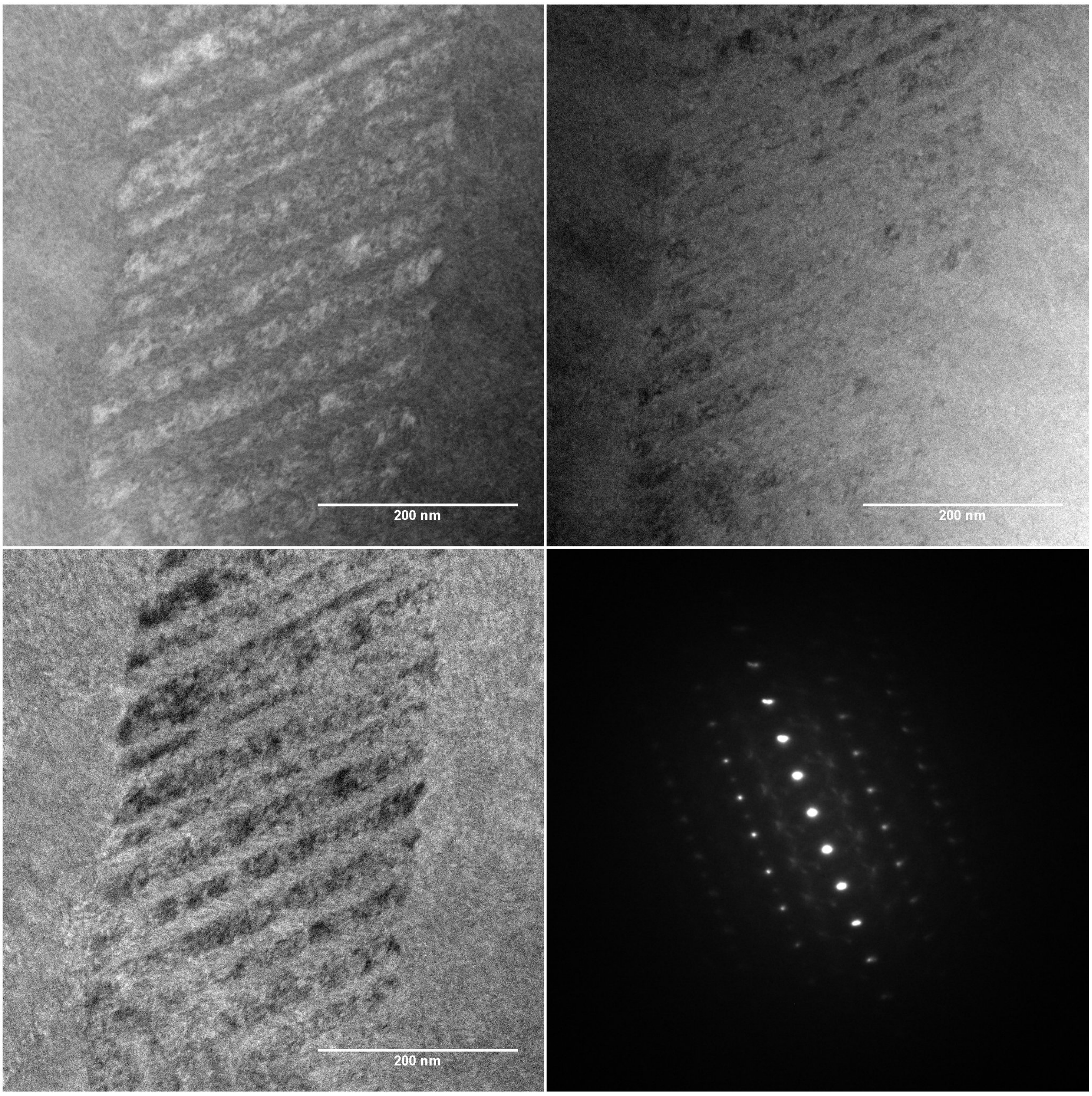

Figure 5.23: BF, HAADF and MAADF TEM images and a SAED pattern (top-left, top-right, bottom-left and bottom-right respectively) of the UNb7 alloy aged at 150°C for 5000 hrs. Information pertaining to the scale for the diffraction pattern in the bottom right panel has been lost preventing accurate indexing of this structure.

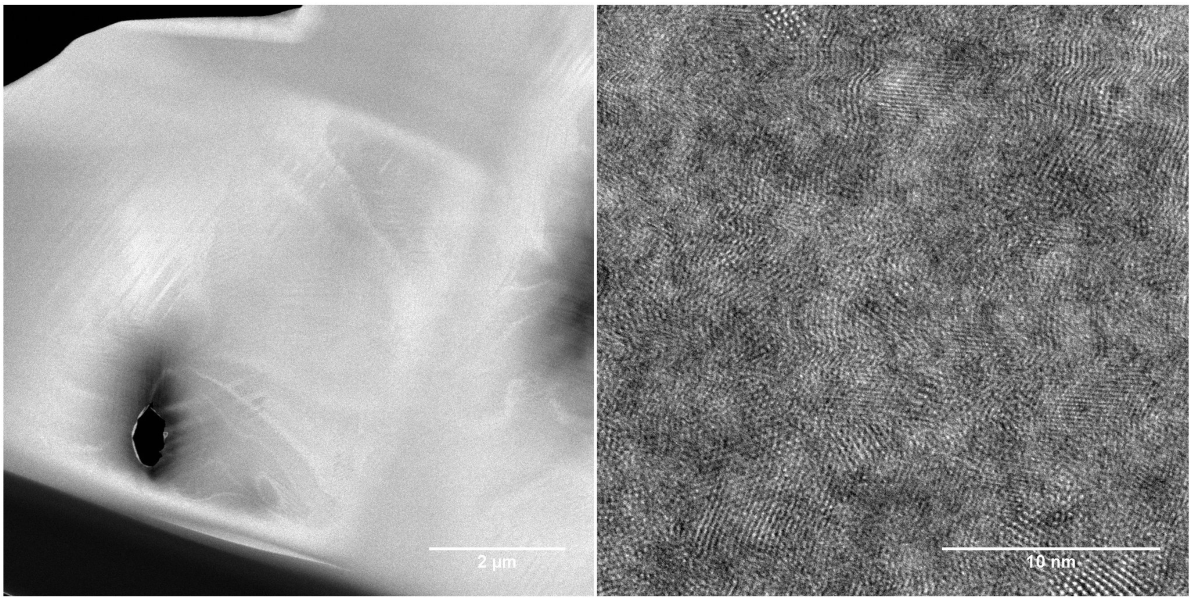

Figure 5.24: 5000 hr aged UNb7. MAADF of foil on left and HAADF of atomic resolution image.

5.4 Discussion

Mechanical trends in the unaged versions of these alloys are generally in keeping with those reported in the literature [30, 279]. However, Brown *et al.* reported a significantly higher elastic modulus in the UNb7 alloy (54 ± 5 GPa) compared to that established here (18.6 ± 0.2 GPa) [31]. But Brown *et al.* also show a plot of hardening rate ($d\sigma/d\varepsilon$) that appears to agree with this lower value relatively well. This appears to be due to disagreement in the very initial shapes of the curves, possibly affected by the style of testing as Brown *et al.* used compression testing [31]. Clarke *et al.* showed differences in the initial behaviour of the U-14 at. %Nb alloy under tensile and compressive strains [52]. Strain rates were relatively similar. Before the onset of plastic deformation and subsequent development of necking, engineering and true stress-strain plots should be in accordance. Figure 5.4 shows that the computational methodology employed in the analysis of the stress strain curves (taking the tangent or physical gradient) picks the greatest possible value of the gradient as the Young's modulus.

Under low temperature ageing, both the UNb5 and UNb7 alloys strengthen along with concomitant losses in ductility and toughness, common features in the vast majority of strengthening mechanisms [210, 285]. Similar effects are also seen in the UNb6 alloy [30]. The strengthening observed by tensile tests is also reciprocated in hardness measurements enabling the establishment of the relation between the two. The ability for strain hardening is lost after the initial ageing treatment and yield points increase. This likely implies that the type of dislocations produced by work hardening are inhibited from forming in the aged material resulting in premature fracture at roughly the point of the start of the strain hardening in the unaged alloy.

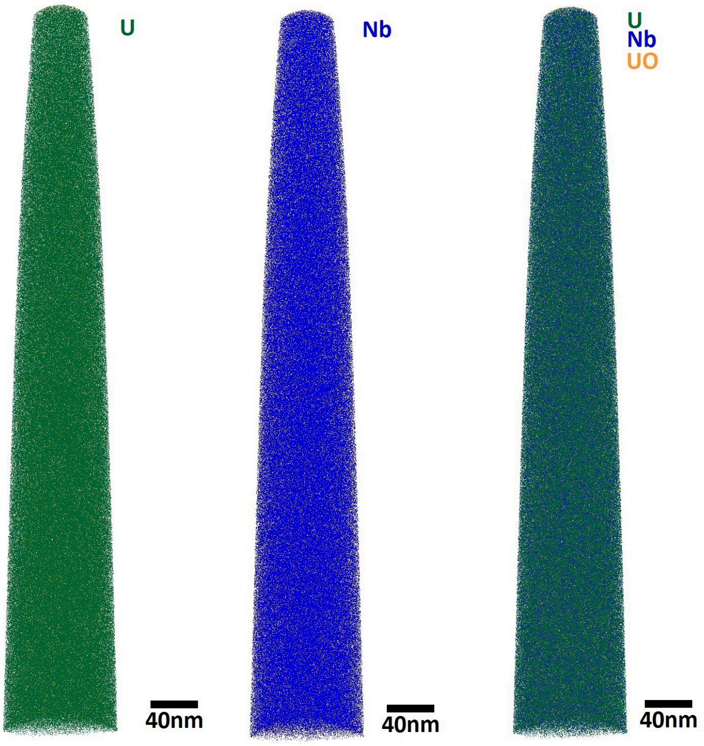

Figure 5.25: An atom probe tomography needle of the UNb7 alloy aged at 150°C for 5000 hrs, as viewed by three reconstructions of the same specimen. The distribution of uranium and niobium can be seen as still highly uniform with no signs of phase separation having taken place.

Brown *et al.* showed that, in accordance with conventional SMA behaviour, the 'austenitic' version of the alloy (γ°) in the vicinity of the transition accommodates recoverable strain up to the yield point through 'motion of existing twin boundaries' and a stress-induced γ° to α'' phase transformation [31], that has also been identified by Vandermeer and Zhang *et al.* [276, 301]. The 'martensitic' unaged UNb5 alloy (α'') shows similar behaviour converting the as-quenched to a detwinned α'' phase microstructure, during the 'easy-flow' portion of the curve. Using aged samples, Brown *et al.* were also able to show that the mechanisms active in accommodating deformation up to the yield point are invariant with low-temperature ageing [31]. However, movement of pre-existing twins and reorganisation into a detwinned environment requires increased driving stresses with ageing. This is separated from the initiation of 'secondary twinning and dislocation mediated plasticity' which are almost unaffected by ageing and exist after the yield point ($\varepsilon \approx 5\,\%$). It was suggested that interfacial defects are unlikely to be occupying the lowest possible energy configurations in the unaged material following rapid quenching. They propose low temperature ageing drives a rearrangement of variant interfaces to lower energy states expected to be less mobile under straining increasing resistance to motion resulting in higher yield stresses. The data shown here is consistent with that of Brown *et al.* and various

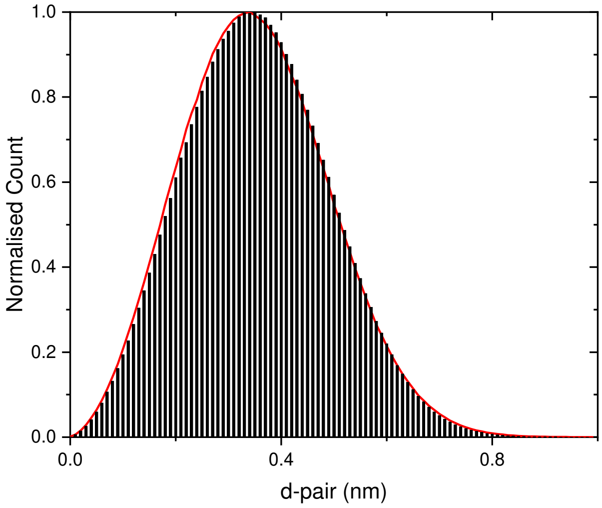

Figure 5.26: Nearest neighbour distribution of niobium atoms in the UNb7 alloy aged at 150°C for 5000 hrs. Mean position was calculated to be 0.3193 ± 0.0009 nm, which is very close to the randomised distribution shown by the red line.

other UNb ageing studies conducted at similar temperatures and durations [31, 51, 105, 279].

Zhang *et al.* followed up on Brown *et al.* with a similar study, also directed at examining the sources of strengthening in low temperature (100 °C) aged α'' phase UNb alloys [298]. Migration of defects such as vacancies and dislocations to twin boundaries were assessed to be responsible for an increase in twinning-detwinning resistance in *loose* agreement with Brown *et al.*, Figure 5.27. Although the α'' phase was established as ultimately unchanged with ageing, anisotropic intergranular strains were found to have decreased at 100 °C compared to room temperature.

XRD patterns displayed decreased microstrain in the α'' phase of the aged UNb5 and UNb6 alloys, Figures 5.8 and 5.9, which may be indicative of diminishing twin interfacial energies as a result of twin rearrangement or defect migration. The decrease in microstrain is observed after the first ageing treatment in keeping with stress-strain curves which do not show a large amount of variation in the aged material until the final curve at 21600 hrs. However, higher temperatures might be expected to facilitate twin movement or defect migration more easily reducing microstrain to a greater extent than lower temperatures. This is contrary to what was observed in the UNb6 alloy and with ageing, microstrain appears to grow again in the UNb6 alloy.

Fitting of UNb7 XRD patterns suggest an increasing contribution from the α'' phase, Figure 5.12, and increasing microstrain in this phase, Figure 5.10. With the previous paragraphs in mind, these results would suggest that reorientation of twin variant interfaces through low temperature ageing is capable of converting some of the γ° phase material into the α'' phase. It

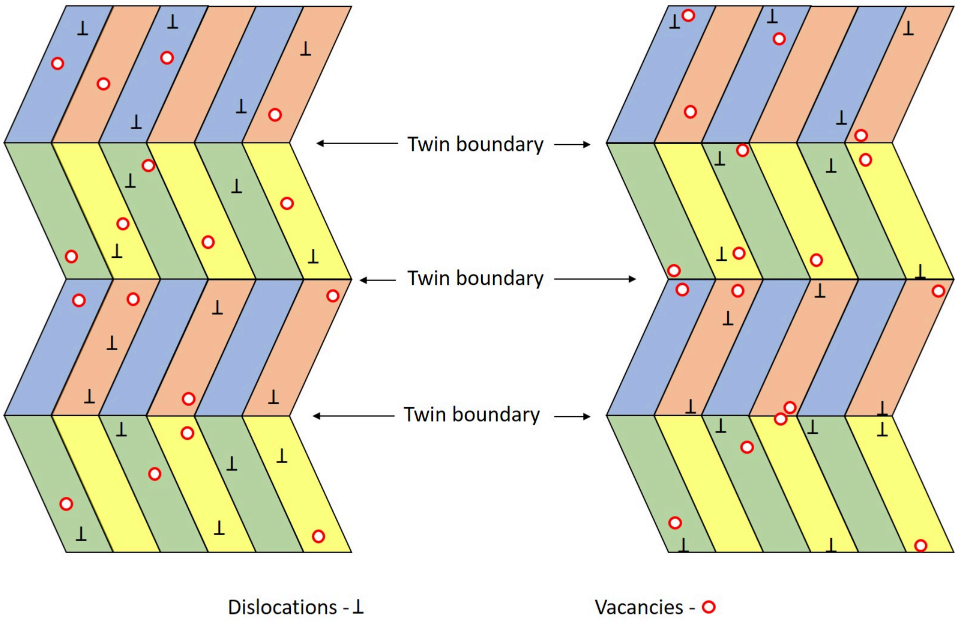

Figure 5.27: Zhang *et al.*'s proposed defect migration within the twin variant structure mechanism. The left side shows unaged (as-quenched) twins, whereas the right side represents material that has been thermally aged promoting defect migration to twin boundaries. Image reproduced from Zhang *et al.* [298].

would seem very unlikely that migration of defects to twin boundaries would be able to permit a phase transformation. Given the close relationship inherent between austenite and martensite phases, small strains are required to force the material to undergo such a transition and this can be observed to occur in unaged materials under macroscopic strains up to 4 % in stress induced transformations [31, 276, 301]. Carpenter and Vandermeer derived the description of the relationship between the α'' and γ° phase [38]. Such a reaction would be expected to increase hardness and strength (martensitic tendencies) and should be consistent with the idea that the lower energy microstructural solution would inhibit motion resulting in higher yield points and a greater Young's modulus, which is observed.

Whilst the patterns are reasonably well modelled and fit statistics are ultimately limited by the quality of the data, there are reasons to believe that alternative models may provide better descriptions of the state of the alloy. Volz *et al.*'s use of Rietveld refinement on these materials using similar quality data was limited by issues encountered in producing reliable fits of the microstrain [279]. Volz *et al.* noticed large shoulders on some diffraction peaks that complicated the patterns and suggested the α'' phase was featuring. Volz *et al.* were forced to use isotropic microstrain terms (as was done here) but acknowledges this as a relatively weak description of the peak shapes with planar defects such as stacking faults suggested as being at play. Clarke and Brown have additionally echoed the need for stacking faults to be properly modelled in this system [51]. This is likely to be most essential for the complicated γ° phase (and its short range ordering behaviour) for which it has been more difficult to produce a complete description of the XRD patterns by employing anisotropic microstrains, Chapter 4. The broad α'' phase contributions (another low symmetry structure) result in substantial overlap of phase contributions that may also include preferred orientation effects.

An alternative explanation to the strengthening in the UNb7 alloy that does not rely on a potentially controversial γ° to α'' phase transition with ageing (as increased temperatures would be expected to stabilise an austenitic phase) might be found by comparing to Hall-Petch or grain-boundary strengthening mechanisms. Grain boundaries are conventionally considered to be points at which dislocation propagation is impeded. Twin boundaries would also be capable of disrupting movement of dislocations and so rearrangement of γ° twins, particularly in a way that might decrease the crystallite size, could lead to increasing yield stresses and a decrease in ductility.

Definitively establishing the behaviour of the aged UNb7 between strains of about 2 - 3% is problematic, Figure 5.6. It is unclear from these stress-strain curves alone whether the γ° phase is still capable of transitioning into the α'' phase during this seemingly easy flow regime. An increase in the density of dislocations may disrupt the movement of twin boundaries and preclude the γ° to α'' transition. The turning point between elastic and plastic regimes in stress-strain curves are often non-trivial [44, 157]. Volz *et al.*'s data would suggest that this ability is weakly held on to even at the ageing at 250 °C. Establishing this would require an in-situ straining diffraction study akin to that of Brown *et al.* but applied to the UNb7 alloy.

Brown *et al.* expressed views that proving their hypothesis would require modelling and high resolution TEM. No attempt has been made to embark on the modelling portion, however some high resolution TEM images, including atomic resolution images in Figures 5.20 and 5.24, have been presented here. Ultimately, it does not appear that the images collected here are particularly helpful as the TEM data was collected with the preconception that chemical segregation was the main ageing mechanism, hence a large amount of time spent collecting EDX maps. Few diffraction patterns were collected and calibrations for the few examples collected were ambiguous. Additionally, preparation of foils was poor and would need to be improved, potentially with advanced final thinning stages (such as PIPS II [3]), before high quality investigations coupled with the necessary diffraction measurements would be able to assist in the two goals of determining stacking fault structure and testing the twin rearrangement mechanism hypothesis. Analysis of aged alloys by TEM would require numerous liftouts to account for the heterogeneous microstructure. However, Figures 5.19 - 5.24 show some examples of TEM micrographs of aged UNb7 alloys that might be displaying evidence of an increased number of stacking faults and smaller domain sizes that would constitute a strengthening and stiffening mechanisms potentially meaning that atomic resolution maps are not necessarily required. The prospect of using a technique such as positron annihilation lifetime spectroscopy (PALS) should be considered if the quantification of defects is to be considered as key to further understanding the strengthening mechanism in this alloy system [77, 271].

At best, EBSD maps collected, Figures 5.16 and 5.17 are not of a sufficient size to enable a statistically significant comparison of twin morphology. In the more realistic scenario, twin rearrangement would be on such a fine scale that EBSD would struggle to meet the resolution requirements. Due to large grain size (yet a complex intra-granular microstructure), large maps recorded with a relatively high spatial resolution would be required to ensure an adequate spread of grain orientations and the ability to detect changes to the twin structure. Additionally, UNb7 maps shown here, Figures 5.18, have been indexed with the γ rather than the γ° phase due to the pseudosymmetry problem. It would be an important advancement to be able to index these maps properly using a tetragonal γ° phase. Also, no α'' phase has been successfully mapped in these patterns which needs resolving as fitting unaged XRD patterns shows the α'' phase to feature in the UNb7 alloy. The UNb5 and UNb6 alloys in comparison consist of only the α'' phase which has been shown to lead to strong fitting of EBSD patterns without incurring adverse pseudosymmetry effects, Chapter 3.

Various papers and reports, have postulated that spinodal decomposition (or another diffusional mechanism) was responsible for the obvious changes to the mechanical properties of the alloys [20, 119, 221, 223, 274, 279, 302]. APT results clearly show that these alloys experience strengthening and loss of ductility without any appreciable changes to the chemical environment (*i.e.* a completely randomly mixed substitutional alloy). These results are in line with Clarke *et al.*'s APT investigations into the UNb6 alloy in which phase separation was deemed an improbable explanation and complement Brown *et al.*'s assessment of neutron diffraction peak widths as not indicative of chemical segregation [30, 51]. Any minor chemical segregation that might have happened (and would be expected to a limited extent due to the miscibility gap) would not be able to explain the substantial changes that have occurred to the mechanical properties as a result of ageing. Original TEM images, Figure 5.2, from which it seems the conclusion of spinodal decomposition was drawn are likely to have been affected by beam damage. An alternative method of confirming lack of chemical segregation might include small angle x-ray or neutron scattering (SAXS/SANS) which has been reported as having been carried out by Zhang *et al.* [300].

Given the original XRD data for the UNb7 alloys, Figure 5.1, it was postulated that the clear resemblance of an α'' phase in the 5000 hr aged specimen (that could be fitted as such by Rietveld refinement) implied an isothermal martensitic reaction occurs at low temperatures transforming the γ° to the α'' phase [249]. In the UNb5 alloy, this reaction would be furthering martensitic tendencies. Remeasured data however, whilst not discounting this theory (and maybe the XRD summary plots, Figures 5.8 - 5.12, could be pointing towards this being the case) prove the evidence for this to not be nearly as certain for this as first assumed.

5.5 Conclusion

This work has reaffirmed that in agreement with recent research, the evidence for chemical segregation of alloy constituents through a phase separation mechanism is scant. Whilst solute segregation is a fairly ubiquitous strengthening mechanism in many binary and ternary alloy systems where a miscibility gap exists, the twinning-detwinning mechanism inherent in these SMAs becomes more difficult to activate - thought to be due to defect migration to twin boundaries.

Previous works on these alloys appear to have been affected by sample preparation leading to initial conclusions of spinodal decomposition. Follow up investigations were therefore carried out to establish the origins of chemical segregation. Meanwhile, foreign national labs have made strong advancements in this field, benefited by the use of in-situ mechanical testing rigs on neutron diffractometers, and should be seen as the standard in the study of the low temperature reaction of these alloys going forward. Particularly, since preparation of these alloys is virtually an unimportant consideration.

Some evidence might be offered in favour of the theories proposed by Brown *et al.* and Zhang *et al.* for example by examining the plots of microstrain as a function of ageing time. Diffraction patterns however are inherently complex and a HRTEM assisted investigation of stacking faults is required to ensure the validity of some elements of the Rietveld refinements.

CHAPTER 6

INVESTIGATIONS INTO THE HIGH TEMPERATURE AGEING OF THE UNB5 AND UNB7 ALLOYS

This chapter examines the transitions that occur in the metastable uranium-niobium alloys in the vicinity of the eutectoid at high temperatures. It is well known, particularly from dilatometry measurements taken on these and similar alloys that the reactions at higher temperatures are swift, making lab based diffraction studies an unsuitable means of investigation. Ex-situ metallography studies have also been widely used to examine the structure and morphology of the aged materials, though this provides little information on the dynamics of the reactions. With the advent of the modern synchrotron, a complementary study capable of collecting diffraction data with high spatial and time resolutions was sought. Crucial to this effort is the Debye-Scherrer geometry, large 2D area detectors and very high energy x-rays. This chapter details the results obtained in a 6 day long experiment focused on high temperature reactions of U-Nb alloys at the I12 beamline, Diamond Light Source, Oxfordshire.

6.1 Introduction

Study of the metastable uranium-transition metal binary and ternary alloys has mostly focused on reactions at the higher temperatures of the $\alpha + \gamma$ phase miscibility gap, generally between 300 °C and the eutectoid at 647 °C [20, 57, 61, 67, 134, 162, 195, 273, 274]. In this region, it is generally accepted that there are at least two distinct reactions that occur under isothermal ageing conditions [61]. From a thermodynamic perspective, the miscibility gap dictates that any metastable alloy present in this region (below 647 °C) will eventually progress towards a two phase arrangement of α-U + γ-Nb.

At higher temperatures, the diffusional $\gamma \rightarrow \alpha$-U + γ-Nb reaction has been examined by a variety of in-situ techniques including resistivity and dilatometry [199, 274], but predominantly via follow-up microscopy and diffraction approaches [51, 197, 230]. This reaction is particularly important for research into the behaviour of U-Mo and U-Nb-Zr γ phase alloys which are currently used as fuel in some research reactors and have been proposed as potential candidates for future fuels [233]. These alloys however display strange behaviour under irradiation through the stabilisation of the γ phase, in what has been hypothesised to be displacement spike events [23], making the situation more complex. Primarily, this transformation would be relevant to UNb alloys during manufacture.

Dean's evaluation of the ageing in a U-7.5 wt% Nb -2.5 wt%Zr (mulberry) alloy, Figure 6.1, showed a reaction extending from the eutectoid (~ 650 °C) to 400 °C and a separate reaction existing at temperatures below 400 °C [61]. Investigations into the U-Nb system have also shown similar behaviour permitting equivalent isothermal decomposition diagrams to be constructed [105]. However, a distinctive property of the U-Nb system is an absence of intermetallic phases [216]. In similar systems, structures such as U_2Mo, UZr_2 and UTi_2 may be found [216]. Due to the extreme width of this gap (bound at room temperature by almost pure α uranium at one end and 76 at. % Nb-24 at. % U at the other), the difference in density between these phases is considerable. But more importantly, the ability for chemical segregation is high. Not only does this reaction completely change the starting phase of the material, thereby drastically altering its mechanical properties, constituents nearly completely separate leaving corrosion prone uranium unalloyed in the material. The lever rule may be applied to determine the expected final phase fractions for a given initial composition.

Studies of the U-Cr system by Townsend and Burke using resistivity and metallography techniques showed that the upper reaction can be split into two mechanisms [268]. This view is somewhat also echoed in Hackenberg *et al.*'s assessment of the U-Nb system in which a 5 component isothermal decomposition diagram was proposed [105], Figure 6.2. 3 'nonlamellar' decomposition mechanisms are described which converge on discontinuous precipitation and coarsening mechanisms at greater timescales.

White, and Townsend and Burke showed that the reaction at the lowest temperatures (below 300 °C) related to an isothermal martensitic transformation over the course of a few minutes [268, 288]. White's U-Cr alloys possessed lower alloy contents of up to 4 at. % Cr (eutectoid of β-U → α-U + Cr exists at 99.1 at. %U, 630 °C) which produced the β phase on quenching. Vandermeer similarly showed that isothermal ageing of the U-14% Nb alloy above the martensitic start temperature (327 °C) produced the martensitic α'' phase. Vandermeer's investigations used primarily dilatometry with some follow up XRD and microscopy. Vandermeer came to the conclusion via 'indirect evidence' that precipitation of niobium is responsible for the transformation to the α'' phase. Hackenberg *et al.*'s equivalent reaction is 'NL2' in which chemical diffusion is present on very small length-scales, such that it can only be observed with atom probe microscopy [20, 51].

Due to the rapid speed of these reactions, in-situ techniques by methods other than dilatome-

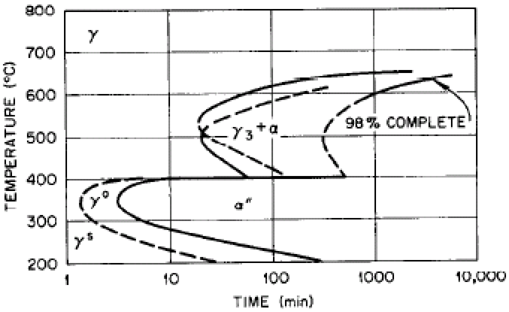

Figure 6.1: Isothermal transformation diagram of the U-Nb-Zr alloy. Image from Dean [61]. More isothermal transformation diagrams for uranium alloys may be found in the 'Atlas of time-temperature diagrams for nonferrous alloys' [282].

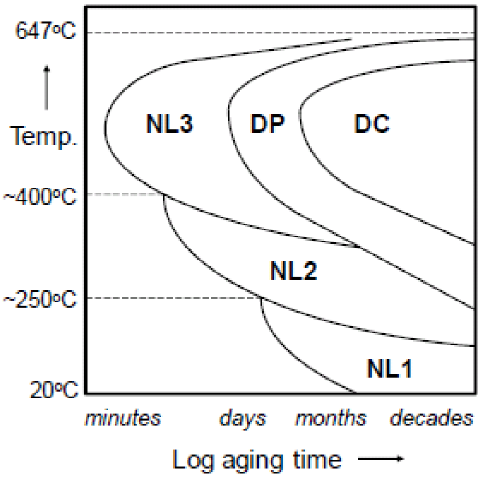

Figure 6.2: Isothermal transformation diagrams diagram of the U-Nb alloy. Image from Hackenberg *et al.* [105].

try and resistivity have not received much attention. Conventional lab-based XRD measurements (using Bragg-Brentano geometries) for these alloys would require typically at least 30 mins for a full scan. Additionally, low energy x-rays are very surface sensitive in uranium and inevitable oxidation of the sample at temperature would obscure the results. Neutron diffraction is not surface sensitive but takes a longer time than x-rays to collect the same data. The modern synchrotron permits time resolved in-situ experiments with high energy x-rays, using the Debye-Scherrer geometry and a 2D detector.

Using in-situ capabilities at the Diamond Light Source, objectives of this experiment and chapter were split across two routes, examining the high and mid temperature reactions. The UNb5 and UNb7 (12.1 and 17.2 at% Nb) alloys used in this study provided the closest available approximations to α'' and γ° phase materials.

6.2 Experimental Configuration

The high temperature ageing behaviour of the UNb5 and UNb7 alloys was investigated at the I12 beamline at Diamond Light Source (DLS) using a bespoke experimental setup. The I12 beamline was designed for imaging and diffraction capabilities of large, dense objects in complex sample environments with in-situ capabilities [66, 69]. I12 also goes by the moniker Joint Engineering, Environmental, and Processing (JEEP) to reflect its intended purpose. High x-ray energies (53-150 keV) make this beamline particularly attractive for the study of very dense materials such as

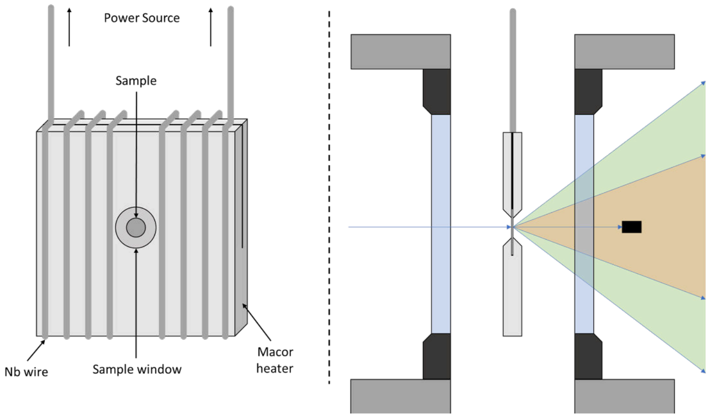

Figure 6.3: Elements of the experimental configuration used for the in-situ experiment at the I12 beamline. The left hand side shows the Macor sample holder and heater. The right hand side shows its position within the evacuated UHV experimental cell.

uranium and its alloys and compounds [242–246]. As the uranium K-edge sits at 115.606 keV [19], photon energies just below minimise the absorption of x-rays and promote transmission and scattering processes. 112 keV was used to ensure that the beam energy was sufficiently clear of the absorption edge.

A custom sample environment which permitted heating of samples under high vacuum conditions was employed to preclude oxidation of the specimen, Figure 6.3. A pyrex cell provided the 'x-ray window' within which the sample was located and through which the x-rays were directed. The sample was encased in a Macor 'heating block' that had been designed in house and crafted using a diamond wire saw. Niobium wire, heated resistively by a TecTra HC 3500 Heater Controller, was wound into grooves cut into the Macor heating block, heating the Macor and the foil in turn. The heating block additionally housed a Type K thermocouple which enabled measurement of the temperature. Calibration was performed using nickel foil to relate the temperature at the point of the thermocouple to that at the foil/sample's position. The heater was suspended in position by the power feedthroughs and Nb wire. The entire apparatus was pumped out by a Pfeiffer HiCube 80, comprising a turbomolecular pump backed by a diaphragm pump. The setup was constructed from CF UHV components permitting a vacuum that could reach 10^{-7} mbar cool and 10^{-5} mbar when heated.

Foils measuring approximately $4 \times 6 \times 0.5\,\mathrm{mm}^3$ were produced through mechanical polishing of unaged UNb5 and UNb7 alloys to a $1/4\,\mu$m finish. Electropolishing of the samples was not deemed to be necessary as the work hardening depth is insignificant in comparison to the thickness of the foil. Contributions to the diffraction patterns of this region would be negligible. If the work damaged layer is estimated to extend up to 200 nm into the material, the contribution of this to the patterns would be approximately 0.08 %.

Due to the limitations of the tomography in being able to resolve features below a micron, samples were also subsequently examined using the FIB and STEM techniques through cross sections and liftouts of foils.

6.2.1 Diffractometer Calibration

The diffractometer was calibrated using CeO_2 powder with a defined lattice parameter of 5.4113 Å using DAWN [18, 86]. CeO_2 is a suitable calibration due to its high crystallinity, numerous diffraction peaks of high multiplicity (fluorite structure) and lack of any higher oxides. Powdered CeO_2 removes all texture, producing full Debye-Scherrer rings, useful for adjusting beamline imperfections such as yaw, pitch and roll. However, the main purposes of the calibration is to determine the distance between sample and detector, and characterise the instrumental broadening of the beamline under the settings used for this experiment. Figure 6.4 shows a CeO_2 calibration diffraction pattern highlighting the uniformity of the rings.

Figure 6.5 shows the azimuthally integrated data with fit. Individual, independent peak fitting was employed for the determination of instrumental resolution parameters as knowledge of the crystal structure is not necessary, only peak positions. Uncorrelated peaks negate any 2θ error arising from the flat panel detector and increases the reliability of the fit.

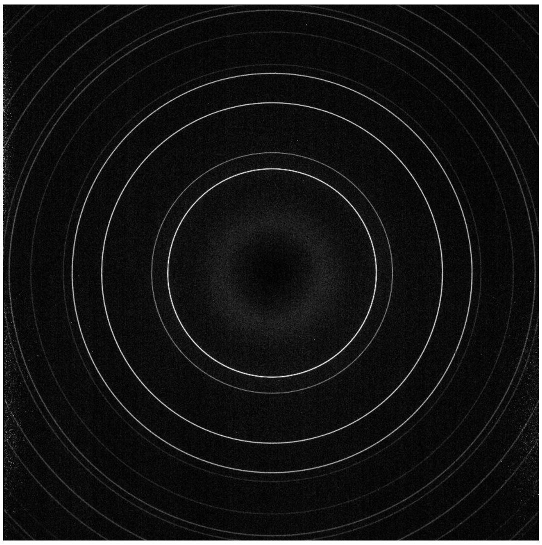

Figure 6.4: Diffraction pattern of the CeO_2 calibration as collected by the 2D detector. The Debye-Scherrer geometry has produced rings that upon azimuthal integration return a 1-dimension diffraction pattern.

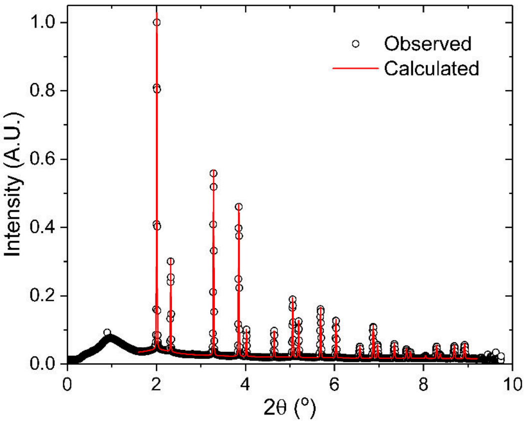

Figure 6.5: Fitted diffraction data of the CeO_2 calibration. The weighted pattern residual, R_{wp}, was minimised at 2.90%. The bump at 1° represents an amorphous glass peak and so was not included in the fit.

Peaks were modelled by a Pseudo-Voigt function containing both Lorentzian and Gaussian peak shape contributions. Instrumental contributions are conventionally regarded to manifest themselves as a Gaussian distribution, whereas sample broadening usually takes the form of a Lorentzian function. Both crystallite size effects and microstrain conventionally generate

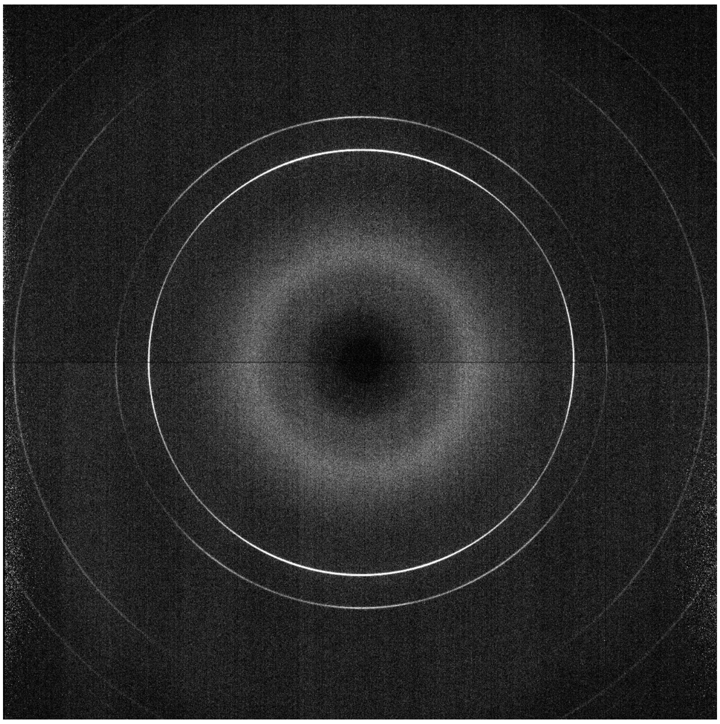

Figure 6.6: Diffraction pattern of the nickel foil. Rings show evidence of texture. The background of the glass is present in this pattern producing the diffuse ring in the centre of the image.

Lorentzian peak shapes though crystallite size effects are generally accepted to induce constant broadening throughout the pattern as opposed to strain which increases with angle.

6.2.2 Heater Calibration

Nickel foil was used in place of the uranium foil samples for the calibration of the heater. A high symmetry (*fcc*) structure with a relatively well known and high thermal expansion coefficient enabled precise measurements of the changing lattice parameter with temperature. Additionally, since diffraction patterns were sufficiently strong, the detector distance was increased to improve diffraction angle resolution. A small grain size and lack of very strong crystallographic texture in the foil meant that the XRD patterns received were full Debye-Scherrer rings, Figure 6.6. The nickel pattern was itself calibrated against ceria powder (NIST 660c) to determine the distance between the sample and the detector, d. A full description of the method of performing the Ni calibration can be found in Appendix A.

6.2.3 Temperature Profiles

Two UNb5 alloy specimens and three UNb7 alloys were examined over the course of the experiment. Additionally, two UNb3 samples were also taken, however, they were found to have phase separated. The first UNb7 alloy was used to gauge reaction rates and test diffraction settings, particularly at temperature.

To effectively explore the time temperature transition landscape, isothermal heating levels of 350 and 500 °C were initially sought. In actuality, runs were performed at 380 and 510°C. Samples were also re-examined at 450°C following the 380°C runs. Schematics of the temperature profiles employed for the UNb5 and UNb7 alloys are shown in Figures 6.7 and 6.8.

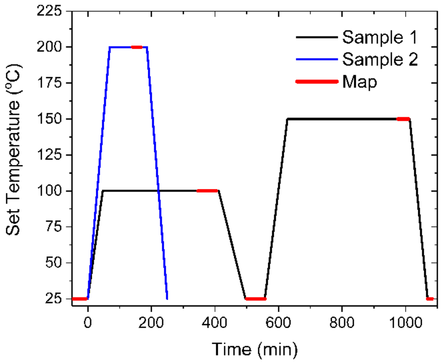

Figure 6.7: Schematics of the temperature profiles of the UNb5 alloys during this study. Ageing treatments similar to those applied to the UNb7 alloy were used for the UNb5 alloy for easy comparison. Sample 2 was found to have fully transformed by the 200 minute mark enabling the heating to be stopped and time devoted to heater calibration.

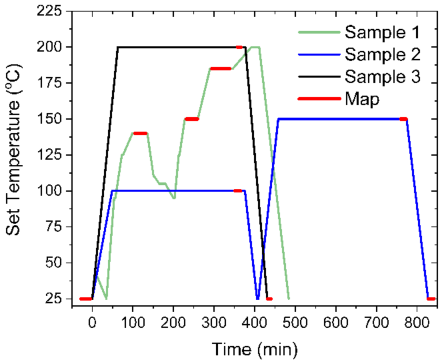

Figure 6.8: Schematics of the temperature profiles of the UNb7 alloys during this study. Sample 1 was used to gauge the behaviour of the alloy and determine rough rates for transitions. Samples 2 and 3 experienced the final ageing profiles with nominal 'set temperatures' of 100, 150 and 200 °C that had been intended to last roughly 7 hours in total with a 5 hour isothermal treatment and approximately hour long heating and cooling ramps.

6.3 Results

6.3.1 UNb5 Unaged State

From a single frame measuring 0.2 × 0.2 mm^2, the UNb5 alloy is relatively strongly textured, Figure 6.9. Using the 8th order spherical harmonics model, the texture index for the initial frame of the heating scan was measured at $J = 1.609$. By using the stepping motors to collect a 121 frame (11 × 11) map, Figure 6.10, and slicing the data using 10° azimuthal slices the statistic was reduced to 1.262 with a standard deviation of 0.133 within these slices. Overall, using the cylindrical texture model, the texture index for a full 2 × 2 mm^2 map was 1.087. This represents a relatively random distribution of crystallite orientations within this sample over this increased volume in which deviations in peak intensity can be relatively easily accounted for using preferred orientation corrections. An IPF for the UNb5 alloy in the unaged state obtained from applying the texture fit to Figure 6.10 is shown in Figure 6.11. The fitted pattern produced from an integrated map in shown in Figure 6.12.

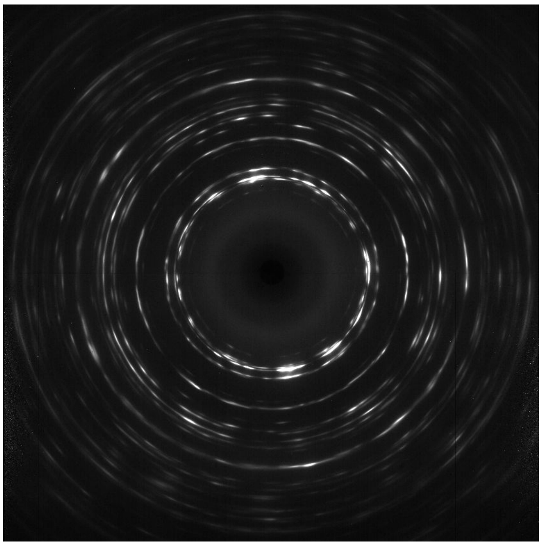

Figure 6.9: The diffraction pattern of a single frame representing an area of $0.2 \times 0.2\,\mathrm{mm}^2$ in the UNb5 alloy.

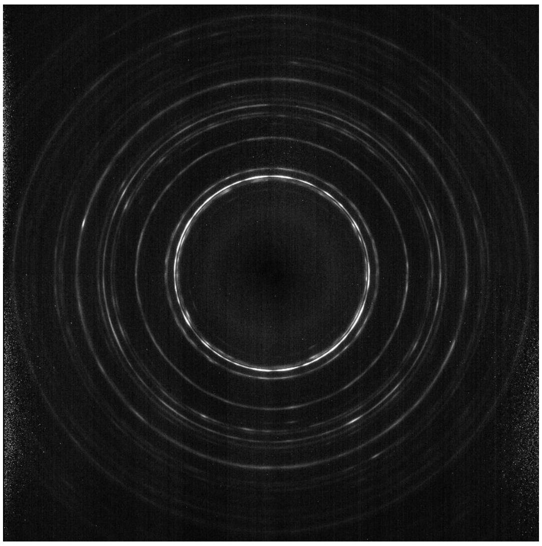

Figure 6.10: The summed diffraction pattern of all frames in the 121-frame map representing an area of $2 \times 2\,\mathrm{mm}^2$ in the UNb5 alloy.

Lattice parameters of the UNb5 alloy in the initial state were a = 2.92 Å, b = 5.85 Å, c = 5.04 Å and $\angle\gamma = 91.23°$. In comparison, the lattice parameters in the previous section were all found to be slightly smaller by 1 - 2%. Discrepancies might be explained by difficulties in calibrating this particular sample. The mean microstrain determined from this data was 17500 which is slightly smaller than the 20000 found in the earlier chapter. Microstrain (using the generalised model) produced very similar distributions for both fits. The differences may be a result of natural variation between grains, differing quality in the characterisation of instrumental parameters or that this data, which is significantly less surface dependent, represents the true nature of the bulk. Therefore, the relative changes in lattice parameters and microstrain is more important than the absolute values.

The patterns were well fitted by a single α'' phase. Using the summed frames data, a pattern residual of $R_{wp} = 3.52\,\%$ was achieved with phase residuals of $RF^2 = 5.31\,\%$ and $RF = 3.35\,\%$.

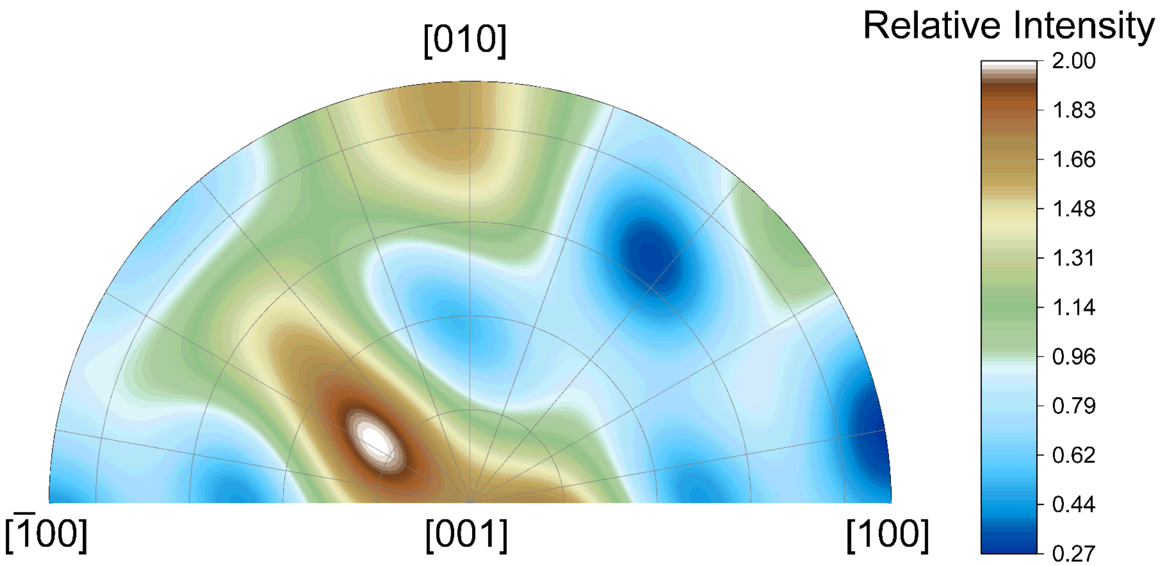

Figure 6.11: An equal area IPF of the texture in the UNb5 alloy in the initial, unaged state. The contour plot is measured in multiples of random distribution.

6.3.2 UNb5 Transient

6.3.2.1 400 °C

Heating the UNb5 alloy to 400 °C was not sufficient to significantly alter the crystallographic configuration of the alloy. The α'' phase remained the sole phase in the pattern and experienced an overall volume expansion, despite featuring a negative thermal expansion coefficient in the b axis. Upon reaching 400 °C, the lattice parameters were then observed to settle throughout isothermal heating, relaxing back towards their original values. Lattice parameters are plotted as a function of time in Figure 6.13. The time taken to reach the maximum temperature was roughly 450 s and is shown on the graph by a vertical line. Heating of the sample was ceased at 24720 s, after which the sample was permitted to cool.

The initial values for this sample were a = 2.9266(3) Å, b = 5.8551(8) Å, c = 5.0526(7) Å and $\angle\gamma = 91.16(1)$ °. Final values were a = 2.9246(8) Å, b = 5.872(2) Å, c = 5.049(1) Å and $\angle\gamma = 91.43(2)$ °. Whilst the a and the c axes are relatively elastic parameters, finishing at roughly the original values, the b axis and the $\angle\gamma$ experience some irreversibility. The $\angle\gamma$ is observed to slightly open as a result of the treatment, increasing by 0.2°. The $\angle\gamma$ acts between the a and b axes and is therefore independent of the c axis. As the a axis is unchanged from the process, the behaviour of the $\angle\gamma$ is linked to that of the expanding b axis. Interestingly, the b axis expands during cooling thereby corroborating a negative thermal expansion coefficient seen in the heating stage. The lattice parameters as a function of temperature throughout the cooling stage are shown in Figure 6.14.

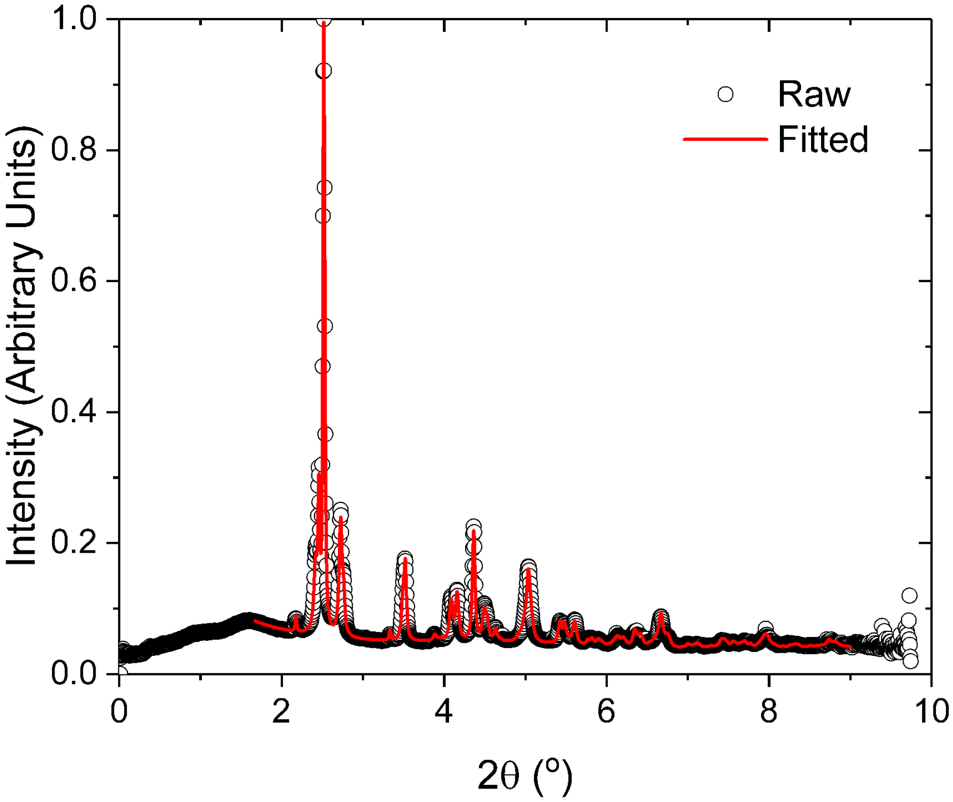

Figure 6.12: Fitted diffraction pattern of the unaged UNb5 alloy. Data is shown by open black circles, the fit by the red line and the residual by the blue line.

Thermal expansion coefficients in each of the axes (and $\angle\gamma$) have been evaluated and are shown in Figure 6.15. Lattice parameters were fitted with a quadratic function as this provided the necessary degrees of freedom to simulate the trends and is easily differentiated, which is required for the evaluation of thermal expansion coefficients. A derivation of the method by which the curves in Figure 6.15 are generated may be found in Appendix B.

Maps were obtained before, during and after heating to 400°C. From these maps, using an identical routine for analysing each data set, the evolving texture in the sample may be evaluated through IPFs, Figure 6.16. The data was gathered from 2×2 mm^2 maps which corresponds to a sampling of a few hundred grains. Maps were gathered from the same area on each occasion. The differences in the Inverse Pole Figures are relatively minor throughout the ageing treatment. Generally, all maps feature a propensity for the [0 0 1] directions and much weaker intensities for the $[2\bar{1}0]$ direction for example. Overall the texture indexes drop from 1.378 to 1.234 to 1.165. This is also reflected in range in the the scales on the figures (measured in multiples of random distribution) which indicate a more uniform texture with ageing. The IPFs point toward a subtle

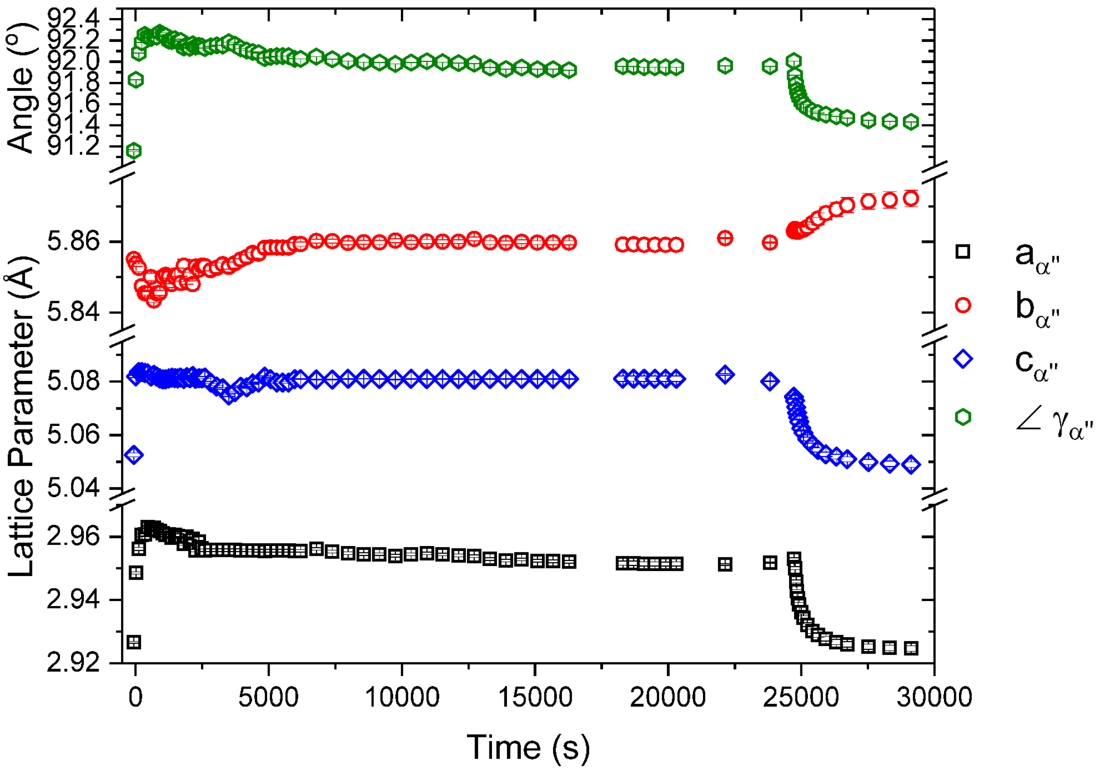

Figure 6.13: Evolution of lattice parameters of the α'' phase for the UNb5 sample heated to 400 °C. The entire cycle is represented here with the heating period extending up to 450 s, the isothermal section lasting until 24720 s and the cooling period lasting until a total time of 29120 s. The negative thermal expansion coefficient in the b-axis may be inferred from the behaviour of the red dots on heating and cooling.

rearrangement of a small percentage of crystallites with ageing.

6.3.2.2 450 °C

When heated to 450 °C, the UNb5 alloy displays a drastically different behaviour to heating to 400°C. Soon after reaching temperature, the 2D diffraction patterns can be observed to develop the start of faint rings that correspond to new α and γ phases. Whilst these rings are still slightly textured owing to the relatively small sampling volume and presently low phase fractions, further ageing leads to more uniform rings as progressively more of the α'' phase is transformed to the α and γ phases through diffusional processes. It is not possible to distinguish whether an intermediate γ^s phase forms during the process as a significant amount of peak overlap is present in these patterns. Figure 6.17 shows the phase fraction compositions of the alloy as a function of

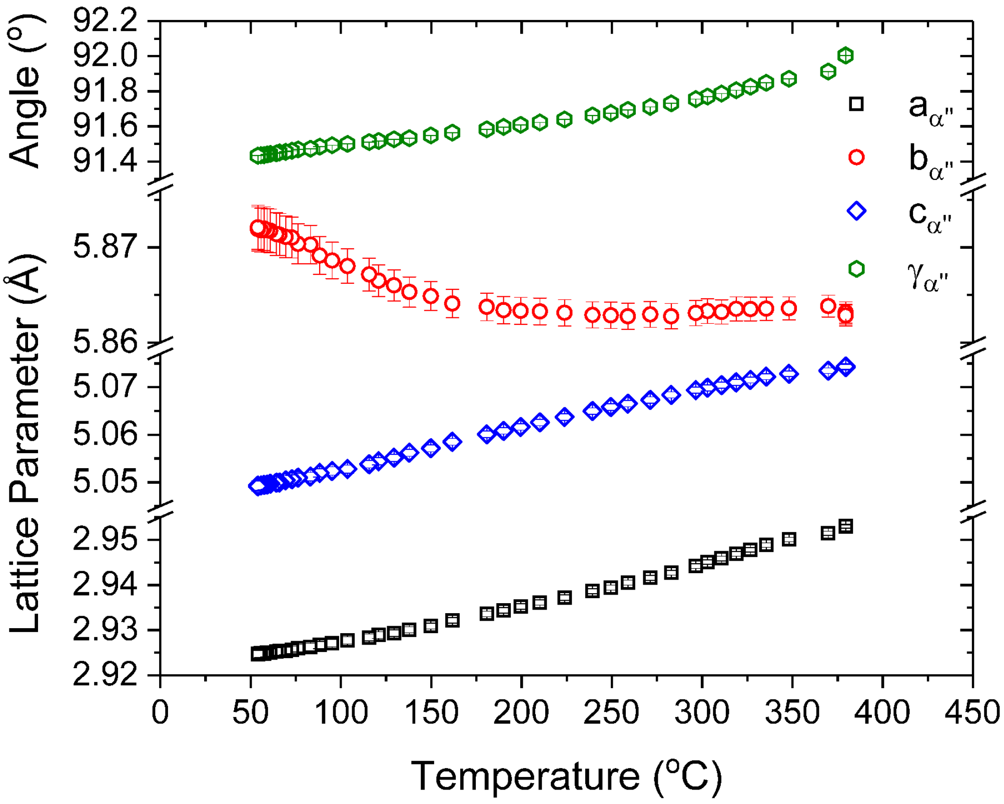

Figure 6.14: Lattice parameters of the α'' phase in cooling in the UNb5 alloy aged at 400°C.

time.

Since the XRD patterns of the α'' and α phases are very similar, the fitting routine struggled to discern between the two phases. Initially, whilst the fraction of the α phase is low, the program greatly overestimates its contribution to the detriment of the α'' phase. The γ phase is relatively undisturbed by this as it possesses an entirely different diffraction pattern. As the only phase in the unaged material ought to be the α'' phase, the early data has been renormalised to reflect this. Data that has been renormalised is shown in grey or pink. Trendlines are based on the fitting of data after 7000 s, the point at which the two patterns of the α'' and α phases become easily distinguishable, but are extended previous to this point. The trendlines generated from fitting the latter half of the data can be seen to adequately satisfy this normalised data.

Figure 6.17 was fitted with exponential decay curves, as might be the expected function for such a reaction. Rate constants for the growth/destruction of these phases are $T_{\alpha''} = 6900 \pm 300$ s, $T_{\alpha} = 6000 \pm 300$ s and $T_{\gamma} = 12600 \pm 1000$ s. It would be expected that in all three cases the rates are equal but magnitudes differ based on the final phase fractions. This is approximately the case for T_{α} and $T_{\alpha''}$.

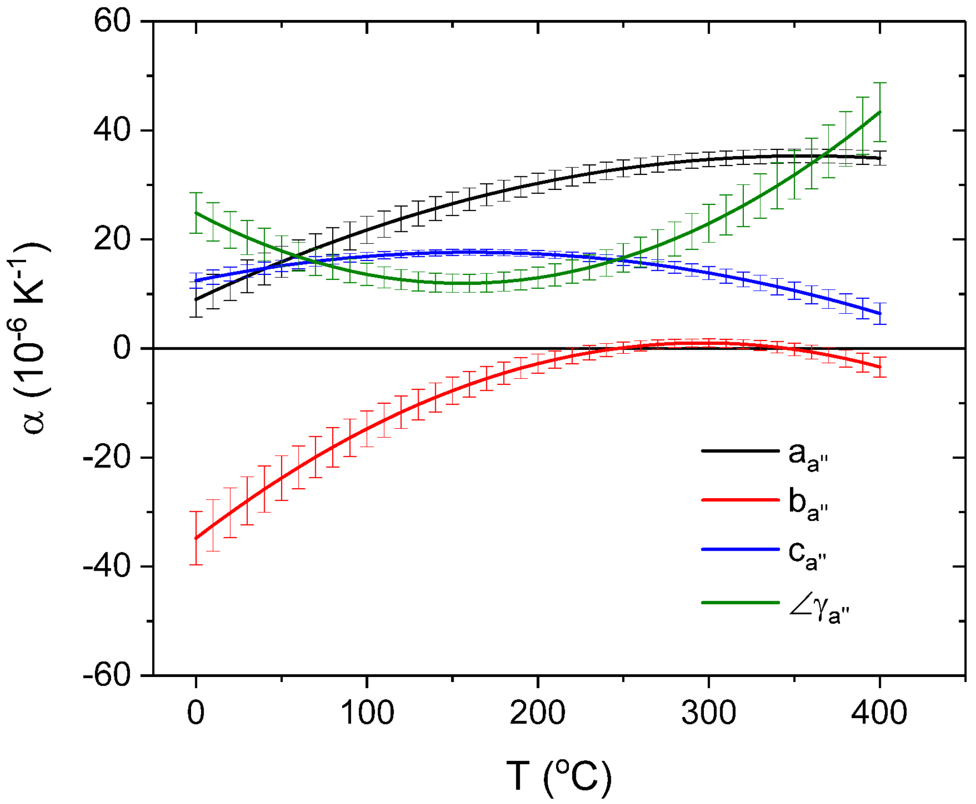

Figure 6.15: Thermal expansion coefficients of the axes of the α'' phase in the cooling of the UNb5 alloy from 400°C.

From the fits, final phase fractions at t → ∞ are $\phi^{\alpha}_{wt} = 88.1(6)\,\%$ and $\phi^{\gamma}_{wt} = 18.86(8)\,\%$. The α phase fraction correlates relatively well with an expected final theoretical percentage of $\phi^{\alpha}_{wt} = 89.7\,\%$. However, the γ phase fraction is slightly high. Correcting for the fact that the eventual state γ phase ought to contain roughly 47.7 wt. % Nb, ϕ^{γ}_{wt} drops to 13.38(6) %. This is still higher than the theoretical percentage of ϕ^{γ}_{wt}=10.3 %. The final data point on the graph at 24500 s corresponds to ϕ^{γ}_{wt}=10.7 % when corrected. It could be argued that the data has levelled out by this point and that the final state is achieved. The data has been fitted with an exponential decay curve but it may be the case that the reaction has essentially ceased by this point and that the functions used to fit the data need additional parameters. Alternatively, there is the possibility that microstrain (which dictates peak shape) or the constrained α and α'' phase fractions are introducing errors in ϕ^{γ}_{wt}, particularly between 5000 and 7500 s portion of the run.

Fitting the patterns required the preferred orientation corrections of the α'' phase to be held constant. This was deemed to be necessary from visual inspection of the 2D diffraction patterns. However, the α and γ phases required some small preferred orientation corrections initially.

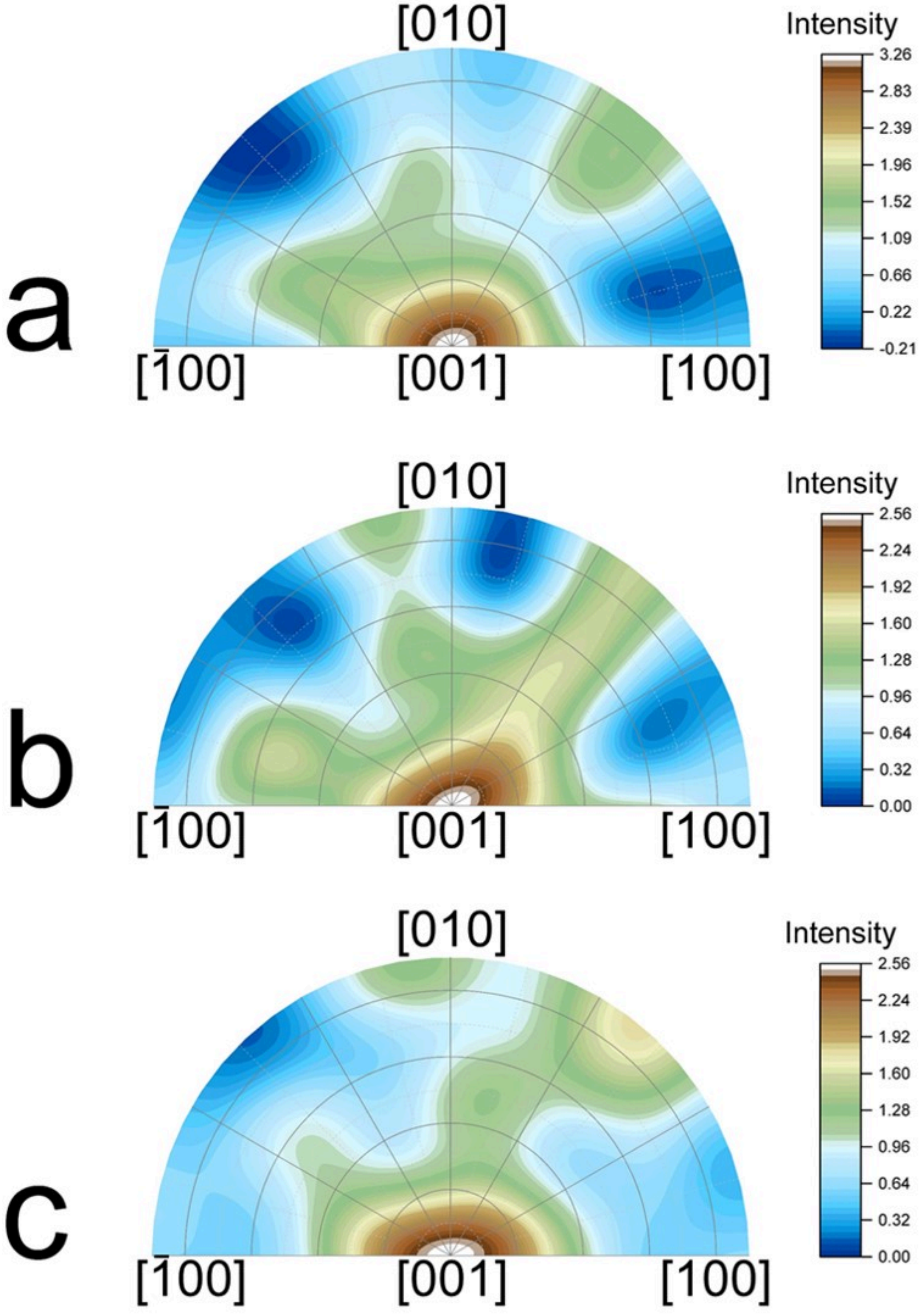

Figure 6.16: Equal area IPFs showing the evolving texture of the UNb5 alloy heated to 400°C. The data in *a* represents the material before heating, *b* was taken at 400°C 6.5 hours after heating began and *c* was obtained after the sample had been allowed to cool.

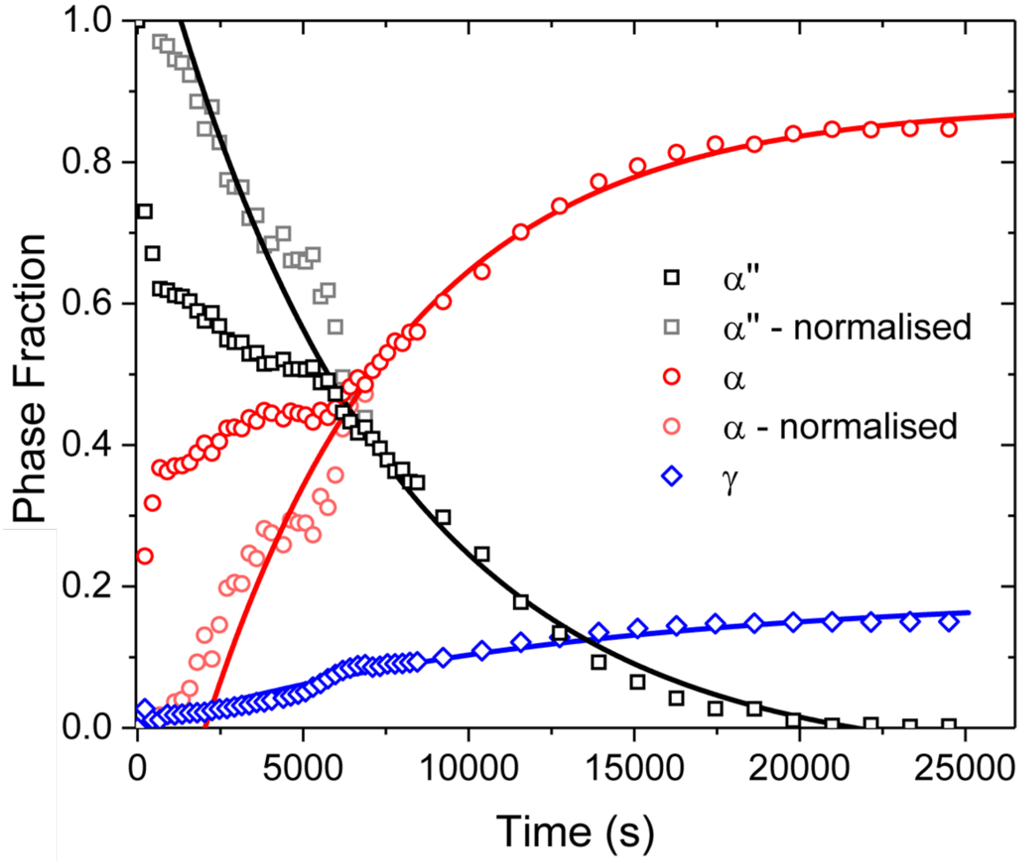

Figure 6.17: Evolution of the fractions of the α'', α and γ phases in the 450°C aged UNb5 sample as a function of time. Data points have been thinned by a factor of two for clarity.

Texture indexes for both phases reduced to nearly unity by the end of the ageing treatment. Microstrains rose from 11400 ± 300 to 34000 ± 4000 for the α'' phase throughout ageing and dropped for the α and γ phases. Figure 6.18 shows the changes in microstrains as a function of time. Microstrain was used as a peak broadening term in favour of crystallite size as competition between the α'' and α phases, and initially small quantities of the α and γ phases caused the sequential refinements to be highly unstable and seldom consistent when modelling crystallite sizes.

Given the complex microstructure of the material, it would be natural to assume that early on the primary cause of peak broadening in the α and γ phases would be due to crystallite size broadening. Therefore, it would be desirable to fit the evolving crystallite size of the α and γ. Attempting to fit single frames with just crystallite size terms was unsuccessful as broadening with angle was strongly present, highlighting that microstrain contributions are significant and

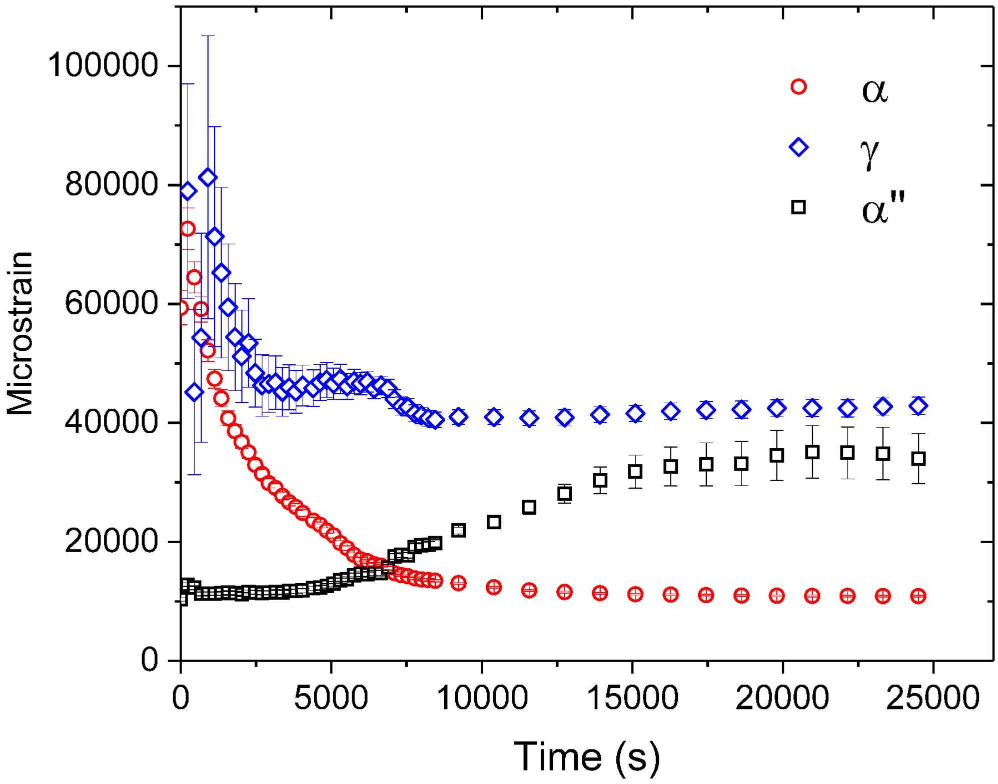

Figure 6.18: Time dependence of microstrain in the α'', α and γ phases throughout ageing of the UNb5 alloy at 450 °C.

appear to dominate. Due to the lack of stability in using crystallographic size effects and the minimal gains in including these terms, they were omitted. Regardless, the microstrain result highlights the sharpening of peaks that occurs through ageing.

6.3.2.3 500 °C

Heating the UNb5 sample to 500 °C produced a rapid transformation from the α'' phase to a two phase mixture of $\alpha + \gamma$. A contour plot of the diffraction patterns through the temperature ramp is shown in Figure 6.19. The reaction begins at around 150 s and is completed by around 300 s. During this time, the temperature is still increasing (from 445 to 480 °C) and as a result, the rate of the reaction is difficult to quantify given no fixed temperature. The ramp rate was set by the power supply but could be characterised by a quadratic equation that is dominated by the linear component early on. In the early stages of heating the initial rise the ramp rate is 1.84 ± 0.02 °C/s.

In heating, the lattice parameters of the initial α'' phase may be observed to alter until

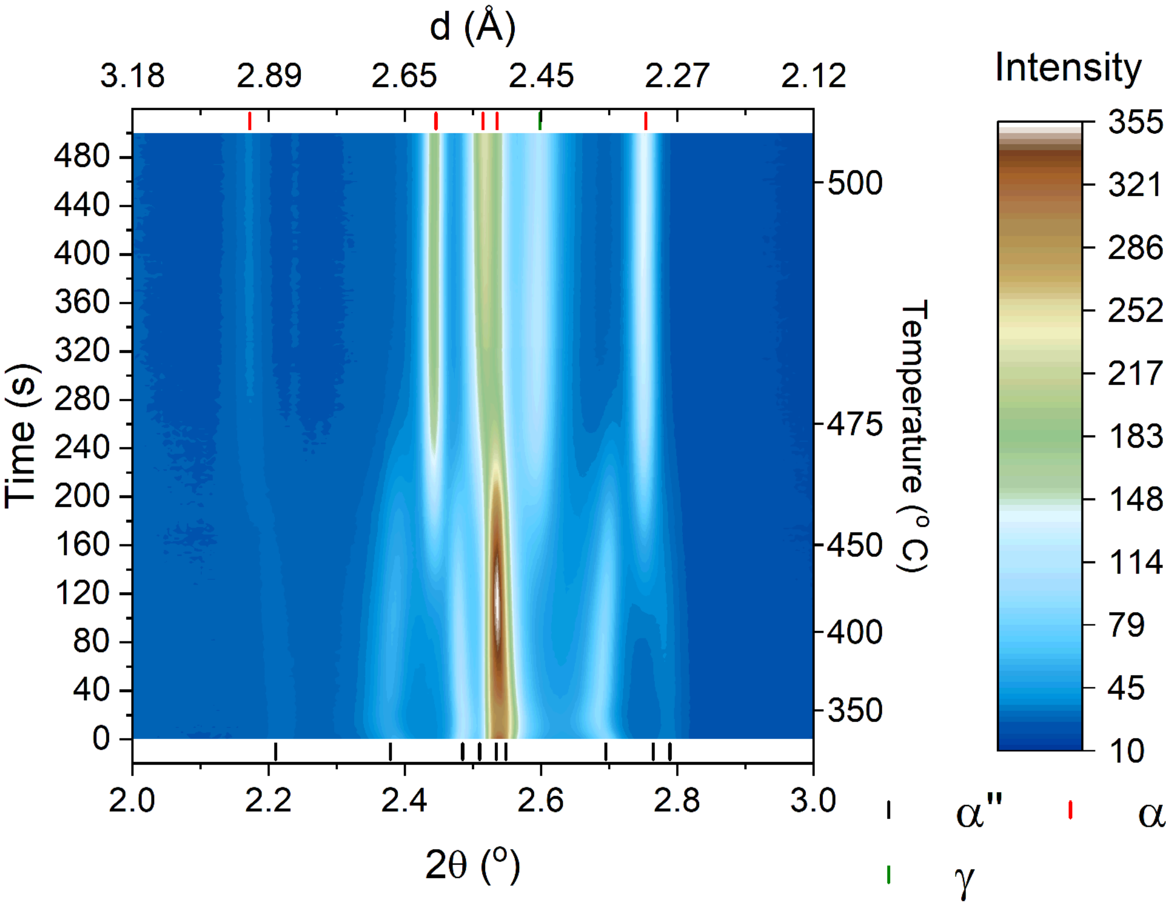

Figure 6.19: Contour plot of the diffraction patterns during the initial ramping of the UNb5 sample to (500 °C).

extinction. The overall trend is complex with volume expansion but shrinking of the a axis and the $\angle\gamma$ closing up towards 90 °. These results contrast with the 450 °C which may point to niobium leaving the lattice at a much faster rate causing the lattice to contract faster than it expands from thermal effects.

Though the lattice parameters and structures are quite similar between the α'' and α phases resulting in a similar set of reflections at similar positions, there is no continuous progression from the α'' to the α phase. The α'' does not slide down the metastable scale, rather the phase has to be destroyed prior to the formation of the α and γ phases. Figure 6.19 clearly demonstrates that the α'' phase does not produce the α phase by a continuous transition, but by shedding of niobium through a diffusional process to create a new phase initially characterised by small domains.

Sequentially fitting the diffraction patterns that comprise Figure 6.19, the evolution of phase fractions throughout heating may be extracted, Figure 6.20. Fitting of the data confirms the α'' phase as the only phase at the start of the scan (which corresponds to approximately 275 °C).

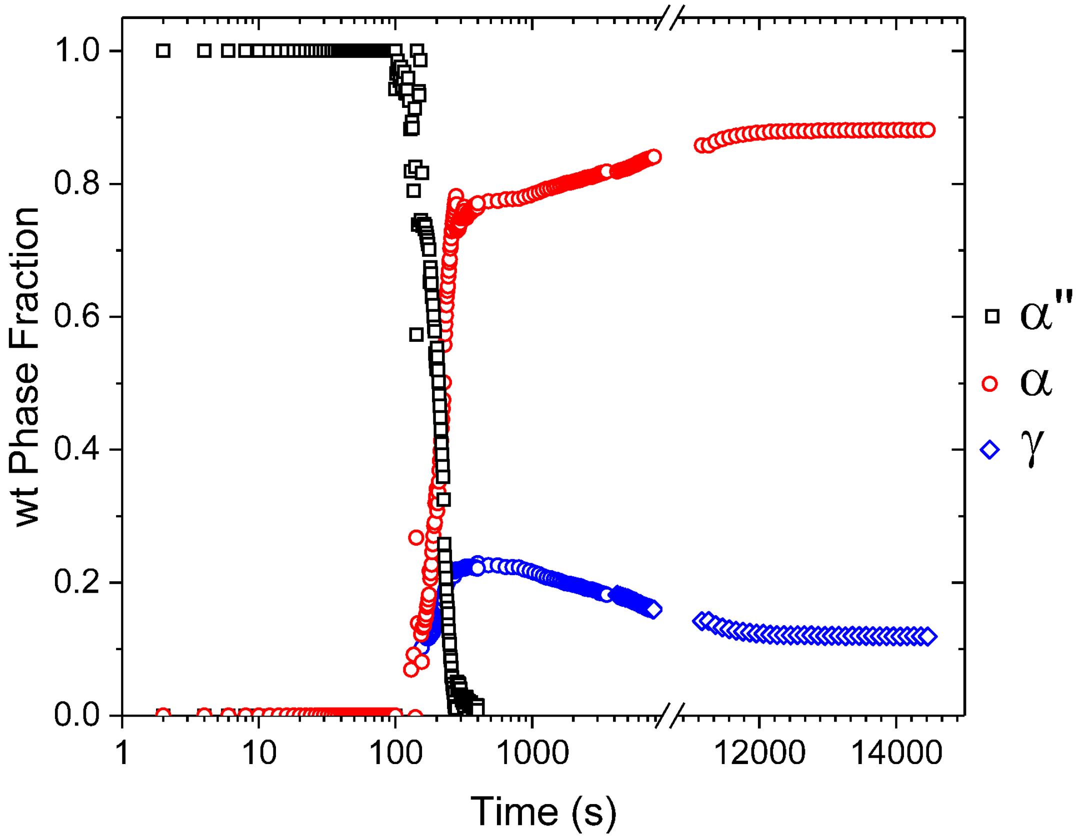

Figure 6.20: Phase fractions of the α'', α and γ phases as a function of time in the UNb5 alloy heated to 500°C.

Figure 6.20 was fitted with Boltzmann sigmoidal relationships between 100 and 300 s (not shown).

After the α'' phase has been consumed, the α phase fraction increases with time whilst the γ phase fraction decreases. This behaviour suggests that initially a significant portion of the alloy has been converted to the γ phase (25 % by weight). This is unstable as the final expected weight fraction of this phase ought to be 10.3 % by weight. As time continues, the fractions approach their expected final states. In this regime, phase fractions have been fitted with exponential decay functions. As the α'' no longer exists by 400 s, the α and γ phases are mirrors of each other so the time constant for this reaction is $T_{\alpha/\gamma} = 4600 \pm 200$ s and final phase fractions at $t \rightarrow \infty$ are $\phi^{\alpha}_{wt} = 87.0$ and $\phi^{\gamma}_{wt} = 13.0\,\%$.

The lattice parameters of the newly created α and γ phases are not constant in the isothermal section of the scan, despite the fact that the final temperature was reached by 1000 s and is very stable thereafter, Figure 6.21. The exception is the a axis of the α phase which is relatively constant throughout the scan. In comparison, the b and c axes of the α phase expand whilst the lattice parameter of the γ phase contracts. This result suggests that the phase contents are not fixed but change in composition with time. Vegard's law may be relatively easily applied to the γ

phase due to the shared *bcc* crystallographic structures of γ-U, γ-Nb and this γ phase. Analysis via Vegard's law would suggest that the niobium content of the γ phase increases over time. The final composition of the γ phase is estimated at 42.3 at. % Nb. However, this value is highly dependent on the initial value of a_{γ^s}, which has been selected to be 3.48 Å as this is the highest value of the data available. Whereas in the next section for the UNb7 alloy, the value was chosen to be 3.53 Å (but this initially contained more uranium). Vegard's law cannot be equally applied to the α phase due to inconsistency in structure types. An overall volume expansion of the α phase however, suggests an increasing uranium content within this phase though variations in lattice parameter are much smaller than in the γ phase.

Figure 6.22 shows the same data as the cooling section of Figure 6.21 but as a function of temperature. Generally, all axes across the two phases behave as expected with positive thermal expansion coefficients exhibited. Thermal expansion coefficients of the crystallographic axes of the α and γ phases have been calculated from Figure 6.22 and are shown in Figure 6.23. Thermal expansion coefficients were calculated by fitting the data of Figure 6.22 with quadratic equations and feeding the equations into,

$$\alpha = \frac{1}{a}\frac{\partial a}{\partial T}. \tag{6.1}$$

A full derivation of this method may be found in the Appendix B. The results of using cubic equations to fit the data are also shown in Figure 6.23. Whilst the cubic and quadratic fits generate largely similar thermal expansion coefficients, the cubic version appears to increase in complexity that may be arising from over fitting the data, particularly at higher temperatures when the temperature is changing the fastest and the errors in temperature are the greatest. The quadratic fits appear to adequately fit the data, Figure 6.22, and produce sensible results, Figure 6.23.

Thermal expansion coefficients of the a and c axes are similar, increasing by a similar magnitude with temperature. The thermal expansion coefficient of the γ phase also increases with temperature, yet at a much slower rate than the a and c axes of the α phase. The thermal expansion coefficient of the b axis on the other hand decreases, but stays positive, pointing to a slowing of the expansion with temperature.

Follow up examination of the alloy using STEM imaged the microstructure of the transformed UNb5 alloy, Figure 6.24 and 6.25. The images show distinctive, alternating light and dark bands present throughout the material. From the bright field image of Figure 6.24, light bands correspond to the niobium rich γ phase whilst the thicker, dark bands are α phase material. Bands are no more than a couple of hundred nanometres across and a micron long. The top right corner of the images show a carbide (either UC or Nb_2C) inclusion.

The high angle annular dark field image of Figure 6.25 shows additional contrast close to the carbide which may be arising from differences in the niobium content of the α phases in between domains. The dark field image (not shown) does not reciprocate these differences in contrast suggesting that the effect is not structural.

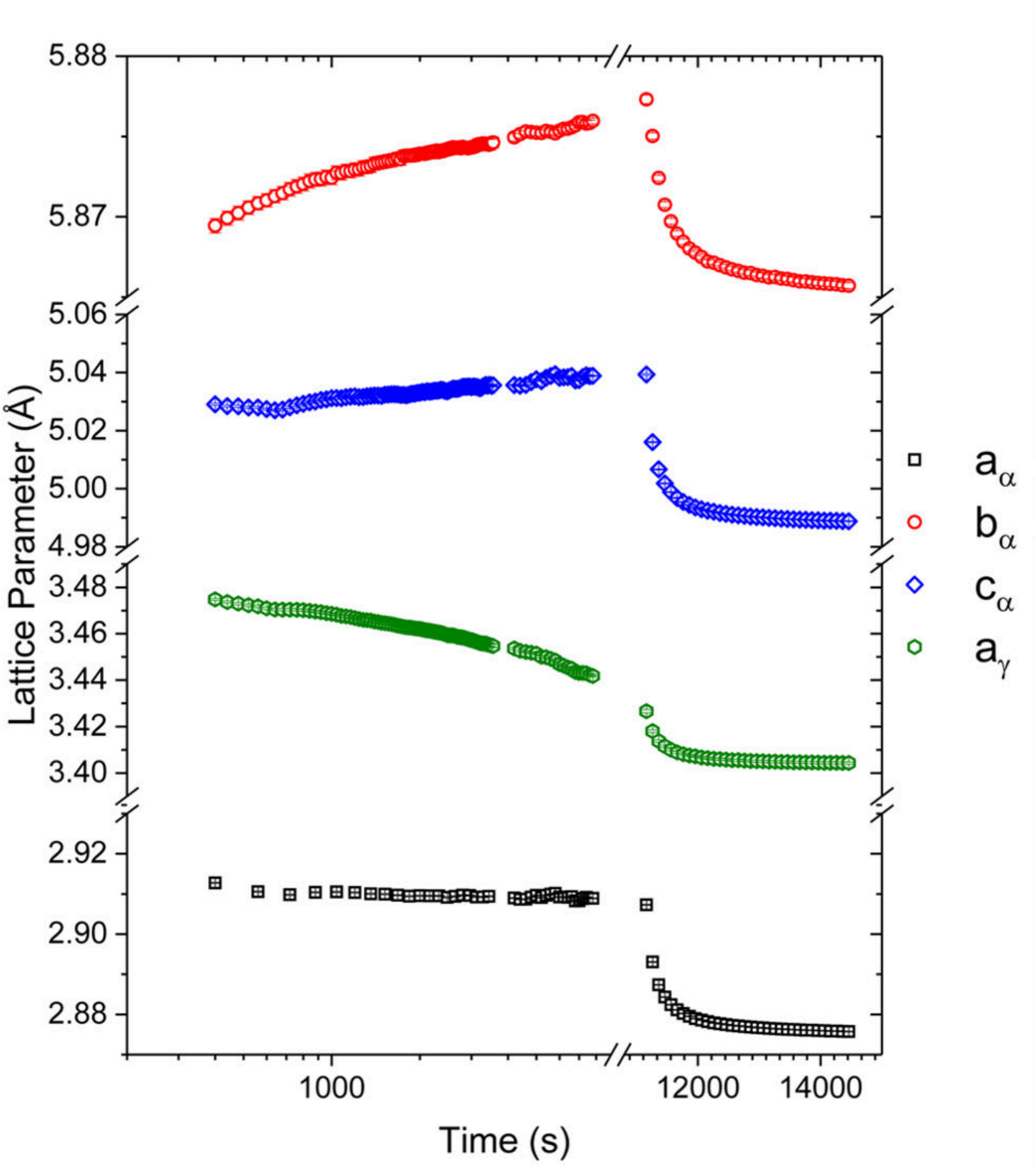

Figure 6.21: Variation in the lattice parameters of the α phase of the 500 °C aged UNb5 alloy with time. Data starts at 400 s once the α'' phase has been consumed. Heating is turned off at 11160 s.

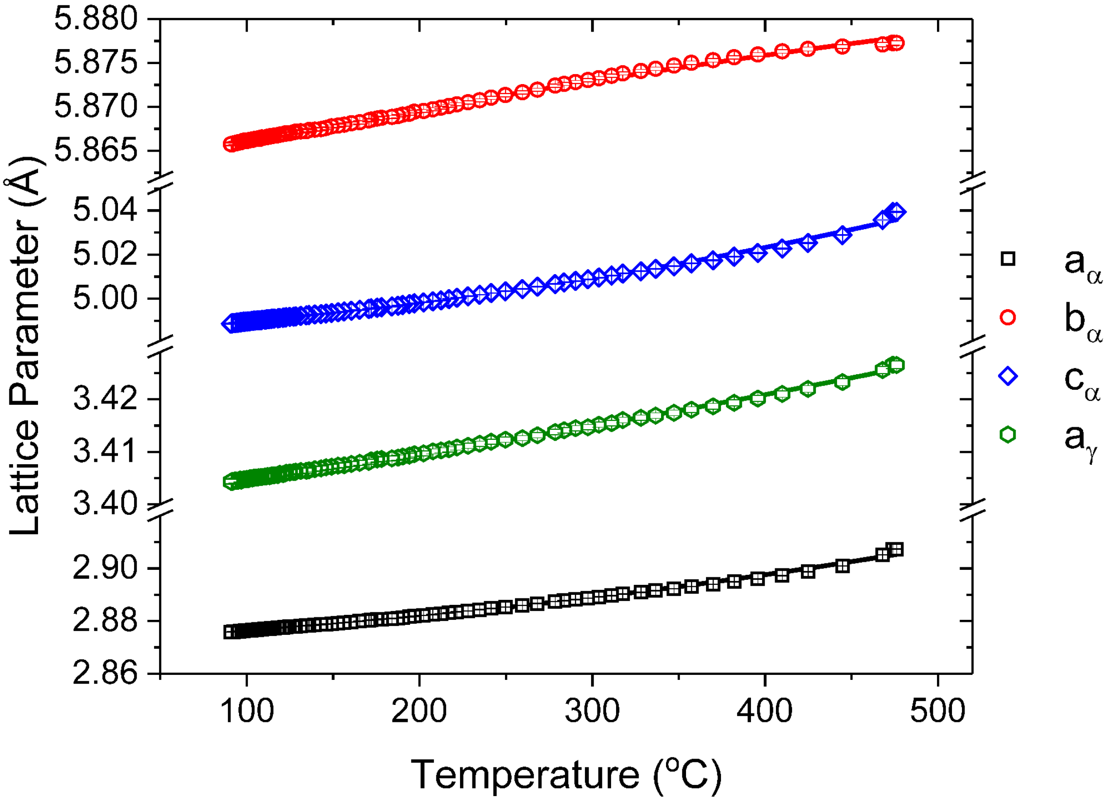

Figure 6.22: Lattice parameters of the as-transformed UNb5 alloy as a function of temperature in cooling.

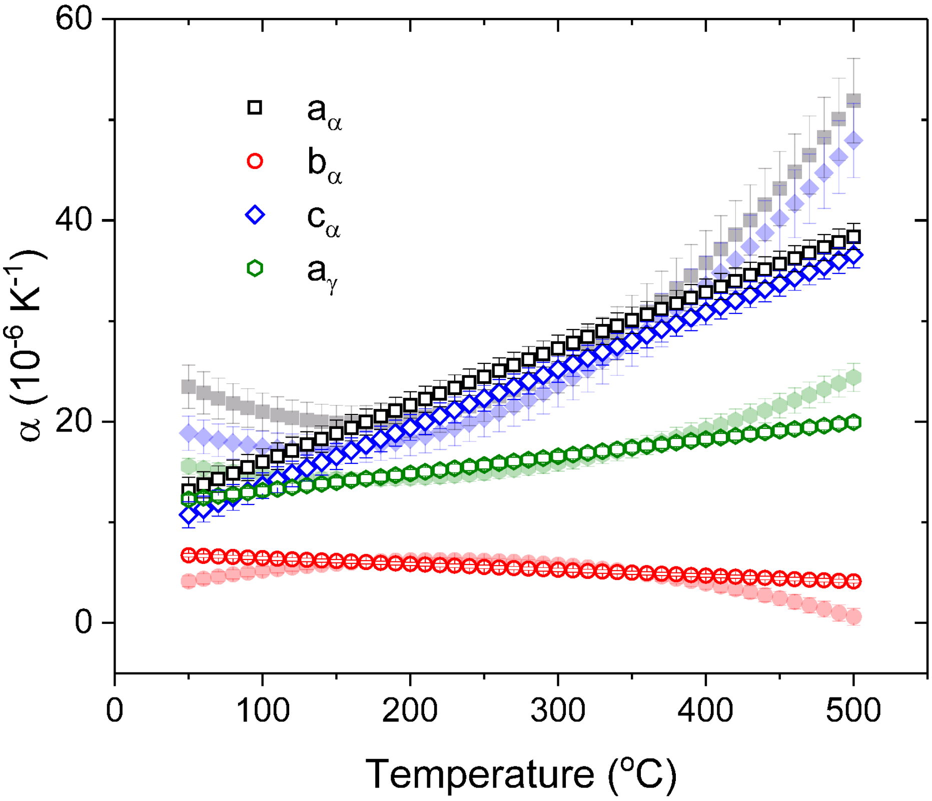

Figure 6.23: Thermal expansion coefficients of the axes of the α and γ phases. Quadratic fits of Figure 6.22 are shown prominently, cubic fits of Figure 6.22 are shown in the background.

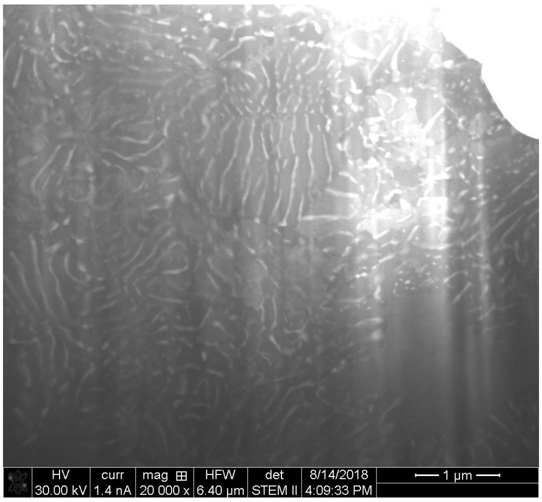

Figure 6.24: STEM bright-field (BF) image of the 500 °C aged UNb5 alloy.

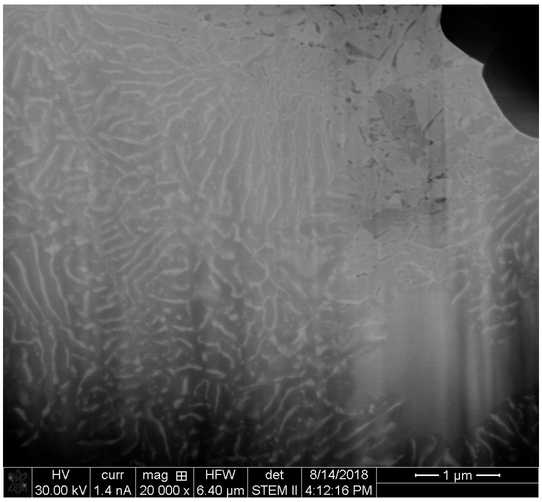

Figure 6.25: STEM high angle annular dark-field (HAADF) image of the 500 °C aged UNb5 alloy.

6.3.3 UNb7 Unaged State

A map measuring 2 × 2 mm^2 was used to assess the state of the starting material in the UNb7 alloy. The grid comprised 121 snapshots with a slit size of 0.2 mm × 0.2 mm (0.2 mm is the conventional slit settings for the beamline). Due to the large grain size in this material, up to 200 μm, the limited sample thickness ($\approx 500\,\mu$m) and the tight slit settings, only a handful of grains would be accessible per exposure. This is evident in the diffraction patterns generated from a single frame. An example is shown in Figure 6.26. The result of the summed map is shown in Figure 6.27.

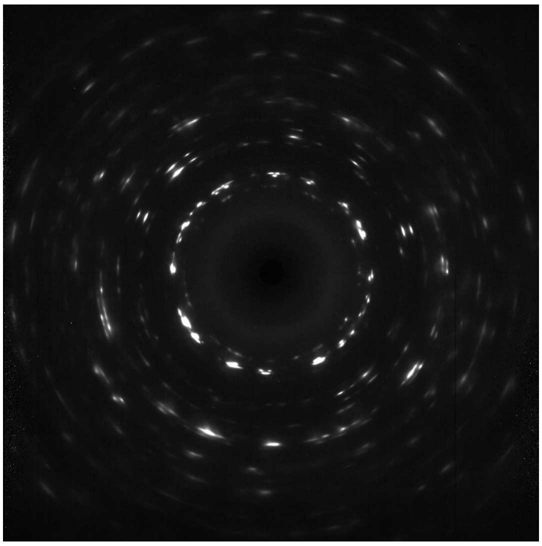

Figure 6.26: The diffraction pattern of a single frame representing an area of 0.2 × 0.2 mm^2 in the UNb7 alloy.

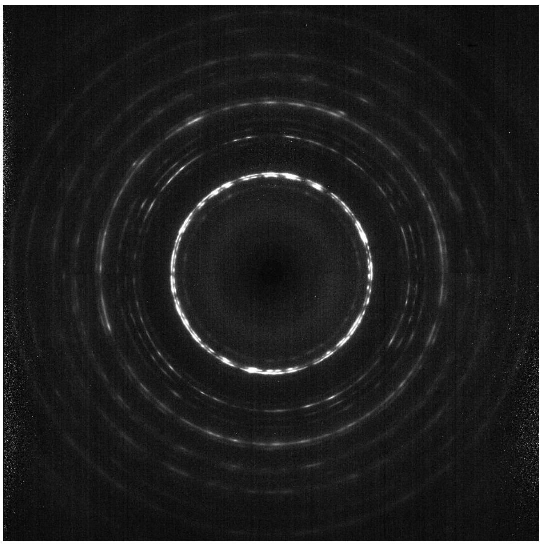

Figure 6.27: The summed diffraction pattern of all frames in the 121-frame map representing an area of 2 × 2 mm^2 in the UNb7 alloy.

The summed diffraction pattern exhibits much fuller Debye-Scherrer rings, though some texture still prevails. Despite this, it is possible to fit the azimuthally integrated pattern relatively easily using preferred orientation models. The fitted, azimuthally integrated pattern of Figure 6.27 is shown in Figure 6.28.

The data in Figure 6.28 was used previously in Chapter 4 to investigate the initial state of the UNb7 alloy and the phases that it is composed of. A detailed description of the starting state of the alloy may be found in Chapter 4. The key results are that the pattern is best described by mixture of γ° and α'' phases in an approximately 2:1 ratio with microstrains of 20400 in the γ° phase and 43100 for the α'' phase. Information regarding crystallite sizes could not be extracted with sufficient certainty as the effects of strain dominate.

Texture of the γ° phase is shown modelled in Figure 6.29. A slight propensity for orientations close to the [001] direction exists, however due to the summing of frames, the overall range of

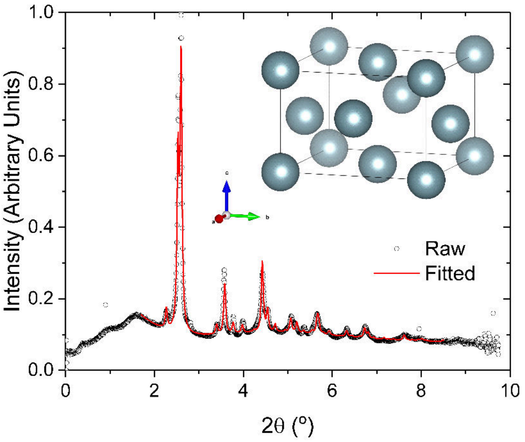

Figure 6.28: Fitted pattern of the map data. The crystal structure of the γ° phase is shown as an inset which was modelled best using the P4/nmm space group. Lattice parameters were determined to be $a = 5.0114(6)\,\text{Å}$ and $c = 3.366(1)\,\text{Å}$. Fractional position of the *2g* atom along the c axis z/c = 0.435(3). $R_{wp} = 6.65\,\%$, $RF^2_{\gamma^o} = 11.37\,\%$.

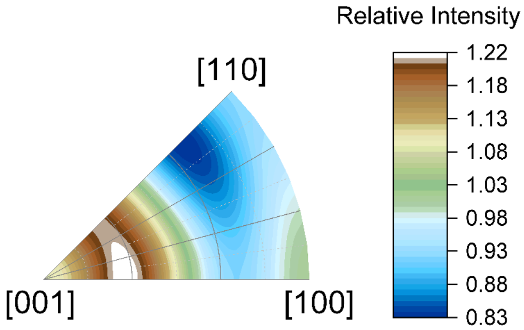

Figure 6.29: Reduced equal area inverse pole figure taking into account the 4/mmm Laue class symmetry of the crystal. Effects of texture can be seen to have been mitigated by the map sampling. Relative intensities across crystal orientations may be seen to vary by as much as 20 %.

texture, as measured in multiples of random distribution (MRD), is relatively low.

6.3.4 UNb7 Transient

6.3.4.1 400 °C

Lattice parameters of the γ° phase as a function of temperature in heating to 400°C are shown in Figure 6.30. In contrast to the room temperature measurement, the patterns are well fitted solely by the γ° phase without any requirements for an α'' phase over this range. By extrapolating back to the starting value of 3.366(1) Å, the c axis shows a large and relatively linear rise ($\alpha = \sim 55 \times 10^{-6}\,\text{K}^{-1}$) to 300 °C. The a axis on the other hand shows much more nuanced behaviour increasing rapidly from a starting point of 5.0114(6) Å to the first available data point at T = 192 °C, a = 5.0354(4) Å. After this point, the a axis is relatively constant in the range of 190-275 °C before dramatically decreasing to 5.0148(3) at 350 °C, roughly the value before any heating was applied. The c axis also rapidly increases as the temperature approaches 350 °C. Heating continues to a maximum of 380 °C after which the behaviour changes again and the a axis length increases whilst the c axis length decreases with extended ageing, Figure 6.30. A decreasing a axis and increasing c axis in the 300-350 °C range can be seen as the γ° phase driving towards the cubic γ phase. Lattice parameters however do not quite reach the cubic γ phase. Imagined in this sense, at their closest point, the lattice parameters reach a maximum

c/a axial ratio of 0.979. Throughout this rise in temperature, diffraction peaks may be observed to significantly sharpen which results in a dramatic drop in the microstrain of the γ° phase and much stronger fit statistics. Microstrain is a minimum after 360 s which corresponds to 349 °C, i.e. just after the discontinuities in Figure 6.30. The fit statistics at this point are $R_{wp} = 8.01\,\%$, $RF^2 = 1.052\,\%$ and $RF = 0.597\,\%$. The fits over this range also highlight the suitability of the P4/nmm space group in describing the γ° phase.

The lattice parameters of the γ° phase as a function of time for the entire heating period are shown in Figure 6.31. The grey and pink data points show the results of fitting the patterns with only the γ° phase. However, shortly after the temperature had reached its maximum value, patterns showed new peaks that could be attributed to an emerging α'' phase. The lattice parameters of the γ° phase in the two phase scenario are shown in Figure 6.31 by black and red data points. Since there is reasonable overlap between the peaks of the γ° and α'' phases, detection of the α'' phase is difficult in low concentrations. Between the end of the heating ramp and 2650s, the α'' fraction is too low to be fit reliably. Preferred orientation corrections were kept constant for these phases throughout the sequential refinement to ensure accurate trends were extracted.

Phase fractions, ϕ, of the α'' and γ° phases as a function of time are shown in Figure 6.32. The data is well fitted by a two component exponential decay function,

$$\phi = A_1 e^{-t/T_1} + A_2 e^{-t/T_2} + \phi_0, \tag{6.2}$$

with time constants of $T_1 = 1300 \pm 50$ s and $T_2 = 9200 \pm 500$ s and a constant of $\phi_{0,\alpha''} = 0.421 \pm 0.002$. A ratio of amplitudes, $A_1/A_2 = 4.0 \pm 0.2$ means that the quicker acting term is the more dominant.

Figure 6.33 shows the lattice parameters of the α'' and γ° phases for the isothermal portion of the scan. The volume of the γ° phase decreases during ageing, whereas the volume of the α'' phase increases over the same period. Figure 6.34 shows the progression of microstrain in the α'' and γ° phases for the isothermal portion of the scan.

6.3.4.2 450 °C

The same sample was reheated to 450 °C for a $5\frac{1}{2}$ hour isothermal exposure following the 400 °C run. Behaviour was similar to the previous run at 400 °C, although the UNb7 alloy did not revert back to a more crystalline, single phase of the γ° structure in initial heating as it had done at the lower temperature, an irreversible transition occurred during ageing at 400 °C. Patterns were fitted with isotropic microstrains for both the α'' and γ° phases to promote stability of the fitting program and to serve as a direct comparison to the previous run. Phase fractions were approximately equal throughout the run oscillating around an equal mix of the two phases.

Crystallinity remained poor with broad peaks in the diffraction pattern that were modelled with large microstrains, as seen in Figure 6.36. Microstrains are in keeping with the previous run in which α'' phase microstrain dropped to approximately 60000 in the cooling stage whereas the γ° microstrain rose to 40000, Figure 6.34.

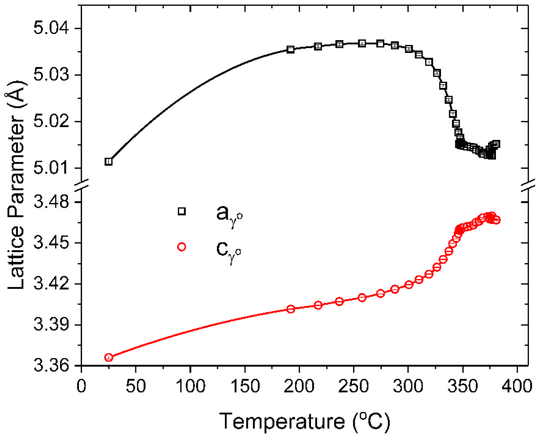

Figure 6.30: Lattice parameters of the γ° phase as a function of temperature during the initial heating ramp of the UNb7 alloy to 400 °C. Data points have been joined up using an Akima spline to illustrate the trend, particularly from room temperature to 200 °C.

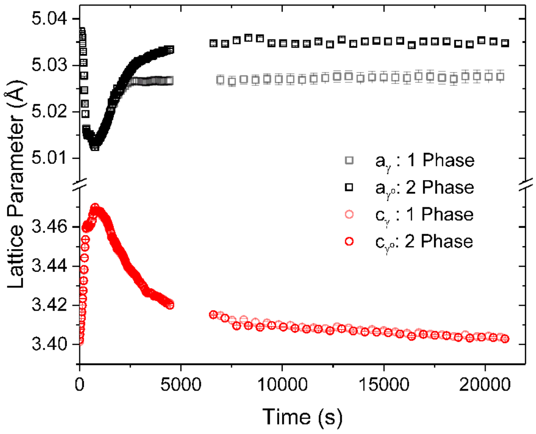

Figure 6.31: Lattice parameters of the γ° phase during ageing of the UNb7 alloy to 400 °C in the scenarios of modelling the patterns with only the γ° phase and modelling with the γ° and α'' phases.

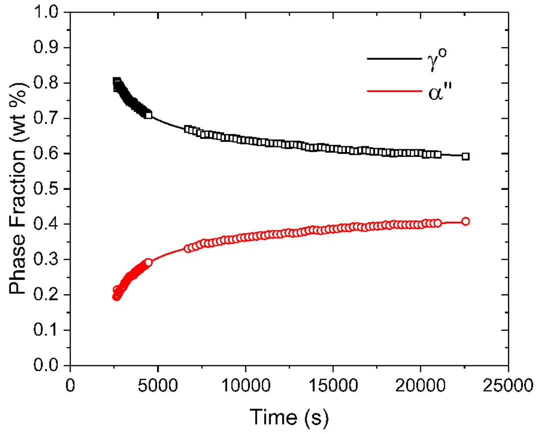

Figure 6.32: Phase fraction by weight of the γ° and the α'' phases in the UNb7 alloy heated to 400 °C.

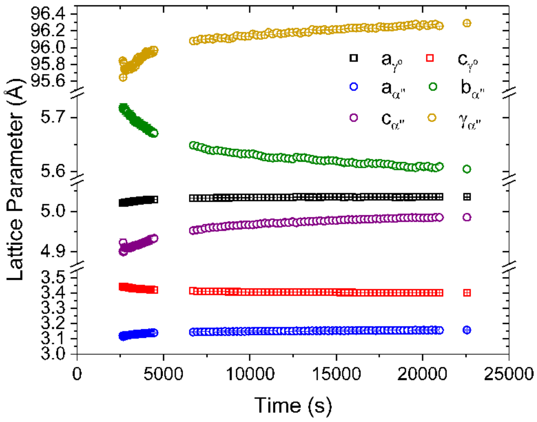

Figure 6.33: Lattice parameters of the γ° and α'' phases as a function of time during the isothermal heating stage of the UNb7 alloy at 400 °C.

Post-experimental examination of this sample with electron and ion-beam techniques showed the sample to be mostly unchanged from the perspective of SEM. However, by taking cross sections of the alloy using a FIB, Figure 6.38, cellular decomposition could be observed to have initiated in the vicinity of carbides. Referring to the reconstructed model of carbides in Chapter 3, Figure 3.18, carbides were not seen to be accompanied by lobes of cellular decomposition. It is therefore likely that carbides within the material are acting as nucleation points for this reaction

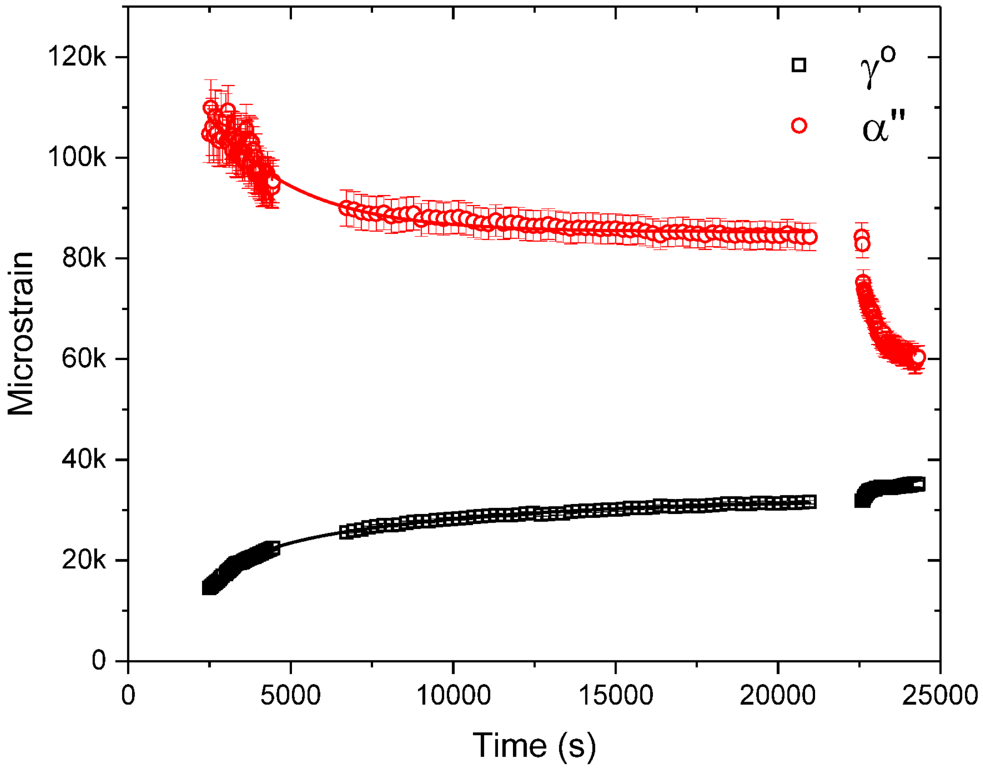

Figure 6.34: Microstrain of the α'' and γ° phases in the UNb7 alloy as a function of time at 400 °C.

permitting diffusion to occur more readily and/or at lower temperatures. This carbide, which is suspected to be UC, based on the morphology and size is not accompanied by niobium carbides as seen in the previous case. Figure 6.35 shows the lattice parameters of the γ° phase decreasing with time at temperature which might suggest small changes in niobium content with time.

Two other carbides imaged in this cross section did not show evidence of similar segregation pointing to the fact that this reaction is in its very early stages. Further cleaning cross sections applied to the carbide revealed its uranium oxide core.

6.3.4.3 500 °C

Figure 6.39 shows the relationship between lattice parameter and temperature during the initial heating ramp. Like the 400 °C run, the γ° phase becomes the sole phase initially during the ramp. In the early stages, the a axis decreases whilst the c axis increases at roughly twice the rate. The γ° phase undergoes a tetragonal to cubic phase transition at 372 °C. This is roughly the same temperature as the similar transition for the 400 °C aged specimen (380 °C), it is assumed that

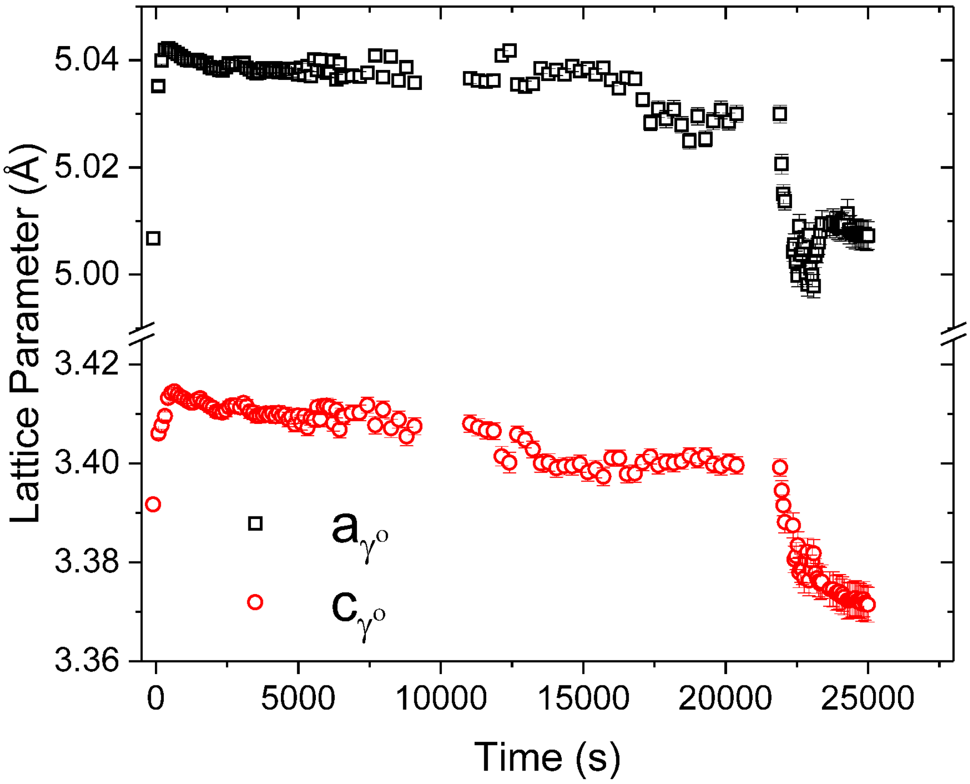

Figure 6.35: Lattice parameters of the γ° phase of the UNb7 alloy as a function of time at 450°C.

the errors associated with this method of calibration are approximately 10 °C, see Appendix A.

Whereas in the 400 °C run a tetragonal to cubic transition was never quite realised, this treatment reached a cubic phase which continued to expand through to the maximum temperature of 500 °C. This might be explained through ramp rates, striving for a higher final temperature, the 500 °C run exhibited a greater ramp rate than the 400 °C run. Vandermeer showed that the austenitic start and finish temperatures (A_S and A_F) are dependent on heating rate with higher ramp rates delivering lower transition temperatures [274]. The effect was attributed to solute migration which in this case may be pushing the transition temperatures just beyond the final temperature of the 400 °C run.

Vandermeer's 1981 work details a metastable phase diagram that might suggest that the γ^s phase exists between the γ° and γ phase in this alloy [276]. The tetragonal γ° phase was retained until the γ phase was reached at 372 °C, in reasonable agreement with the γ phase boundary as determined by Vandermeer. It would therefore seem that it is not possible to convert back to the γ^s phase in reheating this alloy, though it has not been possible to distinguish between the γ and γ^s phases using this data.

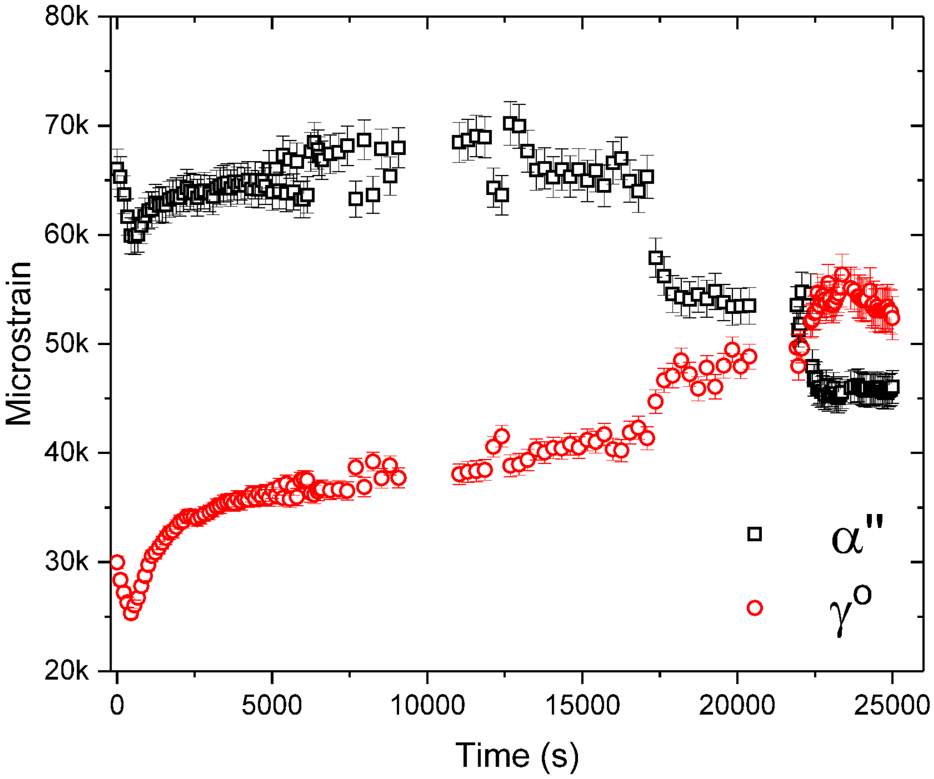

Figure 6.36: Microstrain of the γ° and α'' phases of the UNb7 alloy as a function of time at 450°C.

A contour plot of the full data series is shown in Figure 6.40. Emergence of the γ and subsequently α phases can easily be visualised. Figure 6.41 shows the volume of the γ° and γ phases as a function of time, and the phase composition within the alloy over the same time period. Volume data shown has been renormalised for comparison with the conventional γ phase unit cell. The volume of the γ phase continues to increase until the final temperature of 500 °C is obtained. After reaching the isothermal ageing temperature, the volume of the γ phase decreases in conjunction with the emergence of the α phase. The decreasing unit cell size can be attributed to decreasing uranium content in the γ phase. The content of uranium and niobium in the γ phase can be determined by the application of Vegard's law.

Vegard's law applied to this system is,

$$a_{U_{(1-x)}Nb_x} = (1-x)a_U + x a_{Nb}, \tag{6.3}$$

which can be rearranged to,

$$x = \frac{a_U - a_{Nb}}{a_U - a_{U_{(1-x)}Nb_x}}. \tag{6.4}$$

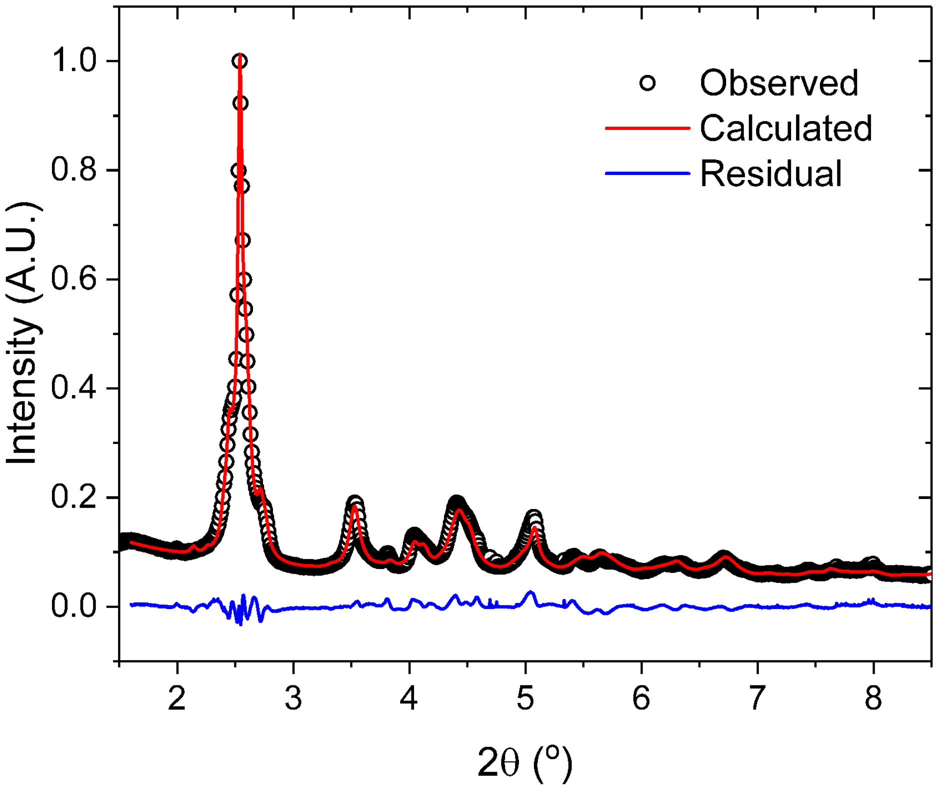

Figure 6.37: Fitted pattern of the UNb7 alloy at room temperature following heating to 450 °C for 6.5 hours. $R_{wp} = 5.59\,\%$, $RF^2_{\gamma^\circ} = 6.74\,\%$, $RF_{\gamma^\circ} = 3.68\,\%$, $RF^2_{\alpha''} = 8.33\,\%$, $RF_{\alpha''} = 3.89\,\%$. $a_{\gamma^\circ} = 5.0137(5)$ Å, $c_{\gamma^\circ} = 3.363(2)$ Å, $a_{\alpha''} = 2.927(1)$ Å, $b_{\alpha''} = 5.912(3)$ Å, $c_{\alpha''} = 4.993(2)$ Å and $\angle\gamma_{\alpha''} = 91.51(6)\,°$.

The lattice parameter of the γ phase as a function of time can therefore be used as an estimate of the niobium content. However, in this case, the starting point is the γ^s phase at 500 °C with a niobium content of around 17.2 at. % (or 7.5 wt. %). This is only about 200 s into the scan and minimal diffusion should have occurred in this time.

As a result, the equation may be further modified to incorporate this start point,

$$x - 17.2 = \frac{a_U - a_{Nb}}{a_U - a_{U_{(1-x)}Nb_x}} \tag{6.5}$$

or,

$$x(t) = 17.2 + \frac{a_\gamma - a_\gamma(t)}{a_{\gamma-U} - a_{Nb}}. \tag{6.6}$$

Vegard's law has previously been used by Jackson to determine a theoretical lattice parameter for a room temperature γ-U, were it possible to stabilise the structure without any alloying

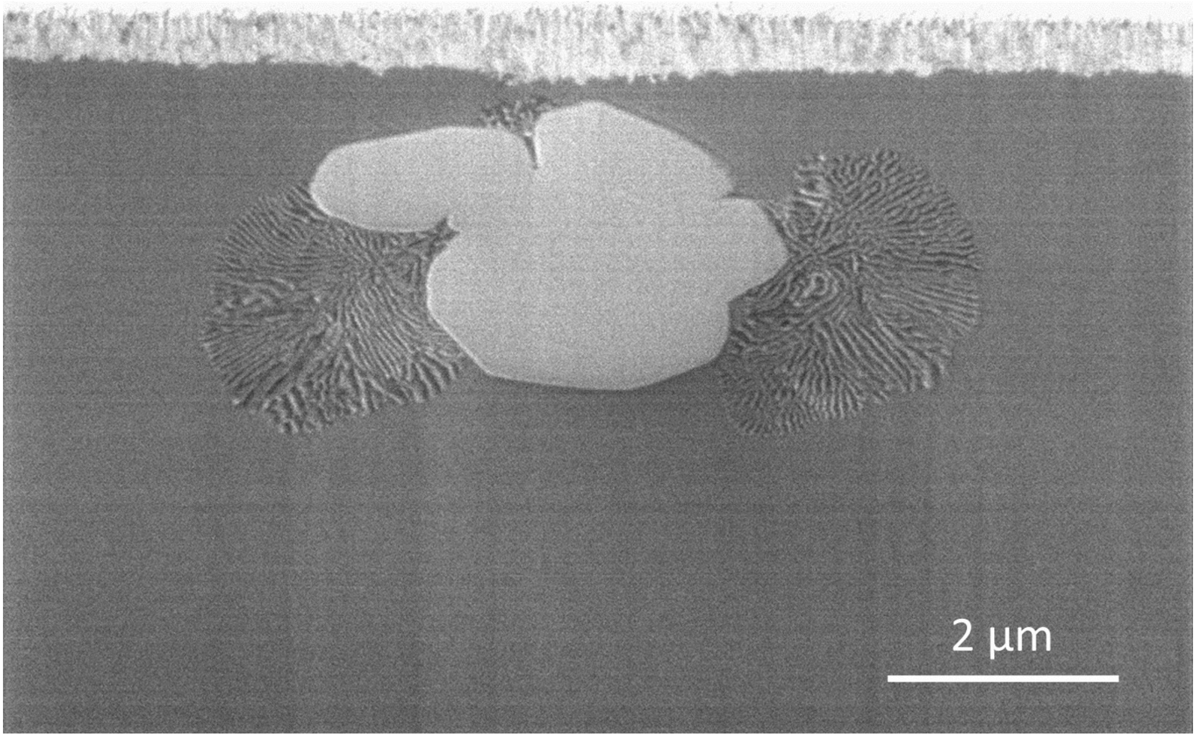

Figure 6.38: FIB-cut cross section of the 450 °C aged sample. The carbide in view has through ageing, been the nucleation site of cellular decomposition. The top of the image shows the oxide layer that has developed during the ageing. For scale, the image is 10.3 μm across.

additions [122]. However, thermal expansion coefficients of niobium and γ-U are unlikely to be the same. The lattice parameter at 500 °C is therefore 3.486 Å whilst for niobium, Kaye and Laby data was used to obtain 3.3205 Å [135]. The lattice parameter for the γ° phase upon reaching 500 °C was 3.5295 Å and was therefore used for a_{γ}.

Vegard's law requires atomic percentages whilst Rietveld programmes will generally output phase fractions as a weight percentage (as compounds and alloys make atomic percentages meaningless). The conversion from atomic to weight percentage for the U-Nb system is provided in Equation 1.1. Therefore, combination of the two equations yields the total content of niobium in the γ phase for a given lattice parameter at 500 °C. Naturally, the relationship will follow the same shape as the red curve in Figure 6.41. Niobium content in the γ phase was calculated to vary between 17.2 and 48.1 at. % Nb (7.5 and 26.57 wt. % Nb) between the initiation of 500 °C and the end of the isothermal heating period, Figure 6.42.

Based on the rarefaction of the γ phase as uranium leaves the matrix to form pure α uranium, corrections to the weight fraction of the γ phase should include the term,

$$y = \frac{93x + 238(1-x)}{238 \times 100\%}. \tag{6.7}$$

But modifying the phase fraction of the γ phase will require normalisation of both the γ and

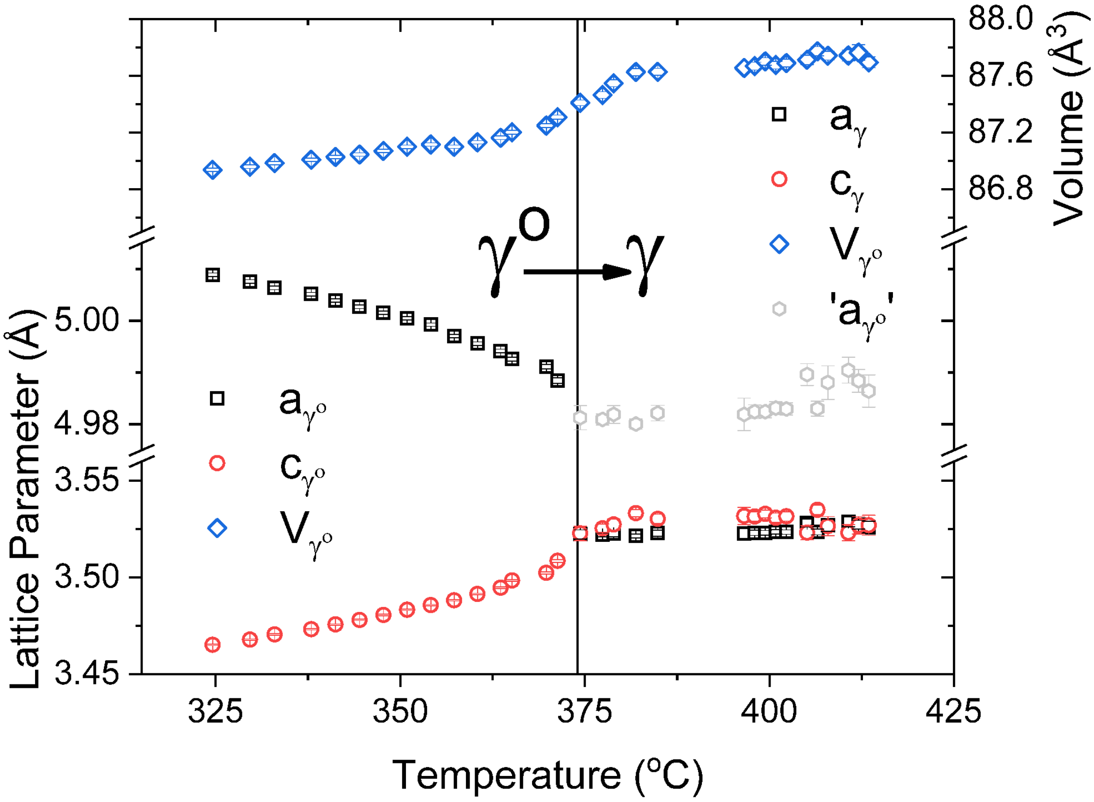

Figure 6.39: Variation in lattice parameter with temperature in the initial heating of the sample. At 372 °C the sample can be said to have gone through a tetragonal to cubic transition, locking into a lattice parameter of 3.52 Å, the same starting lattice parameter for pure bcc γ-uranium. The grey hexagons on the right hand side of the plot shows the size of the a axis were the definition of the γ° cell still being used.

the α phases to constrain their sum to 100 % leading to,

$$\phi^{\gamma}_{wt} \rightarrow \phi^{\gamma}_{wt} \times y \times \frac{100}{y\phi^{\gamma}_{wt} + \phi^{\alpha}_{wt}} \tag{6.8}$$

and

$$\phi^{\alpha}_{wt} \rightarrow \phi^{\alpha}_{wt} \times \frac{100}{y\phi^{\gamma}_{wt} + \phi^{\alpha}_{wt}}, \tag{6.9}$$

where $\phi_{\gamma,wt}$ and $\phi_{\alpha,wt}$ represent the phase fractions in weight percentage of the γ and α phases respectively. Correcting for γ phase constituents has a relatively small effect on the phase fractions, up to 3 % by the end of the run.

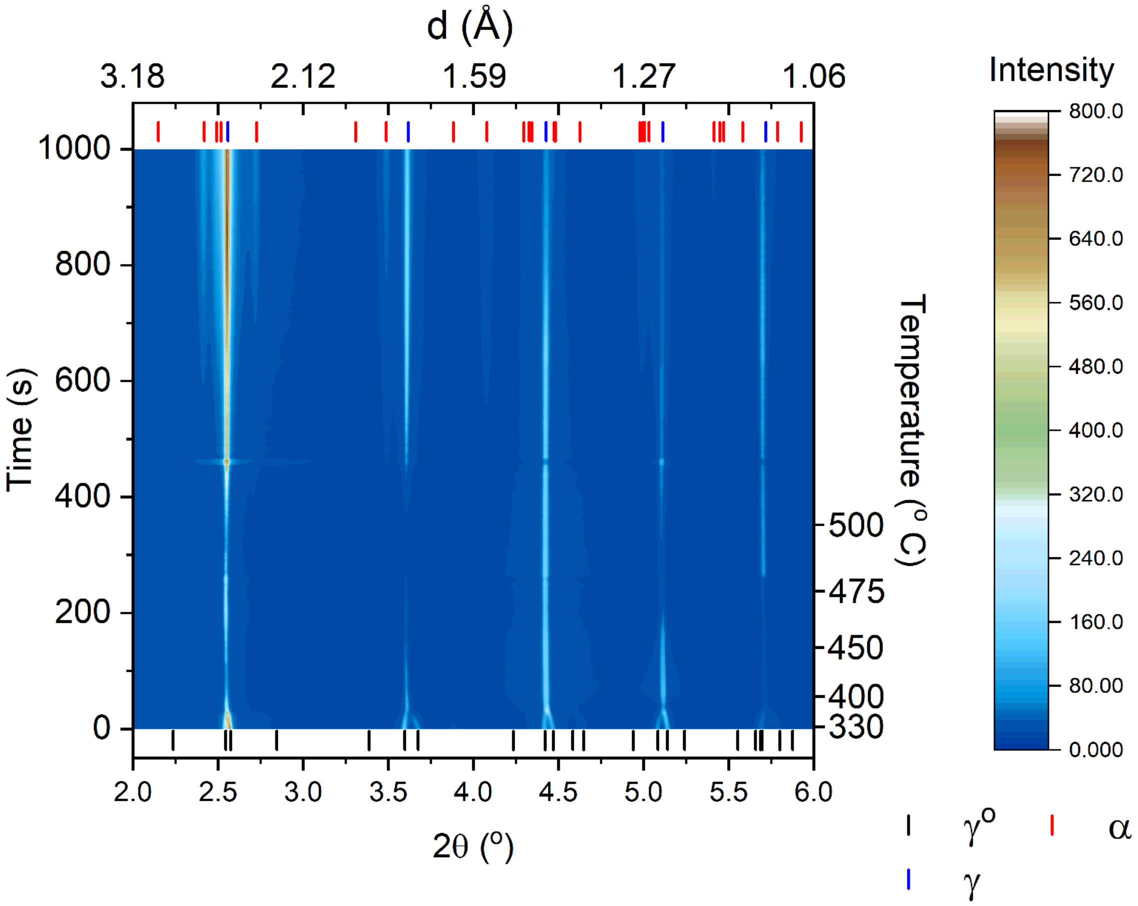

Figure 6.40: Contour plot of the diffraction patterns arising from the initial heating of the UNb7 sample to 500 °C.

The lever rule in the U-Nb system can be written as,

$$\phi^{\alpha} = \frac{\phi_{Nb}^{\alpha+\gamma} - \phi_{Nb}^{\gamma}}{\phi_{Nb}^{\alpha} - \phi_{Nb}^{\gamma}} \tag{6.10}$$

where ϕ^{α} is the mass fraction of the α phase, $\phi_{Nb}^{\alpha+\gamma}$ is the total content of Nb in the alloy (5 or 7.5 wt. % Nb), ϕ_{Nb}^{γ} is the mass fraction of Nb in the γ phase (49 wt. % Nb) and ϕ_{Nb}^{α} is the mass fraction of Nb in the α phase (0 wt. % Nb). In the UNb7 alloy, the final expected phase fraction is $\phi^{\alpha} = 84.6$ wt. % ($\phi^{\gamma} = 15.4$ wt %), whereas for the UNb5 alloy this is $\phi^{\alpha} = 89.7$ wt % ($\phi^{\gamma} = 10.3$ wt %).

Figure 6.43 shows a substantial increase in the microstrain of the γ phase in conjunction with falling α phase microstrains following the reaching of 500 °C and the onset of phase separation. Decreasing microstrains might be expected in the emerging α phase as larger regions of strong crystalline structure may be produced.

Figures 6.44 and 6.45 show the lattice parameters and derived thermal expansion coefficients from the cooling scan respectively. The a axis expands the most, followed by the c axis as would

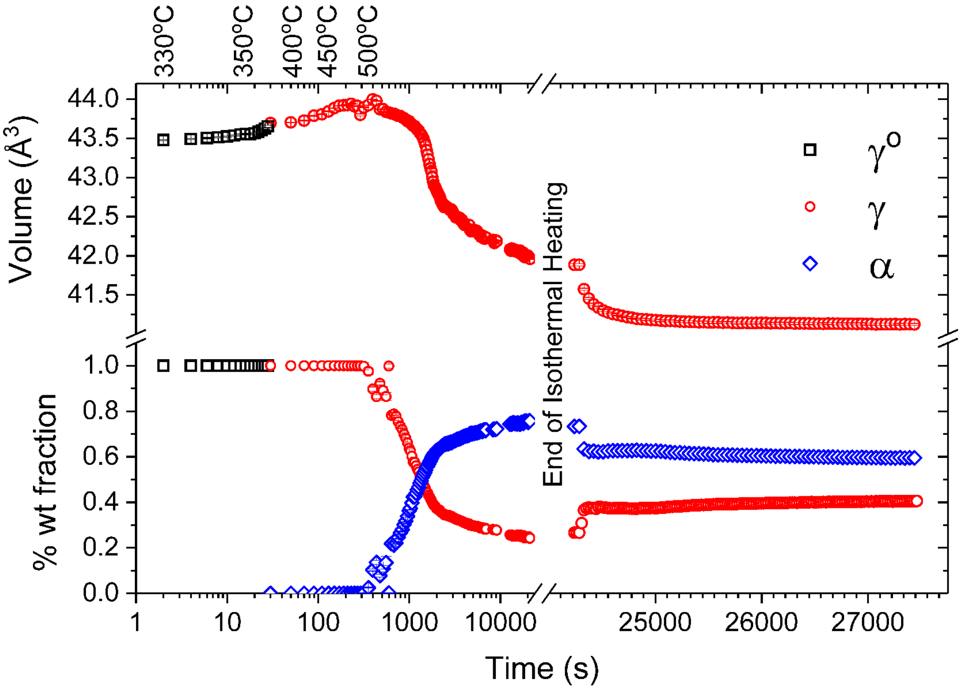

Figure 6.41: Evolution of the γ° / γ phase volumes and phase composition of the UNb7 alloy through ageing at 500 °C. Cooling data following the end of the isothermal heating shows the volume of the niobium rich γ phase decrease. The phase fraction shows anomalous behaviour in cooling that may be ascribed to incorrect temperature factors. Volume of the γ° phase at room temperature before isothermal heating started was 42.267 Å^3. Volume shown here is normalised for the γ phase definition, γ° phase data has been reduced by a factor of two to show the trend.

be expected from literature sources [28, 145]. The b axis was not observed to exhibit a negative thermal expansion coefficient as has been reported previously. Whilst the thermal expansion coefficient in the a phase is comparable to the studies of Bridge *et al.* and Konobeevsky *et al.*, the coefficients for the b and c axes' are not which may be a result of some niobium still present in the α phase matrix, or more probably, the differences in working with polycrystalline and single crystal specimens which was the case for the two references listed here.

Figure 6.46 shows a stitched cross-section of the UNb7 alloy following isothermal heat treatment at 500°C. Within two original grains of the γ° phase, numerous cellular decomposition pockets have formed. There does not appear to be any untransformed regions remaining, in agreement with the the diffraction measurements. However, there is some variation in the progress of coarsening between these regions as band thickness is proportional to the phase constituents. Whilst this affects the α phase less, as the α phase has almost no solubility for niobium, this likely indicates a wide range in the niobium content for γ phase population. This distribution of γ phase environments may be partially responsible for the large microstrain observed in the γ phase.

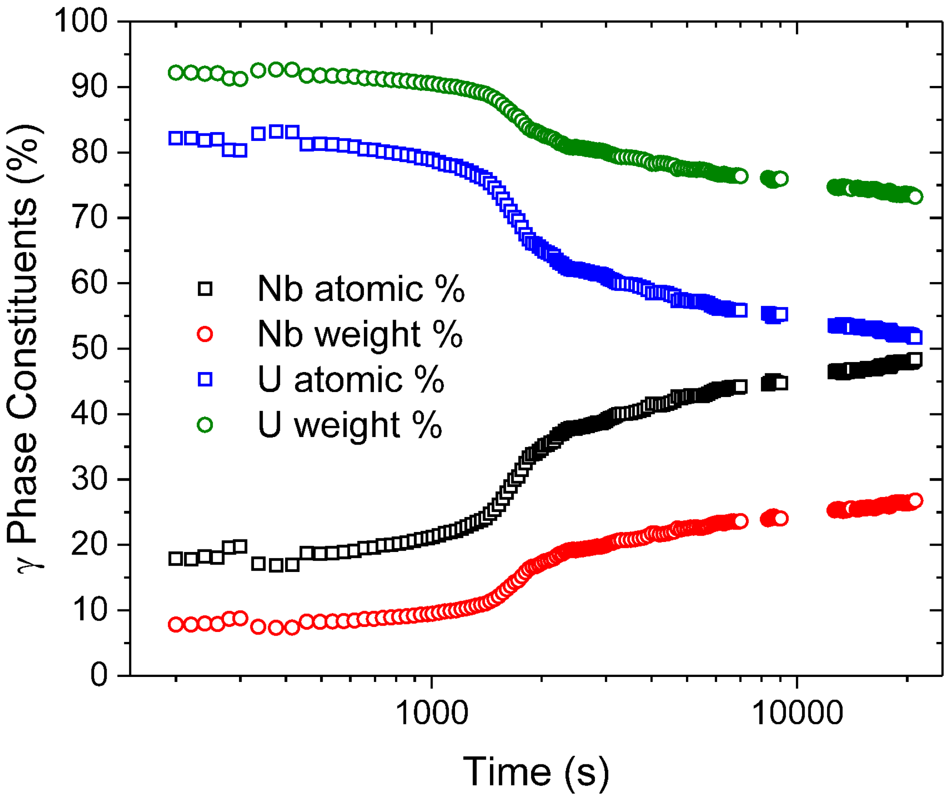

Figure 6.42: Content of the γ phase during isothermal heating of the UNb7 alloy at 500 °C as a function of time.

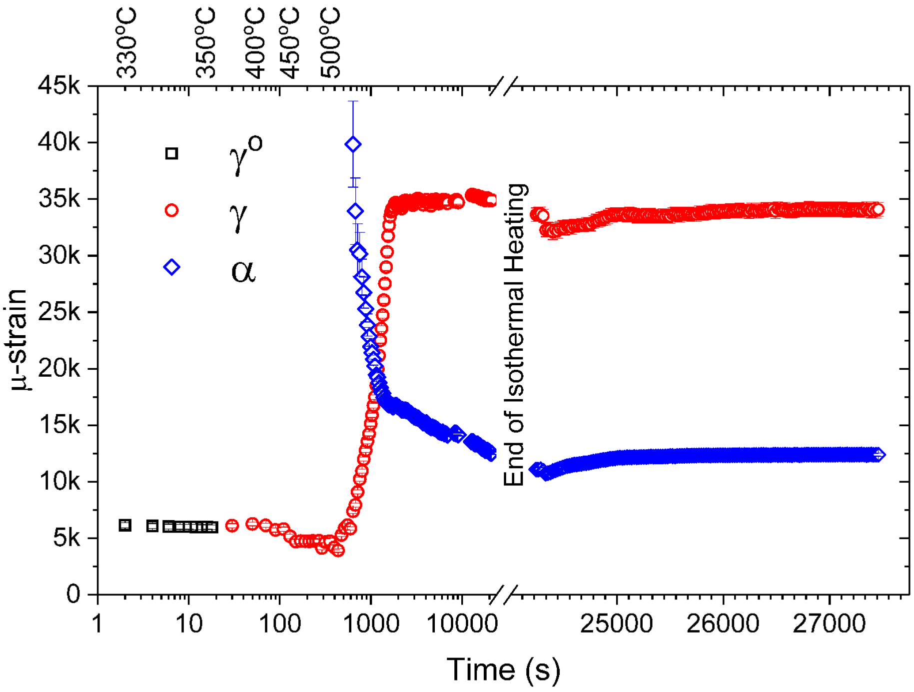

Figure 6.43: Changes to the microstrain during isothermal heating at 500 °C and cooling in the UNb7 alloy. Microstrain in the γ phase was shown to increase significantly during the transition to the α phase eventually levelling off at about 35000.

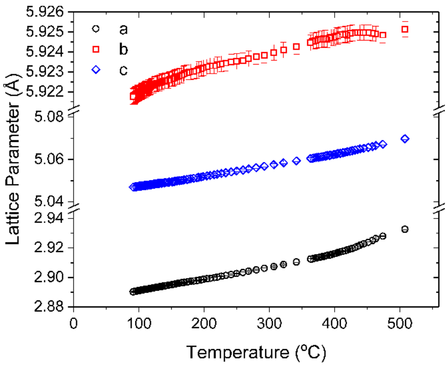

Figure 6.44: Lattice parameters of the α phase in the transformed UNb7 alloy under cooling from 500 °C.

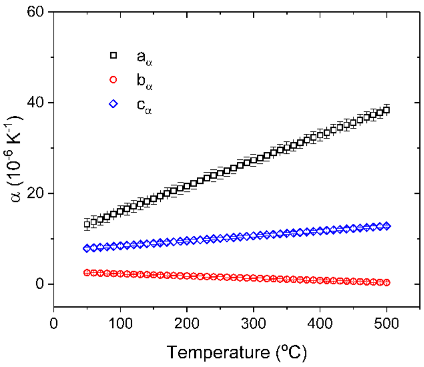

Figure 6.45: Thermal expansion coefficients of each of the three unit cell axes of the α phase in the transformed UNb7 alloy in cooling from 500 °C.

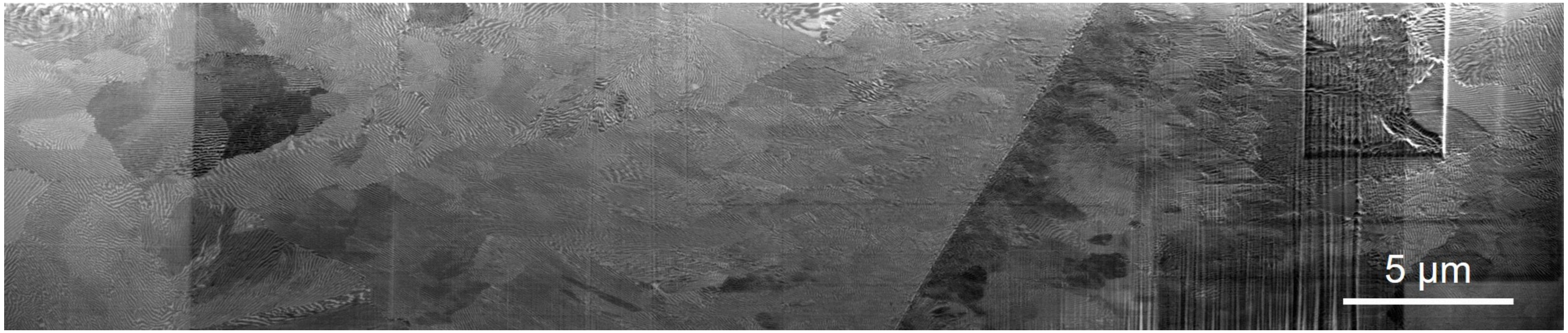

Figure 6.46: FIB-cut cross section of the 500 °C aged UNb7 sample. Within the two original grains in view numerous domains of banded material have formed.

6.4 Discussion

6.4.1 UNb5

The behaviour of the UNb5 alloy under elevated temperatures is largely as expected. Heating the alloy to 450 and 500 °C promoted conversion of the initial α'' phase into a two phase mixture of α and γ with the higher temperature of 500 °C encouraging the reaction to progress quicker. Dean's proposed TTT diagram for the UNbZr system places the nose of the C-curve at 550°C which would suggest that the quickest rates exist at still higher temperatures [61].

Microstrains increased for the outgoing α'' phase but decreased in the emerging α and γ phases. The α phase exhibits much lower levels of microstrain than the γ phase. Given the larger domains present in the α phase, predicted by the diffraction measurements and observed in the STEM images, peak broadening arising from crystallite size would be expected to be lower. However, peak broadening increases heavily with angle implying microstrain dominates. Crystallite sizes would therefore be difficult to extract via this method. STEM images are capable of clearly resolving the microstructure permitting an estimate for the crystallite sizes though this is not trivial and appears to be dictated by the local environment.

In comparison, the 400°C ageing treatment did not show as significant changes to the initial starting phase. The α'' phase remains the only indexed phase throughout and lattice parameters are mostly unchanged as a result of the treatment. Throughout the course of ageing, the lattice parameters drifted towards smaller a and c axis dimensions, a less open $\angle\gamma$ and a larger b axis, characteristics of a less dilute alloy in this system. This trend was seen by Vandermeer also in a U-14 at. % Nb alloy aged at 327 °C [274]. Vandermeer attributed this behaviour to solute atom rearrangement during ageing. However, it was also reported in this paper that alloy developed a γ like phase containing 30-35 at. % Nb after ageing at 327 °C for 11800 s. Rietveld refinements conducted on the more diffusion susceptible UNb5 alloy heated for a longer time and at a higher temperature did not shows this to have also occurred. Direct evidence for chemical segregation in this sample was not found and potentially the length scales of TEM will be required to locate solute segregation.

6.4.2 UNb7

Aged at 500 °C, the UNb7 alloy behaved in a similar manner to the UNb5 alloy. Figure 6.47 shows an APT needle of a similarly aged UNb7 alloy that has progressed to phase separation. The UNb7 alloy however transformed into the austenitic γ phase state initially before phase separation initiated. Diffusion was rapid, although phase changes were slower than for the UNb5 alloy, as would be expected. The ability for the UNb7 to achieve the γ phase, where the UNb5 did not, should also be attributed to the sloping nature of the austenitic start/finish temperature curve rather than the slower rate of phase separation in the UNb7 alloy. At the $\gamma^\circ \rightarrow \gamma$ transition temperature of 372 °C, the UNb5 alloy was still well described by the α'' phase without any signs

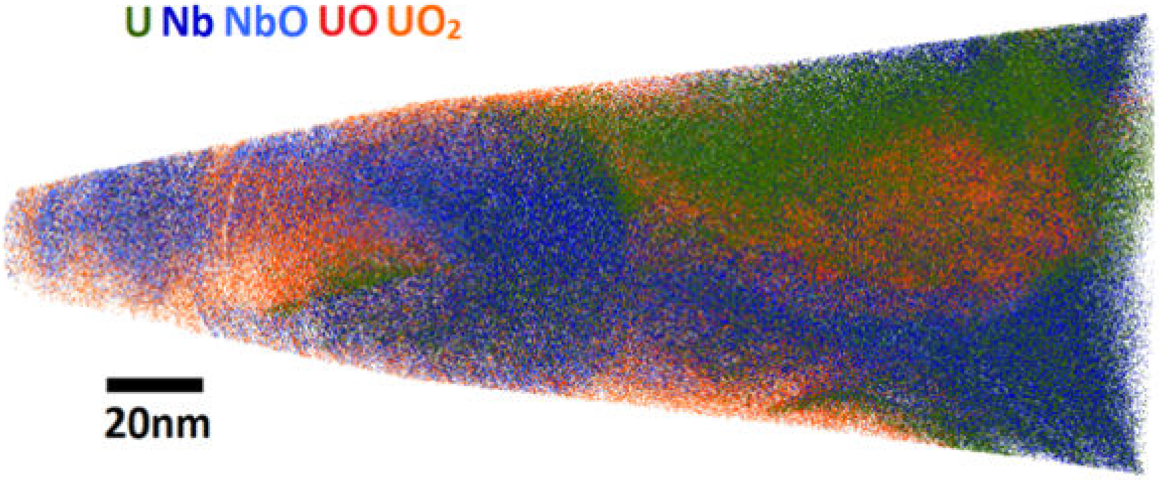

Figure 6.47: An APT needle of a UNb7 alloy that had been heated to 500°C for 2 hours. The ageing of this alloy was done separately to the treatments of the in-situ diffraction experiment. Separation has progressed very far with an almost pure uranium phase shown in green and a blue region that is high in niobium but also contains some uranium. The uranium rich-regions can be seen to have oxidised (during transfer) much quicker than the niobium-rich regions, as expected.

of phase separation strongly affecting the alloy. The γ phase that was created showed much lower levels of strain suggesting that heating had annealed out many of the γ° crystallographic defects.

At 400 °C, the UNb7 alloy exhibited interesting behaviour that can be characterised by complex phases under substantial strains. Initially, during the ramp, the alloy adopts a single γ° phase with lattice parameters following a similar trend to the 500 °C run. The slower ramp rate however has been attributed to the failure of the alloy to achieve the γ phase despite exceeding 372 °C. This would confirm previous reports that the austenitic start (and finish) temperatures are a function of ramp rate.

Subsequently the behaviour of the alloy was further probed in this regime by increasing the temperature to 450 °C. The increased temperature was not capable of inducing full phase separation as was the case for the UNb5 alloy. Ex-situ investigations provide additional insight into the mechanisms. Diffusion and cellular decomposition appears to have initiated at preferential locations which include carbides. Finer phase separation may be present elsewhere but these are not observable using FIB/SEM under these conditions. The decomposition occurring in these two lower temperatures can be considered to be identical. Sequentially fitting the patterns showed the γ° phase to slowly evolve into a two phase mixture which included the α'' phase. Such a reaction is conventionally termed a massive reaction. Massive reactions are characterised by a diffusionless transformation in which the sample gradually transforms into the martensitic phase isothermally portion at a time. These reactions are particularly important in Ti alloys and the bainite phase of steels.

The α'' phase is essentially a version of the α phase where the $\angle\gamma$ is not 90° and lattice parameters and atomic coordinates are slightly altered. XRD showed that fitting of the pattern using α and γ° phases produced a reasonable fit however, not as strong as using the α'' phase and besides, the lattice parameters that it produced for the α phase were 2.91636, 5.95560 and 4.99991 Å, very close to those accepted for the α'' phase, a far cry from the accepted values of 2.854, 5.870 and 4.955 [148]. Additional reasons to believe that it is not the α phase that has emerged can be drawn from the fact that the diffraction patterns still have significant levels of texture.

6.4.3 General/Experimental

Despite various inefficiencies and plenty of scope for improvement in the setup, the experiment was capable of studying the behaviour of the UNb5 and the UNb7 alloys at high temperatures with in-situ XRD capabilities. Study of the rapid diffusional as well as slower acting diffusion-limited transformations were possible.

Aspects that could be improved upon include the temperature controller, as ramp rate was dependent on final temperature; temperature calibration, as Ni foil wrapped around/bonded to the sample would provide a more reliable estimate and sample geometry. Any follow up experiments into this system using a similar methodology might be improved by additionally including transport measurements for comparison with many works present in the literature.

Use of the tomography capabilities on the beamline, although not shown, suggest 112 keV x-rays would permit a sample thickness of up to 3 mm. This also sets up the possibility of performing engineering tests on the samples, particularly as cylindrical shapes are beneficial for the purposes of tomography. Production of strong quality tomographic images using the data collected was difficult given the high aspect ratio of the sample. The foil shape was used as it was previously intended that resistivity measurements would be taken of the sample in-situ. Additionally, this enabled the mass and therefore the radioactivity of the sample to a minimum and ensure adequate transmission of the beam when oriented normal to the sample surface. A thicker sample would additionally reduce the preferred orientation effects that were observed in these samples. Mapping the sample using stage stepping motors were able to increase homogeneity in the patterns. However, this was only a benefit during the mapping runs and for the majority of scans collected, preferred orientation corrections were required impacting the ability to confidently refine parameters such as atomic positions.

The use of high energy x-rays in transmission mode ensure that the bulk of the sample was probed with negligible contributions from the surfaces. Preparation of the samples for such an experiment is therefore simple and easily repeatable.

It should be investigated whether, given the difficulties in extracting information regarding the solute migration in the lower temperature runs, SAXS may be used as an additional capability for any future experiment. Beamlines such as I12 often also permit the collection of SAXS data.

6.5 Conclusions

This experiment was successful in probing new physics regarding the high temperature transitions in the UNb5 and UNb7 alloys. Performing in-situ XRD studies has the benefit of collecting a vast quantity of data and by performing full pattern fitting, obtain properties concerning the crystallographic phases and transitions in these alloys. The advantages over traditional measurements are clear but combination with techniques such as resistivity and microscopy proves to be the most effective means of studying such transitions.

CHAPTER 7

SUMMARY AND FUTURE WORK

This brief final chapter summarises the key findings in this thesis and places them in the context of previous works carried out over the past 50+ years of study into the metastable phases in these materials. Further work required to answer some of the remaining questions is additionally discussed.

7.1 Preparation of Uranium Alloys

Excellent preparation of these alloys was deemed a prerequisite for many subsequent portions of the work presented in this thesis, notably the assessment of the effects of long term ageing by x-ray diffraction. Investigations into the electropolishing process were conducted in order to gain insight into, and ideally improve the preparation processes of uranium and the uranium alloys. Despite being a relatively seasoned technique, many aspects of electropolishing are still not fully understood and subtleties are present on a system to system basis. Some of the most advanced treatments of the process of electropolishing were performed in the 1990s by Grimm, Matlosz and Landolt, aided by electrochemical impedance spectroscopy [101, 151, 163, 165, 166]. However, a significant number of papers detailing electropolishing specifics continue to be published each year. The work presented here in Chapter 3 has sought to emulate these studies for these materials by the application of commonly used electrochemical experiments. It is thought that this is the first systematic study of electrode dynamics in uranium and the uranium-niobium alloys performed in this manner for this purpose. The field of electrochemistry is much broader than the selection of methods used here. It is expected that the processes of electropolishing uranium and uranium alloys would benefit from a variety of other techniques, including electrochemical impedance spectroscopy.

Ex-situ analysis of the resultant surfaces by x-ray and electron diffraction indicate that the methods applied have been successful in producing pristine surfaces enabling the advancement of the studies to subsequent stages with the confidence that residual surface preparation effects are minimised. One key indicator of the high quality surfaces are the respectable EBSD patterns and maps that have been produced. The methods used here present an advancement on previous routines used internally which have relied heavily of the use of extensive FIB milling to facilitate the collection of EBSD patterns. However, it was found that patterns were significantly enhanced by argon ion etching at low potentials which is considered to contribute through the removal of an oxide layer whilst impacting the surface to a much lesser degree than Ga^+ FIB milling would. Argon etching can be discounted from being responsible for removing damaged surface layers as the amount of material removed by electropolishing far exceeds that sputtered away.

EBSD maps of the UNb5 and UNb7 alloys are particularly rare with no other instances known as available in the open literature. A deformed UNb6 EBSD map has been published by Clarke *et al.* [52]. However, it appears that the un-deformed UNb6 alloy, which is much more heavily twinned, has to date not found representation in the literature by an EBSD map. Further study should therefore be applied to these EBSD maps and further instances, so that a larger range of orientations is covered, with the intent of investigating the microstructure and crystallography of the phases. An achievable and worthwhile goal would be to conduct in-situ EBSD analysis of these alloys between straining treatments, rather like Clarke *et al.* have done. At present, it seems that the UNb7 alloy would have the best chance of yielding good results without any further improvements made to the preparation process. An appreciation of the upper limit of pattern quality in these materials might be obtainable through transmission Kikuchi diffraction (TKD).

7.2 Structures of the Metastable Phases

The structures of the α'' and γ° phases found in the UNb5, UNb6 and UNb7 alloys have been re-examined using the modern Rietveld refinement technique accompanied by anisotropic modelling of strains. Applied to the α'' phase, the fitting has modelled the UNb5 and UNb6 alloys well, producing results that correlate well with the twinning behaviour in these alloys. Modelling of the structural positions and atomic sites has also been performed in these alloys. Little attention has been paid to these parameters recently and the best treatment appears to have been conducted by Stewart and Williams on the UMo alloy over 50 years ago [241].

Refining atomic positions in the UNb5 and UNb7 alloys permitted the construction of a nearest neighbour plot which clearly show the progression of atomic shuffling throughout the martensitic transformation. This plot reveals that atoms would experience an eventful change in coordination if the structure for the γ^s phase derived from the UNbZr system by Yakel is to be accepted. It may be worth re-examining the crystallography of the γ^s phase in the uranium-niobium alloy system (>20 at.%Nb) using a high resolution diffractometer using modern methods.

However, fitting of the γ° phase in the UNb7 alloy was less straightforward than in the case of the UNb5 and UNb6 alloys. Using a pattern obtained from the I12 high energy x-ray diffractometer, which ensured the bulk state was accessed, the pattern suggested that either the UNb7 alloy has a higher fraction of the α'' phase than expected or that the structure is more complicated than originally believed. It may be that the γ° phase additionally needs to be examined in greater detail. Including the α'' phase into the fit of the UNb7 alloy was the only means of producing a good fit that wouldn't require a change in crystal symmetry of the γ° phase.

For the purposes of the work presented here, the use of the lab source has sufficed, particularly since the previous chapter had ensured that the surface could be prepared in such a way to be highly representative of the state of the bulk. Regardless, a new systematic assessment of the crystallography of the phases in this system with modern state of the art equipment should be considered if diffraction based experiments continue to be awarded experimental time at premier scientific facilities.

7.3 Low Temperature Transformations

Experiments into the long term ageing behaviour of the uranium-niobium alloys failed to find sources of chemical segregation, in agreement with relatively recently published papers that have discredited the notion that the low temperature reaction is connected to phase separation. One of the clearest indications was given by the APT needle of an aged UNb7 alloy which, as the mechanical data shows, experienced a substantial loss in ductility and increase in strength, just as was the case for Clarke's observations of the U-13 at.%Nb alloy [51].

Papers published since the start of the project have hypothesised the migration of defects and rearrangement of twin boundaries to be responsible for the changes to mechanical properties. Conventional x-ray and neutron diffraction techniques are largely insensitive to this mechanism, therefore requiring a new strategy. The assessment of progressively aged alloys by diffraction in this project has also confirmed that obtaining detailed information on the microstructure is difficult by x-ray diffraction as the unit cells are largely unchanged. Therefore, focusing on the fitting of peak broadening, it was observed that ageing induces an instantaneous decrease in the strain of the α'' phase but progressive increases to the strains of the γ° phase. However, results have in places been affected by external factors such as excessive oxidation due to equipment issues. Examination of the build up of stress in this material would be perfectly suited to a relatively short neutron diffraction study of pre-aged specimens. Diffraction of neutrons would ensure the bulk state was accessed every time, irrespective of the ageing environment, and a texture-free pattern was recorded, essential for the accurate fitting of structural positions.

More work should be done to explore the defect migration and twin boundary migration hypotheses. TEM with electron diffraction would be the obvious candidate to assist with this.

Or, alternatively, positron annihilation spectroscopy which is a technique especially adept at collecting quantitative measures of defect type and population. EBSD is unlikely to be useful in establishing changes to the microstructure as a result of ageing alone due to the length scale of defects and twin boundaries in comparison to the resolution limit of the technique in most microscopes. TKD performed on a TEM may be able to provide the required spatial resolution to map the twins by Kikuchi diffraction.

7.4 High Temperature Transformations

Work presented in the chapter concerning the high temperature reactions in these alloys was collected in May 2018. Zhang *et al.* has since published a manuscript which takes a very similar approach and reports complementary results [300]. Whilst the timing of these events is unfortunate, Zhang *et al.*'s recently published results utilising a very similar methodology validates the decision to examine this reaction in these alloys with modern apparatus. The work presented here is in broad agreement, however, as Zhang *et al.* studied the U-6 wt.%Nb alloy, results are sufficiently distinct. The work presented here also goes further by examining reactions at a wider range of temperatures and has extracted other information such as thermal expansion coefficients, which are predictably anisotropic and therefore may lead to internal stresses that may be of concern to long term ageing.

At the bottom end of the high temperature transformations, the processes are clearly slower and confirm a different class of reaction. Whilst there is some diffusion occurring at these lower temperatures, as was confirmed by ex-situ FIB investigations, production of the α'' phase in the initially γ° phase dominant UNb7 alloy suggests the $\gamma^{\circ} \rightarrow \alpha''$ reaction observed in UNbZr alloys, and occasionally also in UNb alloys, is operative in this alloy.

The high intensity x-ray source and 2D detectors have permitted in-situ diffraction experiments capable of recording fast acting processes such as diffusion in these materials. The UNb5 and UNb7 alloys have illustrated the dependence of composition on the rate of the diffusional transformations. Further investigations into the high temperature reactions, such as the crystallographic transitions occurring during quenching, would be of interest but could be greatly improved by small changes to the experimental setup. The most significant changes would be to increase the size of the specimens as it was shown that the high energy x-rays could accommodate samples a few mm thick. Larger samples would have the immediate effect of producing fuller Debye-Scherrer rings which may be sufficient in unlocking measurements of stress through the $\text{Sin}^2\psi$ method.

APPENDIX A

CALIBRATION OF THE NICKEL HEATER

The linear thermal expansion coefficients of nickel, which was used as calibration of the heater in Chapter 6, were sourced from Touloukian *et al.* [267]. The data is shown in Table A.1 and plotted in Figure A.1.

Figure A.1 has been fitted with the Belehradek function, an offset power function, which takes the form,

$$\alpha = A(T-B)^C, \tag{A.1}$$

where α is the thermal expansion coefficient and T is the temperature. The constants A, B and C were calculated as $(3.81 \pm 0.27) \times 10^{-6}$, 86.6 ± 6.1 K and 0.12 ± 0.01 respectively.

The general formula of the thermal expansion coefficient is,

$$\alpha = \frac{1}{a}\frac{da}{dT}, \tag{A.2}$$

T/ K	α_{Ni}/ 10^{-6} K^{-1}
100	6.6
200	11.3
293	13.4
500	15.3
800	16.8
1100	17.8
1500	20.3

Table A.1: Linear thermal expansion coefficients of nickel. Data originates from Touloukian *et al.* [267].

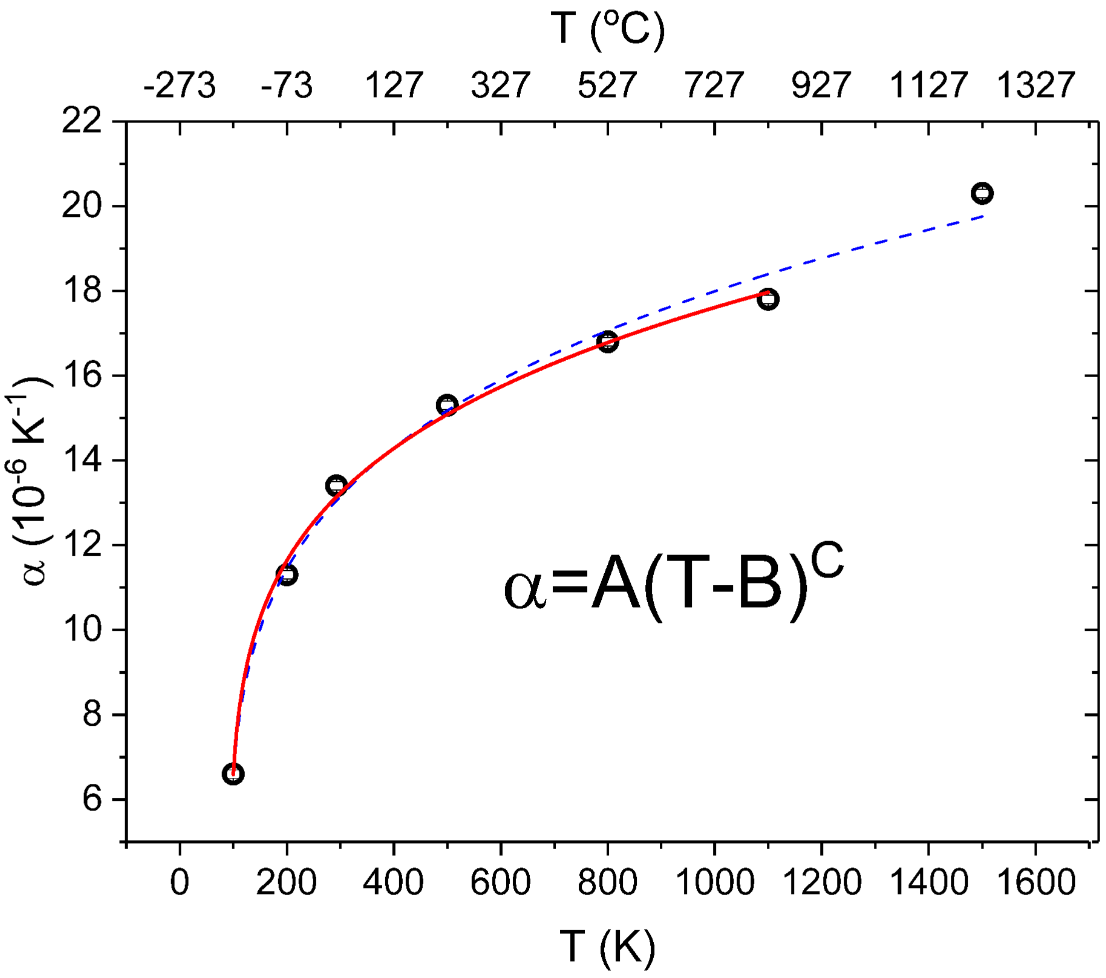

Figure A.1: Thermal expansion coefficient of nickel (heater calibrant) with temperature. The dotted blue line shows the fit using all data points. The solid red line shows the fit having excluded the last data point which is beyond the bounds of the experiment conducted at I12. Errors have been taken to be the precision of measurements.

which integrates to,

$$\int \alpha dT = \int \frac{1}{a} da. \tag{A.3}$$

Substituting in the model used for α based on empirical data, Equation A.1, the lattice parameter, a, may be related to the temperature, T, and the constants, A, B and C,

$$\int A(T-B)^{C} dT = \int \frac{1}{a} da, \tag{A.4}$$

this may be solved as,

$$A\frac{(T-B)^{C+1}}{C+1} = log_e a + log_e x, \tag{A.5}$$

or,

$$A\frac{(T-B)^{C+1}}{C+1} = log_e(ax). \tag{A.6}$$

Taking the exponential of both sides allows the constant, x, to be isolated,

$$ax = e^{\frac{A(T-B)^{C+1}}{C+1}}, \tag{A.7}$$

and,

$$x = \frac{1}{a}e^{\frac{A(T-B)^{C+1}}{C+1}}. \tag{A.8}$$

x may be evaluated using the lattice parameter at room temperature. Using $a = 3.5369\,\text{Å}$ and $T = 293\,\text{K}$, x is calculated to be 0.2834 for nickel.

For the I12 experiment, it was important to be able to calibrate the temperature based on the lattice parameter of the nickel foil. Therefore, Equation A.6 needs to be rewritten with T as the subject,

$$T = B + \left(\frac{C+1}{A}log_e(ax)\right)^{\frac{1}{C+1}}. \tag{A.9}$$

APPENDIX B

CALCULATING THERMAL EXPANSION COEFFICIENTS

The thermal expansion coefficients of the lattice parameters of the γ, γ°, α'' and α phases were determined in Chapter 6. This appendix describes the method by which they were evaluated.

Thermal expansion coefficients may only be assumed to be linear over a narrow range of temperatures. Appendix A shows, the thermal expansion of Ni to be better fitted by a Belehradek function. However, in the range of room temperature to 647 °C, the eutectoid in the uranium-niobium system [188], the relationship is relatively linear.

Uranium alloy thermal expansion coefficients are not trivial and will not necessarily fit a model as different axes exhibit drastically different behaviours [274, 294]. The lattice parameters, nominally a, of the uranium-niobium alloys were generally modelled with second order polynomial equations,

$$a = A + BT + CT^2. \tag{B.1}$$

Quadratic profiles were deemed sufficient to describe the data without adding needless additional terms that only improved the fit quality. The thermal expansion coefficient, α, is given by,

$$\alpha = \frac{1}{a}\frac{da}{dT} \tag{B.2}$$

$$\alpha = \frac{B + 2CT}{A + BT + CT^2} = \frac{F}{G}. \tag{B.3}$$

The error is evaluated by partial differential equations,

$$\left(\frac{\Delta\alpha}{\alpha}\right)^2 = \left(\frac{\Delta F}{F}\right)^2 + \left(\frac{\Delta G}{G}\right)^2, \tag{B.4}$$

with,

$$\begin{aligned}\Delta F^2 &= \left|\frac{\partial F}{\partial X_i}\right|^2 \Delta X_i^2 \\ &= \left|\frac{\partial F}{\partial T}\right|^2 \Delta T^2 + \left|\frac{\partial F}{\partial B}\right|^2 \Delta B^2 + \left|\frac{\partial F}{\partial C}\right|^2 \Delta C^2 \\ &= (2C + 6DT)^2 \Delta T^2 + 1\Delta B^2 + 2T\Delta C^2,\end{aligned} \tag{B.5}$$

and,

$$\begin{aligned}\Delta G^2 &= \left|\frac{\partial G}{\partial X_i}\right|^2 \Delta X_i^2 \\ &= \left|\frac{\partial G}{\partial T}\right|^2 \Delta T^2 + \left|\frac{\partial G}{\partial A}\right|^2 \Delta A^2 + \left|\frac{\partial G}{\partial B}\right|^2 \Delta B^2 + \left|\frac{\partial G}{\partial C}\right|^2 \Delta C^2 \\ &= (B + 2CT + 3DT^2)^2 \Delta T^2 + 1\Delta A^2 + T\Delta B^2 + T^2\Delta C^2.\end{aligned} \tag{B.6}$$

APPENDIX C

ANALYSIS OF STRESS-STRAIN CURVES

The code written to automate the analysis of stress-strain curves presented in Chapter 5 is included below. The code has been written in the Python programming language and utilises elements of the numpy, matplotlib, scipy and pandas libraries.

Nomenclature for the points of interest has followed the conventions of Vandermeer *et al.* [276]. These terms, along with others introduced here for the benefit of the fitting routine are described in the text.

Data is initially read in from a csv file which contains four columns; time, displacement, extension and load. This data is written into a pandas dataframe, and from this initially data, additional columns such as strain and stress are produced. The process of identifying points of interest relies on the examination of the first, second and third differentials. This is performed by numpy's gradient function. The data has small experimental noise that needs to be smoothed out for successive differentials to be extracted. Savitzky-Golay filtering (of the scipy library) acting over windows of a couple of hundred points has been required to sufficiently smooth the data. These differentials are subsequently analysed so that the positions at which they cross the y axis may be extracted. A few work arounds have been used in special cases, for instance if the curve does not cut $y = 0$.

```
import numpy as np
import matplotlib.pyplot as plt
from scipy.signal import savgol_filter
import pandas as pd
import math

def resultsTable(output, POIlist):
    print("\n")
    for i in range(0,9):
        print("\u03B5-{}\t= {:.2f} %,".format(POIlist[i], output['Strain'][i]), end="\t")
```

```
        print("\u03C3-{}\t= {:.1f} MPa,".format(POIlist[i], output[’Stress’][i]), end="\t")
        print("\u03B8-{}\t= {:.1f} GPa,".format(POIlist[i], output[’Diff1’][i]/10), end="\t")
        print("\u03BE-{}\t= {:.1f} TPa".format(POIlist[i], output[’Diff2’][i]/100))

def writeResults(output, POIlist, filename):
    filename = filename.split(".")[0] + ".txt"
    POIlist.pop()
    POIlist.append("gam")
    file = open(filename, "w")
    file.write("Point\tStrain\tStress\tDiff1\tDiff2\n")
    file.write("\t%\tMPa\tGPa\tTPa\n")
    for i in range(0,9):
        file.write("{}\t".format(POIlist[i]))
        file.write("{:.2f}\t".format(output[’Strain’][i]))
        file.write("{:.1f}\t".format(output[’Stress’][i]))
        file.write("{:.2f}\t".format(output[’Diff1’][i]/10))
        file.write("{:.1f}\n".format(output[’Diff2’][i]/100))
    file.close()

def annotations(output, POIlist):
    output = output.reset_index()
    for i in range(0,len(POIlist)):
        plt.annotate("{}".format(POIlist[i]),(output[’Strain’][i]-0.1, 750))
        plt.arrow(output[’Strain’][i], 720, 0, output[’Stress’][i]-700)


def gammaPoint(output, df):
    c = output[’Stress’][3] - (output[’Diff1’][3]*output[’Strain’][3])
    for i in range(1,x-1):
        sig_c = df[’Stress’][i] #Stress on curve
        sig_i = (output[’Diff1’][3]*df[’Strain’][i]) + c #Stress traced back from sigma_g
        if (sig_i-sig_c)/sig_i < 0.005:
            return i

# =============================================================================
# Filename: set as is so can be used directly or called sequentially from a list
# by another script
# =============================================================================

if __name__ == ’__main__’:
    filename = "7_0hrs_1.csv"

# =============================================================================
# Main code
# =============================================================================

df = pd.read_csv(filename, thousands=",")
df = df.drop(df.index[0])

df["Load"] = [col.replace(’,’,’’) for col in df["Load"]]
df = df.apply(pd.to_numeric)

df[’Strain’] = 2*(df[’Extension’]-df[’Extension’][1])
df[’Stress-raw’] = ((df[’Load’]-df[’Load’][1])/1000000)/(math.pi*0.0015**2)
df[’Stress’] = df[’Stress-raw’]
```

```
df['Stress'] = savgol_filter(df['Stress'], 51, 3)

x = df.shape
x = x[0]
y = df.loc[x-1]["Strain"]

df['Diff1'] = np.gradient(df['Stress'])/(y/x)
df['Diff1'] = savgol_filter(df['Diff1'], 201, 3)

df['Diff2'] = np.gradient(df['Diff1'])/(y/x)
df['Diff2'] = savgol_filter(df['Diff2'], 401, 4)

df['Diff3'] = np.gradient(df['Diff2'])/(y/x)
df['Diff3'] = savgol_filter(df['Diff3'], 301, 3)

output = df.iloc[0:0]
pos = []


safety = 6

for i in range(1,x-1):
    if ((df.at[i, 'Diff2'] < 0) & (df.at[i+1, 'Diff2'] > 0)) or (
            (df.at[i, 'Diff2'] > 0) & (df.at[i+1, 'Diff2'] < 0)):
                pos.append(i)
                output = output.append(df.iloc[[i]])
                if len(output.index) == 4:
                    break

#print(len(pos))
#print(pos)

# ==============================================================================
# Section to add in extra terms in case of 7 alloy if second differential
# doesn't cross zero a sufficient number of times.
# ==============================================================================

j = int((x-1)*0.8)
while len(pos) < 4:
    pos.append(j)
    output = output.append(df.iloc[[j]])
    j +=20

# ==============================================================================
# Append fracture point to positions lists and dataframe
# ==============================================================================

pos.append(x-1)
output = output.append(df.iloc[[x-1]])

# ==============================================================================
# Append minima and maxima of second differential curve
# ==============================================================================

output = output.append(df.loc[abs(df['Diff2']) == max(abs(df['Diff2'][pos[0]:pos[1]]))])
```

```
output = output.append(df.loc[abs(df['Diff2']) == max(abs(df['Diff2'][pos[1]:pos[2]]))])
output = output.append(df.loc[abs(df['Diff2']) == max(abs(df['Diff2'][pos[2]:pos[3]]))])
output = output.reset_index()

POIlist = ["E", "I", "II", "g", "f", "d", "12", "t" , "\u03B3"] #\u2081\u2082

z = gammaPoint(output, df)
output = output.append(df.iloc[[z]], sort=False)
output = output.reset_index()
output = output.drop(columns=['level_0', 'index'])

false = output
falselist = POIlist

maximum = output['Diff2'][5]
if output['Strain'][1] > safety:
    for i in range(600, 850):
        if df['Diff2'][i] > maximum:
            maximum = df['Diff2'][i]
            I=i
    output.loc[3] = output.loc[1]
    output.loc[1] = df.loc[I]
    output.loc[2] = np.nan
    output.loc[7] = output.loc[5]
    output.loc[5:6] = np.nan

    false = output
    false = false.drop([2,5,6])

    falselist.remove("II")
    falselist.remove("d")
    falselist.remove("12")

# ============================================================================
# Change gamma point if Diff1 ever passes through 0: Quick fix for UNb7, do not
# use with UNb5, gammaPoint works well.
# ============================================================================
#
#for i in range(1,x-1):
#    if ((df.at[i, 'Diff1'] < 0) & (df.at[i+1, 'Diff1'] > 0)) or (
#            (df.at[i, 'Diff1'] > 0) & (df.at[i+1, 'Diff1'] < 0)):
#               output.loc[8] = df.iloc[i]

# ============================================================================
# Plotting with matplotlib
# ============================================================================
imagename = filename.split(".")[0] + ".png"

plt.figure(num=None, figsize=(6, 4), dpi=100, facecolor='w', edgecolor='k')

plt.plot(df['Strain'], df['Stress'], label="\u03C3")
plt.plot(df['Strain'], df['Diff1'], label="d\u03C3/d\u03B5")
plt.plot(df['Strain'], df['Diff2'], label="d\u00B2\u03C3/d\u03B5\u00B2")
plt.plot(df['Strain'], df['Diff3'], label="d\u00B3\u03C3/d\u03B5\u00B3")
plt.plot(false['Strain'], false['Stress'], 'ro', label="Points of Interest")
```

```
annotations(false, falselist)

plt.axhline(0, color='black')
plt.xlim([0, y+1])
plt.ylim([-200, 800])
plt.xlabel("Strain %")
plt.legend()
plt.savefig(imagename)
plt.show()

POIlist = ["E", "I", "II", "g", "f", "d", "12", "t" , "\u03B3"]

resultsTable(output, POIlist)
writeResults(output, POIlist, filename)
```

BIBLIOGRAPHY

[1] A. P. ABBOTT, G. CAPPER, K. J. MCKENZIE, AND K. S. RYDER, *Voltammetric and impedance studies of the electropolishing of type 316 stainless steel in a choline chloride based ionic liquid*, Electrochimica Acta, 51 (2006), pp. 4420–4425.

[2] J. P. ABRIATA AND J. C. BOLCICH, *The Nb- Zr (Niobium- Zirconium) system*, Journal of Phase Equilibria, 3 (1982), pp. 34–44.

[3] A. AITKALIYEVA, J. W. MADDEN, B. D. MILLER, J. I. COLE, AND J. GAN, *Comparison of preparation techniques for nuclear materials for transmission electron microscopy (TEM)*, Journal of Nuclear Materials, 459 (2015), pp. 241–246.

[4] M. Y. ALI, W. HUNG, AND F. YONGQI, *A review of focused ion beam sputtering*, International journal of precision engineering and manufacturing, 11 (2010), pp. 157–170.

[5] A. ALLISY, *Henri Becquerel: the discovery of radioactivity*, Radiation protection dosimetry, 68 (1996), pp. 3–10.

[6] J. ALS-NIELSEN AND D. MCMORROW, *Elements of modern X-ray physics*, John Wiley & Sons, 2011.

[7] M. ANAGNOSTIDIS, M. COLOMBIE, AND H. MONTI, *Phases Metastables Dans Les Alliages Uranium-Niobium*, Journal of Nuclear Materials, 1 (1964), p. 67.

[8] K. W. ANDREWS, D. J. DYSON, AND S. R. KEOWN, *Interpretation of electron diffraction patterns*, vol. 202, Springer, 1971.

[9] C. L. ANGERMAN, *Transmission electron microscopy of uranium*, Journal of Nuclear Materials, 9 (1963), pp. 109–110.

[10] D. AOKI AND J. FLOUQUET, *Ferromagnetism and superconductivity in uranium compounds*, Journal of the Physical Society of Japan, 81 (2011), p. 11003.

[11] P. E. ARMSTRONG, D. T. EASH, AND J. E. HOCKETT, *Elastic moduli of alpha, beta and gamma polycrystalline uranium*, Journal of Nuclear Materials, 45 (1972), pp. 211–216.

[12] ASTM STANDARD, *E140-12be1, Standard Hardness Conversion Tables for Metals Relationship among Brinell Hardness, Vickers Hardness, Rockwell Hardness, Superficial Hardness, Knoop Hardness, Scleroscope Hardness, and Leeb Hardness*, West Conshohecken, PA: ASTM International, (2012).

[13] A. AUTHIER, *Dynamical theory of X-ray diffraction*, International Tables for Crystallography, (2006), pp. 626–646.

[14] B. J. BAER, H. CYNN, V. IOTA, C.-S. YOO, AND G. SHEN, *Phase diagram and equation of state of praseodymium at high pressures and high temperatures*, Physical Review B, 67 (2003), p. 134115.

[15] T. BALDHOFF AND A. T. MARSHALL, *Characterization of Surface Films Formed on Aluminum during Mass-Transfer Limited Anodic Dissolution in Phosphoric Acid*, Journal of The Electrochemical Society, 164 (2017), pp. C46–C53.

[16] A. BANOS AND T. B. SCOTT, *Statistical analysis of UH3 initiation using electron backscattered diffraction (EBSD)*, Solid State Ionics, 296 (2016), pp. 137–145.

[17] D. J. BARBER, *Radiation damage in ion-milled specimens: characteristics, effects and methods of damage limitation*, Ultramicroscopy, 52 (1993), pp. 101–125.

[18] M. BASHAM, J. FILIK, M. T. WHARMBY, P. C. Y. CHANG, B. EL KASSABY, M. GERRING, J. AISHIMA, K. LEVIK, B. C. A. PULFORD, AND I. SIKHARULIDZE, *Data analysis workbench (DAWN)*, Journal of synchrotron radiation, 22 (2015), pp. 853–858.

[19] J. A. BEARDEN, *Reevaluation of X-ray atomic energy levels*, Rev. Mod. Phys., 39 (1967), p. 125.

[20] G. BEVERINI AND D. V. EDMONDS, *An APFIM study of the aging behavior of uranium-niobium alloy (U-6.0 wt.% Nb)*, in J. Phys. Colloq., vol. 50, 1989, pp. 429–434.

[21] J. F. BINGERT, R. J. HANRAHAN JR, R. D. FIELD, AND P. O. DICKERSON, *Microtextural investigation of hydrided α-uranium*, Journal of alloys and compounds, 365 (2004), pp. 138–148.

[22] M. D. BLAUFOX, *Becquerel and the discovery of radioactivity: early concepts*, in Seminars in nuclear medicine, vol. 26, Elsevier, 1996, pp. 145–154.

[23] M. L. BLEIBERG, L. J. JONES, AND B. LUSTMAN, *Phase changes in pile-irradiated uranium-base alloys*, Journal of Applied Physics, 27 (1956), pp. 1270–1283.

[24] B. BLUMENTHAL, *The transformation temperatures of high-purity uranium*, Journal of Nuclear Materials, 2 (1960), pp. 22–30.

[25] H. E. BOYER, *Hardness testing*, ASM International, 1987, (1987), p. 188.

[26] W. H. BRAGG AND W. L. BRAGG, *The reflection of X-rays by crystals*, Proceedings of the Royal Society of London. Series A, Containing Papers of a Mathematical and Physical Character, 88 (1913), pp. 428–438.

[27] W. L. BRAGG, *The structure of some crystals as indicated by their diffraction of X-rays*, Proceedings of the Royal Society of London. Series A, Containing papers of a mathematical and physical character, 89 (1913), pp. 248–277.

[28] J. R. BRIDGE, C. M. SCHWARTZ, AND D. A. VAUGHAN, *X-ray Diffraction Determination of the Coefficients of Expansion of Alpha Uranium*, JOM, 8 (1956), pp. 1282–1285.

[29] W. BRINER, *The toxicity of depleted uranium*, International journal of environmental research and public health, 7 (2010), pp. 303–313.

[30] D. BROWN, M. BOURKE, A. CLARKE, R. FIELD, R. HACKENBERG, W. HULTS, AND D. THOMA, *The effect of low-temperature aging on the microstructure and deformation of uranium- 6 wt% niobium: An in-situ neutron diffraction study*, Journal of Nuclear Materials, 481 (2016), pp. 164–175.

[31] D. W. BROWN, M. A. M. BOURKE, R. D. FIELD, W. L. HULTS, D. F. TETER, D. J. THOMA, AND S. C. VOGEL, *Neutron diffraction study of the deformation mechanisms of the uranium–7wt.% niobium shape memory alloy*, Materials Science and Engineering: A, 421 (2006), pp. 15–21.

[32] G. BROWN, K. HALBACH, J. HARRIS, AND H. WINICK, *Wiggler and undulator magnets—A review*, Nuclear Instruments and Methods in Physics Research, 208 (1983), pp. 65–77.

[33] H.-J. BUNGE, *Texture analysis in materials science: mathematical methods*, Elsevier, 2013.

[34] G. CAGLIOTI, A. PAOLETTI, AND F. RICCI, *Choice of collimators for a crystal spectrometer for neutron diffraction*, Nuclear Instruments, 3 (1958), pp. 223–228.

[35] R. CAHN, *Plastic Deformation of Alpha-Uranium; Twinning and Slip*, Acta Metallurgica, 1 (1953), pp. 49–70.

[36] E. R. CALEY, *The earliest known use of a material containing uranium*, Isis, 38 (1948), pp. 190–193.

[37] W. D. CALLISTER AND D. G. RETHWISCH, *Materials Science and Engineering: An Introduction*, John Wiley & Sons, 8th editio ed., 2006.

[38] D. A. CARPENTER AND R. A. VANDERMEER, *An X-ray diffraction study of a martensitic transformation in uranium alloys*, Le Journal de Physique Colloques, 43 (1982), pp. C4–395.

[39] J. CATHCART AND G. F. PETERSEN, *The Low-Temperature Oxidation of U-Nb and U-Nb-Zr Alloys*, Journal of Nuclear Materials, 43 (1972), pp. 86–92.

[40] A. CEZAIRLIYAN, *Radiance temperature of niobium at its melting point*, Res. Natl. Bur. Stand. A, 77 (1973), pp. 333–339.

[41] S. CHAKRABORTY, G. CHOUDHURI, J. BANERJEE, R. AGARWAL, K. KHAN, AND A. KUMAR, *Micro-structural study and Rietveld analysis of fast reactor fuels: U–Mo fuels*, Journal of Nuclear Materials, 467 (2015), pp. 618–627.

[42] A. CHANDRA, M. SUMPTION, AND G. S. FRANKEL, *On the mechanism of niobium electropolishing*, Journal of the Electrochemical society, 159 (2012), pp. C485–C491.

[43] N. CHATTERJEE, *Electron Microprobe Analysis*, Massachusetts Institute of Technology, Cambridge, (2012).

[44] Z. CHEN, H. J. BONG, D. LI, AND R. H. WAGONER, *The elastic–plastic transition of metals*, International Journal of Plasticity, 83 (2016), pp. 178–201.

[45] G. CHESNUT AND Y. VOHRA, *A-Uranium Phase in Compressed Neodymium Metal*, Phys. Rev. B, 61 (2000), pp. R3768–R3771.

[46] A. A. CHESWORTH, J. A. CLARKE, G. S. DOBBING, D. J. HOLDER, H. L. OWEN, M. W. POOLE, S. L. SMITH, V. P. SULLER, AND A. WOLSKI, *DIAMOND: a UK national light source project*, in Proceedings of the 1999 Particle Accelerator Conference (Cat. No. 99CH36366), vol. 4, IEEE, 1999, pp. 2433–2435.

[47] P. CHIOTTI, *High temperature crystal structure of thorium*, Journal of The Electrochemical Society, 101 (1954), pp. 567–570.

[48] P. CHIOTTI, H. H. KLEPFER, AND R. W. WHITE, *Lattice Parameters of Uranium from 25 to 1132 C*, Trans. Am. Soc. Met, 51 (1959), pp. 772–782.

[49] H. H. CHISWIK, A. E. DWIGHT, L. T. LLOYD, M. V. NEVITT, AND S. T. ZEGLER, *Advances in the Physical Metallurgy of Uranium and its Alloys*, tech. rep., Second United Nations International Conference on the Peaceful Uses of Atomic Energy, 1958.

[50] A. CLARKE, K. CLARKE, R. MCCABE, C. NECKER, P. PAPIN, R. FIELD, A. KELLY, T. TUCKER, R. FORSYTH, P. DICKERSON, J. FOLEY, H. SWENSON, R. AIKIN, AND D. DOMBROWSKI, *Microstructural evolution of a uranium-10 wt % molybdenum alloy for nuclear reactor fuels*, Journal of Nuclear Materials, 465 (2015), pp. 784–792.

[51] A. Clarke, R. Field, R. Hackenberg, D. Thoma, D. Brown, D. Teter, M. Miller, K. Russell, D. Edmonds, and G. Beverini, *Low temperature age hardening in U–13at.% Nb: An assessment of chemical redistribution mechanisms*, Journal of Nuclear Materials, 393 (2009), pp. 282–291.

[52] A. J. Clarke, R. D. Field, R. J. McCabe, C. M. Cady, R. E. Hackenberg, and D. J. Thoma, *EBSD and FIB/TEM examination of shape memory effect deformation structures in U–14at.% Nb*, Acta materialia, 56 (2008), pp. 2638–2648.

[53] F. G. Cottrell, *Application of the Cottrell equation to chronoamperometry*, Z Physik Chem, 42 (1902), p. 385.

[54] A. G. Crocker, *The crystallography of deformation twinning in alpha-uranium*, Journal of Nuclear Materials, 16 (1965), pp. 306–326.

[55] E. Dabush, J. Sariel, I. Dahan, and G. Kimmel, *XRD Peak Broadening Effects in U-Mo alpha" Phase*, in Denver X-ray conference on Applications of X-ray Analysis, vol. 45, 2002.

[56] F. Dahlkamp, *Uranium Ore Deposits*, Springer-Verlag, 1993.

[57] C. D'Amato, F. S. Saraceno, and T. B. Wilson, *Phase transformations and equilibrium structures in uranium-rich niobium alloys*, Journal of Nuclear Materials, 12 (1964), pp. 291–304.

[58] M. Datta and D. Vercruysse, *Transpassive dissolution of 420 stainless steel in concentrated acids under electropolishing conditions*, Journal of The Electrochemical Society, 137 (1990), pp. 3016–3023.

[59] P. De Bievre and P. D. P. Taylor, *Table of the isotopic compositions of the elements*, International Journal of Mass Spectrometry and Ion Processes, 123 (1993), pp. 149–166.

[60] U. De Oliveira, V. Ocelík, and J. T. M. De Hosson, *Residual stress analysis in Co-based laser clad layers by laboratory X-rays and synchrotron diffraction techniques*, Surface and Coatings Technology, 201 (2006), pp. 533–542.

[61] C. Dean, *A study of the time-temperature transformation behavior of a uranium-7.5 weight per cent niobium-2.5 weight per cent zirconium alloys*, PhD thesis, Oak Ridge, Tennessee, 1969.

[62] S. R. Deans, *The Radon transform and some of its applications*, Courier Corporation, 2007.

[63] A. J. DeArdo, *Niobium in modern steels*, International Materials Reviews, 48 (2003), pp. 371–402.

[64] A. R. DENTON AND N. W. ASHCROFT, *Vegard's law*, Physical review A, 43 (1991), p. 3161.

[65] R. D. DESLATTES, E. G. KESSLER JR, P. INDELICATO, L. DE BILLY, E. LINDROTH, AND J. ANTON, *X-ray transition energies: new approach to a comprehensive evaluation*, Reviews of Modern Physics, 75 (2003), p. 35.

[66] DIAMOND, *Introduction to I12 – JEEP*.

[67] B. DJURIĆ, *Decomposition of gamma phase in a uranium-9.5 wt % niobium alloy*, Journal of Nuclear Materials, 44 (1972), pp. 207–214.

[68] J. DONOHUE AND H. EINSPAHR, *The structure of β-uranium*, Acta Crystallographica Section B: Structural Crystallography and Crystal Chemistry, 27 (1971), pp. 1740–1743.

[69] M. DRAKOPOULOS, T. CONNOLLEY, C. REINHARD, R. ATWOOD, O. MAGDYSYUK, N. VO, M. HART, L. CONNOR, B. HUMPHREYS, G. HOWELL, S. DAVIES, T. HILL, G. WILKIN, U. PEDERSEN, A. FOSTER, N. DE MAIO, M. BASHAM, F. YUAN, AND K. WANELIK, *I12: The Joint Engineering, Environment and Processing (JEEP) beamline at Diamond Light Source*, Journal of Synchrotron Radiation, 22 (2015), pp. 828–838.

[70] S. DRENSLER, L. NEELAKANTAN, C. SOMSEN, G. EGGELER, AND A. W. HASSEL, *Electropolishing of a nickel–titanium–copper shape memory alloy in methanolic sulfuric acid*, Electrochemical and Solid-State Letters, 12 (2009), pp. C1–C4.

[71] B. DU AND I. I. SUNI, *Mechanistic studies of Cu electropolishing in phosphoric acid electrolytes*, Journal of The Electrochemical Society, 151 (2004), pp. C375–C378.

[72] T. C. DUONG, R. E. HACKENBERG, A. LANDA, P. HONARMANDI, A. TALAPATRA, H. M. VOLZ, A. LLOBET, A. I. SMITH, G. KING, S. BAJAJ, A. RUBAN, L. VITOS, P. E. A. TURCHI, AND R. ARROYAVE, *Revisiting thermodynamics and kinetic diffusivities of uranium-niobium with Bayesian uncertainty analysis*, Calphad: Computer Coupling of Phase Diagrams and Thermochemistry, 55 (2016), pp. 219–230.

[73] K. H. ECKELMEYER, *Aging phenomena in dilute uranium alloys*, in Physical metallurgy of uranium alloys, J. Burke, D. Colling, A. Gorum, and J. Greenspan, eds., Boston, Massachusetts, 1976, p. 463.

[74] K. H. ECKELMEYER, A. D. ROMIG, AND L. J. WEIRICK, *The effect of quench rate on the microstructure, mechanical properties, and corrosion behaviour of U-6 wt pct Nb*, Metallurgical Transactions A, 15 (1984), pp. 1319–1330.

[75] M. ECKERT, *Max von Laue and the discovery of X-ray diffraction in 1912*, Annalen der Physik, 524 (2012), pp. A83–A85.

[76] J. W. EDWARDS, R. SPEISER, AND H. L. JOHNSTON, *High temperature structure and thermal expansion of some metals as determined by X-ray diffraction data. I. Platinum, tantalum, niobium, and molybdenum*, Journal of Applied Physics, 22 (1951), pp. 424–428.

[77] M. ELDRUP AND B. N. SINGH, *Accumulation of point defects and their complexes in irradiated metals as studied by the use of positron annihilation spectroscopy–a brief review*, Journal of nuclear materials, 323 (2003), pp. 346–353.

[78] F. ELLINGER AND W. ZACHARIASEN, *Structure of cerium metal at high pressure*, Physical Review Letters, 32 (1974), p. 773.

[79] F. H. ELLINGER, *Crystal structure of delta-prime plutonium and the thermal expansion characteristics of delta, delta-prime, and epsilon plutonium*, JOM, 8 (1956), pp. 1256–1259.

[80] J. EMSLEY, *Nature's building blocks: an AZ guide to the elements*, Oxford University Press, 2011.

[81] G. FEDOROV, E. SMIRNOV, AND V. GUSEV, *Diffusional and Thermodynamic Properties of the gamma-Phase of the System Uranium-Niobium*, Atomnaya Energiya, 32 (1972), pp. 11–14.

[82] E. FERMI, E. AMALDI, O. D'AGOSTINO, F. RASETTI, AND E. SEGRÈ, *Artificial radioactivity produced by neutron bombardment*, Proceedings of the Royal Society of London. Series A, Containing Papers of a Mathematical and Physical Character, 146 (1934), pp. 483–500.

[83] R. D. FIELD, A. J. CLARKE, R. J. MCCABE, D. W. BROWN, C. M. CADY, AND J. G. SWADENER, *Shape-Memory and Post-Shape-Memory Deformation in U-14at.%Nb*, tech. rep., Los Alamos National Laboratory, 2012.

[84] R. D. FIELD, R. J. MCCABE, D. J. ALEXANDER, AND D. F. TETER, *Deformation twinning and twinning related fracture in coarse-grained α-uranium*, Journal of Nuclear Materials, 392 (2009), pp. 105–113.

[85] R. D. FIELD, D. J. THOMA, P. S. DUNN, D. W. BROWN, AND C. M. CADY, *Martensitic structures and deformation twinning in the U–Nb shape-memory alloys*, Philosophical Magazine A, 81 (2001), pp. 1691–1724.

[86] J. FILIK, A. W. ASHTON, P. C. Y. CHANG, P. A. CHATER, S. J. DAY, M. DRAKOPOULOS, M. W. GERRING, M. L. HART, O. V. MAGDYSYUK, AND S. MICHALIK, *Processing two-dimensional X-ray diffraction and small-angle scattering data in DAWN 2*, Journal of applied crystallography, 50 (2017), pp. 959–966.

[87] R. B. FIRESTONE AND V. S. SHIRLEY, *Table of isotopes, 2 volume set*, Table of Isotopes, 2 Volume Set, by Richard B. Firestone, Virginia S. Shirley (Editor), pp. 3168. ISBN 0-471-33056-6. Wiley-VCH, December 1998., (1998), p. 3168.

[88] A. C. FISHER, *Electrode Dynamics*, 1996.

[89] E. S. FISHER AND H. J. MCSKIMIN, *Adiabatic Elastic Moduli of Single Crystal Alpha-Uranium*, Journal of Applied Physics, 29 (1958), pp. 1473–1484.

[90] F. G. FOOTE, *Physical metallurgy of uranium*, Progress in Nuclear Energy, 1 (1956), pp. 81–201.

[91] F. G. FOOTE, *Ternary alloys of uranium, columbium, and zirconium*, aug 1960.

[92] K. FUSHIMI, M. STRATMANN, AND A. W. HASSEL, *Electropolishing of NiTi shape memory alloys in methanolic* H_2SO_4, Electrochimica Acta, 52 (2006), pp. 1290–1295.

[93] L. M. GAMMON, R. D. BRIGGS, J. M. PACKARD, K. W. BATSON, R. BOYER, AND C. W. DOMBY, *ASM Handbook, Volume 9: Metallography and Microstructures*, ASM International, (2004), pp. 899–917.

[94] B. GEDDES, H. LEON, AND X. HUANG, *Superalloys: alloying and performance*, ASM International, 2010.

[95] L. A. GIANNUZZI AND F. A. STEVIE, *A review of focused ion beam milling techniques for TEM specimen preparation*, Micron, 30 (1999), pp. 197–204.

[96] S. GOVINDJEE AND E. KASPER, *A Shape Memory Alloy Model for Uranium-Niobium Accounting for Plasticity*, Journal of Intelligent Material Systems and Structures, 8 (1997), pp. 815–823.

[97] N. GREENWOOD AND A. EARNSHAW, *Chemistry of the Elements*, Butterworth-Heinemann, 2nd ed., 1997.

[98] I. GRENTHE, J. DROŻDŻYNŃSKI, T. FUJINO, E. C. BUCK, T. E. ALBRECHT-SCHMITT, AND S. F. WOLF, *Uranium*, in The chemistry of the actinide and transactinide elements, Springer, 2008, pp. 253–698.

[99] W. P. GRIFFITH AND P. J. T. MORRIS, *Charles Hatchett FRS (1765-1847), chemist and discoverer of niobium*, Notes and Records of the Royal Society of London, 57 (2003), pp. 299–316.

[100] R. D. GRIMM AND D. LANDOLT, *Salt films formed during mass transport controlled dissolution of iron-chromium alloys in concentrated chloride media*, Corrosion Science, 36 (1994), pp. 1847–1868.

[101] R. D. GRIMM, A. C. WEST, AND D. LANDOLT, *AC impedance study of anodically formed salt films on iron in chloride solution*, Journal of the electrochemical society, 139 (1992), pp. 1622–1629.

[102] J.-C. GRIVEAU AND E. COLINEAU, *Superconductivity in transuranic compounds*, Comptes Rendus Physique, 15 (2014), pp. 599–615.

[103] P. HAASEN, *Physical Metallurgy*, Cambridge University Press, Cambridge, third edit ed., 1996.

[104] HACKENBERG AND HEMPHILL, *Property and Lifetime Prediction in Aged U-Nb Alloys : A Statistical Assessment*, Los Alamos Internal, (2009).

[105] R. E. HACKENBERG, M. G. EMIGH, A. M. KELLY, P. A. PAPIN, R. T. FORSYTH, T. J. TUCKER, AND K. D. CLARKE, *The Surprising Occurrence of Non-Steady-State Growth of Divergent Lamellar Decomposition Products in Uranium- Niobium Alloys : A Preliminary Report*, tech. rep., Los Alamos National Laboratory, 2012.

[106] R. E. HACKENBERG, G. M. HEMPHILL, D. J. ALEXANDER, T. J. TUCKER, R. M. J. AIKIN, AND R. T. FORSYTH, *U-Nb Aging and Lifetime Prediction: Assessment for 2012*, tech. rep., Los Alamos National Laboratory, 2012.

[107] R. E. HACKENBERG AND KELLY, *Synthesis and Characterization of Nonbanded U - Nb Plate Material*, tech. rep., Los Alamos National Laboratory, 2007.

[108] A. P. HAMMERSLEY AND C. RIEKEL, *MFIT: Multiple spectra fitting program*, Synchrotron Radiation News, 2 (1989), pp. 24–26.

[109] C. R. HAMMOND, *The elements*, Handbook of chemistry and physics, 81 (2000).

[110] B. HATT, *The orientation relationship between the gamma and alpha structures in uranium-zirconium alloys*, Journal of Nuclear Materials, 19 (1966), pp. 133–141.

[111] B. A. HATT AND J. A. ROBERTS, *The ω-phase in zirconium base alloys*, Acta Metallurgica, 8 (1960), pp. 575–584.

[112] J. HE, I. KABAN, N. MATTERN, K. SONG, B. SUN, J. ZHAO, D. H. KIM, J. ECKERT, AND A. L. GREER, *Local microstructure evolution at shear bands in metallic glasses with nanoscale phase separation*, Scientific reports, 6 (2016), p. 25832.

[113] A. HEWAT, W. I. DAVID, AND L. VAN EIJCK, *Hugo Rietveld (1932–2016)*, Journal of Applied Crystallography, 49 (2016), pp. 1394–1395.

[114] R. G. HEWLETT AND O. E. ANDERSON, *The New World, 1939/1946: Volume I: a History of the United States Atomic Energy Commission*, Pennsylvania State University Press, 1962.

[115] T. P. HOAR AND G. P. ROTHWELL, *The influence of solution flow on anodic polishing. Copper in aqueous o-phosphoric acid*, Electrochimica Acta, 9 (1964), pp. 135–150.

[116] D. HOLDSTOCK AND F. BARNABY, *Hiroshima and Nagasaki: retrospect and prospect*, Psychology Press, 1995.

[117] G. HÖLZER, M. FRITSCH, M. DEUTSCH, J. HÄRTWIG, AND E. FÖRSTER, *$K\alpha_{1,2}$ and $K\beta_{1,3}$ x-ray emission lines of the 3d transition metals*, Physical Review A, 56 (1997), p. 4554.

[118] L. HSIUNG AND J. ZHOU, *Spinodal Decomposition and Order-Disorder Transformation in a Water-Quenched U-6wt % Nb Alloy*, tech. rep., Lawrence Livermore National Laboratory, 2006.

[119] L. HSIUNG AND J. ZHOU, *Low-Temperature Aging Kinetics of a 15-Year Old Water-Quenched U-6wt % Nb Alloy*, Tech. Rep. January, Lawrence Livermore National Laboratory, 2007.

[120] J. ILLINGWORTH AND J. KITTLER, *A survey of the Hough transform*, Computer vision, graphics, and image processing, 44 (1988), pp. 87–116.

[121] T. ISABELL, J. BRINK, M. KAWASAKI, B. ARMBRUSTER, I. ISHIKAWA, E. OKUNISHI, H. SAWADA, Y. OKURA, K. YAMAZAKI, AND T. ISHIKAWA, *Development of a 200kV atomic resolution analytical electron microscope*, Microscopy Today, 17 (2009), pp. 8–11.

[122] R. J. JACKSON, *Reversible martensitic transformations between transition phases of uranium-base niobium alloys*, tech. rep., The DOW Chemical Company, Rocky Flats Division, Golden, Colorado, 1970.

[123] R. J. JACKSON, *Isothermal Transformations Of Uranium–13 Atomic Percent Niobium*, tech. rep., 1971.

[124] R. J. JACKSON, *Metallographic study of segregation in uranium-base niobium alloys*, Metallography, 6 (1973), pp. 347–359.

[125] R. J. JACKSON, *Elastic, plastic, and strength properties of U–Nb and U–Nb–Zr alloys*, in Physical metallurgy of uranium alloys, 1976.

[126] R. J. JACKSON AND W. L. JOHNS, *Temperature-Induced Shape Memory In Polycrystalline Uranium-Base Niobium Alloys: Characterization*, tech. rep., 1970.

[127] C. Jacob and B. Warren, *The Crystalline Structure of Uranium*, Journal of the American Chemical Society, 59 (1937), pp. 2588–2591.

[128] A. H. Jaffey, K. F. Flynn, L. E. Glendenin, W. C. t. Bentley, and A. M. Essling, *Precision measurement of half-lives and specific activities of U 235 and U 238*, Physical review C, 4 (1971), p. 1889.

[129] R. D. James and K. F. Hane, *Martensitic transformations and shape-memory materials*, Acta materialia, 48 (2000), pp. 197–222.

[130] B. Johansson and S. Li, *Itinerant f-electron elements*, Philosophical Magazine, 89 (2009), pp. 1793–1799.

[131] F. Joliot and I. Curie, *Artificial production of a new kind of radio-element*, 1934.

[132] C. Jones, T. Scott, and J. Petherbridge, *Structural deformation of metallic uranium surrounding hydride growth sites*, Corrosion Science, 96 (2015), pp. 144–151.

[133] T. Kakeshita, K. Kuroiwa, K. Shimizu, T. Ikeda, A. Yamagishi, and M. Date, *Effect of magnetic fields on athermal and isothermal martensitic transformations in Fe–Ni–Mn alloys*, Materials Transactions, JIM, 34 (1993), pp. 415–422.

[134] M. M. Karnowsky and R. W. Rohde, *The transformation behavior of a U-16.4 at % Nb-5.6 at % Zr alloy*, Journal of Nuclear Materials, 49 (1973), pp. 81–90.

[135] Kaye & Laby, *Thermal Expansion*, 2010.

[136] A. M. Kelly, R. D. Field, and D. J. Thoma, *Metallographic preparation techniques for U-6 wt.%Nb*, Journal of Nuclear Materials, 429 (2012), pp. 118–127.

[137] A. M. Kelly, D. J. Thoma, R. D. Field, P. S. Dunn, and D. F. Teter, *Metallographic preparation techniques for uranium*, Journal of Nuclear Materials, 353 (2006), pp. 158–166.

[138] T. F. Kelly and D. J. Larson, *Atom probe tomography 2012*, Annual review of materials research, 42 (2012), pp. 1–31.

[139] N. W. Khun, M. Sumption, and G. S. Frankel, *Smoothening of niobium by electropolishing*, Journal of Applied Electrochemistry, 43 (2013), pp. 829–838.

[140] V. B. Kishinevskii, A. A. Tret'yakov, L. I. Gomozov, and O. S. Ivanov, *Kinetics of the Isothermal Transformation of Gamma Solid Solutions of Some Uranium Alloys*, tech. rep., Moscow, Russia, 1968.

[141] M. KNEZEVIC, L. CAPOLUNGO, C. N. TOMÉ, R. A. LEBENSOHN, D. J. ALEXANDER, B. MIHAILA, AND R. J. MCCABE, *Anisotropic stress–strain response and microstructure evolution of textured α-uranium*, Acta Materialia, 60 (2012), pp. 702–715.

[142] K. E. KNIPLING, D. J. ROWENHORST, R. W. FONDA, AND G. SPANOS, *Effects of focused ion beam milling on austenite stability in ferrous alloys*, Materials Characterization, 61 (2010), pp. 1–6.

[143] J. KOIKE, M. KASSNER, R. TATE, AND R. ROSEN, *The Nb-U (niobium-uranium) system*, Journal of Phase Equilibria, 19 (1998), pp. 253–260.

[144] K. KOJIMA AND C. W. TOBIAS, *Solution-Side Transport Processes in the Electropolishing of Copper in Phosphoric Acid*, Journal of The Electrochemical Society, 120 (1973), pp. 1026–1033.

[145] S. T. KONOBEEVSKY, A. S. ZAIMOVSKY, B. M. LEVITSKY, Y. N. SOKURSKY, N. T. CHEBOTAREV, Y. V. BOBKOV, P. P. EGOROV, G. N. NIKOLAEV, AND A. A. IVANOV, *Some physical properties of uranium, plutonium and their alloys*, in Proc. Second United Nations International Conference on the Peaceful Uses of Atomic Energy, vol. 6, United Nations Geneva, 1958, pp. 194–203.

[146] M. KURIHARA, M. HIRATA, R. SEKINE, J. ONOE, AND H. NAKAMATSU, *Theoretical study on the alloying behavior of γ-uranium metal: Γ-uranium alloy with 3d transition metals*, Journal of Nuclear Materials, 326 (2004), pp. 75–79.

[147] A. LANDA, P. SÖDERLIND, AND P. E. TURCHI, *Density-functional study of U-Mo and U-Zr alloys*, Journal of Nuclear Materials, 414 (2011), pp. 132–137.

[148] G. LANDER AND M. H. MUELLER, *Neutron diffraction study of alpha-Uranium at low temperatures*, Acta Crystallographica Section B, 26 (1970), pp. 129–136.

[149] G. H. LANDER, E. FISHER, AND S. BADER, *The solid-state properties of uranium A historical perspective and review*, Advances in Physics, 43 (1994), pp. 1–111.

[150] G. H. LANDER, E. S. FISHER, AND S. D. BADER, *The solid-state properties of uranium A historical perspective and review*, Advances in Physics, 43 (1994), pp. 1–111.

[151] D. LANDOLT, *Fundamental aspects of electropolishing*, Electrochimica Acta, 32 (1987), pp. 1–11.

[152] R. M. LANGFORD AND A. K. PETFORD-LONG, *Preparation of transmission electron microscopy cross-section specimens using focused ion beam milling*, Journal of Vacuum Science & Technology A: Vacuum, Surfaces, and Films, 19 (2001), pp. 2186–2193.

[153] A. C. LAWSON, C. E. OLSEN, J. W. RICHARDSON, M. H. MUELLER, AND G. H. LANDER, *Structure of β-uranium*, Acta Crystallographica Section B, 44 (1988), pp. 89–96.

[154] J. LEHMANN AND R. F. HILLS, *Proposed Nomenclature for Phases in Uranium Alloys*, Journal of Nuclear Materials, 2 (1960), pp. 261–268.

[155] H. LEIDHEISER AND A. T. GWATHMEY, *The influence of crystal face on the electrochemical properties of a single crystal of copper*, Transactions of the Electrochemical Society, 91 (1947), pp. 95–110.

[156] R. LINNEN, D. L. TRUEMAN, AND R. BURT, *Tantalum and niobium*, Critical Metals Handbook, (2014), pp. 361–384.

[157] P. LIPINSKI, M. BERVEILLER, E. REUBREZ, AND J. MORREALE, *Transition theories of elastic-plastic deformation of metallic polycrystals*, Archive of applied Mechanics, 65 (1995), pp. 291–311.

[158] X. J. LIU, Z. S. LI, J. WANG, AND C. P. WANG, *Thermodynamic modeling of the U-Mn and U-Nb systems*, Journal of Nuclear Materials, 380 (2008), pp. 99–104.

[159] L. T. LLOYD AND C. S. BARRETT, *Thermal expansion of alpha Uranium*, Journal of Nuclear Materials, 18 (1966), pp. 55–59.

[160] I. LOA, E. I. ISAEV, M. I. MCMAHON, D. Y. KIM, B. JOHANSSON, A. BOSAK, AND M. KRISCH, *Lattice dynamics and superconductivity in cerium at high pressure*, Physical Review Letters, 108 (2012), pp. 1–5.

[161] V. LOBODYUK AND E. ESTRIN, *Isothermal martensitic transformations*, Physics-uspekhi, 48 (2005), p. 713.

[162] D. A. LOPES, T. A. G. RESTIVO, AND A. F. PADILHA, *Phase transformation studies in U-Nb-Zr alloy*, Nuclear Engineering and Design, 265 (2013), pp. 619–624.

[163] S. MAGAINO, M. MATLOSZ, AND D. LANDOLT, *An impedance study of stainless steel electropolishing*, Journal of the electrochemical society, 140 (1993), pp. 1365–1373.

[164] J. B. MATHIEU, H. J. MATHIEU, AND D. LANDOLT, *Electropolishing of Titanium in Perchloric Acid-Acetic Acid Solution I. Auger Electron Spectroscopy Study of Anodic Films*, Journal of the Electrochemical Society, 125 (1978), pp. 1039–1043.

[165] M. MATLOSZ, *Modeling of impedance mechanisms in electropolishing*, Electrochimica acta, 40 (1995), pp. 393–401.

[166] M. MATLOSZ, S. MAGAINO, AND D. LANDOLT, *Impedance Analysis of a Model Mechanism for Acceptor-Limited Electropolishing*, Journal of the Electrochemical Society, 141 (1994), pp. 410–418.

[167] R. J. MCCABE, L. CAPOLUNGO, P. E. MARSHALL, C. M. CADY, AND C. N. TOMÉ, *Deformation of wrought uranium: experiments and modeling*, Acta Materialia, 58 (2010), pp. 5447–5459.

[168] R. J. MCCABE, A. W. RICHARDS, D. R. COUGHLIN, K. D. CLARKE, I. J. BEYERLEIN, AND M. KNEZEVIC, *Microstructure effects on the recrystallization of low-symmetry alpha-uranium*, Journal of Nuclear Materials, 465 (2015), pp. 189–195.

[169] R. J. MCCABE AND D. F. TETER, *Analysis of recrystallized volume fractions in uranium using electron backscatter diffraction*, Journal of Microscopy, 223 (2006), pp. 33–39.

[170] L. B. MCCUSKER, R. B. VON DREELE, D. E. COX, D. LOUËR, AND P. SCARDI, *Rietveld refinement guidelines*, Journal of Applied Crystallography, 32 (1999), pp. 36–50.

[171] J. MEIJA, T. B. COPLEN, M. BERGLUND, W. A. BRAND, P. DE BIÈVRE, M. GRÖNING, N. E. HOLDEN, J. IRRGEHER, R. D. LOSS, AND T. WALCZYK, *Atomic weights of the elements 2013 (IUPAC Technical Report)*, Pure and Applied Chemistry, 88 (2016), pp. 265–291.

[172] L. MEITNER AND O. R. FRISCH, *Disintegration of uranium by neutrons: a new type of nuclear reaction*, A Century of Nature: Twenty-One Discoveries that Changed Science and the World, (1939), p. 70.

[173] L. MEITNER AND O. R. FRISCH, *Products of the fission of the uranium nucleus*, Nature, 143 (1939), p. 471.

[174] M. MEIXNER, M. KLAUS, AND C. GENZEL, *Sin*$^2\psi$*-based residual stress gradient analysis by energy-dispersive synchrotron diffraction constrained by small gauge volumes. I. Theoretical concept*, Journal of Applied Crystallography, 46 (2013), pp. 610–618.

[175] J. MENDEZ, R. AKOLKAR, T. ANDRYUSHCHENKO, AND U. LANDAU, *A mechanistic model for copper electropolishing in phosphoric acid*, Journal of The Electrochemical Society, 155 (2008), pp. D27–D34.

[176] M. K. MEYER, G. L. HOFMAN, S. L. HAYES, C. R. CLARK, T. C. WIENCEK, J. L. SNELGROVE, R. V. STRAIN, AND K. H. KIM, *Low-temperature irradiation behavior of uranium-molybdenum alloy dispersion fuel*, Journal of Nuclear Materials, 304 (2002), pp. 221–236.

[177] M. K. MILLER, *Atom probe tomography: analysis at the atomic level*, Springer Science & Business Media, 2012.

[178] M. K. MILLER AND R. G. FORBES, *Atom probe tomography*, Materials Characterization, 60 (2009), pp. 461–469.

[179] M. MITCHELL, B. MUFTAKHIDINOV, T. WINCHEN, AND E. AL, *Engauge Digitizer Software*, 2019.

[180] S. MOHAN, D. KANAGARAJ, R. SINDHUJA, S. VIJAYALAKSHMI, AND N. G. RENGANATHAN, *Electropolishing of stainless steel—A review*, Transactions of the IMF, 79 (2001), pp. 140–142.

[181] K. MOMMA AND F. IZUMI, *VESTA 3 for three-dimensional visualization of crystal, volumetric and morphology data*, Journal of Applied Crystallography, 44 (2011), pp. 1272–1276.

[182] M. T. MYERS, B. H. SENCER, AND L. SHAO, *Multi-scale modeling of localized heating caused by ion bombardment*, Nuclear Inst. and Methods in Physics Research, B, 272 (2012), pp. 165–168.

[183] Z. NISHIYAMA, *Martensitic Transformation*, Academic Press, New York, London, 1978.

[184] NIST AND PHYSICAL MEASUREMENT LABORATORY, *X-Ray Mass Attenuation Coefficients*.

[185] G. NOLZE, A. WINKELMANN, AND A. P. BOYLE, *Pattern matching approach to pseudosymmetry problems in electron backscatter diffraction*, Ultramicroscopy, 160 (2016), pp. 146–154.

[186] I. NOWAK AND M. ZIOLEK, *Niobium compounds: preparation, characterization, and application in heterogeneous catalysis*, Chemical Reviews, 99 (1999), pp. 3603–3624.

[187] M. M. NOWELL, R. A. WITT, AND B. W. TRUE, *EBSD sample preparation: Techniques, tips, and tricks*, Microscopy Today, 13 (2005), pp. 44–49.

[188] H. OKAMOTO, *Nb-U (Niobium-Uranium)*, Journal of Phase Equilibria and Diffusion, 30 (2009), p. 411.

[189] C. T. OLOFSON, G. E. MEYER, AND A. L. HOFFMANNER, *Processing and Applications of Depleted Uranium Alloy Products*, tech. rep., Battelle-Columbus Laboratories, Columbus, Ohio, 1976.

[190] F. OPEKAR AND P. BERAN, *Rotating disk electrodes*, Journal of Electroanalytical Chemistry and Interfacial Electrochemistry, 69 (1976), pp. 1–105.

[191] J. ORLOFF, *Handbook of charged particle optics*, CRC press, 2008.

[192] C. OSHIMA, E. BANNAI, T. TANAKA, AND S. KAWAI, *Thermionic work function of LaB6 single crystals and their surfaces*, Journal of Applied Physics, 48 (1977), pp. 3925–3927.

[193] K. OTSUKA AND C. M. WAYMAN, *Shape memory materials*, Cambridge university press, 1999.

[194] R. A. OWEN, R. V. PRESTON, P. J. WITHERS, H. R. SHERCLIFF, AND P. J. WEBSTER, *Neutron and synchrotron measurements of residual strain in TIG welded aluminium alloy 2024*, Materials Science and Engineering: A, 346 (2003), pp. 159–167.

[195] R. W. D. PAIS, A. M. M. DOS SANTOS, F. S. LAMEIRAS, AND W. B. FERRAZ, *Isothermal phase transformation of U-Zr-Nb alloys for advanced nuclear fuels*, in Current Research in Nuclear Reactor Technology in Brazil and Worldwide, IntechOpen, 2013.

[196] S. R. PATI AND M. COHEN, *Nucleation of the isothermal martensitic transformation*, Acta Metallurgica, 17 (1969), pp. 189–199.

[197] T. A. PEDROSA, A. M. M. DOS SANTOS, F. S. LAMEIRAS, P. R. CETLIN, AND W. B. FERRAZ, *Phase transitions during artificial ageing of segregated as-cast U-Mo alloys*, Journal of Nuclear Materials, 457 (2015), pp. 100–117.

[198] C. T. PETERS, P. BOLTON, AND A. P. MIODOWNIK, *The effect of magnetic fields on isothermal martensitic transformations*, Acta metallurgica, 20 (1972), pp. 881–886.

[199] C. PETERSON, W. STEELE, AND S. DIGIALLONARDO, *Isothermal transformation study of some Uranium-base alloys*, tech. rep., University of California, Lawrence Radiation Laboratory, Livermore, California, 1964.

[200] N. L. PETERSON AND R. E. OGILVIE, *Diffusion Studies in the Uranium-Niobium (Columbium) System*, Trans. Met. Soc. AIME, 218 (1960).

[201] PHILIPS, *X'Pert PRO System- User's Guide, Part II - Chapter 1: X-ray Tubes*, tech. rep.

[202] M. T. POSTEK, *An approach to the reduction of hydrocarbon contamination in the scanning electron microscope*, Scanning: The Journal of Scanning Microscopies, 18 (1996), pp. 269–274.

[203] P. D. PREWETT AND G. L. R. MAIR, *Focused ion beams from liquid metal ion sources*, vol. 1, Research Studies PressLtd, 1991.

[204] N. D. PRIEST, *Toxicity of depleted uranium*, The Lancet, 357 (2001), pp. 244–246.

[205] G. RAYNER-CANHAM AND Z. ZHENG, *Naming elements after scientists: an account of a controversy*, Foundations of Chemistry, 10 (2008), pp. 13–18.

[206] L. REIMER, *Emission of backscattered and secondary electrons*, in Scanning Electron Microscopy, Springer, 1998, pp. 135–169.

[207] O. W. RICHARDSON, *The emission of electricity from hot bodies*, Longmans, Green and Company, 1921.

[208] H. RIETVELD, *A profile refinement method for nuclear and magnetic structures*, Journal of applied Crystallography, 2 (1969), pp. 65–71.

[209] H. M. RIETVELD, *Line profiles of neutron powder-diffraction peaks for structure refinement*, Acta Crystallographica, 22 (1967), pp. 151–152.

[210] R. O. RITCHIE, *The conflicts between strength and toughness*, Nature materials, 10 (2011), p. 817.

[211] R. ROBERGE, *Lattice parameter of niobium between 4.2 and 300 K*, Journal of the Less Common Metals, 40 (1975), pp. 161–164.

[212] B. A. ROGERS, D. F. ATKINS, E. J. MANTHOS, AND M. E. KIRKPATRICK, *Uranium-columbium alloy diagram*, Trans. Met. Soc. AIME, 212 (1958).

[213] W. C. RÖNTGEN, *On a new kind of rays*, Science, 3 (1896), pp. 227–231.

[214] H. ROSE, *Ueber die Zusammensetzung der Tantalite und ein im Tantalite von Baiern enthaltenes neues Metall*, Annalen der Physik, 139 (1844), pp. 317–341.

[215] C. ROTTY, A. MANDROYAN, M.-L. DOCHE, AND J. Y. HIHN, *Electropolishing of CuZn brasses and 316L stainless steels: Influence of alloy composition or preparation process (ALM vs. standard method)*, Surface and Coatings Technology, 307 (2016), pp. 125–135.

[216] F. ROUGH AND A. BAUER, *Constitution of uranium and thorium alloys*, tech. rep., Battelle Memorial Institute, Columbus, Ohio, 1958.

[217] E. RUSKA, *Die elektronenmikroskopische abbildung elektronenbestrahlter oberflächen*, Zeitschrift für Physik, 83 (1933), pp. 492–497.

[218] E. RUSKA, *The development of the electron microscope and of electron microscopy*, Reviews of modern physics, 59 (1987), p. 627.

[219] I. SCHNELL AND R. C. ALBERS, *Zirconium under pressure: phase transitions and thermodynamics*, Journal of Physics: Condensed Matter, 18 (2006), p. 1483.

[220] R. A. SCHWARZER, D. P. FIELD, B. L. ADAMS, M. KUMAR, AND A. J. SCHWARTZ, *Present state of electron backscatter diffraction and prospective developments*, in Electron backscatter diffraction in materials science, Springer, 2009, pp. 1–20.

[221] T. SCOTT, K. HALLAM, AND C. YOUNES, *An experimental investigation into the ageing behaviour of UNb7 alloys*, tech. rep., University of Bristol, 2012.

[222] T. SCOTT AND C. JONES, *Microstructural Characteristaion of Uranium-Niobium (6%) Alloys Using Complementary Diffraction Analysis Techniques*, tech. rep., University of Bristol, 2010.

[223] T. SCOTT, J. MACFARLANE, K. HALLAM, AND C. YOUNES, *An experimental investigation into the ageing behaviour of UNb5 alloys*, tech. rep., University of Bristol, 2013.

[224] T. B. SCOTT, J. R. PETHERBRIDGE, I. FINDLAY, J. GLASCOTT, AND G. C. ALLEN, *Recrystallisation of uranium resulting from electron beam welding*, Journal of Alloys and Compounds, 475 (2009), pp. 766–772.

[225] V. F. SEARS, *Neutron scattering lengths and cross sections*, Neutron news, 3 (1992), pp. 26–37.

[226] D. N. SEIDMAN, *Three-dimensional atom-probe tomography: Advances and applications*, Annu. Rev. Mater. Res., 37 (2007), pp. 127–158.

[227] G. Y. SERGEEV, V. V. TITOVA, AND K. A. BORISOV, *Metallurgy of Uranium and Some Reactor Materials*, 1960.

[228] C. H. SHIH, B. L. AVERBACH, AND M. COHEN, *Some characteristics of the isothermal martensitic transformation*, JOM, 7 (1955), pp. 183–187.

[229] P. SIGMUND, *Energy density and time constant of heavy-ion-induced elastic-collision spikes in solids*, Applied Physics Letters, 25 (1974), pp. 169–171.

[230] V. P. SINHA, G. J. PRASAD, P. V. HEGDE, R. KESWANI, C. B. BASAK, S. PAL, AND G. P. MISHRA, *Development, preparation and characterization of uranium molybdenum alloys for dispersion fuel application*, Journal of Alloys and Compounds, 473 (2009), pp. 238–244.

[231] J. C. SLATER, *Atomic radii in crystals*, The Journal of Chemical Physics, 41 (1964), pp. 3199–3204.

[232] J. V. SMITH, *Tutorial review. synchrotron x-ray sources: instrumental characteristics. new applications in microanalysis, tomography, absorption spectroscopy and diffraction*, Analyst, 120 (1995), pp. 1231–1245.

[233] J. SNELGROVE, G. HOFMAN, M. MEYER, C. TRYBUS, AND T. WIENCEK, *Development of very-high-density low-enriched-uranium fuels*, Nuclear Engineering and Design, 178 (1997), pp. 119–126.

[234] R. L. SNYDER, H. J. BUNGE, AND J. FIALA, *Defect and microstructure analysis by diffraction*, Oxford Univ. Press, 1999.

[235] P. SÖDERLIND, O. ERIKSSON, B. JOHANSSON, J. M. WILLS, AND A. M. BORING, *A unified picture of the crystal structures of metals*, 1995.

[236] H. E. SOSTMAN, *Melting point of gallium as a temperature calibration standard*, Review of Scientific Instruments, 48 (1977), pp. 127–130.

[237] J. G. SPEER AND D. V. EDMONDS, *An Investigation of the gamma to alpha Martensitic Transformation in Uranium Alloys*, Acta Metallurgica, 36 (1988), pp. 1015–1033.

[238] R. SPRINGELL, B. DETLEFS, G. LANDER, R. WARD, R. COWLEY, N. LING, W. GOETZE, R. AHUJA, W. LUO, AND B. JOHANSSON, *Elemental engineering: Epitaxial uranium thin films*, Physical Review B, 78 (2008), p. 193403.

[239] H. T. STEEPLE AND T. ASHWORTH, *The minimum-residual refinement of β-uranium from polycrystalline data*, Acta Crystallographica, 21 (1966), pp. 995–998.

[240] P. W. STEPHENS, *Phenomenological model of anisotropic peak broadening in powder diffraction*, Journal of Applied Crystallography, 32 (1999), pp. 281–289.

[241] D. STEWART AND G. I. WILLIAMS, *The Structure and Occurence of the Metastable Monoclinic Phase, α", in Uranium-Molybdenum Alloys*, Journal of Nuclear Materials, 20 (1966), pp. 262–268.

[242] C. A. STITT, N. J. HARKER, K. R. HALLAM, C. PARASKEVOULAKOS, A. BANOS, S. RENNIE, J. JOWSEY, AND T. B. SCOTT, *An investigation on the persistence of uranium hydride during storage of simulant nuclear waste packages*, PLoS ONE, 10 (2015), pp. 1–13.

[243] C. A. STITT, M. HART, N. J. HARKER, K. R. HALLAM, J. MACFARLANE, A. BANOS, C. PARASKEVOULAKOS, E. BUTCHER, C. PADOVANI, AND T. B. SCOTT, *Nuclear waste viewed in a new light; a synchrotron study of uranium encapsulated in grout*, Journal of Hazardous Materials, 285 (2015), pp. 221–227.

[244] C. A. STITT, C. PARASKEVOULAKOS, A. BANOS, N. J. HARKER, K. R. HALLAM, A. DAVENPORT, S. STREET, AND T. B. SCOTT, *In-situ, time resolved monitoring of uranium in BFS:OPC grout. Part 1: Corrosion in water vapour.*, Scientific reports, 7 (2017), p. 7999.

[245] C. A. STITT, C. PARASKEVOULAKOS, A. BANOS, N. J. HARKER, K. R. HALLAM, H. PULLIN, A. DAVENPORT, S. STREET, AND T. B. SCOTT, *In-situ, time resolved monitoring of uranium in BFS:OPC grout. Part 2: Corrosion in water*, Scientific Reports, 8 (2018), p. 9282.

[246] C. A. STITT, C. PARASKEVOULAKOS, N. J. HARKER, A. BANOS, K. R. HALLAM, C. P. JONES, AND T. B. SCOTT, *Real time, in-situ deuteriding of uranium encapsulated in*

grout; effects of temperature on the uranium-deuterium reaction, Corrosion Science, 127 (2017), pp. 270–279.

[247] E. STURCKEN AND B. POST, *The atomic position parameter in alpha uranium*, Acta Crystallographica, 13 (1960), p. 852.

[248] C. SURYANARAYANA AND M. G. NORTON, *X-ray diffraction: a practical approach*, Springer Science & Business Media, 2013.

[249] J. E. SUTCLIFFE, C. P. JONES, J. E. DARNBROUGH, K. R. HALLAM, R. S. SPRINGELL, P. RYAN, T. CARTWRIGHT, AND T. B. SCOTT, *Low Temperature Ageing Behaviour of U-Nb γ-o Phase Alloys*, arXiv preprint arXiv:1803.05700, (2018).

[250] J. E. SUTCLIFFE, J. R. PETHERBRIDGE, T. CARTWRIGHT, R. SPRINGELL, T. B. SCOTT, AND J. E. DARNBROUGH, *Preparation and analysis of strain-free uranium surfaces for electron and x-ray diffraction analysis*, arXiv preprint arXiv:1803.05712, (2018).

[251] J. E. SUTCLIFFE, J. R. PETHERBRIDGE, T. CARTWRIGHT, R. SPRINGELL, T. B. SCOTT, AND J. E. DARNBROUGH, *Preparation and analysis of strain-free uranium surfaces for electron and x-ray diffraction analysis*, Materials Characterization, 158 (2019), p. 109968.

[252] K. TANGRI, D. K. CHAUDHURI, AND C. N. RAO, *Metastable phases in uranium alloys with high solute solubility in the BCC gamma phase. Part I — the system U-Nb*, Journal of Nuclear Materials, 15 (1965), pp. 288–297.

[253] K. TANGRI AND G. I. WILLIAMS, *Metastable phases in the uranium-molybdenum*, 2 (1961), pp. 226–233.

[254] M. A. TARSELLI, *Subtle niobium*, Nature chemistry, 7 (2015), p. 180.

[255] THE NOBEL PRIZE, *Enrico Fermi - Biographical, nobelprize.org/prizes/physics/1938/fermi/biographical/, Accessed: 2019-07-16.*

[256] THE NOBEL PRIZE, *Ernst Ruska - Biographical, nobelprize.org/prizes/physics/1986/ruska/, Accessed: 2019-07-16.*

[257] THE NOBEL PRIZE, *Henri Becquerel - Biographical, nobelprize.org/prizes/physics/1903/becquerel/biographical/, Accessed: 2019-07-16.*

[258] THE NOBEL PRIZE, *Otto Hahn - Biographical, nobelprize.org/prizes/chemistry/1944/hahn/biographical/, Accessed: 2019-07-16.*

[259] THE NOBEL PRIZE, *The Nobel Prize in Physics 1903, nobelprize.org/prizes/physics/1903/summary/, Accessed: 2019-07-16.*

[260] THE NOBEL PRIZE, *The Nobel Prize in Physics 1914, nobelprize.org/prizes/physics/1914/summary/, Accessed: 2019-07-16.*

[261] THE NOBEL PRIZE, *The Nobel Prize in Physics 1915, nobelprize.org/prizes/physics/1915/summary/, Accessed: 2019-07-16.*

[262] THE NOBEL PRIZE, *The Nobel Prize in Physics 1986, nobelprize.org/prizes/physics/1986/summary/, Accessed: 2019-07-16.*

[263] J. THEWLIS AND H. STEEPLE, *The β-uranium structure*, Acta Crystallographica, 7 (1954), pp. 323–328.

[264] K. THOMPSON, D. LAWRENCE, D. J. LARSON, J. D. OLSON, T. F. KELLY, AND B. GORMAN, *In situ site-specific specimen preparation for atom probe tomography*, Ultramicroscopy, 107 (2007), pp. 131–139.

[265] H. TIAN, S. G. CORCORAN, C. E. REECE, AND M. J. KELLEY, *The mechanism of electropolishing of niobium in hydrofluoric–sulfuric acid electrolyte*, Journal of the Electrochemical Society, 155 (2008), pp. D563–D568.

[266] B. TOBY AND R. VON DREELE, *GSAS-II: the genesis of a modern open-source all purpose crystallography software package*, Journal of Applied Crystallography, 46 (2013), pp. 544–549.

[267] Y. S. TOULOUKIAN, R. K. KIRBY, R. E. TAYLOR, AND P. D. DESAI, *Thermal expansion: metallic elements and alloys*, vol. 2, IFI/Plenum New York, 1975.

[268] R. TOWNSEND AND J. BURKE, *Direct Evidence for Three Transformation Mechanisms for the beta to alpha Phase Change in Uranium - Chromium Alloys*, Nature, 207 (1965), pp. 161–164.

[269] C. W. TUCKER, *The crystal structure of the β phase of uranium*, Acta Crystallographica, 4 (1951), pp. 425–431.

[270] C. W. TUCKER AND P. SENIO, *An improved determination of the crystal structure of β-uranium*, Acta Crystallographica, 6 (1953), pp. 753–760.

[271] F. TUOMISTO AND I. MAKKONEN, *Defect identification in semiconductors with positron annihilation: experiment and theory*, Reviews of Modern Physics, 85 (2013), p. 1583.

[272] C. VALOT, S. CONRADSON, D. TETER, D. THOMA, AND E. PETERSON, *Local Atomic Structure in Uranium-Niobium Shape Memory Alloys*, in Plutonium Futures-The Science, vol. 673, 2003, pp. 219–220.

[273] R. A. VANDERMEER, *Recent Observations of Phase Transformations in a U-Nb-Zr Alloy*, tech. rep., Oak Ridge National Lab., Tenn. (USA), 1973.

[274] R. A. VANDERMEER, *Phase Transformations in a Uranium 14% Nb Alloy*, Acta Metallurgica, 28 (1980), pp. 383–393.

[275] R. A. VANDERMEER, *Shape Memory Effect in Uranium-Niobium Alloys Below Room Temperature*, Tech. Rep. March, Lawrence Livermore National Laboratory, 1985.

[276] R. A. VANDERMEER, J. C. OGLE, AND W. G. NORTHCUTT, *A Phenomenological Study of the Shape Memory Effect in Polycrystalline Uranium-Niobium Alloys*, Metallurgical Transactions, 12 (1981), pp. 733–741.

[277] R. A. VANDERMEER, J. C. OGLE, AND W. SNYDER JR, *Shape Memory Effects in a Uranium + 14 at.% Niobium Alloy*, Scripta Metallurgica, 12 (1978), pp. 243–283.

[278] C. A. VOLKERT AND A. M. MINOR, *Focused ion beam microscopy and micromachining*, MRS bulletin, 32 (2007), pp. 389–399.

[279] H. M. VOLZ, R. E. HACKENBERG, A. M. KELLY, W. L. HULTS, A. C. LAWSON, R. D. FIELD, D. F. TETER, AND D. J. THOMA, *X-ray diffraction analyses of aged U-Nb alloys*, Journal of Alloys and Compounds, 444-445 (2007), pp. 217–225.

[280] R. B. VON DREELE, *Quantitative texture analysis by Rietveld refinement*, Journal of Applied Crystallography, 30 (1997), pp. 517–525.

[281] M. VON LAUE, *Eine quantitative prüfung der theorie für die interferenz-erscheinungen bei röntgenstrahlen*, Verlag der Kgl. Bayer. Akad. der Wiss., 1912.

[282] V. VOORT AND F. GEORGE, *Atlas of Time-Temperature Diagrams for Nonferrous Alloys*, ASM international, 1991.

[283] C. WAGNER, *Contribution to the theory of electropolishing*, Journal of the electrochemical society, 101 (1954), pp. 225–228.

[284] B. E. WARREN AND B. L. AVERBACH, *The effect of cold-work distortion on X-ray patterns*, Journal of applied physics, 21 (1950), pp. 595–599.

[285] Y. WEI, Y. LI, L. ZHU, Y. LIU, X. LEI, G. WANG, Y. WU, Z. MI, J. LIU, H. WANG, AND H. GAO, *Evading the strength–ductility trade-off dilemma in steel through gradient hierarchical nanotwins*, Nature Communications, 5 (2014), p. 3580.

[286] U. WELZEL, J. LIGOT, P. LAMPARTER, A. C. VERMEULEN, AND E. J. MITTEMEIJER, *Stress analysis of polycrystalline thin films and surface regions by X-ray diffraction*, Journal of Applied Crystallography, 38 (2005), pp. 1–29.

[287] D. W. WHEELER AND S. T. MORRIS, *Micro-mechanical characterisation of uranium*, Journal of Nuclear Materials, 385 (2009), pp. 122–125.

[288] D. WHITE, *Transformation Kinetics in Uranium-Chromium Alloys*, JOM, 7 (1955), pp. 1221–1228.

[289] G. K. WILLIAMSON AND W. H. HALL, *X-ray line broadening from filed aluminium and wolfram*, Acta metallurgica, 1 (1953), pp. 22–31.

[290] A. WINKELMANN, *Dynamical simulation of electron backscatter diffraction patterns*, in Electron backscatter diffraction in materials science, Springer, 2009, pp. 21–33.

[291] S. I. WRIGHT AND M. M. NOWELL, *EBSD image quality mapping*, Microscopy and microanalysis, 12 (2006), pp. 72–84.

[292] Y. WU, Q. WU, S. ZHU, Z. PU, Y. ZHANG, Q. WANG, D. LANG, AND Y. ZHANG, *Effect of niobium element on the electrochemical corrosion behavior of depleted uranium*, Journal of Nuclear Materials, 478 (2016), pp. 7–12.

[293] H. YAKEL, *Crystal Structures of Transition Phases Formed in U-16.6at%Nb-5.64at%Zr Alloys*, Journal of Nuclear Materials, 33 (1969), pp. 286–295.

[294] V. YEMEL'YANOV AND A. YEVSTYUKHIN, *The Metallurgy of Nuclear Fuel*, Pergamon Press Ltd., 1969.

[295] R. A. YOUNG, *The Rietveld Method*, vol. 5, International union of crystallography, 1993.

[296] W. H. ZACHARIASEN, *Crystal chemical studies of the 5f-series of elements. XVII. The crystal structure of neptunium metal*, Acta Crystallographica, 5 (1952), pp. 660–664.

[297] ZEISS, *Zeiss Sigma Family: Your Field Emission SEMs for High Quality Imaging and Advanced Analytical Microscopy, Product Information, Version 2.4.*

[298] C. ZHANG, H. WANG, J. LI, B. PANG, Y. XIA, Y. LIU, G. SUN, X. ZHANG, T. FA, AND X. WANG, *The aging-effect-modulated mechanical behavior in U-Nb shape memory alloys through the modified twinning-detwinning process of the α" phase*, Materials and Design, 162 (2019), pp. 94–105.

[299] C. ZHANG, L. XIE, Z. FAN, H. WANG, X. CHEN, J. LI, AND G. SUN, *Straightforward understanding of the structures of metastable α" and possible ordered phases in uranium-niobium alloys from crystallographic simulation*, Journal of Alloys and Compounds, 648 (2015), pp. 389–396.

[300] J. Zhang, D. W. Brown, B. Clausen, S. C. Vogel, and R. E. Hackenberg, *In Situ Time-Resolved Phase Evolution and Phase Transformations in U-6 Wt Pct Nb*, Metallurgical and Materials Transactions A, 50 (2019), pp. 2619–2628.

[301] Y. Zhang, X. Wang, Q. Xu, and Y. Li, *X-ray diffraction study of low temperature aging in U–5.8wt.%Nb*, Journal of Nuclear Materials, 456 (2015), pp. 41–45.

[302] J. Zhou and L. M. Hsiung, *Long-term phase instability in a water-quenched uranium alloy*, J. Mater. Res., 21 (2006), pp. 904–909.

[303] P. Zhou, D. Xiao, W. Wang, G. Sang, Y. Zhao, D. Zou, and L. He, *Twinning behavior of polycrystalline alpha-uranium under quasi static compression*, Journal of Nuclear Materials, 478 (2016), pp. 83–90.

[304] A. Zubelewicz, F. L. Addessio, and C. M. Cady, *A constitutive model for a uranium-niobium alloy*, Journal of Applied Physics, 100 (2006).